3.0. TRAC CLOSURE MODELS

Section 3.0. serves as a basic reference or road map to the thermal-hydraulic closure relations in TRAC. Additional detail on TRAC's closure models can be found in the appendices of this document. The relevant appendices are indicated in the following sections.

Before we discuss the closure relations, we will define the nomenclature to be used. In all cases, the subscript g (for gas) refers to a mixture of water vapor and noncondensable gas. The subscripts v (for vapor) and a (for air) denote properties or parameters specifically relating to the water vapor and noncondensable gas, respectively. Similarly, the subscript l (for liquid) applies specifically to properties relating to liquid water. In cases of a two-phase mixture, the subscript m (for mixture) is applied.

NOMENCLATURE

A:	area
a_i:	interfacial-area concentration
a_{if}:	interfacial area per unit volume
B_{cell}:	cell volume
c:	drag coefficient
C_{an}:	roughness parameter to account for waviness
C_d:	drag coefficient for spherical droplets
c_{Db}:	bubble drag coefficient
C_{eva}:	coefficient of evaporation
c_f:	coefficient of friction
c_p:	specific heat
C_r:	waviness factor
Ca:	capillary number
D, d:	diameter
D_h:	hydraulic diameter
D_o:	diffusion coefficient
e:	internal energy
E:	entrainment fraction
f:	friction factor
F:	adjustment factor
F_e:	evaporation fraction
f_{fo}:	single-phase friction factor
f_l:	liquid fraction contacting wall

F_s: sink function to account for the effect of entrained droplets

F_u: cold-wall fraction

fcdrop: numerical factor

ffd: numerical factor

ffs: numerical factor

g: gravitational acceleration

G: mass flux ($kg \cdot m^{-2} \cdot s^{-1}$)

Gr: Grashof number

h: enthalpy

H: heat-transfer factor

H_{ALV}: liquid-side heat-transfer factor during flashing

H_{ALVE}: liquid-side heat-transfer factor during condensation and evaporation

H_{CHTA}: gas-to-liquid sensible heat-transfer factor

H_{CHTI}: vapor-side heat-transfer factor ($W \cdot K^{-1}$)

h_{fg}: latent heat of vaporization

h_{fls}: liquid-side heat-transfer coefficient associated with flashing

h_{forc}: wall-to-liquid heat-transfer coefficient during single-phase forced convection

h_{gl}: gas-to-liquid sensible heat-transfer coefficient ($W \cdot m^{-2} \cdot K^{-1}$)

h_{gNC}: turbulent natural-convection heat-transfer coefficient

h_{gturb}: turbulent forced-convection heat-transfer coefficient

h_{ig}: interface-to-gas heat-transfer coefficient ($W \cdot m^{-2} \cdot K^{-1}$)

h_{il}: interface-to-liquid heat-transfer coefficient ($W \cdot m^{-2} \cdot K^{-1}$)

H_l: liquid height

h_M: mass-transfer coefficient

h_r: radiation heat-transfer coefficient

h_{wg}: wall-to-gas heat-transfer coefficient

h_{wl}: wall-to-liquid heat-transfer coefficient

h_{wllam}: Rohsenow-Choi correlation heat-transfer coefficient for laminar flow

h_{wlturb}: Dittus-Boelter correlation heat-transfer coefficient for turbulent forced convection

h_Γ: subcooled-boiling heat-transfer coefficient

h'_v: vapor enthalpy of the bulk vapor if the vapor is condensing, or the vapor saturation enthalpy if the liquid is vaporizing

j: superficial velocity

$j_{g,\,bubble}$: terminal bubble rise velocity

k: thermal conductivity, coordinate index, or phase index

L: length

L_l: stratified liquid level

L_o: Laplace coefficient

m: solute concentration in liquid phase

M_i: total interfacial drag force

$N_{\mu g}$: viscosity number

Nu: Nusselt number

P: pressure, or equivalent channel perimeter in Section 3.5.5.6.

P_s: profile slip factor

Pe: Peclet number

Pr: Prandtl number

q: heat-transfer rate per unit volume

q''': internal heat generation within heat structure

q_{CHF}: critical heat flux

q_d: power deposited directly per unit volume

q_{gl}: gas-to-liquid sensible heat transfer per unit volume

q_{ig}: interfacial heat transfer to gas phase per unit volume

q_{il}: interfacial heat transfer to liquid phase per unit volume

q_{min}: heat flux at the minimum stable film-boiling temperature

q_{total}: total wall heat flux

q_{trans}, q_{TR}: total transition-boiling heat flux

q_{wg}: wall-to-gas heat transfer per unit volume

q_{wl}: wall-to-liquid heat transfer per unit volume

r_d: drag radius

R_s: ideal gas constant for steam ($J \cdot kg^{-1} \cdot K^{-1}$)

r_{sm}: Sauter mean radius

Re: Reynolds number

S: suppression factor in Chen correlation

S_i: width of the stratified interface

S_r: slip ratio

Sc: Schmidt number

Sh: Sherwood number

St: Stanton number

t: time

T: temperature

T_{ld}: liquid temperature at the point of bubble detachment

T_{min}: minimum stable film-boiling temperature

T_{NH}: homogeneous nucleation temperature

T_{sv}: saturation temperature corresponding to the vapor partial pressure

V: velocity ($m \cdot s^{-1}$)

V_c: critical Helmholtz velocity

V^*_{max}: maximum dimensionless circulation velocity at the surface of the drop

W, WF: weighting factor

We: Weber number

We_e: effective Weber number

x: mass quality

X: static quality or dummy variable

x_e: equilibrium quality

x_f: flow quality

x_l: liquid mass fraction

X_{TT}: Martinelli factor

Y_b: bubble height

Z: axial elevation

Z_{CHF}: elevation at critical heat flux

α: gas volume fraction (i.e., void fraction)

α_{ag}: void fraction at the agitated/post-agitated IAF regime transition

α_b: bubble volume fraction

α_d: droplet area fraction

α_{dd}: volume fraction of the dispersed droplets

α_{DP}: void fraction at the dispersed (post-agitated)/highly dispersed flow regime transition

α_f: volume fraction of the liquid film

α_g: combined-gas void fraction

α_{gs}: average void fraction in the liquid slug

α_l: liquid fraction

α_{SM}: void fraction at the smooth/rough-wavy IAF regime transition

α_w: wall void fraction

Γ: interfacial mass-transfer rate per unit volume

Γ_i: mass-transfer rate per unit volume from interfacial heat transfer

Γ_{sub}: mass-transfer rate per unit volume from subcooled boiling at a heated wall

Γ^+: maximum of Γ and zero (evaporation or flashing)
Γ^-: minimum of Γ and zero (condensation)
Δx: cell length
δ: vapor-film thickness
δ_f: liquid-film thickness
λ: Taylor wavelength
ε: wall roughness or emissivity
μ: viscosity
ρ: density
σ: surface tension
σ_r: Stefan-Boltzmann constant
τ: shear stress
τ_f: interfacial shear
ξ: wet wall area fraction (transition boiling)

Subscripts

a: noncondensable gas
a: annular film
ag: agitated IAF to post-agitated (dispersed) transition
am: annular-mist flow
B: factor related to the Bromley correlation
b: bubble
bs, bubbly: bubbly slug flow
c, core: core
c, cr, crit: critical
CHF: critical heat flux
churn: churn (transition) flow
cond: condensation
D: factor related to the Denham correlation
d: droplet
dd: dispersed droplets
df: highly dispersed flow
DP: transition between dispersed (post-agitated) and highly dispersed flow regime
dr: factor related to the Dougall-Rohsenow correlation
drop: droplet field

ds:	post-agitated and dispersed flow
evap/cond:	evaporation and/or condensation
f:	film or mist flow
fBB:	factor related to the Bromley correlation
fd:	cold-wall liquid-film flow
forc:	forced convection
fr:	free-stream bubbles
g:	combined-gas mixture
hor:	horizontal
i:	interfacial
inv:	inverted annular flow
l:	liquid
lam:	laminar flow
m:	two-phase mixture
map:	basic flow-regime map
max:	maximum
min:	minimum
mod-CSO:	factor related to the momentum-transfer analogy of Chen, Sundaram, and Ozkaynak
nc:	in the presence of noncondensables
NC:	natural convection
near-wall:	near-wall liquid
nucb:	nucleate boiling
post-ag, pa:	post-agitated (or dispersed) flow
plug:	plug flow
r:	relative
rad:	radial component
rw:	rough-wavy inverted annular flow
s:	steam
sat:	saturation
sb:	subcooled boiling; bubbly and transition flow
sub:	subcooled boiling
slug:	liquid slug
SM, sm:	smooth inverted annular flow
st, strat:	stratified flow
trans, t:	transition (churn) flow

TR, tb:	transition boiling
TP:	two-phase
turb:	turbulent flow
v:	water vapor
w:	wall
W-C:	Webb-Chen correlation
θ:	azimuthal component

3.1. Overview of Closure Relations

With the eight conservation equations presented in Section 2.0., TRAC solves for eight dependent variables: the liquid and gas field velocities (V_l, V_g), the liquid and gas field temperatures (T_l, T_g), void fraction (α); pressure (P), the partial pressure of noncondensables (P_a), and the solute concentration (m). However, to achieve closure on the above equations, numerous other parameters must be specified, many of which are dependent on the specific local conditions. The key variables of interest pertain to interfacial heat transfer and drag, wall heat transfer and drag, interfacial mass transfer, thermodynamic and material properties, and geometry. This section will refine these closure needs further through definitions and brief discussion. Subsequent sections then will detail the individual flow-regime-dependent and heat-transfer-regime-dependent closure models.

Beginning with the combined-gas field, TRAC assumes that Dalton's law applies. In other words, the total pressure is equivalent to the sum of the partial pressures of the water vapor and the noncondensable gas, or

$$P = P_v + P_a \, . \tag{3-1}$$

Also within the combined-gas field, TRAC bases the total gas density and the total gas internal energy on sums of the water vapor and noncondensable components. The total gas density and internal energy thus are expressed by

$$\rho_g = \rho_v + \rho_a \tag{3-2}$$

and

$$\rho_g e_g = \rho_v e_v + \rho_a e_a \, . \tag{3-3}$$

With regard to fluid mass closure, TRAC defines Γ, the interfacial mass-transfer rate per unit volume, as the sum of the mass-transfer rates from interfacial heat transfer and subcooled boiling, or

$$\Gamma = \Gamma_i + \Gamma_{sub} \, . \tag{3-4}$$

The mass-transfer rate caused by interfacial heat transfer is evaluated from the thermal energy jump relation

$$\Gamma_i = \frac{q_{il} + q_{ig}}{(h_g - h_l)} . \tag{3-5}$$

Similarly, the mass-transfer rate from subcooled boiling is defined as

$$\Gamma_{sub} = \frac{h_\Gamma A_w (T_w - T_l)}{B_{cell} (h_g - h_l)} . \tag{3-6}$$

Additional discussion of the interfacial mass-transfer rate terms can be found in Section 3.4.

In terms of fluid energy closure, the heat-transfer rates per unit volume q_{il}, q_{ig}, and q_{gl} are required by either the interfacial mass-transfer jump relation (see previous paragraph), the conservation equations for mixture and combined-gas energy (see Section 2.1.), or both. The interface-to-liquid heat-transfer rate, the interface-to-gas heat-transfer rate, and the liquid-to-gas sensible heat-transfer rate, respectively, are given by the following equations:

$$q_{il} = \begin{cases} (h_{il})_{evaporation/condensation} \cdot A_i \dfrac{(T_l - T_{sv})}{B_{cell}} & T_l \le T_{sat} \\ \dfrac{(h_{il})_{evap/cond} \cdot A_i (T_l - T_{sv}) + (h_{il})_{flashing} \cdot A_i (T_l - T_{sat})}{B_{cell}} & T_l > T_{sat} , \end{cases} \tag{3-7}$$

$$q_{ig} = \frac{P_v}{P} h_{ig} A_i \frac{(T_g - T_{sv})}{B_{cell}} , \tag{3-8}$$

and

$$q_{gl} = \frac{P_a}{P} h_{gl} A_i \frac{(T_g - T_l)}{B_{cell}} . \tag{3-9}$$

The interface-to-liquid heat-transfer equation superimposes a flashing term when the liquid temperature exceeds the saturation temperature based on the total pressure. When the liquid temperature is below the saturation temperature based on total pressure, but is above the saturation temperature corresponding to the water vapor partial pressure, evaporation occurs. Likewise, condensation takes place when the liquid temperature is below the saturation temperature of the steam.

In addition, fluid energy closure requires a definition of the wall-to-liquid and the wall-to-gas heat-transfer rates per unit volume. The wall-to-liquid and the wall-to-gas heat-transfer rates are defined such that

$$q_{wl} = h_{wl} A_w \frac{(T_w - T_l)}{B_{cell}} \tag{3-10}$$

and

$$q_{wg} = h_{wg} A_w \frac{(T_w - T_g)}{B_{cell}} . \tag{3-11}$$

Within individual heat structures, the temperature field is calculated via the classical heat-conduction equation

$$\rho c_p \frac{\partial T}{\partial t} = \nabla \cdot (k \nabla T) + q''' .$$

Finally, coupling between the heat-structure surface and the fluid fields is dependent on the wall temperature defined such that

$$T_w = T(\text{at wall surface}).$$

Using the above definitions, we can quickly sort the remaining parameters for closure into one of four categories: input requirements, thermodynamic and transport fluid properties, material properties, and local-condition-dependent parameters. Within the input requirement category, parameters such as the wall surface area, cell volume, and hydraulic diameter are obtained either directly from or calculated from input geometry. The terms for power deposited directly in the combined-gas or liquid fields likewise are defined through input. For purposes of discussion, the internal heat-generation term for the heat structures also will be treated as input. In reality, the user may specify input data tables or exercise TRAC's point-kinetics model. For additional information on the code's reactor physics modeling, see Appendix M and Ref. 3-1.

Under the category of thermodynamic and transport fluid properties, TRAC provides parameters such as the density, viscosity, thermal conductivity, internal energy, and enthalpy for the liquid, vapor, and noncondensable components. The code also calculates saturation properties for the liquid and vapor components. These properties are obtained from polynomial fits of steam table data for the liquid and vapor and from ideal gas behavior for the noncondensables. For additional detail, see Appendix A.

To solve the heat-conduction equation within a given heat structure, the code requires material property data for density, specific heat, and thermal conductivity. TRAC contains a library of temperature-dependent properties for materials such as mixed-oxide fuel, zircaloy, stainless steel, and Inconel. For additional detail, see Appendix B.

For materials not included in the library, the temperature-dependent properties are obtained through input.

Closure of the equation solution set is approached by defining an additional 10 parameters via constitutive relationships, each of the parameters being dependent on local conditions. The parameters in question are the interfacial area (A_i), the interfacial mass-transfer rate (Γ), the interfacial drag coefficient (c_i), the wall drag coefficients for the liquid and combined-gas fields (c_{wl}, c_{wg}), the interfacial heat-transfer coefficients for the liquid and combined-gas fields (h_{il}, h_{ig}), the heat-transfer coefficient for the liquid-to-gas sensible heat transfer (h_{gl}), and the wall heat-transfer coefficients for the liquid and combined-gas fields (h_{wl}, h_{wg}). Table 3-1. identifies the field equations in which each of the 10 parameters is present. The relationship between closure parameter and field equation is illustrated further by Figs. 3-1a. through 3-1d. In general, TRAC assumes that the local-condition-dependent parameters can be treated in a quasi-steady manner, thereby eliminating time dependencies associated with the closure relationships. The implications of TRAC's quasi-steady assumption are discussed in detail in Appendix D.

Sections 3.2. to 3.8. will outline both the TRAC flow-regime map and the 10 closure parameters listed above. Summaries of the key closure models and correlations for each parameter are presented in Tables 3-2. through 3-7.

Note: **TRAC-M/F90 and TRAC-M/F77 Reflood Models.** TRAC-M/F90 (Version 3.0) contains a core-reflood model that was brought over from TRAC-PF1/MOD2. TRAC-M/F77, Version 5.5.2, also contains, in addition to this model, a more recent reflood model, with new closure relations, that was developed for analysis of simultaneous top-down/bottom-up quenching. An additional option for the newer model in TRAC-M/F77 allows for use of the closure relations in TRAC-PF1/MOD1 with multiple quench fronts. This document only describes the reflood model that is in TRAC-M/F90 (in this section, and in Appendices E, G, and H). A detailed discussion of the theory and use of the new TRAC-M/F77 top-down/bottom-up reflood model is given in Ref. 3-51. This includes discussion of a new optimization methodology that was developed as part of the TRAC-M/F77 reflood effort. Assessment of the new model is provided in Ref. 3-52. and in the TRAC-M/F77 Developmental Assessment Manual (Refs. 3-53. and 3-54.).

TABLE 3-1.
Requirements for Closure:
Flow/Heat-Transfer Regime-Dependent Parameters

Closure Parameter		Field Equations					
		Mass		Momentum		Energy	
	Applicable Sections	Liquid	Combined Gas	Liquid	Combined Gas	Total	Combined Gas
A_i	(3.3., F.1.)	X	X	X	X		X
Γ	(3.4., F.1., G)	X	X	X	X		X
c_i	(3.5., H.1.)			X	X		
c_{wl}	(3.6., H.2.)			X			
c_{wg}	(3.6., H.2.)				X		
h_{il}	(3.7., F.1.)	X	X	X	X		X
h_{ig}	(3.7., F.1.)	X	X	X	X		X
h_{gl}	(3.7., F.1.)						X
h_{wl}	(3.8., F.2.)	X	X	X	X	X	X
h_{wg}	(3.8., F.2.)					X	X

A_i = interfacial area.
Γ = interfacial mass-transfer rate.
c_i = interfacial drag coefficient.
c_{wl} = wall drag coefficient (liquid phase).
c_{wg} = wall drag coefficient (gas phase).
h_{il} = interface-to-liquid heat-transfer coefficient.
h_{ig} = interface-to-gas heat-transfer coefficient.
h_{gl} = gas-to-liquid sensible heat-transfer coefficient.
h_{wl} = wall-to-liquid heat-transfer coefficient.
h_{wg} = wall-to-gas heat-transfer coefficient.

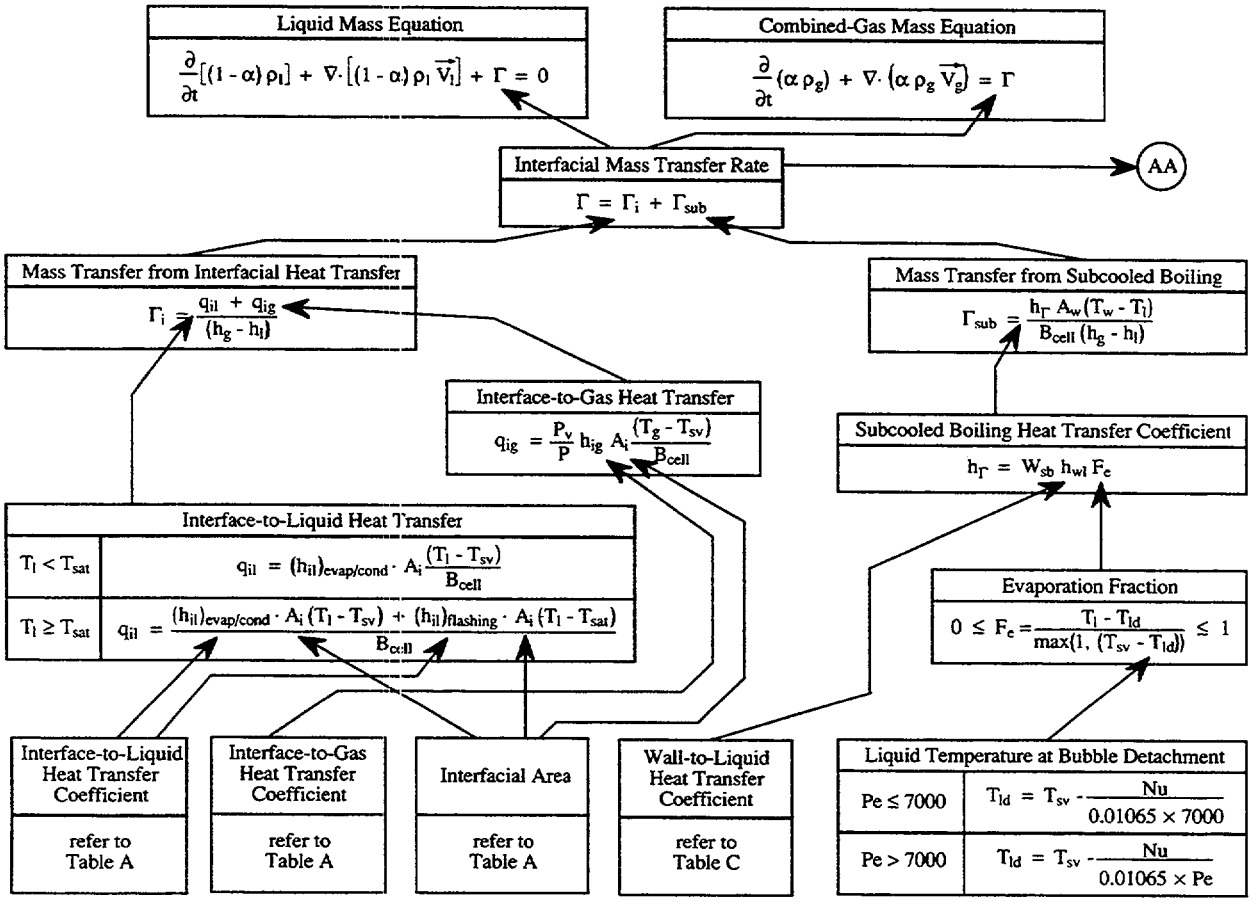

Fig. 3-1a. Mapping of regime-dependent parameters—liquid and combined-gas mass equations.

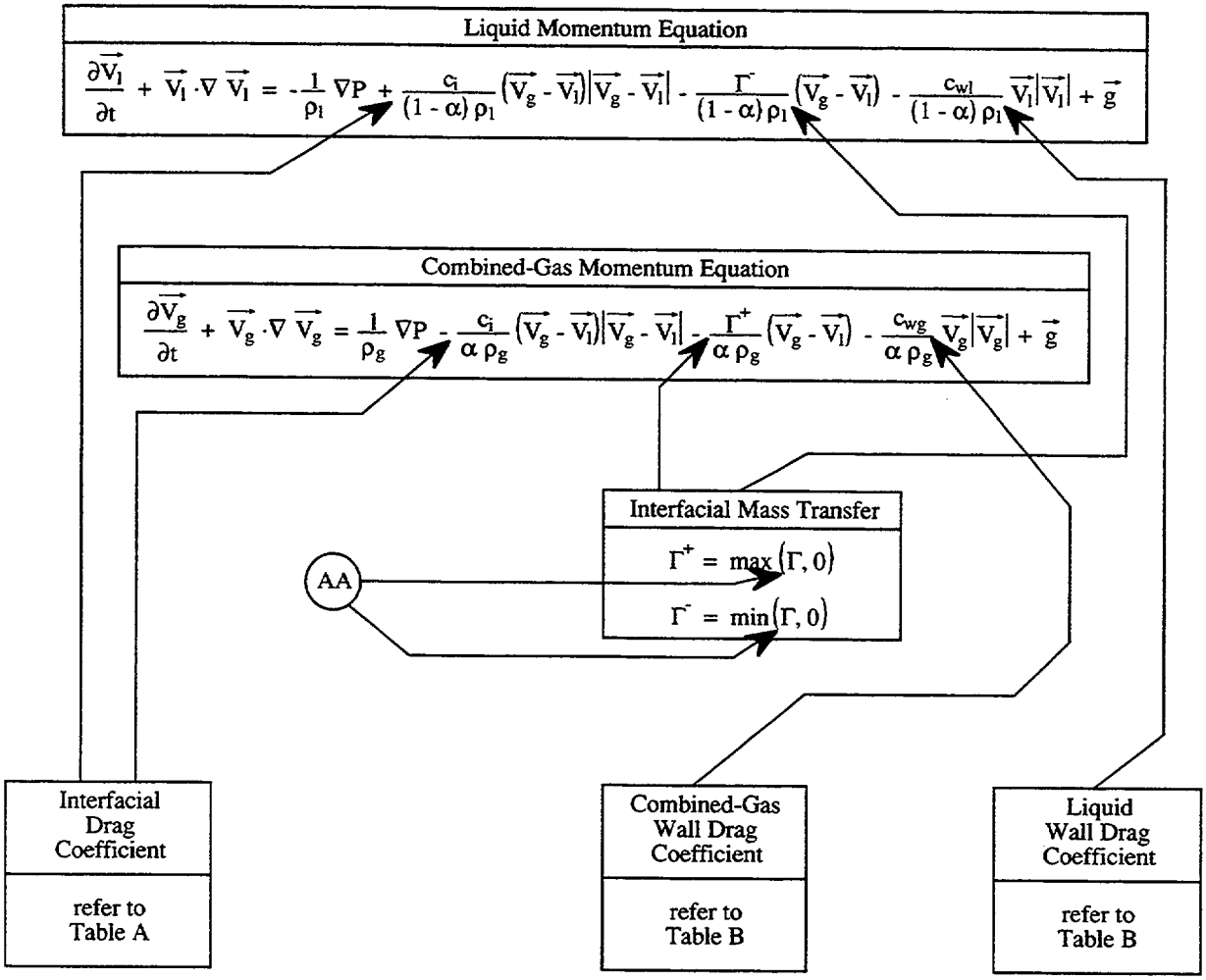

Fig. 3-1b. Mapping of regime-dependent parameters—liquid and combined-gas momentum equations.

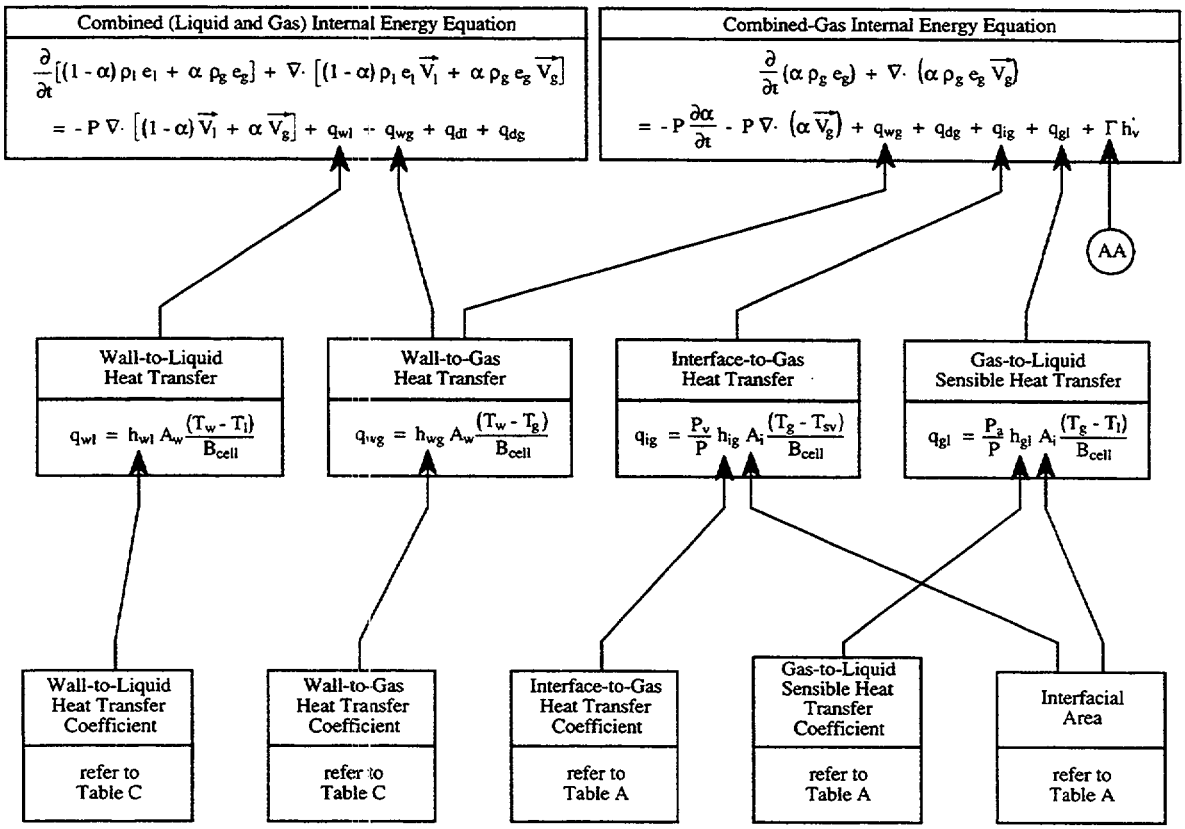

Fig. 3-1c. Mapping of regime-dependent parameters—total and combined-gas energy equations.

Table A:

Flow Regime	Section Numbers		
	A_i	c_i	h_{il}, h_{ig}, and h_{gl}
Bubbly Slug (1)[a]	3.3.1., F.1.1.1.	3.5.1., H.1.1.	3.7.1., F.1.1.
Churn (2)	3.3.2., F.1.3.	3.5.2., H.1.4.	3.7.2., F.1.3.
Annular-Mist (1)	3.3.3., F.1.2.1.	3.5.3., H.1.2.	3.7.3., F.1.2.
Stratified (3)	3.3.4., F.1.4.1.	3.5.4., H.1.3.	3.7.4., F.1.4.
Plug (3)	3.3.5., F.1.5.1.		3.7.5., F.1.5.
Reflood (4)	3.3.6., F.1.6.	3.5.5., H.1.5.	3.7.6., F.1.6.
Presence of Noncondensables (4)			3.7.7., F.1.7.

a. "Bubbly Slug" here is a collective term for the bubbly, bubbly slug, and bubbly slug transition regimes.

Table B:

Flow Regime	Section Numbers c_{wl} and c_{wg}
Single-Phase	3.6.1., H.2.
Two-Phase	3.6.2., H.2.
Horizontal Stratified	3.6.3., H.2.1.2.

Table C:

Heat-Transfer Regime	Section Numbers h_{wl} and h_{wg}
Natural Convection to Liquid	3.8.1., F.2.1.1., F.2.2.1.
Forced Convection to Liquid	3.8.2., F.2.1.1., F.2.2.1.
Nucleate Boiling (5)	3.8.3., F.2.1.2., F.2.2.2.
Transition Boiling (5)	3.8.5., F.2.1.3., F.2.2.3.
Film Boiling	3.8.7., F.2.1.4., F.2.2.4.
Single-Phase Vapor	3.8.8., F.2.1.5., F.2.2.5.
Condensation	3.8.9., F.2.1.6., F.2.2.6.
Two-Phase Forced Convection (6)	3.8.10., F.2.1.7., F.2.2.7.

Notes:
(1) Basic Flow Map
(2) Interpolation Regime
(3) Superimposed on Basic Map
(4) Specialized Regime
(5) Includes differentiated core reflood model

Fig. 3-1d. Mapping of flow/heat-transfer regime-dependent parameters—applicable document sections.

TABLE 3-2.
TRAC Closure Relation Summary:
Flow-Regime Criteria and Interfacial Area

Flow Regime	Flow-Regime Criteria	Interfacial Area (A_i)
Bubbly Flow	$\alpha \leq 0.3$ or $\alpha \leq 0.5$ and $G \geq 2700$ kg/m^2-s	based on Ishii and Mishima (Ref. 3-6.)
Bubbly Slug Transition	$0.3 < \alpha \leq 0.5$ and $2000 < G < 2700$ kg/m^2-s	based on Ishii and Mishima (Ref. 3-6.)
Bubbly Slug Flow	$0.3 < \alpha \leq 0.5$ and $G \leq 2000$ kg/m^2-s	based on Ishii and Mishima (Ref. 3-6.)
Churn Flow	$0.5 < \alpha \leq 0.75$	weighted average of bubbly slug and annular-mist interfacial areas
Annular-Mist Flow	$\alpha > 0.75$	superimpose film and droplet fields; droplet area based on the droplet diameter defined by Kataoka (Ref. 3-10.) or Kitscha and Kocamustafaogullari (Ref. 3-11.) and on the entrainment fraction of Ishii and Mishima (Ref. 3-9.); film area based on geometry and entrainment fraction
Transition to Stratified Flow	1D components: gas (or liquid) velocity between one and ten times the critical velocity 3D components: gas velocity between one and two times the critical velocity	weighted average of stratified-flow and basic flow-regime-map interfacial areas
Stratified Flow	1D components: critical velocity criteria 3D vessel: horizontal stratified flow uses critical relative velocity of Mishima and Ishii; (Ref. 3-2.) vertical stratified flow uses terminal bubble rise velocity criterion	interfacial area for horizontal stratified flow based on circular pipe geometry; interfacial area for vertical stratified flow based on average cross-sectional area
Plug Flow	liquid side under condensation mode; void fraction (over three contiguous cells) must satisfy plugging criterion	based on circular pipe geometry
Reflood: Bubbly Flow	transition to IAF defined by mechanistic elevation model based on critical heat flux, film-boiling heat flux, and void fraction	defined as above
IAF	flow regime defined by mechanistic elevation models based on capillary number and limited by a range of void fractions	based on liquid-core geometry

TABLE 3-2. (cont)
TRAC Closure Relation Summary:
Flow-Regime Criteria and Interfacial Area

Flow Regime	Flow-Regime Criteria	Interfacial Area (A_j)
Dispersed Flow	flow regime defined by mechanistic elevation model based on capillary number and limited by a range of void fractions	superimpose droplet and film fields (similar to annular-mist-flow regime); droplet area based on the droplet diameter defined by Kataoka or Kitscha and Kocamustafaogullari (Ref. 3-11.); film area based on geometry and the stable liquid-film thickness

TABLE 3-3.
TRAC Closure Relation Summary:
Interfacial Mass Transfer

Total Interfacial Mass-Transfer Rate (Γ)	Sum of the mass-transfer rates from interfacial heat transfer and subcooled boiling
Mass Transfer Caused by Interfacial Heat Transfer (Γ_i)	Based on the sum of the interface-to-gas and interface-to-liquid heat-transfer rates
Mass Transfer Caused by Subcooled Boiling (Γ_{sub})	Based on Lahey's mechanistic model (Ref. 3-14.) for the evaporation fraction and on the modified Saha-Zuber OSV (onset of significant voiding) correlation (Ref. 3-15.) (**Note:** This model is used only when the subcooled-boiling heat-transfer coefficient is nonzero)

TABLE 3-4.
TRAC Closure Relation Summary:
Interfacial Drag

Flow Regime	Interfacial Drag Coefficient (c_i)
Bubbly Flow, Bubbly Slug Flow, Bubbly Slug Transition	Defined as per Ishii and Chawla (Ref. 3-16.) (bubble diameter and profile slip based on Ishii; (Ref. 3-7.) bubble drag coefficient for three Reynolds number regimes based on Stokes drag law, the empirical relation proposed by Schiller and Nauman, (Ref. 3-7.) and the recommendation of Bird, Stewart, and Lightfoot (Ref. 3-18.)
Churn Flow	Weighted average of bubbly slug and annular-mist interfacial drag coefficients
Annular-Mist Flow	Based on drift velocity developed by Kataoka and Ishii (Ref. 3-12.) and total interfacial shear force defined as per Ishii and Mishima (Ref. 3-6.) (film interface friction factor obtained from Wallis (Ref. 3-20.); droplet diameter based on Kataoka, Ishii, and Mishima (Ref. 3-10.); droplet drag coefficient based on Ishii and Chawla (Ref. 3-16.); entrainment based on Kataoka and Ishii (Ref. 3-12.)
Transition to Stratified Flow	Weighted average of stratified and flow-regime map interfacial drag coefficients
Stratified Flow	Derived from the method of Taitel and Dukler (Ref. 3-21.) (interfacial friction factor based on Ohnuki et al. (Ref. 3-22.)
Plug Flow	No specific model for interfacial drag
Reflood: Subcooled Boiling	Composed of the drag coefficient from bubbles at the wall (based on the Colebrook turbulent friction factor) and by the drag coefficient from free-stream bubbles (based on Ishii (Ref. 3-7.)
Smooth IAF	Based on smooth tube friction factor correlations (laminar and turbulent flow)
Rough-Wavy IAF	Based on Colebrook friction factor for rough walls (relative roughness based on Ishii entrained droplet diameter (Ref. 3-17.)
Agitated IAF	Same as rough-wavy IAF
Post-Agitated (Dispersed) Flow	Weighted average of agitated IAF and highly dispersed interfacial drag coefficients
Highly Dispersed Flow	Composed of separate droplet and film terms; droplet interfacial drag based on form drag of Ishii and Chawla (Ref. 3-16.) and on Ishii (Ref. 3-7.) droplet size; film interfacial drag based on modified Wallis friction factor (film thickness derived by Pasamehmetoglu (Ref. 3-13.)

TABLE 3-5.
TRAC Closure Relation Summary:
Wall Drag

Model Type	Wall-to-Liquid Drag Coefficient (c_{wl})	Wall-to-Gas Drag Coefficient (c_{wg})
Single-Phase	Single-phase liquid: based on the modified friction-factor correlation (Ref. 3-25.) Single-phase vapor: zero	Single-phase liquid: zero Single-phase vapor: based on the modified Churchill friction-factor correlation (Ref. 3-25.)
Two-Phase, Homogeneous	Based on the modified Churchill friction-factor correlation (Ref. 3-25.) using the two-phase mixture Reynolds number	Based on the modified Churchill friction-factor correlation (Ref. 3-25.) using the two-phase mixture Reynolds number
Two-Phase, Horizontal Stratified	Laminar flow: based on fully developed laminar friction-factor relation Turbulent flow: based on McAdams friction-factor correlation	Laminar flow: based on fully developed laminar friction-factor relation Turbulent flow: based on McAdams friction-factor correlation

TABLE 3-6.
TRAC Closure Relation summary:
Interfacial Heat Transfer

Flow Regime	Interface-to-Liquid Heat-Transfer Coefficient (h_{il})	Interface-to-Gas Heat-Transfer Coefficient (h_{ig})	Liquid-to-Gas Sensible Heat-Transfer Coefficient (h_{gl})
Bubbly Flow, Bubbly Slug Flow, Bubbly Slug Transition	Condensation or evaporation: based on the Chen and Mayinger (Ref. 3-26.) and the Whittaker (Ref. 3-27.) Nusselt number correlations Flashing: based on liquid superheat Subcooled boiling: h_{il} is weighted to include Lahey and Moody model (Ref. 3-28.)	1000 W/m^2-K	1000 W/m^2-K
Churn Flow	Cond/evap: based on weighted average of annular-mist and bubbly slug heat-transfer factors Flashing: based on maximum of weighted heat-transfer factor and liquid superheat relation	Based on weighted average of annular-mist and bubbly slug heat-transfer factors	Based on weighted average of annular-mist and bubbly slug heat-transfer factors
Annular-Mist Flow	Cond/evap: superimpose droplet and film field Droplet field: based on transient conduction solution (Ref. 3-29.) Film field: based on Bankoff correlation for Stanton number (Ref. 3-32.) Flashing: based on maximum of weighted heat-transfer factor and liquid superheat relation	Superimpose droplet and film field Droplet field: based on Ryskin correlation for Nusselt number (Ref. 3-31.) Film field: based on Bankoff correlation for Stanton number (Ref. 3-32.)	Superimpose droplet and film field Droplet field: based on Ryskin correlation for Nusselt number (Ref. 3-31.) Film field: based on Bankoff correlation for Stanton number (Ref. 3-32.)

TABLE 3-6. (cont)
TRAC Closure Relation summary:
Interfacial Heat Transfer

Flow Regime	Interface-to-Liquid Heat-Transfer Coefficient (h_{il})	Interface-to-Gas Heat-Transfer Coefficient (h_{ig})	Liquid-to-Gas Sensible Heat-Transfer Coefficient (h_{gl})
Transition to Stratified Flow	Cond/evap: weighted average of stratified and flow-regime-map heat-transfer factors Flashing: based on maximum of weighted heat-transfer factor and liquid superheat relation	Heat-transfer factor equivalent to value calculated from basic flow-regime map	Heat-transfer factor equivalent to value calculated from basic flow-regime map
Stratified Flow	Cond/evap: based on Linehan Stanton number relation (Ref. 3-33.) Flashing: based on maximum of weighted heat-transfer factor and liquid superheat relation	Heat-transfer factor equivalent to value calculated from basic flow-regime map	Heat-transfer factor equivalent to value calculated from basic flow-regime map
Plug Flow	Condensation: weighted average of flow-regime-map, stratified, and plug-flow heat-transfer factors (plug-flow HTC is calculated from a constant Stanton number model)	Heat-transfer factor equivalent to value calculated from basic flow-regime map	Heat-transfer factor equivalent to value calculated from basic flow-regime map
Reflood: Bubbly Flow	Cond/evap: weighted average of bubbly, IAF, and dispersed-flow heat-transfer factors Defined as above, this table	Weighted average of bubbly, IAF, and dispersed-flow heat-transfer factors Defined as above, this table	Weighted average of bubbly, IAF, and dispersed-flow heat-transfer factors Defined as above, this table
IAF	Based on HTVSSL model for subcooled liquid Kinetic theory of evaporation for flashing (Ref. 3-34.)	$3x10^3$ W/m^2-K	10^3 W/m^2-K

TABLE 3-6. (cont)
TRAC Closure Relation summary:
Interfacial Heat Transfer

Flow Regime	Interface-to-Liquid Heat-Transfer Coefficient (h_{il})	Interface-to-Gas Heat-Transfer Coefficient (h_{ig})	Liquid-to-Gas Sensible Heat-Transfer Coefficient (h_{gl})
Dispersed Flow	Heat-transfer factor equivalent to IAF value Flashing: based on maximum of above evap/cond factor and liquid superheat relation	Based on Unal (Ref. 3-34.) model	Weighted average of Ryskin (Ref. 3-31.) and Bankoff (Ref. 3-32.) models
Effect of Noncondensables	Evaporation: heat-transfer factor calculated by flow-regime-independent diffusion model Condensation: heat-transfer factor adjusted using model of Sklover and Rodivilin (Ref. 3-35.)	No modification	No modification

TABLE 3-7.
TRAC Closure Relation Summary:
Wall-to-Fluid Heat Transfer

Heat-Transfer Regime	Wall-to-Liquid Heat-Transfer Coefficient (h_{wl})	Wall-to-Gas Heat-Transfer Coefficient (h_{wg})
Natural Convection to Liquid	Laminar and turbulent natural-convection correlations (Ref. 3-36.)	zero
Forced Convection to Liquid	Dittus-Boelter correlation (Ref. 3-37.)	zero
Nucleate Boiling	Based on the total heat flux [as determined by the Chen correlation (Ref. 3-38.)] minus the wall-to-gas heat flux	Maximum of either the natural-convection (Ref. 3-40.) or Dougall-Rohsenow (Ref. 3-28.)correlations
Critical Heat Flux	Biasi correlation (Ref. 3-41.)	Biasi correlation (Ref. 3-41.)
Transition Boiling	Based on the total heat flux minus the wall-to-gas heat flux (the total heat flux is a weighted average of q_{CHF}, calculated via Biasi, and q_{min}, which is based on natural-convection (Ref. 3-40.), Dougall-Rohsenow (Ref. 3-28.), modified Bromley (Ref. 3-43.), and radiation heat-transfer coefficients) reflood model: total heat flux based on exponential decrease from q_{CHF} to q_{film}	Maximum of either the natural-convection (Ref. 3-40.) or Dougall-Rohsenow (Ref. 3-28.) correlations reflood model: Webb-Chen correlation (Ref. 3-44.)
Minimum Stable Film-Boiling Temperature	Based on the Fauske homogeneous nucleation temperature (Ref. 3-46.)	Based on the Fauske homogeneous nucleation temperature (Ref. 3-46.)
Film Boiling	Based on the modified Bromley film-boiling heat-transfer coefficient (Ref. 3-43.) and a radiation term Reflood model: based on the Denham (Ref. 3-47.) and modified Bromley (Ref. 3-43.) correlations and a radiation term	Maximum of either the natural-convection (Ref. 3-40.) or Dougall-Rohsenow (Ref. 3-28.) correlations Reflood model: based on Webb-Chen correlation (Ref. 3-44.)
Single-Phase Vapor	Zero	Maximum of the turbulent natural-convection correlation and either the Sieder-Tate (Ref. 3-18.) or Dittus-Boelter (Ref. 3-37.) correlations
Condensation	Zero or the maximum of the laminar natural-convection, turbulent natural-convection, and Chen (Ref. 3-38.) ($S = 0$) correlations	Based on Nusselt, turbulent natural-convection (Ref. 3-48.) and turbulent forced-convection (Ref. 3-36.) correlations

TABLE 3-7. (cont)
TRAC Closure Relation Summary:
Wall-to-Fluid Heat Transfer

Heat-Transfer Regime	Wall-to-Liquid Heat-Transfer Coefficient (h_{wl})	Wall-to-Gas Heat-Transfer Coefficient (h_{wg})
Two-Phase Forced Convection	Maximum of the Rohsenow-Choi (Ref. 3-49.) and Dittus-Boelter (Ref. 3-37.) correlations	Zero or the maximum of the turbulent natural-convection (Ref. 3-36.) and Dittus-Boelter (Ref. 3-37.) correlations

3.2. Flow-Regime Map

The flow-regime map in TRAC is not used directly by the field equations presented in Section 2.0. Nonetheless, each of the closure models for interfacial mass, momentum, and energy transfer are dependent on the local fluid conditions, including flow regime. The determination of flow regime thus is an important intermediate calculation for evaluating the respective interfacial parameters.

TRAC adopts a very simple flow-regime map that generally is assumed to apply for both vertical and horizontal flow geometries. The basic flow-regime map consists of bubbly flow, bubbly slug flow, bubbly slug transition, churn-flow, and annular-mist-flow regions. These regions are displayed graphically in mass-flux/void-fraction space in Fig. 3-2. In addition, the specialized flow regimes of stratified flow and plug flow may be superimposed on the basic flow-regime map, subject to certain physical and phenomenological criteria. The code also includes specialized flow-regime models to represent the post-critical-heat-flux (CHF) behavior under core reflood conditions.

The following sections will outline the various flow regimes modeled by TRAC and their respective existence criteria. A summary of the flow-regime criteria also is presented in Table 3-2. Additional details, including the basis for the flow-regime map, a description of the flow-regime models as coded, and assessment of the map, are given in Appendix E.

3.2.1. Bubbly Slug Flow

In discussing the bubbly slug flow regime, this section will collectively refer to the bubbly, bubbly slug transition, and bubbly slug flow regimes depicted in Fig. 3-2. Bubbly flow can be characterized by the combined-gas phase being distributed as individual bubbles in a continuous liquid phase. The bubbly flow regime is defined to exist when the void fraction (α) is ≤ 0.3 for all mass fluxes (G). Bubbly flow also exists when $\alpha \leq 0.5$ and $G \geq 2700$ kg/m^2-s. However, when the void fraction drops below 1.0×10^{-6}, the flow is assumed to be single-phase liquid.

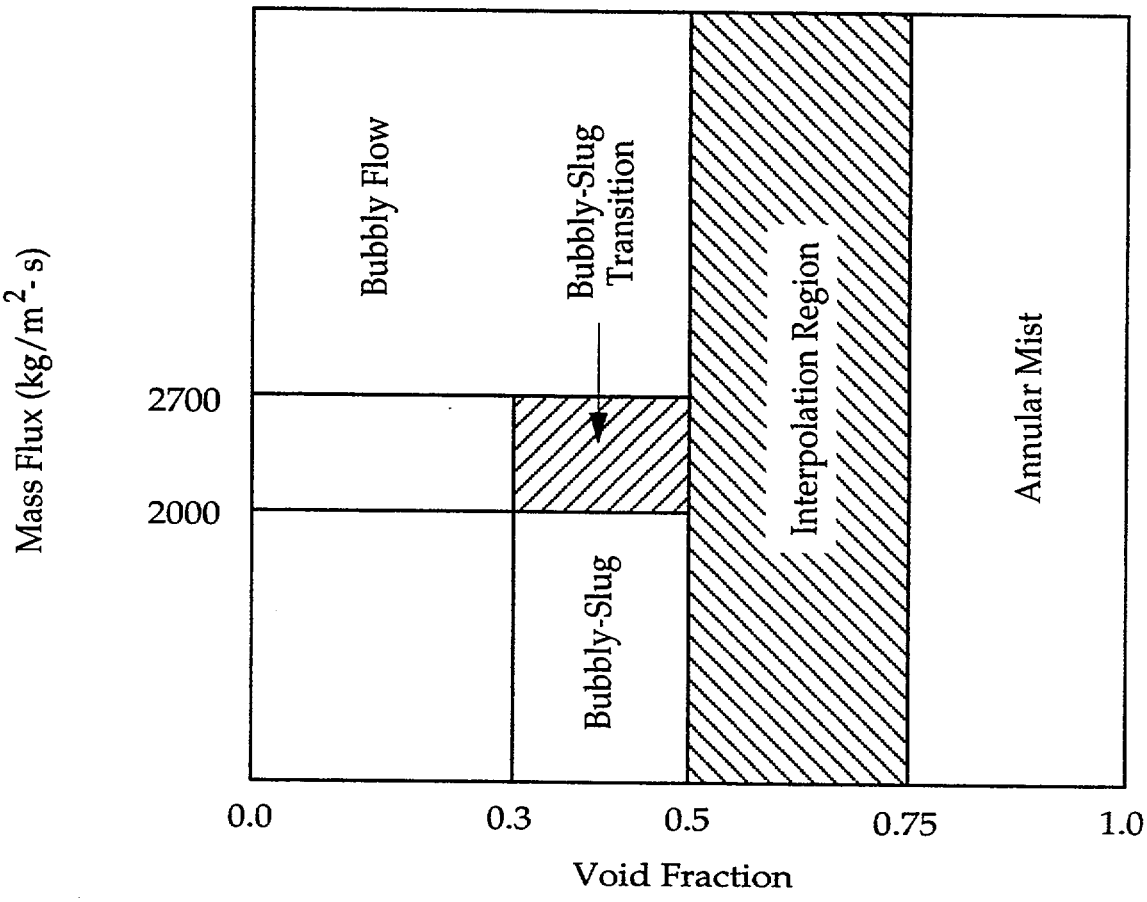

Fig. 3-2. TRAC flow-regime map.

Bubbly slug flow, or slug flow, is characterized by large combined-gas bubbles that are separated from the channel wall by a thin liquid film. The large bubbles are separated from one another by liquid slugs that may contain smaller entrained gas bubbles. In TRAC, the bubbly slug regime is defined to exist for $0.3 < \alpha \leq 0.5$ and $G \leq 2000$ kg/m^2-s.

The bubbly slug transition regime is defined to exist for $0.3 < \alpha \leq 0.5$ and $2000 < G < 2700$ kg/m^2-s. It serves as a interpolation regime between bubbly and slug flows.

3.2.2. Churn Flow

Churn flow (also referred to as transition flow) exists for void fractions in the range of $0.5 < \alpha \leq 0.75$. Physically, this flow regime is characterized by the breakup of the large vapor bubbles associated with slug flow. However, TRAC does not include any churn-flow-specific closure models. Rather, it treats churn flow as an interpolation regime between void-fraction values of 0.5 and 0.75. The interfacial-drag and heat-transfer closure parameters for churn flow are calculated as a weighted average of the appropriate bubbly slug and annular-mist values.

3.2.3. Annular-Mist Flow

For void fractions >0.75, the annular-mist-flow regime is assumed to be present. Annular-mist flow is characterized by a liquid film adjacent to the channel wall, a continuous central gas core, and entrained liquid droplets dispersed within the central gas core. However, with void fractions >0.999999, the flow is assumed to be single-phase vapor.

3.2.4. Stratified Flow

At low liquid and vapor velocities, the individual phases may separate (stratify) and form a relatively smooth interface. Thus, subject to critical velocity criteria, TRAC superimposes the stratified-flow regime on the basic flow-regime map described in Sections 3.2.1. through 3.2.3. For a given closure parameter of interest, the transition to stratified flow is accomplished by a weighted average of the parameter value from the appropriate flow-regime-map model and the stratified-flow model. This transition can be expressed by

$$X_{map,st} = (1 - W_{st})X_{map} + W_{st}X_{st} , \tag{3-12}$$

where X is the closure parameter of interest and W_{st} is the stratified-flow weighting factor.

In 1D components, the weighting factors for both vertical and horizontal stratified flow are void-fraction dependent. For transitions from bubbly slug flow to stratified flow ($\alpha \leq 0.5$), the weighting factor is calculated by

$$0 \leq W_{st,bubbly} = \frac{1}{9}\left(10 - \frac{V_l}{V_{l,cr}}\right) \leq 1 \tag{3-13}$$

for the critical velocity

$$V_{l,cr} = \frac{0.2}{(1 - \alpha)} . \tag{3-14}$$

It is evident that this weighting factor will be nonzero for liquid velocities between 1 and 10 times the critical velocity. Once the liquid velocity is less than or equal to the critical velocity, the flow becomes fully stratified. For transitions between annular-mist and stratified flow ($\alpha > 0.75$), the weighting factor is calculated by

$$0 \leq W_{st,am} = \frac{1}{9}\left(10 - \frac{V_g}{V_{g,cr}}\right) \leq 1 \tag{3-15}$$

for the critical velocity

$$V_{g,cr} = \frac{1}{\alpha}\left[\frac{0.2}{V_l(1 - \alpha)}\right]^{0.435} . \tag{3-16}$$

In this case, the flow becomes fully stratified when the gas velocity is less than or equal to the critical velocity presented in the previous equation. Additionally, for transitions from churn flow to stratified flow ($0.5 < \alpha \leq 0.75$), the weighting factor is calculated by

$$W_{st,churn} = \left(\frac{0.75 - \alpha}{0.25}\right) W_{st,bubbly} + \left(\frac{\alpha - 0.5}{0.25}\right) W_{st,am} . \quad (3\text{-}17)$$

For horizontal stratification to occur, 1D components also are subject to the constraint that their inclination must be within ±10 degrees of horizontal.

In a 3D vessel component, the stratification criteria are evaluated separately for the horizontal plane (horizontal stratified flow) and along the vertical axis (vertical stratified flow). In the horizontal plane, the weighting factor is calculated such that

$$0 \leq W_{st} = \left(2 - \frac{V_{g,hor}}{V_{r,cr}}\right) \leq 1 . \quad (3\text{-}18)$$

In this case, the horizontal gas velocity ($V_{g,hor}$) is defined as a function of the radial and azimuthal velocity components, where

$$V_{g,hor} = \sqrt{V_{g,rad}^2 + V_{g,\theta}^2} . \quad (3\text{-}19)$$

The relative critical velocity is calculated from the model of Mishima and Ishii (Ref. 3-2.), given by

$$V_{r,cr} = 0.487 \sqrt{\frac{g(\rho_l - \rho_g)(D_h - H_l)}{\rho_g}} , \quad (3\text{-}20)$$

where H_l is the liquid height and D_h is the hydraulic diameter. Within the 3D vessel component, the void fractions at upper and lower consecutive levels also must satisfy the criterion that the upper void fraction be >0.9 and the lower void fraction be <0.1. Otherwise, W_{st} is set to zero. Also for vessels, the term $(D_h - H_l)$ in Eq. (3-20) is replaced by the arithmetic average of the axial widths of the two levels.

Along the vertical axis of a 3D component, the stratified-flow weighting factor is calculated by

$$0 \leq W_{st} = \left(2 - \frac{|j_g|}{j_{g,bubble}}\right) \leq 1 . \quad (3\text{-}21)$$

In the equation above, the terminal bubble rise velocity is evaluated by

$$j_{g,bubble} = \frac{\alpha}{1 - C_0 \alpha} \cdot \sqrt{2} \cdot \left[\frac{g \sigma (\rho_l - \rho_g)}{\rho_l^2}\right]^{1/4} \quad (3\text{-}22)$$

for

$$C_0 = 1.2 + 0.2\sqrt{\frac{\rho_g}{\rho_l}} \tag{3-23}$$

and with $\alpha = 0.3$. The void-fraction criterion for consecutive levels (discussed above) also must be satisfied for vertical stratified flow. For additional detail, see Appendix E, Section E.2.7.

3.2.5. Plug Flow

Plug flow in horizontal flow channels is roughly analogous to slug flow in a vertical channel. However, the code uses the plug-flow regime only for interfacial heat-transfer purposes. The other closure parameters are based on the basic flow-regime/stratified-flow map. For plug flow to exist, TRAC requires that the liquid side be in condensation ($T_l < T_{sv}$). The existence of plug flow further is limited by the void fraction in three consecutive cells. The code contains logic to check that at least one of the three cells has a void fraction >0.50 but <0.75. If both the condensation and void-fraction criteria are met, TRAC superimposes the plug-flow regime on the bubbly slug/churn/annular-mist/stratified-flow regimes through the use of a weighting factor. The weighting factor W_{plug} is defined in Section 3.3.5. The superposition methodology is presented in Section 3.3.5. and 3.7.5. Additional detail is available in Appendix F, Section F.1.5.

3.2.6. Reflood

The reflood flow-regime model is included in TRAC to simulate the post-CHF behavior of the fluid in a reactor core during the refill and reflood phase of a LOCA. Based on the observations of Ishii and his coworkers (Refs. 3-3. to 3-5.), the reflood model is divided into several discrete regimes. Moving downstream from the point at which the critical heat flux occurs, these regimes are identified as transition boiling, smooth inverted annular flow, rough-wavy inverted annular flow, agitated inverted annular flow, dispersed (or post-agitated) flow, and highly dispersed flow (see Fig. 3-3.). As the name suggests, smooth inverted annular flow (IAF) is characterized by a vapor film near the heated wall and a stable liquid core central to the flow channel. Rough-wavy IAF likewise is characterized by a fairly stable liquid core; however, in this case, the interface has become rough. In agitated IAF, the central liquid core begins to break up into large slugs. Both the dispersed and highly dispersed regimes are characterized by the presence of individual liquid droplets dispersed through a continuous gas phase. However, a liquid film is allowed to form in the dispersed regimes if a cold wall is adjacent to the hydraulic cell.

The transitions between flow regimes are taken from the work of Obot and Ishii (Ref. 3-5.) and are based largely on the capillary number

$$Ca = \frac{\mu_l V_l}{\sigma} . \tag{3-24}$$

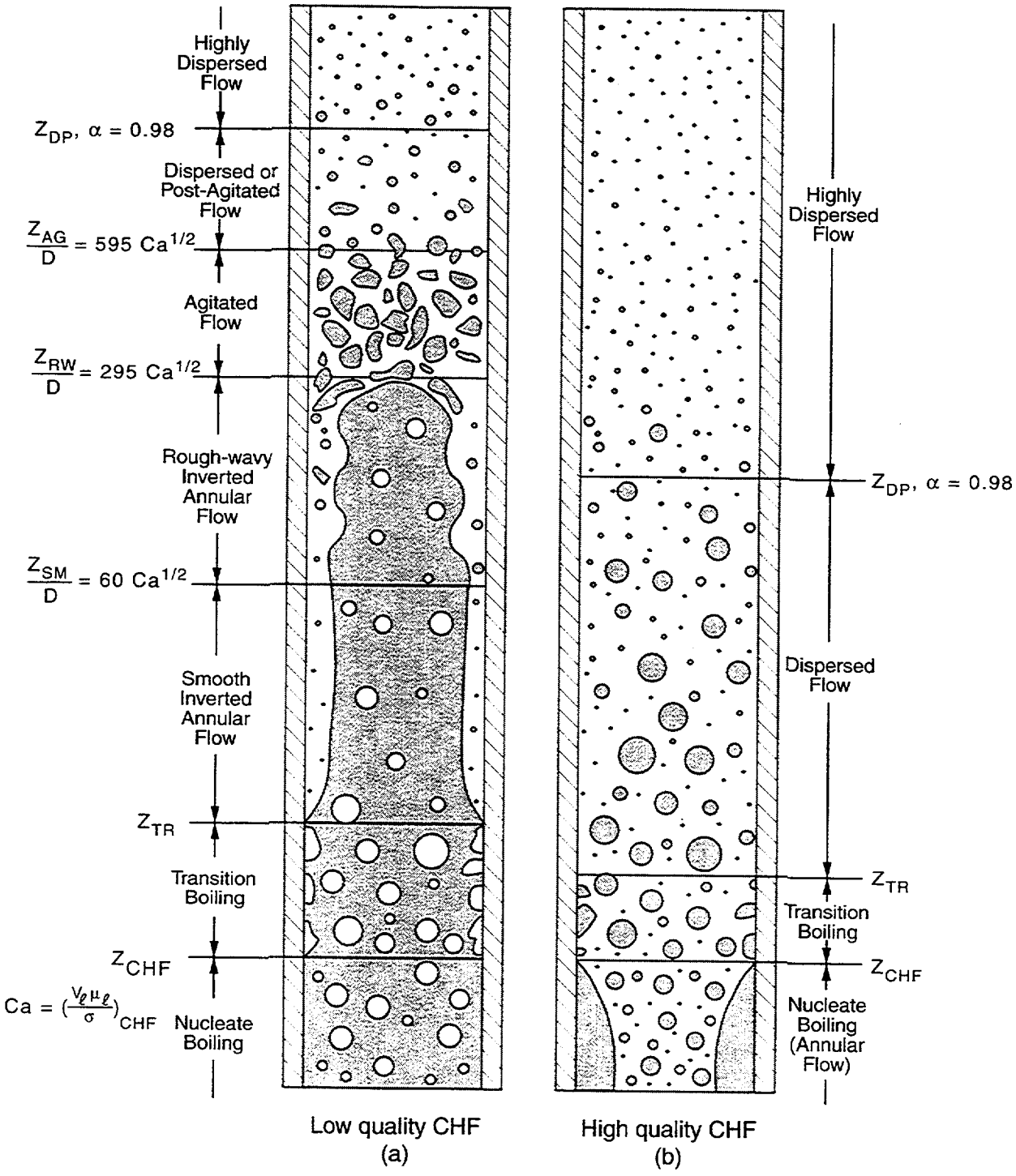

Fig. 3-3. Reflood flow regimes.

In terms of elevation above the quench front, Obot and Ishii define the transition between smooth and rough-wavy IAF as occurring at

$$\frac{L}{D} = 60 \cdot Ca^{1/2} . \tag{3-25}$$

The transition from rough-wavy to agitated IAF similarly is defined by

$$\frac{L}{D} = 295 \cdot Ca^{1/2} . \tag{3-26}$$

From agitated IAF to dispersed flow (post-agitated IAF), the transition criterion is

$$\frac{L}{D} = 595 \cdot Ca^{1/2} . \tag{3-27}$$

The TRAC implementation of the above criteria includes additional constraints based on void fraction to force the IAF regimes to occur within certain void-fraction ranges. These constraints assume that each IAF regime occurs in the following void-fraction ranges:

smooth IAF	$0.05 < \alpha < 0.3$
rough-wavy IAF	$0.3 < \alpha < 0.4$
agitated IAF	$0.4 < \alpha < 0.75$
post-agitated IAF	$0.75 < \alpha < 0.98$
highly dispersed flow	$\alpha > 0.98$.

Additionally, the transition from transition boiling to smooth inverted annular flow is defined as a function of the critical heat flux, the film-boiling heat flux, and the void fraction. The corresponding transition elevation, Z_{TR}, is discussed briefly in Section 3.8.5.1.

Finally, for interfacial heat transfer (including the interfacial area), the individual regimes described above are consolidated into the bubbly flow, inverted-annular-flow, and dispersed-flow models. In this case, the bubbly flow model is assumed to represent the subcooled nucleate-boiling, nucleate-boiling, and transition-boiling regimes. The inverted-annular-flow model incorporates the separate regimes of smooth IAF, rough-wavy IAF, and agitated IAF. The dispersed-flow model represents both dispersed and highly dispersed flows.

3.3. Interfacial Area

As seen in Section 3.1., fluid mass, momentum, and energy closure requires that the interfacial area A_i between the liquid and combined-gas phases be specified. Specifically, the interfacial area is needed to define the heat-transfer rates per unit volume for the interface-to-liquid heat transfer, the interface-to-gas heat transfer, and the liquid-to-gas sensible heat transfer. Because the interfacial-area parameter is highly dependent on

flow regime, the following sections will elaborate on the individual models as coded within TRAC. A summary of the interfacial-area models also is provided in Table 3-2.

3.3.1. Bubbly Slug Interfacial Area

In discussing the bubbly slug flow regime, this section will refer collectively to the bubbly, bubbly slug transition, and bubbly slug flow regimes depicted in Fig. 3-2. The total interfacial area for a given hydraulic cell in bubbly slug flow is defined as the product of an area concentration and the cell volume, or

$$A_i = A_{i,bs} = a_{i,bs} \cdot B_{cell} \,. \tag{3-28}$$

Based on the work of Ishii and Mishima (Ref. 3-6.), the interfacial-area concentration is calculated as a function of the average void fraction within the liquid slug, α_{gs}, such that

$$a_{i,bs} = \frac{C^*}{D^*} \frac{\alpha - \alpha_{gs}}{1 - \alpha_{gs}} + \frac{6\,\alpha_{gs}}{D_b} \frac{1 - \alpha}{1 - \alpha_{gs}} \tag{3-29}$$

for

$$\alpha_{gs} = \begin{cases} 0.3 & G < 2000 \text{ kg/m}^2\text{-s} \\ 0.3 + 0.2\,(G - 2000)/700 & 2000 \le G < 2700 \text{ kg/m}^2\text{-s} \\ 0.5 & G \ge 2700 \text{ kg/m}^2\text{-s} \,. \end{cases} \tag{3-30}$$

However, if the cell void fraction α is found to be $<\alpha_{gs}$, then α_{gs} is set equal to α.

In the area concentration equation, the Sauter mean bubble diameter D_b is defined as a function of the Laplace coefficient L_o (Ref. 3-7.), where

$$D_b = 2\,L_o \tag{3-31}$$

and

$$L_o = \sqrt{\frac{\sigma}{g\,(\rho_l - \rho_g)}} \,. \tag{3-32}$$

The bubble diameter is also subject to the constraint that $0.1 \text{ mm} \le D_b \le 0.9 D_h$.

Finally, the parameters C^* and D^* are included to account for the presence of cap bubbles or vapor slugs. The two parameters are defined as a function of hydraulic diameter such that

$$C^* = \begin{cases} 4.5 & D_h < D_{h,crit} \\ 16 & D_h \ge D_{h,crit} \end{cases} \tag{3-33}$$

$$D^* = \begin{cases} D_h & D_h < D_{h,crit} \\ D_{h,crit} & D_h \geq D_{h,crit} \end{cases} \quad (3\text{-}34)$$

where $D_{h,crit}$ is a critical hydraulic diameter for slug-to-cap-bubble transition, calculated as

$$D_{h,crit} = 50\, L_o \ . \quad (3\text{-}35)$$

The parameters C^* and D^* have been modified from the original reference to include large-diameter flow channels.

3.3.2. Churn-Flow Interfacial Area

The interfacial area for the churn- (or transition-) flow regime is calculated as a weighted average of the bubbly slug and annular-mist interfacial areas. The churn-flow interfacial area thus is defined by

$$A_i = (1 - W_t) \cdot A_{i,bs} + W_t \cdot A_{i,am} \ , \quad (3\text{-}36)$$

where

$$W_t = \frac{\alpha - 0.5}{0.25} \quad (3\text{-}37)$$

and $0 \leq W_t \leq 1$. In the above equation for interfacial area, the bubbly slug area term is evaluated using the methodology presented in Section 3.3.1. at a void fraction of 0.5. Similarly, the annular-mist area term is evaluated using the model presented in Section 3.3.3. at a void fraction of 0.75.

The churn-flow interfacial area is determined by interpolation between the bubbly slug and annular-mist interfacial-area models. The interfacial area can change by several factors of 10 between the two regimes. The interpolation method given here was developed specifically for implementation into TRAC. The interpolation algorithm itself embodies no physics; it is a mathematical operation. However, the interpolation algorithm provides a transition between two regimes, which are represented by physical models.

3.3.3. Annular-Mist Interfacial Area

For annular-mist flow, the interfacial area is based on a superposition of the film and droplet fields such that

$$A_i = A_{i,am} = (1 - W_f) \cdot (A_{i,drop} + A_{i,film}) + W_f \cdot A_{i,drop,max} \ , \quad (3\text{-}38)$$

where

$$W_f = \begin{cases} 0 & \max(V_l, V_g) < 10\ V_c \\ 0.5\ (\max(V_l, V_g)/V_c) - 5 & 10\ V_c \le \max(V_l, V_g) \le 12\ V_c \\ 1 & \max(V_l, V_g) > 12\ V_c \end{cases} \quad (3\text{-}39)$$

for the critical velocity

$$V_c = \left[\frac{g\,\sigma\,(\rho_l - \rho_g)}{\rho_g^2}\right]^{1/4}, \quad (3\text{-}40)$$

where V_c is based upon a Helmholtz disturbance wave.

The superposition method given here was developed specifically for implementation into TRAC.

The interfacial-area term for the droplets is defined by

$$A_{i,drop} = \frac{\alpha}{1 - \alpha_d}\left(\frac{6\,\alpha_d}{D_d}\right) B_{cell}, \quad (3\text{-}41)$$

where α_d represents the droplet fraction in the gas core. The droplet fraction is estimated as a function of the entrainment E, where

$$\alpha_d = E\,\frac{(1 - \alpha)\,V_l}{\alpha\,V_g}. \quad (3\text{-}42)$$

From Ishii and Mishima (Refs. 3-8. and 3-9.), the entrainment is calculated by

$$E = \tanh\left(7.25\text{e-}07\ We_e^{1.25}\ Re_l^{0.25}\right) \quad (3\text{-}43)$$

for the liquid Reynolds number

$$Re_l = \frac{\rho_l\,(1 - \alpha)\,V_l\,D_h}{\mu_l} \quad (3\text{-}44)$$

and the effective Weber number

$$We_e = \frac{\rho_g\,(\alpha\,V_g)^2\,D_h}{\sigma}\left(\frac{\rho_l - \rho_g}{\rho_g}\right)^{1/3}. \quad (3\text{-}45)$$

Additionally, the Sauter mean droplet diameter is calculated as

$$D_d = \min(D_{d1}, D_{d2}), \quad (3\text{-}46)$$

provided that $84\ \mu m \le D_d \le 4\ mm$. The first term D_{d1} is based on the correlation of Kataoka (Ref. 3-10.), where

$$D_{d1} = (7.96e\text{-}3) \cdot \frac{\sigma}{\rho_g (\alpha V_g)^2} Re_g^{2/3} \left(\frac{\rho_g}{\rho_l}\right)^{-1/3} \left(\frac{\mu_g}{\mu_l}\right)^{2/3} . \tag{3-47}$$

The second droplet diameter D_{d2} likewise is based on the work of Kataoka and of Kitscha and Kocamustafaogullari (Ref. 3-11.), such that

$$D_{d2} = 0.254\ L_o \left[-0.13\ We_m + \sqrt{16 + (0.13\ We_m)^2}\right] . \tag{3-48}$$

In the above droplet relations, the Reynolds number and Weber number are given by

$$Re_g = \frac{\rho_g\ \alpha\ V_g\ D_h}{\mu_g} \tag{3-49}$$

and

$$We_m = \frac{\rho_g (\alpha V_g)^2 L_o}{\sigma} . \tag{3-50}$$

Finally, if we assume that all droplets are entrained, then

$$\alpha_d = 1 - \alpha . \tag{3-51}$$

Thus, it follows that

$$A_{i,drop,max} = B_{cell} \cdot \frac{6(1 - \alpha)}{D_d} . \tag{3-52}$$

From geometry, the interfacial-area term for the liquid film can be specified as

$$A_{i,film} = B_{cell} \cdot \frac{4\ C_r}{D_h} \sqrt{\frac{\alpha}{1 - \alpha_d}} , \tag{3-53}$$

where the parameter C_r is included to account for waviness of the liquid interface (Ref. 3-12.). The surface waviness factor is ignored for thick films. However, as the liquid film becomes very thin (<25 mm), it is assumed that the film breaks down and rivulets form. Under these conditions, the surface wave parameter is defined by

$$C_r = \frac{D_h (1 - \alpha)}{l_{min}} \le 1 \tag{3-54}$$

for $l_{min} = 0.1$ mm.

The modeling equations for the annular-mist interfacial area are coded as given in the original references cited above. The rivelt model given here is heuristic and was developed specifically for implementation into TRAC.

3.3.4. Stratified-Flow Interfacial Area

For fully stratified flow, the interfacial area can be calculated from the cell geometry. For horizontal stratified flow, the interfacial area is given by

$$A_i = A_{i,strat} = D_h \cdot \Delta \times \sqrt{1 - \left(1 - \frac{2 L_l}{D_h}\right)^2}\ , \tag{3-55}$$

where L_l and Δx represent the stratified liquid level and the cell length, respectively. For a cylindrical channel cross section, the calculation method for the liquid level is discussed in Appendix H (Section H.1.3.2.). Similarly, for vertical stratified flow, the interfacial area is specified such that

$$A_i = A_{i,strat} = \frac{B_{cell}}{\Delta x}\ . \tag{3-56}$$

These interfacial-area models are based on the idealized geometry of the interface and thus are exact.

As discussed in Section 3.2., the stratified-flow regime is superimposed on the basic flow-regime map shown in Fig. 3-2. Thus, when the flow is not fully stratified, the code interpolates between the interfacial area determined for stratified flow, calculated as above, and the value otherwise determined with respect to the basic flow-regime map. In other words,

$$A_i = A_{i,map,strat} = (1 - W_{st})\, A_{i,map} + W_{st}\, A_{i,strat} \tag{3-57}$$

for the weighting factor W_{st}, where $0 \le W_{st} \le 1$. The weighting factor is calculated as a function of both void fraction (flow regime) and critical velocity. In general, for 1D components, the weighting factor is nonzero for velocities less than 10 times the critical velocity (see Section 3.2.4.). For additional detail, see Appendix E (Section E.2.7.).

The interpolation method given here was developed specifically for implementation into TRAC. The interpolation algorithm itself embodies no physics; it is a mathematical operation. However, the interpolation algorithm provides a transition between two regimes, which are represented by physical models.

3.3.5. Plug-Flow Interfacial Area

When the bulk liquid temperature is below the saturation temperature of the vapor (condensation mode), full or partial liquid plugging may exist if there are large differences in the void fraction across three contiguous hydraulic cells. Based on a cylindrical channel geometry, the plug-flow interfacial area is calculated by

$$A_{i,plug} = M_{plug} \cdot \frac{\pi D_h^2}{4}, \tag{3-58}$$

where

$$M_{plug} = \begin{cases} 2 & \text{plug in one cell only} \\ 1 & \text{plug confined to two or more cells.} \end{cases} \tag{3-59}$$

The plug-flow-area model is based on the idealized geometry of the flow field in a cylindrical flow channel.

The above interfacial area for plug flow is superimposed on the flow-regime-map/ stratified-flow value according to the following relation:

$$A_i = A_{i,map,strat,plug} = (1 - W_{plug})\, A_{i,map,strat} + W_{plug}\, A_{i,plug} \tag{3-60}$$

for

$$W_{plug} = \frac{(\alpha_{max} - \alpha_{min})(\alpha_{max} - 0.5)(0.75 - \alpha_{min})}{(0.75 - 0.5)^3} \tag{3-61}$$

and $0 \le W_{plug} \le 1$. Finally, the maximum and minimum void fractions are defined such that

$$\alpha_{max} = \max(\alpha_{cell\ i-1},\ \alpha_{cell\ i},\ \alpha_{cell\ i+1})$$

and

$$\alpha_{min} = \min(\alpha_{cell\ i-1},\ \alpha_{cell\ i},\ \alpha_{cell\ i+1})$$

for the three contiguous cells $i - 1$, i, and $i + 1$.

The interpolation method given here was developed specifically for implementation into TRAC. The interpolation algorithm itself embodies no physics; it is a mathematical operation. However, the interpolation algorithm provides a transition between two regimes, which are represented by physical models.

3.3.6. Reflood Interfacial Area

Under core-reflood conditions, TRAC utilizes the flow-regime map of Ishii and his coworkers (Refs. 3-3. to 3-5.). Within this flow-regime map, separate interfacial-area models are provided for the three general regions of bubbly flow, inverted annular flow, and dispersed flow. The code calculates the overall interfacial area for a given hydraulic cell based on the weighted average of these individual reflood interfacial areas, or

$$A_i = A_{i,reflood} = W_{sb} \cdot A_{i,bubbly} + W_{inv} \cdot A_{i,inv} + W_{ds} \cdot A_{i,ds} \,. \tag{3-62}$$

In the above equation, the linear weighting factors W_{sb}, W_{inv} and W_{ds} are based on the relative axial distance within each cell for which the appropriate flow regime is present. The calculation of these weighting factors is presented in Appendix F (Section F.1.6., Table F-4.). Additional detail of the interfacial-area models likewise can be found in Appendix F.

The interpolation method given here was developed specifically for implementation into TRAC. The interpolation algorithm itself embodies no physics; it is a mathematical operation. However, the interpolation algorithm provides a transition between two regimes, which are represented by physical models.

3.3.6.1. Bubbly Flow Model. The interfacial area for bubbly flow under reflood conditions is identical to that presented in Section 3.3.1., except that the void fraction is restricted to the range $0.05 \le \alpha \le 0.3$.

3.3.6.2. Inverted-Annular-Flow Model. From geometry, the hydraulic diameter of the inverted liquid core is given by

$$D_{h,core} = D_h \sqrt{1 - \alpha} \,. \tag{3-63}$$

Thus, the interfacial area can be specified such that

$$A_{i,inv} = \pi \, D_{h,core} \, \Delta x \,, \tag{3-64}$$

where Δx is the cell length.

The inverted annular interfacial-area model is based on the idealized geometry of the interface and thus is exact.

When the flashing of superheated liquid occurs ($T_l > T_{sat}$), an additional interfacial area for bubbles existing in the liquid core is added to $A_{i,inv}$. In this case,

$$A_{i,inv} = \pi \left(D_{h,core} - 2\,\delta\right) \Delta x + \frac{6\,\alpha_{fr}\,B_{cell}}{d_b} \,, \tag{3-65}$$

where α_{fr} is the void fraction in the liquid core, d_b is the bubble diameter, and δ is the vapor-film thickness.

The interfacial-area model is based on the idealized geometry of the interface and thus is exact.

3.3.6.3. Dispersed-Flow Model. In dispersed flow, the total interfacial area is based on a superposition of the droplet and film fields, where

$$A_{i,ds} = A_{i,drop} + A_{i,film} \cdot \tag{3-66}$$

The interfacial area of the liquid film can be defined as

$$A_{i,film} = \frac{4\,\alpha_f\,B_{cell}}{D_h}, \tag{3-67}$$

where the liquid fraction of the film, α_f, can be calculated by

$$\alpha_f = \frac{4\,F_u\,\delta_f}{D_h} \cdot \tag{3-68}$$

In the above equation, F_u is the cold-wall fraction adjacent to the hydro cell. The liquid-film thickness, δ_f, was derived by Pasamehmetoglu (Ref. 3-13.), such that

$$\delta_f = \frac{0.0025\,\rho_l\,V_g^2}{g\,\rho_l - \dfrac{0.75\,\rho_g\,V_g^2}{D_h}}, \tag{3-69}$$

subject to the constraint that $10^{-17} \le \delta_f \le 5$ mm.

The film liquid fraction also can be estimated by

$$\alpha_f = F_u(1-\alpha)W_{fd}, \tag{3-70}$$

where W_{fd} is the cold-wall weighting factor such that

$$W_{fd} = \begin{cases} 0 & \alpha \le \min(\alpha_{ag}, 0.7) \\ 5\left[\dfrac{0.98-\alpha^*}{0.98-\min(\alpha_{ag}, 0.7)}\right]^{0.35} & \min(\alpha_{ag}, 0.7) < \alpha < 0.98 \\ 5 & \alpha \ge 0.98, \end{cases} \tag{3-71}$$

where α_{ag} is the void fraction at the agitated-to-post-agitated inverted-annular-flow (IAF) regime transition and α^* is the void fraction constrained to be between 0.3 and 0.9995.[1]

The film liquid fraction, α_f, is selected as the minimum of the values obtained from the above equations.

---

1. In TRAC-M/F77, the exponent 0.35 in Eq. (3-71) is 0.5 for the reflood model that is based on MOD2.

Given the volume fraction of the liquid film, it follows that the volume fraction of the droplets must be expressed by

$$\alpha_{dd} = 1 - \alpha_f - \alpha \, . \tag{3-72}$$

Now, the droplet interfacial area is defined by

$$A_{i,drop} = B_{cell} \cdot \frac{6\,\alpha_{dd}}{D_d} \, , \tag{3-73}$$

where D_d is the Sauter mean droplet diameter. For dispersed flow, this droplet diameter is equivalent to that expressed in Section 3.3.3., based on the work of Kataoka (Ref. 3-10.) and of Kitscha and Kocamustafaogullari (Ref. 3-11.).

The interfacial area for the dispersed-flow regime accounting for liquid on the walls is based on an idealized flow field structure and thus is exact. The correlations used in the modeling are coded as given in the original references. The liquid-film-fraction weighting factor given here is original to TRAC.

3.4. Interfacial Mass Transfer

Closure for interfacial mass transfer is achieved through the term Γ, which is defined as the rate of interfacial mass transfer per unit volume. As stated in Section 3.1., the total mass-transfer rate is actually the sum of two components: mass transfer caused by interfacial heat transfer Γ_i and mass transfer caused by subcooled boiling at a heated wall Γ_{sub}:

$$\Gamma = \Gamma_i + \Gamma_{sub} \, . \tag{3-74}$$

As previously noted, the interfacial mass transfer caused by interfacial heat transfer is defined by the jump relation

$$\Gamma_i = \frac{q_{il} + q_{ig}}{(h_g - h_l)} \, . \tag{3-75}$$

The individual terms for interfacial heat transfer to the gas and to the liquid were defined in Section 3.1. To solve for the heat-transfer terms, we first must determine the flow-regime-dependent interfacial area and interfacial heat-transfer coefficients as presented in Sections 3.3. and 3.7., respectively. A positive value for Γ_i indicates vapor generation at the interface. Conversely, a negative value indicates liquid generation.

The interfacial mass transfer caused by subcooled boiling likewise is defined by the equation

$$\Gamma_{sub} = \frac{h_\Gamma A_w (T_w - T_l)}{B_{cell} (h_g - h_l)} \, . \tag{3-76}$$

The subcooled-boiling term is important for hydraulic cells coupled to a heated wall. Specifically, the term is included to improve the prediction of void fraction near the saturation point. For subcooled boiling to take place, the cell-averaged liquid temperature must be below the saturation temperature; at the same time, the wall temperature must be above T_{sat}.

When the above conditions are satisfied, the actual mass-transfer rate is in turn dependent on the subcooled-boiling liquid heat-transfer coefficient h_Γ, as defined by

$$h_\Gamma = W_{sb}\, h_{wl}\, F_e \ , \tag{3-77}$$

where h_{wl} is the wall-to-liquid heat-transfer coefficient as presented in Section 3.8. The subcooled-boiling weighting factor, W_{sb}, is empirically based and is calculated such that

$$0 \le W_{sb} = 5\,(0.7 - \alpha) \le 1 \ . \tag{3-78}$$

W_{sb} equals 1.0 for void fractions ranging from 0.0 to 0.5. Above a void fraction of 0.5, the weighting factor ramps linearly to zero. Finally, F_e is the evaporation fraction based on Lahey's mechanistic model (Ref. 3-14.), where

$$0 \le F_e = \frac{T_l - T_{ld}}{\max(1,\ (T_{sv} - T_{ld}))} \le 1 \ . \tag{3-79}$$

The liquid temperature at bubble detachment T_{ld} provides the criteria by which bubbles reside solely on the wall or bubbles may detach and move into the bulk fluid without collapsing. As demonstrated by the above equation, when T_{ld} exceeds the bulk liquid temperature, the evaporation fraction, and thus the mass-transfer rate, becomes zero. In this way, the code does not calculate any void generation associated with bubbles residing solely on the wall. However, once the bulk fluid temperature exceeds T_{ld}, the bubbles may detach and the calculated mass-transfer rate then becomes nonzero.

The value of the liquid temperature at bubble detachment is determined via the modified Saha-Zuber (Ref. 3-15.) correlation for the point of net vapor generation. Saha and Zuber (Ref. 3-15.) correlated the point of net vapor generation as a function of Nusselt, Stanton, and Peclet numbers, where

$$\mathrm{Nu} = 455 \qquad \text{if} \quad \mathrm{Pe} \le 70{,}000 \ , \tag{3-80}$$

and

$$\mathrm{St} = 0.0065 \quad \text{if} \quad \mathrm{Pe} > 70{,}000 \ . \tag{3-81}$$

A summary of the interfacial mass-transfer parameters is presented in Table 3-3.

3.5. Interfacial Drag

As shown in Section 2.1.1., the liquid- and gas-field momentum equations each include a term for the interfacial shear force. Closure of these equations thus requires that we specify the interfacial drag coefficient, c_i. However, the value of the interfacial drag coefficient is dependent on flow regime. A discussion of the individual flow-regime-dependent models can be found in the following sections. Likewise, a summary of the interfacial drag-coefficient models is presented in Table 3-4.

3.5.1. Bubbly Slug Flow Interfacial Drag Coefficient

In discussing the bubbly flow regime, this section will collectively refer to the bubbly, bubbly slug transition, and bubbly slug flow regimes depicted in Fig. 3-2. Following the methodology of Ishii and Chawla (Ref. 3-16.), TRAC defines the interfacial drag coefficient for bubbly slug flow as

$$c_i = \frac{0.75\, c_{Db}\, \alpha\, \rho_l\, P_s}{D_b}\ , \tag{3-82}$$

where c_{Db} is the bubble drag coefficient, D_b is the bubble diameter, and P_s is the profile slip. Under special circumstances, namely when bubbly slug flow is encountered in an upper plenum, the code redefines the interfacial drag coefficient according to the correlation of Wilson. Specific detail of the Wilson model is not included in this section but can be found in Appendix H, Section H.1.1.10.

For the above equation, the bubble diameter is defined as a function of the Laplace coefficient [as recommended by Ishii (Ref. 3-7.)] and the channel hydraulic diameter such that

$$D_b = 2L_o(1 - XS) + \min(40L_o, 0.9D_h) \cdot XS \tag{3-83}$$

for

$$L_o = \sqrt{\frac{\sigma}{g\,(\rho_l - \rho_g)}} \tag{3-84}$$

and

$$XS = \begin{cases} 0.0 & \text{bubbly flow} \\ \dfrac{(2700 - G)}{(2700 - 2000)} \cdot \dfrac{(\alpha - 0.3)}{(0.5 - 0.3)} & \text{bubbly slug transition} \\ \dfrac{(\alpha - 0.3)}{(0.5 - 0.3)} & \text{bubbly slug flow.} \end{cases}$$

The value of the bubble diameter further is constrained by the limitation that

$$0.0001\ \text{m} < D_b < \min(40\ L_o,\ 0.9\ D_h)\ . \tag{3-85}$$

The interpolation method given here, including the weighting factor, was developed specifically for implementation into TRAC. The interpolation algorithm itself embodies no physics; it is a mathematical operation. However, the interpolation algorithm provides a transition between two regimes, which are represented by physical models. The lower limit set on the bubble diameter given here is heuristic and was developed specifically for implementation into TRAC.

The profile slip factor is included to account for the migration of bubbles toward the higher-velocity region of the channel. The profile slip factor, likewise based on Ishii (Ref. 3-7.), is defined as

$$P_s = \frac{(C_1 V_g - C_0 V_l)^2}{(V_r)^2} \tag{3-86}$$

for

$$C_0 = 1.2 + 0.2 \sqrt{\frac{\rho_g}{\rho_l}} \tag{3-87}$$

and

$$C_1 = \frac{1.0 - C_0 \alpha_b}{1.0 - \alpha_b} , \tag{3-88}$$

where V_r is the relative velocity. For 3D components, TRAC limits the relative velocity such that $V_r \geq 0.01$ m/s.

The profile-slip factor is used in TRAC, as given in the source references for this constitutive model.

Additionally, the bubble drag coefficient is defined as a function of the Reynolds number such that

$$c_{Db} = \begin{cases} 240.0 & Re_b < 0.1031 \quad (3\text{-}89) \\ \frac{24.0}{Re_b}\left(1.0 + 0.15\, Re_b^{0.687}\right) & 0.1031 < Re_b < 989.0 \quad (3\text{-}90) \\ 0.44 & Re_b > 989.0 \quad (3\text{-}91) \end{cases}$$

for

$$Re_b = \frac{D_b V_r \rho_l}{\mu_l}. \tag{3-92}$$

The value of the bubble drag coefficient in each of the three Reynolds-number regimes corresponds to Stoke's drag law ($Re_b < 0.1031$), the empirical relation proposed by Schiller and Nauman ($0.1031 < Re_b < 989.0$, Ref. 3-17.), and the recommendation of Bird, Stewart, and Lightfoot ($Re_b > 989.0$, Ref. 3-18.).

The Reynolds numbers at the transition points have been chosen to provide continuity to the drag coefficient.

3.5.2. Churn-Flow Interfacial Drag Coefficient

In the churn-flow regime (void fractions between 0.5 and 0.75), TRAC calculates the interfacial drag coefficient as a weighted average of both the bubbly slug drag coefficient and the annular-mist drag coefficient. The churn flow (or "transition") interfacial drag coefficient thus is defined as

$$c_{itrans} = c_{iam} W_t + c_{ibs} (1-W_t) \tag{3-93}$$

for

$$W_t = 4\alpha - 2 \ , \tag{3-94}$$

where $0.0 \le W_t \le 1.0$. In the above equation, the bubbly slug interfacial drag coefficient c_{ibs} is evaluated at a void fraction of 0.5. The methodology for calculating the bubbly slug interfacial drag coefficient was discussed in Section 3.5.1. Likewise, the annular-mist interfacial drag coefficient c_{iam} is evaluated at a void fraction of 0.75. Details of the annular-mist interfacial drag coefficient are presented in Section 3.5.3.

The interpolation method for the drag coefficient in the churn flow given here was developed specifically for implementation into TRAC. The interpolation algorithm itself embodies no physics; it is a mathematical operation. However, the interpolation algorithm provides a transition between two regimes, which are represented by physical models.

3.5.3. Annular-Mist-Flow Interfacial Drag Coefficient

In the annular-mist-flow regime, the total interfacial drag force is assumed to be a superposition of the separate drag forces caused by the entrained droplets and the annular film. The annular-mist interfacial drag coefficient thus is defined by

$$c_i = \frac{M_i}{|V_r| V_r} \tag{3-95}$$

for

$$M_i = M_{id} + M_{ia} \ ,$$

where M_{id} and M_{ia} represent the drag forces caused by the droplet field and the annular film, respectively. The global model was created by Ishii and Mishima (Ref. 3-19.). In the above equation, the relative velocity V_r is based on the drift-flux formulation of Ishii (Ref. 3-30.). Details of Kataoka and Ishii's relative velocity model (Ref. 3-12.) can be found in Appendix H (Section H.1.2.1.).

The interfacial drag force caused by the annular film is calculated via the model of Ishii and Mishima (Ref. 3-19.) such that

$$M_{ia} = a_{if} \cdot \tau_f \ , \tag{3-96}$$

where τ_f is the interfacial shear. The interfacial area per unit volume a_{if} is

$$a_{if} = \frac{4\, C_{an}}{D} \sqrt{\frac{\alpha}{1 - \alpha_d}} \ , \tag{3-97}$$

where C_{an} is a roughness parameter to account for waviness in the film ($C_{an} \geq 1$). In the above equation, the area fraction of the droplets α_d is calculated as the ratio of the liquid and gas superficial velocities multiplied by the entrainment, or

$$\alpha_d = \frac{j_l}{j_g} E \ . \tag{3-98}$$

The entrainment E in turn is based on the correlation of Kataoka and Ishii (Ref. 3-12.), where

$$E = \tanh\left(7.25\text{e-}07\ We_d^{1.25}\ Re_l^{0.25}\right) \tag{3-99}$$

for the liquid Reynolds number

$$Re_l = \frac{\rho_l\, j_l\, D}{\mu_l} \tag{3-100}$$

and for the droplet Weber number

$$We_d = \frac{\rho_g\, j_g^2\, D}{\sigma}\left(\frac{\rho_l - \rho_g}{\rho_g}\right)^{1/3} = 4.0 \ . \tag{3-101}$$

Additionally, the shear force τ_f is calculated from

$$\tau_f = 0.5\ f_i\ \rho_c (V_g - V_f)^2 \ , \tag{3-102}$$

where ρ_c is the density of the gas/droplet core and V_f is the annular film velocity. The film interfacial friction factor f_i is based on the Wallis (Ref. 3-20.) correlation given by

$$f_i = 0.005\,[1 + 75(1 - \alpha)] \quad . \tag{3-103}$$

The interfacial drag force caused by the entrained droplet field likewise is based on the model of Ishii and Mishima (Ref. 3-19.), where

$$M_{id} = a_i \left[\frac{c_d}{4} \left(\frac{r_{sm}}{r_d} \right) \frac{\rho_g (V_g - V_d)^2}{2} \right] \tag{3-104}$$

and

$$a_i = \frac{\alpha}{1 - \alpha_d} \left(\frac{3\,\alpha_d}{r_{sm}} \right) \quad . \tag{3-105}$$

In the above equations, c_d is the droplet drag coefficient, r_{sm} is the Sauter mean radius, r_d is the drag radius, V_d is the droplet velocity, and α_d is the area fraction of the droplet (as defined above). The droplet drag coefficient is estimated using the correlation of Ishii and Chawla (Ref. 3-16.), where

$$c_d = \frac{24}{Re_d} \left(1.0 + 0.1\ Re_d^{0.75} \right) \tag{3-106}$$

for

$$Re_d = \frac{D_d \rho_g |V_g - V_d|}{\mu_m} \tag{3-107}$$

and

$$\mu_m = \frac{\mu_g}{(1 - \alpha_d)^{2.5}} \quad . \tag{3-108}$$

The droplet diameter D_d is evaluated using the model of Kataoka, Ishii, and Mishima (Ref. 3-10.) such that

$$D_d = \frac{2.0}{\rho_g j_g^2} \left[0.005\ \sigma \left(\frac{\mu_g}{\mu_l} \right)^{2/3} Re_g^{2/3} \left(\frac{\rho_g}{\rho_l} \right)^{1/3} \right] \tag{3-109}$$

for $0.000042 < D_d < 0.002$ m. The Sauter mean radius likewise is dependent on the droplet diameter (Ref. 3-12.), as shown by

$$r_{sm} = 0.796\ \frac{D_d}{2} \quad . \tag{3-110}$$

Additionally, the ratio of the Sauter mean radius over the drag radius is defined to be 1.0 for spherical particles. Finally, the relative velocity between the gas phase and the entrained droplets ($V_g - V_d$) is calculated from the model of Ishii (Ref. 3-30.). Details of Ishii's relative velocity formulation can be found in Appendix H (Section H.1.2.1.).

The correlations that make up the annular-mist interfacial drag model are used in TRAC, as given in the source references for this constitutive model.

3.5.4. Stratified-Flow Interfacial Drag Coefficient

For fully stratified flow, the interfacial drag coefficient is defined per the method of Taitel and Dukler (Ref. 3-21.). Specifically, the drag coefficient is calculated such that

$$c_i = \frac{1}{2} f_i \rho_g \frac{S_i}{A_{flow}}, \tag{3-111}$$

where f_i is the interfacial friction factor, S_i is the width of the stratified interface, and A_{flow} is the flow area. For 3D components, the above relation simplifies to

$$c_i = \frac{1}{2} f_i \rho_g \frac{1}{D_h}. \tag{3-112}$$

For 1D components, the flow area and width of the stratified interface are determined assuming a circular channel cross section. Details of the TRAC methodology can be found in Appendix H (Section H.1.3.2.).

Additionally, both 1D and 3D components use the interfacial friction-factor correlation of Ohnuki (Ref. 3-22.) such that

$$f_i = 1.84\, f_{wg}, \tag{3-113}$$

where

$$f_{wg} = \begin{cases} 16.0\,(Re_g)^{-1} & \text{laminar flow} \\ 0.079\,(Re_g)^{-0.25} & Re_g < 10^5 \\ 0.0008 + 0.05525\,(Re_g)^{-0.237} & Re_g \geq 10^5. \end{cases} \tag{3-114}$$

The correlations are used in TRAC, as given in the source references for this constitutive model.

As mentioned in Section 3.2., the stratified-flow regime is superimposed on the basic flow-regime map shown in Fig. 3-2. Thus, when the flow is not fully stratified, the code interpolates between the drag coefficient determined for stratified flow, calculated as above, and the value otherwise determined with respect to the basic flow-regime map. In other words,

$$c_i = (1 - W_{st})\, c_{imap} + W_{st}\, c_{ist} \tag{3-115}$$

for the weighting factor W_{st}, where $0 \le W_{st} \le 1$. The weighting factor is calculated as a function of both void fraction (flow regime) and critical velocity. In general, for 1D components, the weighting factor is nonzero for velocities less that 10 times the critical velocity (see Section 3.2.4.). For additional details, see Appendix E (Section E.2.7.).

The interpolation method given here, including the weighting factor, was developed specifically for implementation into TRAC. The interpolation algorithm itself embodies no physics; it is a mathematical operation. However, the interpolation algorithm provides a transition between two regimes, which are represented by physical models.

3.5.5. Reflood Interfacial Drag Coefficient

Under core-reflood conditions, TRAC utilizes the flow-regime map of Ishii and his coworkers (Refs. 3-3. to 3-5.). As such, the code provides separate interfacial drag models for each of the following reflood flow regimes: subcooled boiling, smooth inverted annular flow, rough-wavy inverted annular flow, agitated inverted annular flow, dispersed flow, and highly dispersed flow. A limited discussion of these flow regimes can be found in Section 3.2.6. In terms of interfacial drag, the overall interfacial drag coefficient for a given hydraulic cell is defined as the weighted average of the individual reflood flow-regime drag coefficients, or

$$c_i = \mathrm{WFSB} \cdot c_{i,sb} + \mathrm{WFSM}\, c_{i,sm} + \mathrm{WFRW}\, c_{i,rw} + \mathrm{WFMDS}\, c_{i,pa} + \mathrm{WFHDS}\, c_{i,df}. \quad (3\text{-}116)$$

In the above equation, the individual interfacial drag coefficients correspond to subcooled boiling, smooth IAF, rough-wavy IAF, post-agitated (or dispersed) flow, and highly dispersed flow, respectively. Note the apparent omission of a separate interfacial drag coefficient for agitated IAF. In reality, it is included within the rough-wavy coefficient and weighting factor. The linear weighting factors *WFSB, WFSM, WFRW, WFMDS,* and *WFHDS* are based on the axial distance within a given hydraulic cell in which the appropriate flow regime is present. The calculation of these weighting factors is discussed in Appendix H (Section H.1.5.7.). The following paragraphs will summarize the models for each of the above drag coefficients. Additional model details likewise can be found in Appendix H.

The interpolation method given here, including the weighting factor, was developed specifically for implementation into TRAC. The interpolation algorithm itself embodies no physics; it is a mathematical operation.

3.5.5.1. Subcooled-Boiling Model. Throughout the regimes of subcooled nucleate boiling, nucleate boiling, and transition boiling, TRAC applies the subcooled-boiling interfacial drag model. This model assumes that the interfacial drag coefficient $c_{i,sb}$ comprises the drag coefficient from bubbles located at the wall $c_{i,w}$ and the drag coefficient from free-stream bubbles $c_{i,fr}$. However, the definition of the interfacial drag coefficient is dependent on whether the bulk liquid is subcooled, saturated, or superheated. Specifically, if $T_l \ge T_{sat}$,

$$c_{i,sb} = \frac{c_{i,w} \cdot V_l^2 + ffs \cdot c_{i,fr} \cdot V_r^2}{(\alpha_w + \alpha_{fr}) V_r^2} \quad (3\text{-}117)$$

for $\alpha_w > 0$, and

$$c_{i,sb} = \frac{ffs \cdot c_{i,fr}}{\alpha_{fr}} \quad (3\text{-}118)$$

for $\alpha_w \leq 0$, where $ffs = 0.00125$. The numerical factor ffs was not part of the original correlation. Otherwise, if $T_l < T_{sat}$,

$$c_{i,sb} = c_{i,w} . \quad (3\text{-}119)$$

In the above equations, the drag coefficient for bubbles that reside on the wall is defined using an analogous form of the Colebrook turbulent friction factor, where

$$c_{i,w} = \frac{2 \rho_g}{D_h} \left[1.14 - 2.0 \log \left(\frac{\varepsilon}{D_h} \right) \right]^{-2} . \quad (3\text{-}120)$$

In other words, the code assumes that the interfacial drag can be likened to that of flow through a rough pipe, where the roughness parameter ε is dependent on the bubble height from the wall Y_b such that

$$\varepsilon = 0.01 Y_b . \quad (3\text{-}121)$$

The bubble height parameter in turn is calculated based on the work of Collier (Ref. 3-23.). This parameter is given by the relation

$$Y_b = C \left[\frac{\sigma D_h}{\tau_w} \right]^{1/2} \cdot \left[1 + C' \left(\frac{g (\rho_l - \rho_g) D_h}{\tau_w} \right) \right]^{-1/2} \quad (3\text{-}122)$$

for

$$\tau_w = \frac{f_{fo} G^2}{2 \rho_l} , \quad (3\text{-}123)$$

where the constants C and C' are equal to 0.015 and 0.0, respectively. The above wall shear stress is dependent on the single-phase friction factor f_{fo}. This friction factor is evaluated for a relative roughness ε/D_h equal to 10^{-4}. Thus,

$$f_{fo} = \frac{1}{\left[1.14 - 2 \log \frac{\varepsilon}{D_h} \right]^2} = 0.01197037 . \quad (3\text{-}124)$$

The modeling of interfacial drag for subcooled boiling, including the drag caused by bubbles on the wall (as given above), is heuristic. The model is made up of correlations available from the literature, and the coefficients in these correlations are those in the source references for this constitutive model.

Alternatively, the drag coefficient for free-stream bubbles is derived from Ishii's bubbly flow drag force (Ref. 3-7.), where

$$c_{i,fr} = \frac{\alpha_{fr}}{d_b} f(\alpha) \rho_l \frac{(C_l V_v - C_0 V_l)^2}{(V_v - V_l)^2} \tag{3-125}$$

for

$$f(\alpha) = \left[\frac{1 + 17.67 (1 - \alpha_{fr})^{1.3}}{18.67 (1 - \alpha_{fr})^{1.5}} \right]^2 \tag{3-126}$$

and

$$d_b = 2 \sqrt{\frac{\sigma}{g (\rho_l - \rho_g)}} . \tag{3-127}$$

The coefficients C_0 and C_1 were defined in Section 3.5.1.

The bubbly flow drag-force model for free-stream bubbles is used in TRAC, as given in the source references for this constitutive model.

The free-stream void is related to the combined-gas void and the wall void by

$$\alpha_{fr} = \alpha_g - \alpha_w . \tag{3-128}$$

Based on Collier (Ref. 3-23.), the wall void is defined such that

$$\alpha_w = \begin{cases} \frac{\pi}{6} \frac{Y_b}{D_h} & T_l + 5 < T_{sat} \quad (3\text{-}129) \\ \frac{\pi}{6} \frac{Y_b}{D_h} [0.2 (T_{sat} - T_l)] & T_{sat} - 5 \le T_l < T_{sat} \quad (3\text{-}130) \\ 0 & T_l \ge T_{sat} . \quad (3\text{-}131) \end{cases}$$

Finally, the above model for $c_{i,sb}$ is applied as shown for cell void fractions between 0.0 and 0.5. For cell void fractions >0.98, $c_{i,sb}$ is replaced with the annular-mist interfacial drag coefficient discussed in Section 3.5.3. Between void fractions of 0.5 and 0.98, the code uses a linear weighting of the subcooled-boiling and annular-mist drag coefficients. A discussion of this weighting factor is presented in Appendix H (Section H.1.5.1.1.). The interpolation method given here, including the weighting factor, was developed

specifically for implementation into TRAC. The interpolation algorithm itself embodies no physics; it is a mathematical operation. However, the interpolation algorithm provides a transition between two regimes, which are represented by physical models.

3.5.5.2. Smooth Inverted-Annular-Flow Model. In the smooth IAF regime, the drag coefficient $c_{i,sm}$ is defined such that

$$c_{i,sm} = 2 \rho_g f_{i,sm} \frac{(1 - \alpha_g)^{1/2}}{D_h}, \tag{3-132}$$

where $f_{i,sm}$ is calculated from the smooth-tube friction-factor relations

$$f_{i,sm} = \begin{cases} 16\, Re_g^{-1} & Re_g < 1189.39 \quad \text{(laminar flow)} \quad (3\text{-}133) \\ 0.079\, Re_g^{-0.25} & Re_g \geq 1189.39 \quad \text{(turbulent flow)} \quad (3\text{-}134) \end{cases}$$

for

$$Re_g = \frac{\frac{(D_h - D_c)}{2} \alpha_g \rho_v V_v}{\mu_v}. \tag{3-135}$$

In the above Reynolds number, the diameter of the inverted liquid core D_c is given by

$$D_c = (\alpha_l)^{1/2} D_h . \tag{3-136}$$

These are standard engineering correlations applied in a manner that is original to TRAC. The correlations are used in TRAC, as reported in the source references for this constitutive model.

To prevent discontinuity, if $c_{i,sm}$ is greater than one-third the value of $c_{i,sb}$, then $c_{i,sm}$ is set equal to one-third $c_{i,sb}$. Additionally, if the cell void fraction is >0.98, $c_{i,sm}$ is assumed to equal the drag coefficient for highly dispersed flow, $c_{i,df}$. Below void fractions of 0.75, the code calculates the smooth IAF drag coefficient, as presented above. Between void fractions of 0.75 and 0.98, TRAC uses a linear weighting of the smooth IAF and highly dispersed drag coefficients. The interpolation method given here, including the weighting factor, was developed specifically for implementation into TRAC. The interpolation algorithm itself embodies no physics; it is a mathematical operation. However, the interpolation algorithm provides a transition between two regimes, which are represented by physical models. Detail of the weighting factor is presented in Appendix H (Section H.1.5.2.5.).

3.5.5.3. Rough-Wavy Inverted-Annular-Flow Model. The interfacial drag coefficient for rough-wavy IAF is identical to that of the smooth IAF regime, with the exception of the friction factor $f_{i,rw}$. The drag coefficient thus is expressed as

$$c_{i,rw} = 2 \rho_g f_{i,rw} \frac{(1 - \alpha_g)^{1/2}}{D_h} . \tag{3-137}$$

Because of the presence of waves and droplets, we expect the interfacial friction to be increased over smooth IAF. The rough-wavy friction factor is evaluated from the Colebrook equation for fully turbulent flow over rough surfaces, where

$$f_{i,rw} = \begin{cases} 0.7694675 & \varepsilon/D_h > 1 \quad (3\text{-}138) \\ \left[1.14 - 2.0 \log \left(\frac{\varepsilon}{D_h}\right)\right]^{-2} & \varepsilon/D_h < 1. \quad (3\text{-}139) \end{cases}$$

These are standard engineering correlations. The correlations are used in TRAC, as reported in the source references for this constitutive model.

In the above equation, the relative roughness is evaluated as a function of the droplet diameter such that

$$\frac{\varepsilon}{D_h} = 80 \frac{d_d}{D_h} . \tag{3-140}$$

The numerical coefficient on the right-hand side of this model was determined to be 80 by comparison of TRAC predictions with Cylindrical-Core Test Facility (CCTF) pressure-drop data. The modeling approach given here is heuristic and was developed specifically for implementation into TRAC.

Additionally, the droplet diameter is calculated from the model of Ishii (Ref. 3-7.), where

$$d_d = 0.612825 \left(\frac{\sigma}{g (\rho_l - \rho_g)}\right)^{1/2} N_{\mu g} \tag{3-141}$$

for the viscosity number

$$N_{\mu g} = \frac{\mu_g}{\left[\rho_g \sigma \sqrt{\frac{\sigma}{g (\rho_l - \rho_g)}}\right]^{1/2}} . \tag{3-142}$$

Similar to the smooth IAF model, if $c_{i,rw}$ is found to be greater than twice the value of $c_{i,sm}$, then the drag coefficient is adjusted to ensure a smooth transition. Likewise, if the cell void fraction is >0.98, $c_{i,rw}$ is assumed to equal the drag coefficient for highly dispersed flow, $c_{i,df}$. Below void fractions of 0.75, the code calculates the rough-wavy IAF drag

coefficient, as presented above. Between void fractions of 0.75 and 0.98, TRAC used a linear weighting of the rough-wavy and highly dispersed drag coefficients. The interpolation method given here, including the weighting factor, was developed specifically for implementation into TRAC. The interpolation algorithm itself embodies no physics; it is a mathematical operation. However, the interpolation algorithm provides a transition between two regimes, which are represented by physical models. A discussion of the coefficient adjustment and weighting methodology is presented in Appendix H (Section H.1.5.3.5.).

3.5.5.4. Agitated Inverted-Annular-Flow Model. In the agitated IAF regime, the interfacial drag coefficient is defined by

$$c_{i,ag} = c_{i,rw} ,$$

where $c_{i,rw}$ is calculated as presented above.

3.5.5.5. Post-Agitated-Flow Model. In the post-agitated- (dispersed-) flow regime, the interfacial drag coefficient $c_{i,pa}$ is calculated as a weighted average of the rough-wavy and highly dispersed flow drag coefficients. The interpolation method given here, including the weighting factor, was developed specifically for implementation into TRAC. The interpolation algorithm itself embodies no physics; it is a mathematical operation. However, the interpolation algorithm provides a transition between two regimes, which are represented by physical models. Details of the weighting methodology are discussed in Appendix H (Section H.1.5.6.).

3.5.5.6. Highly Dispersed Flow Model. The highly dispersed flow regime is characterized by small liquid droplets distributed throughout the vapor and by liquid films that may form on unheated surfaces. Thus, based on the work of Cappiello (Ref. 3-24.), the total interfacial drag coefficient for the highly dispersed flow regime is calculated as a function of the drag coefficient for the dispersed droplets $c_{i,dd}$ and of the drag coefficient for the liquid film $c_{i,f}$. In other terms,

$$c_{i,df} = \frac{c_{i,dd} V_r^2 + c_{i,f} V_v^2}{\left(V_v - \frac{\alpha_{dd} V_d}{1 - \alpha_g}\right)^2} . \qquad (3\text{-}143)$$

The dispersed-droplet drag coefficient is given by

$$c_{i,dd} = fcdrop \cdot \frac{0.75 \alpha_{dd} \rho_g C_d}{d_d} , \qquad (3\text{-}144)$$

where $fcdrop = 0.015$. The numerical factor, *fcdrop*, was not a part of the original correlation. Similar to the rough-wavy regime, the droplet diameter d_d is calculated as per Ishii (Ref. 3-7.) such that

$$d_d = 1.838 \left(\frac{\sigma}{g(\rho_l - \rho_g)}\right)^{1/2} (N_{\mu g})^{1/3} \tag{3-145}$$

for the viscosity number

$$N_{\mu g} = \frac{\mu_g}{\left[\rho_g \sigma \sqrt{\frac{\sigma}{g(\rho_l - \rho_g)}}\right]^{1/2}} . \tag{3-146}$$

The drag coefficient for spherical droplets, C_d, is based on the work of Ishii and Chawla (Ref. 3-16.), where

$$C_d = \frac{24}{Re_d}\left(1.0 + 0.1\ Re_d^{0.75}\right) \tag{3-147}$$

for

$$Re_d = \frac{\rho_v\, d_d V_r}{\mu_m} , \tag{3-148}$$

$$V_r = V_v - V_d , \tag{3-149}$$

and

$$\mu_m = \frac{\mu_v}{(1 - \alpha_{dd})^{2.5}} . \tag{3-150}$$

The droplet velocity was estimated by Cappiello (Ref. 3-24.) as

$$V_d = V_v - 2.462 \left[\frac{(\rho_l - \rho_v)\, g\, d_d}{2\, \rho_v}\right]^{1/2} . \tag{3-151}$$

In addition, the droplet liquid fraction is defined as

$$\alpha_{dd} = 1 - \alpha_f - \alpha_g , \tag{3-152}$$

where α_f is the volume fraction associated with the liquid film.

The film void fraction can be obtained from geometry such that

$$\alpha_f = \frac{P\, \delta_f\, F_u}{A_{flow}} , \tag{3-153}$$

where P is the equivalent channel perimeter, δ_f is the film thickness, and F_u is the area fraction of the unheated surfaces. The film thickness was derived by Pasamehmetoglu (Ref. 3-13.) and can be expressed by

$$\delta_f = \frac{0.0025\ \rho_l\ V_g^2}{g\ \rho_l - \frac{0.75\ \rho_g\ V_g^2}{D_h}} \ . \qquad (3\text{-}154)$$

The correlations in the model are used in TRAC, as given in the source references for this constitutive model.

The film void fraction also can be limited by the total liquid void fraction available to be deposited on the unheated surface area. If the liquid and the unheated surface areas are distributed homogeneously within a control volume, the amount of liquid might be considered to be

$$\alpha_f = F_u\left(1 - \alpha_g\right) \ .$$

However, with cross flow between subchannels and the ability of liquid to "hang" on an unheated wall, the film void fraction actually may become greater than the above expression. To account for this effect, the film void fraction is given by

$$\alpha_f = F_u\left(1 - \alpha_g\right) W \ , \qquad (3\text{-}155)$$

where W is the cold-wall liquid fraction weighting factor defined by the following:

$$W = \begin{cases} 0 & \alpha \le \min(\alpha_{ag},\ 0.7) \\ 5\left[\dfrac{0.98 - \alpha}{0.98 - \min(\alpha_{ag},\ 0.7)}\right]^{0.35} & \min(\alpha_{ag},\ 0.7) < \alpha < 0.98 \\ 5 & \alpha \ge 0.98 \ , \end{cases}$$

where α_{ag} is the void fraction at the agitated-to-post-agitated IAF regime transition.

The weighting factor was developed specifically for implementation into TRAC.

Ultimately, the liquid-film fraction is based on the minimum of the above two methods, or

$$\alpha_f = \min\left(\frac{P\delta_f F_u}{A_{flow}}\ ,\ F_u(1-\alpha_g)W\right) . \qquad (3\text{-}156)$$

Finally, the interfacial drag coefficient on the liquid film is estimated by

$$c_{i,f} = ffd \cdot \frac{2\,\rho_g\,f_{i,f}}{D_h} \tag{3-157}$$

($ffd = 0.5$), using the modified Wallis friction factor (Ref. 3-20.), where

$$f_{i,f} = 0.005\,(1 + 75\,\alpha_f)\,. \tag{3-158}$$

The coefficient *ffd* was not a part of the original correlation. The numerical value was determined by comparison of TRAC predictions with CCTF Run 14 pressure-drop data.

3.6. Wall Drag

At the fluid/wall interface, closure of the liquid- and gas-field momentum equations requires two additional parameters: the wall drag coefficient for the liquid phase c_{wl} and the wall drag coefficient for the combined-gas c_{wg}. For 1D components, these two drag coefficients are defined such that

$$c_{wl} = \frac{\alpha_l\,\rho_l\,c_{fl}}{D_h} \tag{3-159}$$

and

$$c_{wg} = \frac{\alpha_g\,\rho_g\,c_{fg}}{D_h}\,, \tag{3-160}$$

where c_{fl} and c_{fg} are the coefficients of friction for the liquid and gas phases, respectively. For 3D components, the drag coefficients c_{wlk} and c_{wgk} essentially are identical to their 1D counterparts, except for the addition of the subscript k, which denotes the r, θ, or z coordinate directions.

In addition, the liquid- and gas-phase coefficients of friction are related to the Fanning friction factor such that

$$c_{fl} = c_{fg} = 2\,f\,.$$

The friction factor f in turn is determined by one of three model types: the single-phase model, the two-phase homogeneous model, or the horizontal stratified-flow model. As the name implies, the single-phase wall drag model is employed for single-phase liquid or single-phase vapor conditions. Likewise, the two-phase homogeneous wall drag model is called for each of the regimes included in the basic two-phase flow-regime map: bubbly slug, churn, and annular-mist flows. Under stratified-flow conditions, TRAC uses the horizontal-stratified-flow wall drag model.

A summary table of the key correlations for wall drag is provided in Table 3-5.

3.6.1. Single-Phase Wall Drag Model

For single-phase flow, TRAC uses a model in which the friction factor is obtained from the modified Churchill equation (Ref. 3-25.).

The Churchill equation (Ref. 3-25.) is a fit to the Moody diagram for laminar, transition, and turbulent flow. In the code, the Churchill friction factor is defined as

$$f_{Churchill} = 2\left[\left(\frac{8}{Re}\right)^{12} + \frac{1}{(a+b)^{3/2}}\right]^{1/12}, \tag{3-161}$$

where

$$a = \left[2.475 \ln\left(\frac{1}{\left(\frac{7}{Re}\right)^{0.9} + \frac{0.27\,\varepsilon}{D_h}}\right)\right]^{16} \tag{3-162}$$

and

$$b = \left(\frac{37530}{Re}\right)^{16} \tag{3-163}$$

for $Re \geq 100$.

The Churchill correlation is used in TRAC as given in the source reference for this constitutive model. Use of the Moody curves, and mathematical representations of the curves, for calculation of the single-phase friction factor in a variety of flow-channel geometries is a common engineering practice.

3.6.2. Two-Phase Homogeneous Wall Drag Model

The friction factor for two-phase flow likewise is obtained from the Churchill equation (see Section 3.6.1.). The single-phase Reynolds number is replaced by a two-phase mixture Reynolds number, or

$$Re_m = \frac{G_m D_h}{\mu_m} = \frac{(j_g \rho_g + j_l \rho_l) D_h}{\mu_m}.$$

In the above equation, the mixture viscosity μ_m is defined as a function of the static quality X, where

$$\mu_m = \left[\frac{X}{\mu_g} + \frac{(1-X)}{\mu_l}\right]^{-1} \tag{3-164}$$

for

$$X = \frac{1}{1 + \frac{(1 - \alpha_g)\,\rho_l}{\alpha_g\,\rho_g\,S_r}}\ , \tag{3-165}$$

where the slip between phases is small, or

$$S_r = 1.0\ .$$

As with the single-phase model, the mixture Reynolds number also must be ≥100 to prevent division by zero in the friction-factor equations.

The TRAC friction-factor model takes the coefficient of friction for the liquid phase to be

$$c_{fl} = 2f$$

and the coefficient of friction for the vapor phase to be

$$c_{fg} = c_{fl}\ ,$$

where the friction factor, *f*, is obtained from the Churchill equation using the two-phase Reynolds number given above.

Use of a two-phase Reynolds number in a single-phase friction-factor correlation is one method of determining the two-phase friction factor. The modeling approach needs to be validated by comparison with experimental data.

3.6.3. Two-Phase Horizontal Stratified Wall Drag Model

For fully stratified-flow conditions, the wall drag coefficients for each phase are determined using the friction-factor relation

$$f = 0.046\ Re^{-0.2} \tag{3-166}$$

for $Re \geq 1502$ (turbulent flow) and

$$f = \frac{16}{Re} \tag{3-167}$$

for $Re < 1502$ (laminar flow). In the above equations, the Reynolds number is evaluated for each phase based on

$$Re_k = \max\left(100,\ \frac{\rho_k\,|V_k|\,D_k}{\mu_k}\right), \tag{3-168}$$

where $k = l$ (for liquid) or g (for gas). The hydraulic diameters, D_l and D_g, are based on the flow area and wetted perimeter for the respective phases; they replace the hydraulic diameter based on total flow area and total wetted perimeter, D_h, both in the Reynolds-number and the drag-coefficient definitions.

Application of standard engineering correlations to each phase in a two-phase mixture under separated flow conditions is a common practice for two-fluid models of two-phase flows. The modeling approach needs to be validated by comparison with experimental data.

In the transition region between stratified and nonstratified flow, TRAC interpolates between the stratified and nonstratified wall drag coefficients based on the weighting-factor methodology discussed in Section 3.2.4.

3.7. Interfacial Heat Transfer

As seen in Section 3.1., closure of the mass, momentum, and energy equations requires that we specify the interfacial heat-transfer coefficients h_{il}, h_{ig}, and h_{gl}. These coefficients are needed to define the heat-transfer rates per unit volume for the interface-to-liquid heat transfer, the interface-to-gas heat transfer, and the liquid-to-gas sensible heat transfer, respectively. Because the interfacial heat-transfer parameters are highly dependent on flow regime, the following sections will elaborate on the individual models as coded within TRAC. A summary of the interfacial heat-transfer models also is provided in Table 3-6.

In many cases, the interfacial heat-transfer coefficients are expressed in terms of a heat-transfer factor H. By definition, the heat-transfer factor for a given flow regime is expressed as the product of the interfacial heat-transfer coefficient and the interfacial area corresponding to that flow regime. The following sections will focus on four specific heat-transfer factors:

$$H_{ALV} = (h_{il})_{flashing} \cdot A_i \,, \tag{3-169}$$

$$H_{ALVE} = (h_{il})_{evap/cond} \cdot A_i \,, \tag{3-170}$$

$$H_{CHTI} = h_{ig} \cdot A_i \,, \tag{3-171}$$

and

$$H_{CHTA} = h_{gl} \cdot A_i \,. \tag{3-172}$$

As indicated above, the heat-transfer factors H_{ALV} and H_{ALVE} correspond to interface-to-liquid heat transfer via flashing for $T_l \geq T_{sat}$ and via evaporation or condensation for $T_l < T_{sat}$. Similarly, the heat-transfer factors H_{CHTI} and H_{CHTA} correspond to interface-to-

gas heat transfer and liquid-to-gas sensible heat transfer, respectively. A description of the flow-regime-dependent interfacial-area models can be found in Section 3.3.

3.7.1. Bubbly Slug Interfacial Heat Transfer

In discussing the bubbly slug flow regime, this section collectively will refer to the bubbly, bubbly slug transition, and bubbly slug flow regimes depicted in Fig. 3-2. During condensation or evaporation ($T_l < T_{sat}$), the heat-transfer coefficient h_{il} for bubbly slug flow is evaluated by the Nusselt number correlations of Chen and Mayinger (Ref. 3-26.) and of Whittaker (Ref. 3-27.). The Nusselt number correlations are given by

$$\mathrm{Nu} = \begin{cases} 116.7\sqrt{\mathrm{Pr_l}} & \mathrm{Re} \geq 10^4 \\ 0.185\,\mathrm{Re}^{0.7}\sqrt{\mathrm{Pr_l}} & \mathrm{Re} < 10^4 \quad \text{(Chen and Mayinger)} \\ 2 + \left(0.4\sqrt{\mathrm{Re}} + 0.06\,\mathrm{Re}^{2/3}\right)\mathrm{Pr_l}^{0.4} & \text{low Re} \quad \text{(Whittaker)} \end{cases} \tag{3-173}$$

where

$$\mathrm{Nu} = \frac{h_{il}\,D_b}{k_l}, \tag{3-174}$$

$$\mathrm{Re} = \frac{\rho_l\,D_b\,(V_g - V_l)}{\mu_l}, \tag{3-175}$$

and where D_b is the Sauter mean bubble diameter defined in Section 3.3.1. The Chen and Mayinger correlation is recommended for Reynolds numbers $<10^4$. However, at low Reynolds numbers, this correlation yields a smaller Nusselt number than that of the Whittaker correlation for solid spheres. Under these circumstances, the modified Whittaker correlation (expressed above) is used to calculate the Nusselt number. Additionally, at a high Reynolds number ($Re \geq 10^4$), the Nusselt number is assumed to be independent of the Reynolds number. The above correlation for high Reynolds numbers was derived from the Chen and Mayinger correlation by setting $Re = 10^4$.

The Whittaker correlation is modified from its original form by neglect of a viscosity-ratio correction.

Once the appropriate heat-transfer coefficient has been calculated, the heat-transfer factor H_{ALVE} can be defined such that

$$H_{ALVE,bubbly\text{-}slug} = h_{il} \cdot A_{i,bubbly\text{-}slug} \cdot \tag{3-176}$$

Under subcooled-boiling conditions ($h_\Gamma > 0$, see Section 3.4.), the above liquid-side heat-transfer factor is modified to account for the condensation of vapor in contact with the subcooled bulk liquid. Specifically,

$$H_{ALVE,bubbly,sub} = W_{sub} \cdot H_{ALVE,sub} + (1 - W_{sub}) \cdot H_{ALVE,bubbly} \tag{3-177}$$

for the weighting factor

$$W_{sub} = 10\,(0.2 - \alpha)\,, \tag{3-178}$$

where $0 \le W_{sub} \le 1$. The subcooled-boiling heat-transfer factor is obtained from the model of Lahey and Moody (Ref. 3-28.) such that

$$H_{ALVE,sub} = H_o\, B_{cell}\, h_{fg}\, \frac{\rho_l\, \rho_g}{\rho_l - \rho_g}\, \alpha \tag{3-179}$$

for

$$H_o = 0.075\ (\text{s-K})^{-1}. \tag{3-180}$$

During flashing ($T_l > T_{sat}$), the liquid-side heat-transfer factor is determined by the relation

$$H_{ALV,bubbly\text{-}slug} = (2.0e{+}8)\cdot\,(T_l - T_{sat})\cdot\,B_{cell}\,, \tag{3-181}$$

where

$$1.0e{+}6 \le \frac{H_{ALV,bubbly\text{-}slug}}{B_{cell}} \le 2.0e{+}8\,. \tag{3-182}$$

Finally, the interface-to-gas and the liquid-to-gas heat-transfer coefficients are approximated by

$$h_{ig} = h_{gl} = 1000\ \text{W/m}^2\cdot\,\text{K} \tag{3-183}$$

In terms of heat-transfer factors,

$$H_{CHTI,bubbly\text{-}slug} = H_{CHTA,bubbly\text{-}slug} = 1000\cdot\,A_{i,bubbly\text{-}slug}\,. \tag{3-184}$$

The weighting factors and constant heat-transfer coefficients used in this modeling are heuristic and were developed specifically for implementation into TRAC. These empirical factors are largely untested.

3.7.2. Churn-Flow Interfacial Heat Transfer

In the churn-flow or transition-flow regime, the interfacial heat-transfer factors (H_{ALVE}, H_{ALV}, H_{CHTI}, and H_{CHTA}) are defined as a weighted average of the appropriate bubbly slug and annular-mist heat-transfer factors. The generalized weighting is given by the equation

$$X_{transition} = (1 - W_t)\cdot\,X_{bubbly\text{-}slug} + W_t\cdot\,X_{annular\text{-}mist}\,,$$

where X represents the heat-transfer factors H_{ALVE}, H_{ALV}, H_{CHTI}, and H_{CHTA}. The weighting factor W_t was defined in Section 3.3.2. During flashing conditions, however, the liquid-side heat-transfer factor H_{ALV} is redefined as the maximum of the value obtained from the above weighted average and the value obtained from the expression

$$H_{ALV,transition} = (2.0e+8)\cdot (T_l - T_{sat})\cdot B_{cell} , \tag{3-185}$$

where

$$1.0e+6 \le \frac{H_{ALV,transition}}{B_{cell}} \le 2.0e+8 . \tag{3-186}$$

The constant heat-transfer coefficients given here are heuristic and were developed specifically for implementation into TRAC.

In all cases, the bubbly slug heat-transfer factors are evaluated by the expressions presented in Section 3.7.1., using a void fraction of 0.5. Similarly, the annular-mist heat-transfer factors are evaluated by the model presented in Section 3.7.3., using a void fraction of 0.75.

The interpolation method given here, including the weighting factor, was developed specifically for implementation into TRAC. The interpolation algorithm itself embodies no physics; it is a mathematical operation. However, the interpolation algorithm provides a transition between two regimes, which are represented by physical models.

3.7.3. Annular-Mist Interfacial Heat Transfer

In the annular-mist-flow regime, calculation of the interfacial heat-transfer factors is based on a superposition of the droplet and film fields. This can be generalized by the equation

$$X_{annular\text{-}mist} = (1 - W_f)\cdot (X_{drop} + X_{film}) + W_f\cdot X_{drop,max} , \tag{3-187}$$

where X represents the heat-transfer factors H_{ALVE}, H_{ALV}, H_{CHTI}, and H_{CHTA}. The weighting factor W_f was defined in Section 3.3.3. During flashing, however, the liquid-side heat-transfer factor H_{ALV} is redefined as the maximum of the value obtained from the above weighted average and the value obtained from the expression

$$H_{ALV,annular\text{-}mist} = (2.0e+8)\cdot (T_l - T_{sat})\cdot B_{cell} , \tag{3-188}$$

where

$$1.0e+6 \le \frac{H_{ALV,annular\text{-}mist}}{B_{cell}} \le 2.0e+8 . \tag{3-189}$$

The constant heat-transfer coefficients given here are heuristic and were developed specifically for implementation into TRAC.

Beginning with the droplet field, the liquid-side heat-transfer coefficient is evaluated based on a transient conduction solution (Ref. 3-29.), where

$$Nu = \frac{h_{il,drop} D_d}{k_l} = \frac{\pi}{3} C_c \frac{1 + T^*}{T^*} \tag{3-190}$$

for

$$T^* = \left[1 - \exp\left(-4 \pi^2 C_c \frac{k_l t_d}{2 \rho_l c_{p,l} D_d^2}\right)\right]^{1/2}, \tag{3-191}$$

$$t_d = \frac{D_h}{V_r}, \tag{3-192}$$

and $C_c = 1.0$. In this case, the relative velocity (Ref. 3-30.) is given by

$$V_r = 2.462 \sqrt{g \frac{\rho_l - \rho_g}{\rho_g} \frac{D_d}{2}} \ . \tag{3-193}$$

The Sauter mean droplet diameter D_d is calculated as specified in Section 3.3.3.

After solving for the liquid-side heat-transfer coefficient, the relevant condensation heat-transfer factors can be defined such that

$$H_{ALVE,drop} = h_{il,drop} \cdot A_{i,drop} \tag{3-194}$$

and

$$H_{ALVE,drop,max} = h_{il,drop} \cdot A_{i,drop,max} \ , \tag{3-195}$$

and the relevant flashing heat-transfer factors can be defined such that

$$H_{ALV,drop} = h_{il,drop} \cdot A_{i,drop} \tag{3-196}$$

and

$$H_{ALV,drop,max} = h_{il,drop} \cdot A_{i,drop,max} \ . \tag{3-197}$$

The above interfacial-area terms likewise are calculated as specified in Section 3.3.3.

The vapor-side heat-transfer coefficient for the droplet field is evaluated using the method of Ryskin (Ref. 3-31.), where

$$Nu = \frac{h_{ig,drop}\, D_d}{k_g} = 2 + \sqrt{V^*_{max} \cdot Pe} \tag{3-198}$$

for the Peclet number

$$Pe = \frac{\rho_g\, c_{p,g}\, D_d\, V_r}{k_g} . \tag{3-199}$$

The maximum dimensionless circulation velocity at the surface of the drop is defined such that

$$V^*_{max} = \frac{1.5}{1 + \dfrac{2.8\,(1 + 2\lambda)(2 + 3\kappa)}{(2 + 3\lambda)\sqrt{Re_g}}} , \tag{3-200}$$

where

$$Re_g = \frac{\rho_g\, D_d\, V_r}{\mu_g} ,$$

$$\lambda = \sqrt{\frac{\rho_l\, \mu_l}{\rho_g\, \mu_g}} ,$$

and

$$\kappa = \frac{\mu_l}{\mu_g} .$$

The relative velocity term V_r and the droplet diameter D_d are equivalent to the values used for the liquid-side heat transfer. The vapor-side heat-transfer factors thus can be calculated by

$$H_{CHTI,drop} = h_{ig,drop} \cdot A_{i,drop} \tag{3-201}$$

and

$$H_{CHTI,drop,max} = h_{ig,drop} \cdot A_{i,drop,max} . \tag{3-202}$$

The direct sensible heat transfer between liquid and gas in the droplet field also uses the model of Ryskin (Ref. 3-31.). For this application, however, each of the combined-gas parameters has been replaced by its counterpart for the noncondensables. The gas-to-liquid heat-transfer coefficient therefore is defined as a function of Nusselt number, where

$$Nu = \frac{h_{gl,drop}\, D_d}{k_a} = 2 + \sqrt{V^*_{max} \cdot Pe} \qquad (3\text{-}203)$$

for

$$Pe = \frac{\rho_a\, c_{p,a}\, D_d\, V_r}{k_a}$$

and

$$V_r = 2.462 \sqrt{g \frac{\rho_l - \rho_a}{\rho_a} \frac{D_d}{2}} \,.$$

The circulation velocity term is similarly expressed by

$$V^*_{max} = \frac{1.5}{1 + \dfrac{2.8\,(1 + 2\lambda)(2 + 3\kappa)}{(2 + 3\lambda)\sqrt{Re_a}}}$$

for

$$Re_a = \frac{\rho_a\, D_d\, V_r}{\mu_a} \,,$$

$$\lambda = \sqrt{\frac{\rho_l\, \mu_l}{\rho_a\, \mu_a}} \,,$$

and

$$\kappa = \frac{\mu_l}{\mu_a} \,.$$

Based on the above heat-transfer coefficient, the appropriate heat-transfer factors are defined such that

$$H_{CHTA,drop} = h_{gl,drop} \cdot A_{i,drop}$$

and

$$H_{CHTA,drop,max} = h_{gl,drop} \cdot A_{i,drop,max} .$$

As with the liquid-side and vapor-side models, the above interfacial heat-transfer terms and the droplet diameter D_d are calculated as described in Section 3.3.3.

Alternatively, for the liquid film, all three heat-transfer coefficients (h_{il}, h_{ig}, and h_{gl}) are defined as a function of the Stanton number such that

$$St = \frac{h_{il,film}}{\rho_l c_{p,l} V_l} = \frac{h_{ig,film}}{\rho_g c_{p,g} |V_g - V_l|} = \frac{h_{gl,film}}{\rho_a c_{p,a} |V_g - V_l|} . \quad (3\text{-}204)$$

The above Stanton number criterion is based on the model of Bankoff (Ref. 3-32.), where

$$St = 0.0045 \left(\frac{\rho_g V_g \mu_l}{\rho_l V_l \mu_g} \right)^{1/3} . \quad (3\text{-}205)$$

The film-field heat-transfer factors in turn are defined by

$$H_{ALVE,film} = h_{il,film} \cdot A_{i,film} , \quad (3\text{-}206)$$

$$H_{ALV,film} = h_{il,film} \cdot A_{i,film} , \quad (3\text{-}207)$$

$$H_{CHTI,film} = h_{ig,film} \cdot A_{i,film} , \quad (3\text{-}208)$$

and

$$H_{CHTA,film} = h_{gl,film} \cdot A_{i,film} \quad (3\text{-}209)$$

for the liquid-film interfacial area defined in Section 3.3.3. All correlations used in the annular-mist interfacial heat-transfer modeling are used in TRAC, as reported in the source references for this constitutive model.

3.7.4. Stratified-Flow Interfacial Heat Transfer

Under fully stratified-flow conditions, the liquid-side heat-transfer coefficient is evaluated using the constant Stanton number criterion suggested by Linehan (Ref. 3-33.), where

$$St = \frac{h_{il,strat}}{\rho_l c_{p,l} V_l} = 0.0073 . \quad (3\text{-}210)$$

The liquid-side heat-transfer factors thus are defined by

$$H_{ALVE,strat} = h_{il,strat} \cdot A_{i,strat}$$

and

$$H_{ALV,strat} = h_{il,strat} \cdot A_{i,strat} ,$$

where the stratified-flow interfacial area is calculated as discussed in Section 3.3.4.

The Linehan criterion is used in TRAC, as given in the source reference for this constitutive model.

However, when the flow is not fully stratified, the code interpolates between the heat-transfer factors for stratified flow, as calculated above, and the values otherwise determined with respect to the basic flow-regime map. In general form, this can be expressed as

$$X_{map,strat} = (1 - W_{st}) \cdot X_{map} + W_{st} \cdot X_{strat} ,$$

where X represents the heat-transfer factors H_{ALVE} and H_{ALV} and where $0 \le W_{st} \le 1$. The weighting factor W_{st} is calculated as a function both of void fraction (flow regime) and critical velocity. In general, for 3D components, the weighting factor is nonzero for velocities less that 10 times the critical velocity (see Section 3.2.4.). For additional detail, the reader is referred to Appendix E (Section E.2.7.).

As noted for bubbly slug, annular-mist, and transition flows, the liquid-side heat-transfer factor for flashing under stratified-flow conditions ($H_{ALV,map,strat}$) likewise is redefined as the maximum of the value obtained from the above weighted average and the value obtained from the expression

$$H_{ALV,map,strat} = (2.0e+8) \cdot (T_l - T_{sat}) \cdot B_{cell} , \qquad (3\text{-}211)$$

where

$$1.0e+6 \le \frac{H_{ALV,map,strat}}{B_{cell}} \le 2.0e+8 . \qquad (3\text{-}212)$$

The constant heat-transfer coefficients given here are heuristic and were developed specifically for implementation into TRAC.

Finally, no modifications are made to the vapor-side and sensible heat-transfer factors for stratified flow. Thus,

$$H_{CHTI,map,strat} = H_{CHTI,map}$$

and

$$H_{CHTA,map,strat} = H_{CHTA,map} .$$

The interpolation method given here, including the weighting factor, was developed specifically for implementation into TRAC. The interpolation algorithm itself embodies no physics; it is a mathematical operation. However, the interpolation algorithm provides a transition between two regimes, which are represented by physical models. The constant heat-transfer coefficients were developed specifically for implementation into TRAC.

3.7.5. Plug-Flow Interfacial Heat Transfer

Under plug-flow conditions, the liquid-side heat-transfer coefficient is calculated from the constant Stanton number relation

$$St = \frac{h_{il,plug}}{\rho_l c_{p,l} V_l} = 0.02 . \qquad (3\text{-}213)$$

Thus, the heat-transfer factor $H_{ALVE,plug}$ can be defined such that

$$H_{ALVE,plug} = h_{il,plug} \cdot A_{i,plug} ,$$

where the interfacial-area term is calculated as specified in Section 3.3.5.

The above heat-transfer factor then is superimposed on the corresponding factor calculated from the bubbly slug, annular-mist, churn, and stratified-flow models, as appropriate. This can be expressed by

$$H_{ALVE,map,strat,plug} = (1 - W_{plug}) H_{ALVE,map,strat} + W_{plug} H_{ALVE,plug}$$

for the weighting factor W_{plug} defined in Section 3.3.5.

Because plug flow can occur only when the liquid side is condensing, a definition of the liquid-side heat-transfer factor for flashing (H_{ALV}) is unnecessary. Moreover, there are no modifications made to the vapor-side and sensible heat-transfer factors for plug flow. In other words,

$$H_{CHTI,map,strat,plug} = H_{CHTI,map,strat}$$

and

$$H_{CHTA,map,strat,plug} = H_{CHTA,map,strat} .$$

The constant-Stanton-number model is used in TRAC, as given in the source references for this constitutive model. The overall modeling of the plug-flow interfacial heat transfer given here is heuristic and was developed specifically for implementation into TRAC. The interpolation method presented, including the weighting factor, was developed specifically for implementation into TRAC. The interpolation algorithm itself embodies no physics; it is a mathematical operation. However, the interpolation algorithm provides a transition between two regimes, which are represented by physical models.

3.7.6. Reflood Interfacial Heat Transfer

During reflood of the core region, TRAC utilizes the flow-regime map of Ishii and his coworkers (Refs. 3-3. to 3-5.) (see Section 3.2.6.). Consistent with the interfacial areas defined in Section 3.3.6., the code calculates the overall reflood heat-transfer factors for a given hydraulic cell based on the weighted average of the individual heat-transfer factors for bubbly, inverted annular, and dispersed flow. This can be generalized by the equation

$$X_{reflood} = W_{sb} \cdot X_{bubbly} + W_{inv} \cdot X_{inv} + W_{ds} \cdot X_{ds} , \quad (3\text{-}214)$$

where X represents each of the heat-transfer factors H_{ALVE}, H_{CHTI}, and H_{CHTA}. In the above equation, the linear weighting factors W_{sb}, W_{inv}, and W_{ds} are based on the relative axial distance within each cell for which the appropriate flow regime is present. The calculation of these weighting factors is presented in Appendix F (Section F.1.6., Table F-4.).

The interpolation method given here, including the weighting factor, was developed specifically for implementation into TRAC. The interpolation algorithm itself embodies no physics; it is a mathematical operation. However, the interpolation algorithm provides a transition between two regimes, which are represented by physical models.

For flashing conditions, the liquid-side heat-transfer factor H_{ALV} is defined as the maximum of H_{ALVE} (calculated by the above relation) and the value obtained from the expression

$$H_{ALV,reflood} = (2.0e+8) \cdot (T_l - T_{sat}) \cdot B_{cell} , \quad (3\text{-}215)$$

where

$$1.0e+6 \leq \frac{H_{ALV,reflood}}{B_{cell}} \leq 2.0e+8 . \quad (3\text{-}216)$$

The constant heat-transfer coefficients given here are heuristic and were developed specifically for implementation into TRAC.

The following paragraphs summarize the calculation methodology for the bubbly, inverted-annular-, and dispersed-flow interfacial heat-transfer factors. Additional details of the reflood interfacial heat-transfer models likewise can be found in Appendix F.

3.7.6.1. Bubbly Flow. The interfacial heat-transfer coefficients (h_{il}, h_{ig}, and h_{gl}) and heat-transfer factors (H_{ALVE}, H_{CHTI}, and H_{CHTA}) for bubbly flow under reflood conditions, except for the flashing model, are identical to those defined in Section 3.7.1. The corresponding interfacial area is determined by the expressions presented in Section 3.3.1. When $T_l > T_{sat}$ (i.e., the liquid is superheated), a simple flashing model is used to determine the liquid-side heat-transfer factor. This simple model uses the kinetic theory of evaporation from liquid surfaces (Ref. 3-34., p. 56). The liquid-side heat-transfer coefficient associated with flashing is

$$h_{fls} = C_{eva}\left[0.01857\frac{\rho_v h_{fg}^2}{T_{sat}^{1.5}}\right], \tag{3-217}$$

where the coefficient of evaporation, C_{eva}, is defined for bubbly and annular-mist-flow regimes in the nucleate-boiling region, and h_{fg} is the latent heat of vaporization. The coefficient of evaporation is considered to be void-fraction-dependent in the bubbly flow regime when the cell void fraction is between 0.3 and 0.5. Currently, C_{eva} is given the value 0.0002 for all void fractions up to 0.5 in the bubbly flow.

The numerical value in the model, 0.01857, has been changed from the original value, 0.04, given by Hsu and Graham (Ref. 3-34., p. 56). In addition, the factor C_{eva} was not a part of the original correlation.

3.7.6.2. Inverted Annular Flow. The liquid-side heat-transfer factor is calculated as follows:

If $T_l < T_{sat}$, the heat-transfer coefficient is calculated using the standard subcooled heat-transfer correlations for the given flow regime.

If $T_l > T_{sat}$, i.e., the liquid is superheated, then

$$H_{ALV,inv} = h_{fls} A_{i,inv}, \tag{3-218}$$

where

$$h_{fls} = C_{eva}\left[0.01857\frac{\rho_v h_{fg}^2}{T_{sat}^{1.5}}\right], \tag{3-219}$$

and the coefficient of evaporation for the flashing model, C_{eva}, is set to 0.002.

The numerical value in the model, 0.01857, has been changed from the original value, 0.04, given by Hsu and Graham (Ref. 3-34., p. 56). In addition, the factor C_{eva} was not a part of the original correlation.

Additionally, the vapor-side heat-transfer factor and the liquid-to-gas sensible heat-transfer factor are defined by the simple relations

$$H_{CHTI,inv} = h_{ig,inv} \cdot A_{i,inv} \tag{3-220}$$

and

$$H_{CHTA,inv} = h_{gl,inv} \cdot A_{i,inv}\,, \tag{3-221}$$

where

$$h_{ig,inv} = 3 \times 10^3 \text{ W/m}^2\text{-K}$$

and

$$h_{gl,inv} = 10^3 \text{ W/m}^2\text{-K}\,.$$

The interfacial area for inverted annular flow is calculated as described in Section 3.3.6.

3.7.6.3. Dispersed Flow. The following are used to calculate the liquid-side heat-transfer factor:

If $T_l < T_{sat}$, the heat-transfer coefficient is calculated using the standard subcooled heat-transfer correlations for the given flow regime.

If $T_l > T_{sat}$, the liquid is superheated and

$$H_{ALV,ds} = h_{fls} A_{i,ds}\,, \tag{3-222}$$

where

$$h_{fls} = C_{eva}\left[0.01857\frac{\rho_v h_{fg}^2}{T_{sat}^{1.5}}\right] \tag{3-223}$$

and the coefficient of evaporation for the flashing model, C_{eva}, is set to 0.002.

The numerical value in the model, 0.01857, has been changed from the original value, 0.04, given by Hsu and Graham (Ref. 3-34., p. 56). In addition, the factor C_{eva} was not a part of the original correlation.

The vapor-side heat-transfer factor is defined by

$$H_{CHTI,ds} = 10^{-6}\ W/K \tag{3-224}$$

for $\alpha_{hom} \geq 1$ and $(1 - \alpha_{dd}) \leq 0.95$. If the cell $\alpha < 0.98$ (post-agitated dispersed-flow regime),

$$H_{CHTI,pa} = H'_{CHTI}\left[\frac{\alpha - \alpha_{SM}}{\alpha_{DP} - \alpha_{SM}}\right]^{0.01}, \tag{3-225}$$

where α_{SM} and α_{DP} are the void fractions at the flow-regime transitions between smooth/rough-wavy IAF and dispersed (post-agitated)/highly dispersed flows, respectively.

If the cell $\alpha \geq 0.98$ (highly dispersed flow regime),

$$H_{CHTI,df} = H'_{CHTI}.$$

In the above equation, the factor H'_{CHTI} is calculated from a modified form of Unal's model for vapor generation (Ref. 3-34.), where

$$H'_{CHTI} = (0.05)\cdot 0.315\exp\left(-C_{u1}\frac{P}{P_{cr}}\right)\left[V_g\rho_g\frac{1-\alpha_{dd}}{\alpha_{hom}}\right]^{C_{u2}}$$

$$\cdot\frac{k_g Pr_g^{0.33}}{\mu_g^{0.55}(2L_o^2)^{0.725}}B_{cell}\left[\frac{\sqrt{\rho_g\sigma L_o}}{\mu_g}\right]^{0.4833}. \tag{3-226}$$

The constants C_{u1} and C_{u2} are equivalent to 30 and 0.33, respectively. The numerical factor, 0.05, was not a part of the original correlation.

The homogeneous void fraction α_{hom} is given by

$$\alpha_{hom} = \frac{x_l\,\rho_l}{x_l\,\rho_l + (1 - x_l)\,\rho_g} \tag{3-227}$$

for the mass fraction

$$x_l = \frac{\rho_g\,V_g\,(1 - \alpha_{dd})}{\rho_g\,V_g\,(1 - \alpha_{dd}) + \rho_l\,V_l\,\alpha_{dd}}. \tag{3-228}$$

The droplet fraction α_{dd} is calculated as presented in Section 3.3.6.

Finally, in the presence of noncondensables, the liquid-to-gas sensible heat-transfer factor is calculated from the linear weighting

$$H_{CHTA,ds} = W_{fd}\cdot\left(A_{i,drop}\cdot h_{gl,drop} + A_{i,film}\cdot h_{gl,film}\right) + (1 - W_{fd})\cdot A_{i,drop,max}\cdot h_{gl,drop}. \tag{3-229}$$

The weighting factor W_{fd} and the interfacial-area terms are defined in Section 3.3.6.3.

The interpolation method and weighting factor are heuristic and are developed specifically for TRAC.

The heat-transfer coefficient for the droplet field $h_{gl,drop}$ is based on the model of Ryskin (Ref. 3-31.) for annular-mist flow. Similarly, the heat-transfer coefficient for the film field $h_{gl,film}$ is calculated from Bankoff's model for annular-mist flow. Both heat-transfer coefficient models are discussed in Section 3.7.3. Both correlations are used in TRAC, as given in the source references for this constitutive model.

3.7.7. Effect of Noncondensables

In the presence of noncondensables, TRAC modifies the liquid-side heat-transfer factor H_{ALVE} during condensation and evaporation. Under evaporation conditions ($T_{sv} < T_l < T_{sat}$), H_{ALVE} is calculated by a diffusion model in which

$$H_{ALVE,nc} = h_M h_{fg} (\rho_s - \rho_g + \rho_a) A_i . \tag{3-230}$$

Here, the steam density ρ_s at the interface is estimated using the ideal gas approximation

$$\rho_s = \frac{(P_{sat})_{T_{sat}=T_l}}{R_s T_l} . \tag{3-231}$$

The mass-transfer coefficient h_M is determined, independent of flow regime, as a function of the Sherwood number

$$Sh = \frac{h_M D_h}{D_o} , \tag{3-232}$$

where

$$Sh = \begin{cases} 3.656 & Re \le 2300 \quad (3\text{-}233) \\ 0.023\, Re^{0.8}\, Sc^{1/3} & Re > 2300 \quad (3\text{-}234) \end{cases}$$

for the Schmidt number

$$Sc = \frac{\mu_g}{\rho_g D_o} \tag{3-235}$$

and the Reynolds number

$$Re = \frac{G_g D_h}{\mu_g} . \tag{3-236}$$

The mass-transfer modeling for evaporation is based on the heat- and mass-transfer analogy. The analogy has been shown to be correct for the conditions for which the heat-transfer-coefficient correlation is correct.

The diffusion coefficient D_o is evaluated from

$$D_o = \frac{10^{-3}}{P}\left(-699.2438 + 4.9249\ T_g + 0.0171\ T_g^2\right). \tag{3-237}$$

The diffusion coefficient is a curve fit to the theoretical equation for diffusion of steam in air.

During condensation ($T_l < T_{sv}$), H_{ALVE} is modified according to the empirical correlation of Sklover and Rodivilin (Ref. 3-35.), where

$$0.1 \le \frac{H_{ALVE,nc}}{H_{ALVE}} = \frac{h_{il,nc}}{h_{il}} = 0.366\left(\frac{\rho_g - \rho_a}{\rho_a}\right)^{0.2}\left(\frac{G_v}{G_l}\right)^{0.2} \le 1.0\ . \tag{3-238}$$

For the special case of fully stratified flow, the above equation is modified slightly such that

$$0.1 \le \frac{H_{ALVE,nc}}{H_{ALVE}} = \frac{h_{il,nc}}{h_{il}} = 0.366\left(\frac{\rho_g - \rho_a}{\rho_a}\right)^{0.2}\left(\frac{G_v}{G_l}\right)^{0.2} \le 0.9\ .$$

However, in either equation, the liquid and vapor mass fluxes are limited by

$$3000 \le G_l \le 18{,}000\ \text{kg/m}^2\text{-s} \tag{3-239}$$

and

$$0 \le G_v \le 640\ \text{kg/m}^2\text{-s}\ . \tag{3-240}$$

Recall from Section 3.1. that the interface-to-gas heat transfer per unit volume is adjusted by the ratio of the vapor partial pressure to the total pressure, or

$$q_{ig} = \frac{P_v}{P} H_{CHTI} \frac{(T_g - T_{sv})}{B_{cell}}\ . \tag{3-241}$$

Likewise, the liquid-to-gas sensible heat transfer per unit volume is adjusted by the ratio of the noncondensable partial pressure to the total pressure such that

$$q_{gl} = \frac{P_a}{P} H_{CHTA} \frac{(T_g - T_l)}{B_{cell}}\ . \tag{3-242}$$

Thus, modifications to either heat-transfer factor (H_{CHTI} or H_{CHTA}) to account for the presence of noncondensables are not performed.

3.8. Wall Heat Transfer

Final closure of the fluid energy equations requires that the wall-to-liquid and wall-to-gas heat-transfer rates per unit volume be specified such that

$$q_{wl} = h_{wl} A_w \frac{(T_w - T_l)}{B_{cell}} \tag{3-243}$$

and

$$q_{wg} = h_{wg} A_w \frac{(T_w - T_g)}{B_{cell}} . \tag{3-244}$$

This likewise requires the calculation of the wall-to-liquid and wall-to-gas heat-transfer coefficients h_{wl} and h_{wg}. These heat-transfer coefficients already are assumed to include the fraction of the wall contacted by each respective phase, or

$$h_{wl} = f_l \cdot h'_{wl} \tag{3-245}$$

and

$$h_{wg} = (1 - f_l) \cdot h'_{wg} , \tag{3-246}$$

where f_l is the liquid fraction contacting the wall and h'_{wl} and h'_{wg} are the separate phasic heat-transfer coefficients.

The heat-transfer coefficients h_{wl} and h_{wg} clearly are functions of the heat-transfer regime that is present. TRAC considers eight individual heat-transfer regimes:

1. forced convection to a single-phase liquid (regime 1),
2. nucleate boiling (regime 2),
3. transition boiling (regime 3),
4. film boiling (regime 4),
5. convection to a single-phase vapor (regime 6),
6. convection to a two-phase mixture (regime 7),
7. condensation (regime 11), and
8. natural convection to a single-phase liquid (regime 12).

In addition to these eight regimes, the code includes models for the critical heat flux, which establishes the boundary between nucleate and transition boiling, and the minimum stable film-boiling temperature, which provides the boundary between transition boiling and film boiling. Under core reflood conditions, the code also provides revised models for transition boiling and film boiling that correspond to the flow-regime map of Ishii and his coworkers (Refs. 3-3. to 3-5.) (see Section 3.2.6.). In the following sections, the individual models for h_{wl} and h_{wg} will be discussed for each of the heat-transfer regimes. A summary of these correlations also is provided in Table 3-7.

3.8.1. Natural Convection to Liquid

In the heat-transfer regime for natural convection to a single-phase liquid, the wall-to-liquid heat-transfer coefficient is determined by one of two correlations. These include the correlation for laminar flow (Ref. 3-36.),

$$h_{wl} = 0.59 \frac{k_l}{D_h} (Gr \cdot Pr)^{0.25} , 10^4 < (Gr \cdot Pr) < 10^9 , \tag{3-247}$$

or the correlation for turbulent flow (Ref. 3-36.),

$$h_{wl} = 0.10 \frac{k_l}{D_h} (Gr \cdot Pr)^{0.3333} , \qquad 10^9 < (Gr \cdot Pr) < 10^{13} .$$

In the above equation, the Grashof number and Prandtl number are defined as

$$Gr = \frac{g \beta |T_w - T_l| \rho_f^2 D_h^3}{\mu_l^2} \tag{3-248}$$

and

$$Pr = \frac{\mu_l c_{p,l}}{k_l} . \tag{3-249}$$

Additionally, the parameters β and ρ_f are approximated as

$$\beta = -\frac{\partial \rho_l}{\partial T} \frac{1}{\rho_f} \tag{3-250}$$

and

$$\rho_f = \rho_l + \frac{\partial \rho_l}{\partial T} (T_f - T_l) \tag{3-251}$$

for

$$T_f = 0.5 (T_w + T_l) . \tag{3-252}$$

Under single-phase liquid conditions, the wall-to-gas heat-transfer coefficient is defined to be zero, or

$$h_{wg} = 0.$$

In the correlation for the laminar-flow natural-convection heat-transfer coefficient, the equivalent diameter is used in place of the distance over which the local value of the heat-transfer coefficient has been averaged. The same substitution has been performed in the turbulent correlation; however, the characteristic dimension cancels out of this correlation. Both of these correlations are used widely in engineering analyses of single-phase heat transfer under natural-convection conditions.

3.8.2. Forced Convection to Liquid

During single-phase forced convection to a liquid, TRAC calculates the wall-to-liquid heat-transfer coefficient via the Dittus-Boelter relation (Ref. 3-37.):

$$h_{wl} = h_{forc} = 0.023 \frac{k_l}{D_h} Re_l^{0.8} Pr_l^{0.4} , \tag{3-253}$$

where

$$Re_l = \frac{|V_l| \rho_l (1 - \alpha) D_h}{\mu_l} \tag{3-254}$$

and

$$Pr_l = \frac{\mu_l c_{p,l}}{k_l} . \tag{3-255}$$

For a single-phase liquid, the wall-to-gas heat-transfer coefficient is zero, or

$$h_{wg} = 0.$$

The Dittus-Boelter correlation is used widely in engineering analyses of single-phase forced-convection heat-transfer applications. The basic form of the correlation is based firmly on theoretical considerations, and it has been found to be applicable to a variety of fluids and flow-channel geometries. The correlation is used in TRAC as it is given in the literature.

3.8.3. Nucleate Boiling

In the nucleate-boiling heat-transfer regime, the total wall heat flux is given by Chen (Ref. 3-38.) as the summation of nucleate-boiling and convective mechanisms, where

$$q_{total} = h_{forc} (T_w - T_l) + h_{nucb} (T_w - T_{sat}) . \tag{3-256}$$

The wall-to-liquid heat flux then is calculated from the above total by subtracting the wall-to-gas heat flux. In terms of the wall-to-liquid heat-transfer coefficient, this can be expressed as

$$h_{wl} = \frac{[h_{forc}(T_w - T_l) + h_{nucb}(T_w - T_{sat}) - h_{wg}(T_w - T_g)]}{(T_w - T_l)} .$$

Chen (Ref. 3-38.) calculates the heat-transfer coefficient for the convective component h_{forc} from a modified form of the Dittus-Boelter correlation (Ref. 3-37.) such that

$$h_{forc} = 0.023 \frac{k_l}{D_h} \left(\frac{|V_l| \rho_l (1 - \alpha) D_h}{\mu_l} \right)^{0.8} \left(\frac{\mu_l c_{p,l}}{k_l} \right)^{0.4} \cdot F . \quad (3\text{-}257)$$

The adjustment factor F in turn is based on the Martinelli factor X_{TT}, where

$$F = \begin{cases} 1.0 & (X_{TT})^{-1} \le 0.10 \quad (3\text{-}258) \\ 2.35 \left(X_{TT}^{-1} + 0.213 \right)^{0.736} & (X_{TT})^{-1} > 0.10 \quad (3\text{-}259) \end{cases}$$

for

$$X_{TT}^{-1} = \left(\frac{x}{1 - x} \right)^{0.9} \left(\frac{\rho_l}{\rho_g} \right)^{0.5} \left(\frac{\mu_g}{\mu_l} \right)^{0.1} , \quad (3\text{-}260)$$

subject to the constraint that $(X_{TT})^{-1} \le 100$.

The nucleate-boiling term is based on the work of Forster and Zuber (Ref. 3-39.) for pool boiling. The heat-transfer coefficient h_{nucb} thus is defined by

$$h_{nucb} = 0.00122 \frac{k_l^{0.79} c_{p,l}^{0.45} \rho_l^{0.49}}{\sigma^{0.5} \mu_l^{0.29} h_{fg}^{0.24} \rho_g^{0.24}} (T_w - T_{sat})^{0.24} (P_w - P)^{0.75} \cdot S , \quad (3\text{-}261)$$

where P_w is the saturation pressure corresponding to the wall temperature and S is a suppression factor to account for the fact that the liquid superheat is not constant across the boundary layer. The suppression factor is evaluated from

$$S = \begin{cases} (1 + 0.12 \, Re_{TP}^{1.14})^{-1} & Re_{TP} < 32.5 \quad (3\text{-}262) \\ (1 + 0.42 \, Re_{TP}^{0.78})^{-1} & 32.5 \le Re_{TP} \le 70.0 \quad (3\text{-}263) \end{cases}$$

for

$$Re_{TP} = 10^{-4} \frac{|V_l| \rho_l (1 - \alpha) D_h}{\mu_l} \cdot F^{1.25} , \tag{3-264}$$

with the limitation that $Re_{TP} \leq 70$. At void fractions >0.7, this suppression factor is modified to produce the correct limit of 0.0 as the void fraction approaches 1.0. Further information on the interpolation scheme is available in Appendix F (Section F.2.1.2.4.).

The Chen correlation (Ref. 3-38.) has evolved over time since it was introduced. The version used in TRAC is the latest form given in the literature. The correlation is used in TRAC as it has appeared in the literature. The extensive comparisons of predictions of the correlation with experimental data are summarized in Appendix F.

Additionally, the wall-to-gas heat-transfer coefficient h_{wg} is defined as the maximum of the values obtained from the natural-convection and Dougall-Rohsenow (forced-convection) correlations, or

$$h_{wg} = \max(h_{NC}, h_{dr}) .$$

The vapor natural-convection correlation (Ref. 3-40.) was obtained from vertical planes and cylinders in the turbulent flow regime ($10^9 < Gr \cdot Pr < 10^{13}$) and is given by

$$h_{NC} = 0.13 \, k_g \left[\frac{\rho_g^2 \, g \, |T_w - T_g|}{\mu_g^2 \, T_g} \right]^{0.3333} \cdot Pr_g^{0.3333} . \tag{3-265}$$

The Dougall-Rohsenow correlation for forced convection (Ref. 3-28.) is defined by

$$h_{dr} = 0.023 \frac{k_g}{D_h} Re_{TP}^{0.8} \, Pr_g^{0.4} . \tag{3-266}$$

In the above equation, the two-phase Reynolds number is defined by

$$Re_{TP} = \frac{[|V_g| \alpha + |V_l| (1 - \alpha)]}{\mu_g} \rho_g \, D_h . \tag{3-267}$$

Likewise, in both expressions, the Prandtl number is given by

$$Pr_g = \frac{\mu_g \, c_{p,g}}{k_g} . \tag{3-268}$$

These correlations are used in TRAC in the same form as that given in the references. The characteristic dimension has been canceled out of the natural-convection correlation.

Final adjustments are performed on both the wall-to-liquid and the wall-to-gas heat-transfer coefficients to provide smooth transitions between heat-transfer regimes. Additional details of these adjustments are presented in Appendix F (Section F.2.1.2.4.).

3.8.4. Critical Heat Flux

The critical heat-flux model provides the transition point or boundary between the nucleate- and transition-boiling heat-transfer regimes. The code uses the empirical correlation of Biasi Ref. 3-41.). The Biasi correlation is coded as

$$q_{CHF} = \max(q_{CHF1}, q_{CHF2}) \tag{3-269}$$

for

$$q_{CHF1} = \frac{1.883e+07}{D_h^n |G|^{1/6}} \left[\frac{f_p}{|G|^{1/6}} - x_e \right] \tag{3-270}$$

and

$$q_{CHF2} = \frac{3.78e+07}{D_h^n |G|^{0.6}} h_p [1 - x_e] . \tag{3-271}$$

In the above equation, the parameters n, f_p, and h_p are defined as follows:

$$n = \begin{cases} 0.6 & D_h < 1 \text{ cm} \end{cases} \tag{3-272}$$

$$\begin{cases} 0.4 & D_h \geq 1 \text{ cm}, \end{cases} \tag{3-273}$$

$$f_p = 0.7249 + 0.099 P \exp(-0.032 P) , \tag{3-274}$$

and

$$h_p = -1.159 + \frac{8.99 P}{10 + P^2} + 0.149 P \exp(-0.019 P) . \tag{3-275}$$

Although q_{CHF} is expressed in W/m^2, the above mass flux G is expressed in g/cm^2-s, the pressure P in bars, and the hydraulic diameter D_h in centimeters. The parameter x_e represents the equilibrium quality.

However, at low mass fluxes and at high void fractions, the code modifies the critical-heat-flux calculation. Below a mass flux of 200 kg/m^2-s, the Biasi correlation is evaluated with a constant mass flux, where $|G| = 200$ kg/m^2-s. Similarly, at void fractions >0.98, the critical heat flux is assumed to be very small. TRAC uses the value $q_{CHF} = 1.0$ W/m^2. Between void fractions of 0.97 and 0.98, TRAC linearly interpolates q_{CHF} from the value calculated by Biasi and 1.0.

The Biasi correlation is used in TRAC as given in the source references.

3.8.5. Transition Boiling

Under normal conditions, the total wall heat flux for transition boiling is defined as the sum of nucleate-boiling and film-boiling heat-transfer terms, weighted by the fraction of wall area that is wet (Ref. 3-42.). The total heat flux also is defined as the sum of the wall-to-liquid and wall-to-gas phasic heat-flux terms. The total heat flux thus can be expressed by

$$q_{trans} = \xi \cdot q_{CHF} + (1 - \xi) \cdot q_{min} = h_{wl} \cdot (T_w - T_l) + h_{wg} \cdot (T_w - T_g) \quad (3\text{-}276)$$

for the wet-wall area fraction

$$\xi = \left(\frac{T_w - T_{min}}{T_{CHF} - T_{min}} \right)^2 . \quad (3\text{-}277)$$

In the first definition of the total heat flux, the critical heat flux q_{CHF} is calculated as presented in Section 3.8.4. The heat flux (q_{min}) at the minimum stable film-boiling temperature (T_{min}) is given as

$$q_{min} = h_{wlmin} \cdot (T_{min} - T_l) + h_{wgmin} \cdot (T_{min} - T_g) + h_{fBB} \cdot (T_{min} - T_{sat}) . \quad (3\text{-}278)$$

For this expression, the heat-transfer coefficient h_{wgmin} is evaluated as the maximum of the natural-convection or the Dougall-Rohsenow correlations, or

$$h_{wgmin} = \max(h_{NC}, h_{dr}) . \quad (3\text{-}279)$$

Both the natural-convection and the Dougall-Rohsenow correlations were presented in Section 3.8.3. For purposes of computing h_{wgmin}, however, the appropriate properties in either correlation are evaluated at the minimum stable film-boiling temperature T_{min}. Similarly, the liquid heat-transfer coefficient h_{wlmin} is calculated by

$$h_{wlmin} = h_r \cdot \left(\frac{T_{min} - T_{sat}}{T_{min} - T_l} \right) \quad (3\text{-}280)$$

for the radiation heat-transfer coefficient

$$h_r = (0.9999 - \alpha)\, \sigma_r\, \varepsilon \left(\frac{T_{min}^4 - T_{sat}^4}{T_{min} - T_{sat}} \right) . \quad (3\text{-}281)$$

And finally, the heat-transfer coefficient h_{fBB} is based on the modified Bromley correlation for film boiling (Ref. 3-43.) such that

$$h_{fBB} = 0.62 \cdot \left(\frac{\rho_g\, k_g^3\, (\rho_l - \rho_g)\, g\, h_{fg}'}{\mu_g\, (T_w - T_{sat})\, \lambda} \right)^{0.25} \quad (3\text{-}282)$$

for the Taylor wavelength

$$\lambda = 2\pi \cdot \left(\frac{\sigma}{g(\rho_l - \rho_g)}\right)^{1/2} \tag{3-283}$$

and the modified latent heat

$$h'_{fg} = h_{fg} + 0.5\, c_{p,g}(T_g - T_{sat}) . \tag{3-284}$$

Now, the wall-to-gas phasic heat-transfer coefficient also is evaluated as the maximum of the natural-convection and the Dougall-Rohsenow correlations such that

$$h_{wg} = \max(h_{NC}, h_{dr}) . \tag{3-285}$$

Both of the correlations in question were defined in Section 3.8.3. and will not be repeated here. Based on the value of h_{wg} and the above calculation of the total heat flux for transition boiling, the wall-to-liquid phasic heat-transfer coefficient can be determined from

$$h_{wl} = \frac{q_{trans} - h_{wg}(T_w - T_g)}{(T_w - T_l)} . \tag{3-286}$$

In those situations where the cell void fraction is >0.98, a final interpolation is performed on the total heat flux q_{trans} to provide a smooth transition between heat-transfer regimes. Details of the interpolation scheme can be found in Appendix F (Section F.2.1.3.4.).

The transition-boiling heat-transfer model given here is heuristic and was developed specifically for implementation into TRAC.

3.8.5.1. Core Reflood. Under core reflood conditions, the heat-transfer-coefficient models for the transition-boiling regime take a slightly different form. Specifically, the total transition-boiling heat flux is assumed to decrease exponentially as a function of axial distance from the critical to the film-boiling heat flux. This can be expressed as

$$q_{TR} = q_{CHF} \cdot \exp(-B(Z - Z_{CHF})) \tag{3-287}$$

such that

$$q_{TR} = q_{CHF} \quad \text{at} \quad Z = Z_{CHF} , \tag{3-288}$$

and

$$q_{TR} = q_{film} \quad \text{at} \quad Z = Z_{TR} . \tag{3-289}$$

The length of the transition-boiling region thus can be specified by

$$Z_{TR} - Z_{CHF} = \frac{-\ln\left(\frac{q_{film}}{q_{CHF}}\right)}{B} . \quad (3\text{-}290)$$

In the above equation, the critical heat flux q_{CHF} is calculated as defined in Section 3.8.4. However, the ratio of the film-boiling to the critical heat flux is assumed to be constant such that

$$\frac{q_{film}}{q_{CHF}} = 1.2e\text{-}10 . \quad (3\text{-}291)$$

The parameter B is a function of both void fraction and flow direction. The value of this parameter for different flow conditions is discussed in Appendix F (Section F.2.2.3.3.).

The wall-to-gas heat-transfer coefficient likewise is redefined for core reflood conditions. It is evaluated using the Webb-Chen correlation (Ref. 3-44.), where

$$h_{wg} = h_{mod\text{-}CSO}(1 + F_s)\left[1 + 0.8\left(\frac{L}{D}\right)^{-1}\right] . \quad (3\text{-}292)$$

In this equation, $h_{mod\text{-}CSO}$ is the heat-transfer coefficient based on the momentum-transfer analogy of Chen, Sundaram, and Ozkaynak (Ref. 3-45.). The parameter F_s is a sink function to account for the effect of entrained droplets. The L/D term is included to account for entrance effects. Definitions of $h_{mod\text{-}CSO}$ and F_s are provided in Appendix F (Section F.2.2.4.1.).

The Webb-Chen (Ref. 3-44.) and Chen, Sundaram, and Ozkaynak (Ref. 3-45.) correlations are used in TRAC, as given in the source references for this constitutive model.

The wall-to-liquid heat-transfer coefficient then is calculated from the total heat flux and h_{wg}, as given by

$$h_{wl} = \frac{q_{TR} - h_{wg}(T_w - T_g)}{(T_w - T_l)} . \quad (3\text{-}293)$$

When the cell void fraction is >0.995, a final interpolation is performed on q_{TR} and h_{wg} to provide a smooth transition between heat-transfer regimes. Details of the interpolation scheme can be found in Appendix F (Section F.2.2.3.4.).

3.8.6. Minimum Stable Film-Boiling Temperature

The minimum stable film-boiling temperature provides the transition point between the transition-boiling and film-boiling heat-transfer regimes. In the code, T_{min} is defined by

$$T_{min} = T_{NH} + (T_{NH} - T_l)\cdot R^{1/2} , \quad (3\text{-}294)$$

where

$$R = \frac{k_l \rho_l c_{p,l}}{k_w \rho_w c_{p,w}}, \tag{3-295}$$

and where T_{NH} is the homogeneous nucleation temperature (Ref. 3-46.). The homogeneous nucleation temperature in turn is evaluated from a third-order polynomial fit to the work of Fauske (Ref. 3-46.). Computation of T_{NH} is discussed in detail in Appendix F (Section F.2.1.9.). The final value of the minimum stable film-boiling temperature then is determined from the criterion

$$T_{min} = \max(T_{min}, T_{sat} + 0.0001\ K). \tag{3-296}$$

The minimum film-boiling temperature is used in TRAC as given in the source references.

3.8.7. Film Boiling

In the film-boiling regime, the wall-to-liquid heat transfer is based on the sum of radiation heat-transfer effects and near-wall liquid effects. Specifically, the wall-to-liquid heat-transfer coefficient is defined by

$$h_{wl} = (h_r + h_{fBB}) \cdot \left(\frac{T_w - T_{sat}}{T_w - T_l}\right), \tag{3-297}$$

where the radiation term h_r is calculated as presented in Section 3.8.5. and the near-wall liquid-effects term h_{fBB} is calculated from the modified Bromley equation, also presented in Section 3.8.5.

The wall-to-gas phasic heat-transfer coefficient is evaluated as the maximum of the natural-convection and the Dougall-Rohsenow correlations, or

$$h_{wg} = \max(h_{NC}, h_{dr}). \tag{3-298}$$

Both the natural-convection heat-transfer coefficient and the Dougall-Rohsenow coefficient are calculated as presented in Section 3.8.3. However, if the cell void fraction is >0.97, the coefficient h_{wg} is modified slightly to ensure a smooth transition between heat-transfer regimes. Details of the modification are presented in Appendix F (Section F.2.1.5.4.).

The overall modeling of the film-boiling regime is original to TRAC. The correlations that make up the model are used in TRAC as given in the source references.

3.8.7.1. Core Reflood. Under core reflood conditions, the wall-to-liquid heat-transfer coefficient still is based on the sum of radiative effects and near-wall liquid effects, or

$$h_{wl} = (h_r + h_{near\text{-}wall}) \cdot \left(\frac{T_w - T_{sat}}{T_w - T_l}\right). \tag{3-299}$$

In this case, however, the near-wall liquid effects are based on either the modified Bromley correlation (Ref. 3-43.) or the correlation of Denham (Ref. 3-47.) such that

$$h_{near\text{-}wall} = fcn(h_{fBB}, h_{Denham}) . \quad (3\text{-}300)$$

Denham's equation is given by

$$h_{Denham} = 0.4472 \left[\frac{g(\rho_l - \rho_v)}{\mu_v V_v} \right]^{1/2} . \quad (3\text{-}301)$$

The modified Bromley (Ref. 3-43.) coefficient h_{fBB} and the radiation term h_r both were defined in Section 3.8.5.

The exact functional dependence of the near-wall term to h_{fBB} and h_{Denham} is controlled by the particular reflood flow regime. For example, if the flow regime is smooth inverted annular flow, then

$$h_{near\text{-}wall} = h_{Denham} .$$

In the rough-wavy-flow regime, $h_{near\text{-}wall}$ is a weighted average of the Denham (Ref. 3-47.) and Bromley (Ref. 3-43.) correlations such that

$$h_{near\text{-}wall} = W_D \cdot h_{Denham} + W_B \cdot h_{fBB} . \quad (3\text{-}302)$$

In the agitated inverted-annular-flow and the post-agitated (dispersed-flow) regimes, $h_{near\text{-}wall}$ is based on a weighted value from the modified Bromley correlation (Ref. 3-43.). For highly dispersed flow, $h_{near\text{-}wall}$ is zero. Details of the appropriate weighting factors can be found in Appendix F (Section F.2.2.4.1.).

The wall-to-gas heat-transfer coefficient is redefined as a function of the Webb-Chen correlation (see Section 3.8.5.). Here again, the functional dependence is controlled by the particular reflood flow regime. For smooth inverted annular flow,

$$h_{wg} = 0 .$$

In the highly dispersed flow regime,

$$h_{wg} = h_{W\text{-}C} .$$

For rough-wavy inverted annular flow through dispersed flow, h_{wg} is interpolated linearly (as a function of void fraction) between zero and the Webb-Chen correlation value $h_{W\text{-}C}$. The appropriate weighting factor is defined in Appendix F (Section F.2.2.4.1.).

At void fractions >0.995, the wall-to-liquid heat-transfer coefficient is reevaluated as a function of the above relations and the single-phase vapor value ($h_{wl} = 0$). Likewise, if the

void fraction is >0.9999, the wall-to-gas heat-transfer coefficient is interpolated from the above relations and the value for single-phase vapor. Additional details of the interpolation scheme for both h_{wl} and h_{wg} can be found in Appendix F (Section F.2.2.4.1.).

The overall modeling of the film-boiling regime for reflood conditions is heuristic and was developed specifically for implementation into TRAC. The correlations that make up the model are used in TRAC as given in the source references.

3.8.8. Single-Phase Vapor

Under single-phase vapor conditions, the wall-to-liquid heat-transfer coefficient is equal to zero:

$$h_{wl} = 0.0 .$$

Alternatively, the wall-to-gas heat-transfer coefficient is defined as the maximum of the coefficient for turbulent natural convection and the coefficient for turbulent forced convection, or

$$h_{wg} = \max(h_{gNC}, h_{gturb}) .$$

The coefficient for turbulent natural convection is given by

$$h_{gNC} = 0.13 \left(\frac{k_g}{D_h}\right) Gr_g^{0.3333} Pr_g^{0.3333} . \quad (3\text{-}303)$$

The coefficient for turbulent forced convection is calculated from either the Sieder-Tate or the Dittus-Boelter equations. The choice of equation is dependent on the film temperature T_f, where

$$T_f = 0.5 (T_w + T_g) . \quad (3\text{-}304)$$

If $T_f \geq T_{sv}$, the code uses the Sieder-Tate equation (Ref. 3-18.), given by

$$h_{gturb} = 0.027 \left(\frac{k_g}{D_h}\right) Re_g^{0.8} Pr_g^{0.3333} \left(\frac{\mu_g}{\mu_w}\right)^{0.14} . \quad (3\text{-}305)$$

If $T_f < T_{sv}$, the code calculates h_{gturb} from the Dittus-Boelter relation such that

$$h_{gturb} = 0.023 \frac{k_g}{D_h} Re_g^{0.8} Pr_g^{0.4} . \quad (3\text{-}306)$$

Under the conditions that the cell void fraction is between 0.97 and 1.0, TRAC interpolates between the single-phase heat-transfer coefficients described in this section and the appropriate two-phase heat-transfer coefficients. Details of the interpolation scheme can be found in Appendix F (Section F.2.1.5.4.).

As in the case of single-phase liquid heat transfer, these correlations are accepted widely and are used for engineering analyses of heat transfer under the stated conditions.

3.8.9. Condensation

The condensation heat-transfer regime may exist under the conditions that the wall temperature is less than both the combined-gas and the saturated-vapor temperature, the void fraction is >0.05, and the mass quality is >0.71. When these criteria are met and vapor condenses on a cold wall, the wall-to-liquid and wall-to-gas heat-transfer coefficients are described by the following:

$$h_{wl} = 0.0 \tag{3-307}$$

and

$$h_{wg} = h'''_{gcond} \tag{3-308}$$

for the mass quality x equal to 1.0, or

$$h_{wl} = h'_{wl} + \left(0.0 - h'_{wl}\right) \cdot \frac{x - 0.71}{1.0 - 0.71} \tag{3-309}$$

and

$$h_{wg} = h'_{wg} + \left(h'''_{gcond} - h'_{wg}\right) \cdot \frac{x - 0.71}{1.0 - 0.71} \tag{3-310}$$

for

$$0.71 < x < 1.0 .$$

In the above equation, the condensation heat-transfer coefficient originally was based on the theoretical analysis of Nusselt (Ref. 3-48.) such that

$$h_{gcond} = 0.9428 \left[\frac{\rho_l^2 \, g \, k_l^3 \, h_{fg}}{\mu_l \, L \, (T_{sv} - T_w)} \right]^{0.25} . \tag{3-311}$$

However, to account for ripples that develop on the liquid film, the Nusselt coefficient is modified by

$$h'_{gcond} = h_{gcond} \cdot (1 - WF) + \max(h_2, h_{gcond}) \cdot WF \tag{3-312}$$

for

$$WF = \min\left[1.0, \max\left(0.0, \frac{L - 0.2}{1.8}\right)\right], \tag{3-313}$$

where L is the cell length. The heat-transfer coefficient h_2 is expressed by

$$h_2 = 0.003\left[\frac{\rho_l^2\, g\, k_l^3\, L\,(T_{sv} - T_w)}{h_{fg}\,\mu_l^3}\right]^{0.5} \tag{3-314}$$

and was derived empirically for liquid-film Reynolds numbers >350 (Ref. 3-48.). The condensation heat-transfer coefficient then is modified further such that

$$h''_{gcond} = h'_{gcond}\frac{(T_{sv} - T_w)}{\max(|T_g - T_w|,\, 0.01)} \tag{3-315}$$

and

$$h'''_{gcond} = \max\left(h''_{gcond},\, h'_{wg}\right) \tag{3-316}$$

for

$$h'_{wg} = \max(h_{gNC},\, h_{gturb})\,. \tag{3-317}$$

The turbulent natural-convection heat-transfer coefficient h_{gNC} and the turbulent forced-convection heat-transfer coefficient h_{gturb} are given by

$$h_{gNC} = 0.13\left(\frac{k_g}{D_h}\right) Gr_v^{0.3333}\, Pr_g^{0.3333} \tag{3-318}$$

and

$$h_{gturb} = 0.023\,\frac{k_g}{D_h}\, Re_g^{0.8}\, Pr_g^{0.3}\,, \tag{3-319}$$

respectively.

Finally, the wall-to-liquid heat-transfer coefficient h'_{wl} is defined by

$$h'_{wl} = \max(h_{NC1},\, h_{NC2},\, h_{forc})\,, \tag{3-320}$$

where (Ref. 3-48.)

$$h_{NC1} = 0.59\left(\frac{k_l}{D_h}\right) Gr_l^{0.25}\, Pr_l^{0.25}\,. \tag{3-321}$$

and (Ref. 3-37.)

$$h_{NC2} = 0.10 \left(\frac{k_l}{D_h}\right) Gr_l^{0.3333} Pr_l^{0.3333} . \quad (3\text{-}322)$$

The coefficient h_{forc} is calculated from the Chen correlation (Ref. 3-38.), where S equals zero. Thus,

$$h_{forc} = 0.023 \frac{k_l}{D_h} \left(\frac{V_l \rho_l (1 - \alpha) D_h}{\mu_l}\right)^{0.8} Pr_l^{0.4} \cdot F . \quad (3\text{-}323)$$

The overall approach to modeling condensation is heuristic and was developed specifically for implementation into TRAC. The correlations that make up the model are used in the form given in the source references for this constitutive model.

3.8.10. Two-Phase Forced Convection

At the user's option, the heat-transfer correlations for the two-phase forced-convection regime may be used in lieu of those presented for nucleate, transition, and film boiling. Within the two-phase forced-convection model, the liquid heat-transfer coefficient is evaluated as the maximum of the Rohsenow-Choi correlation (Ref. 3-49.) for laminar forced convection (h_{wllam}) and the Dittus-Boelter correlation for turbulent forced convection (h_{wlturb}). In other words,

$$h_{wl} = \max(h_{wllam}, h_{wlturb}) , \quad (3\text{-}324)$$

where

$$h_{wllam} = \frac{4 k_l}{D_h} \quad (3\text{-}325)$$

and

$$h_{wlturb} = 0.023 \frac{k_l}{D_h} Re^{0.8} Pr^{0.4} . \quad (3\text{-}326)$$

In the above equation, the Reynolds number is defined by

$$Re = \frac{G_m D_h}{\mu_m} , \quad (3\text{-}327)$$

the Prandtl number is defined by

$$Pr = \frac{\mu_l c_{p,l}}{k_l} , \quad (3\text{-}328)$$

and the mixture viscosity (Ref. 3-50.) is expressed as a function of the flow quality x_f such that

$$\mu_m = \left[\frac{x_f}{\mu_g} + \frac{(1 - x_f)}{\mu_l}\right]^{-1} . \tag{3-329}$$

Alternatively, the wall-to-gas heat-transfer coefficient is given by

$$h_{wg} = \begin{cases} 0.0 & \alpha < 0.98 \quad (3\text{-}330) \\ \max(h_{gNC}, h_{gturb}) & \alpha \geq 0.98 , \quad (3\text{-}331) \end{cases}$$

where the coefficient h_{gNC} is evaluated from the turbulent natural-convection correlation

$$h_{gNC} = 0.13 \left(\frac{k_g}{D_h}\right)\left(\frac{\rho_g^2 \, g \, |T_w - T_g|}{\mu_g^2 \, T_g}\right)^{0.3333} Pr_g^{0.4} , \tag{3-332}$$

and h_{gturb} is evaluated from the Dittus-Boelter correlation for turbulent forced convection

$$h_{gturb} = 0.023 \frac{k_g}{D_h} Re_g^{0.8} \, Pr_g^{0.4} . \tag{3-333}$$

In this case, the Reynolds and Prandtl numbers are calculated by

$$Re_g = \frac{\rho_g \, V_g \, D_h}{\mu_g} \tag{3-334}$$

and

$$Pr_g = \frac{\mu_g \, c_{p,g}}{k_g} . \tag{3-335}$$

Finally, when the cell void fraction is >0.98, the liquid and gas heat-transfer coefficients are interpolated from the values calculated for two-phase forced convection (as defined in this section) and the values calculated for single-phase vapor (see Section 3.8.8.). Details of the interpolation scheme are presented in Appendix F (Section F.2.1.7.4.).

The overall approach to modeling two-phase forced convection is heuristic and was developed specifically for implementation into TRAC. The correlations that make up the model are used in the form given in the source references.

REFERENCES

3-1. B. R. Bandini, "A Three-Dimensional Transient Neutronics Routine for the TRAC-PF1 Reactor Thermal Hydraulic Computer Code," Thesis, Pennsylvania State University (May 1990).

3-2. K. Mishima and M. Ishii, "Theoretical Prediction of Onset of Horizontal Slug Flow," *Trans. ASME, J. Fluids Engineering*, **102**, 441–445 (1980).

3-3. M. Ishii and G. DeJarlais, "Flow Visualization Study of Inverted Annular Flow of Post Dryout Heat Transfer Region," *Nuclear Engineering and Design*, **99**, 187–199 (1987).

3-4. M. Ishii and G. DeJarlais, "Flow Regime Transition and Interfacial Characteristics of Inverted Annular Flow," *Nuclear Engineering and Design*, **95**, 171–184 (1986).

3-5. N. T. Obot and M. Ishii, "Two-Phase Flow Regime Transition Criteria in Post-Dryout Region Based on Flow Visualization Experiments," *Int. J. Heat Mass Transfer*, **31**, 12, pp. 2559–2570 (1988).

3-6. M. Ishii and K. Mishima, "Study of Two-Fluid Model and Interfacial Area," Argonne National Laboratory report ANL-80-111 (NUREG/CR-1873) (1980).

3-7. J. F. Lime, "Memorandum on Interfacial Drag from M. Ishii to R. Nelson, July 28, 1987," Los Alamos National Laboratory document LA-UR-01-1591 (March 2001).

3-8. M. Ishii and K. Mishima, "Correlation for Liquid Entrainment in Annular Two-Phase Flow of Low-Viscous Fluid," Argonne National Laboratory report ANL/RAS/LWR 81-2 (1981).

3-9. M. Ishii and K. Mishima, "Droplet Entrainment Correlation in Annular Two-Phase Flow," *Int. J. Heat Mass Transfer*, **32**, 1835–1846 (1989).

3-10. I. Kataoka, M. Ishii, and K. Mishima, "Generation and Size Distribution of Droplet in Annular Two-Phase Flow," *Trans. ASME, J. Fluid Engineering*, **105**, 230–238 (1983).

3-11. J. Kitscha and G. Kocamustafaogullari, "Breakup Criteria for Fluid Particles," *Int. J. Multiphase Flow*, **15**, 573–588 (1989).

3-12. I. Kataoka and M. Ishii, "Mechanism and Correlation of Droplet Entrainment and Deposition in Annular Two-Phase Flow," Argonne National Laboratory report ANL-82-44 (NUREG/CR-2885) (1982).

3-13. K. Pasamehmetoglu, "A Formula for Limiting Film Thickness on Cold Walls," Los Alamos National Laboratory memorandum to J. W. Spore (September 1, 1989).

3-14. R. T. Lahey, "A Mechanistic Subcooled Boiling Model," *Proc. 6th Int. Heat Transfer Conf.* (Toronto, Canada, 1978), Vol. 1, pp. 293–297.

3-15. P. Saha and N. Zuber, "Point of Net Vapor Generation and Vapor Void Fraction in Subcooled Boiling," *Proc. 5th Int. Heat Transfer Conf.* (Tokyo, Japan, 1974), Paper B4.7.

3-16. M. Ishii and T. C. Chawla, "Local Drag Laws in Dispersed Two-Phase Flow," Argonne National Laboratory report ANL-79-105 (NUREG/CR-1230) (December 1979).

3-17. L. Shiller and A. Z. Nauman, *Ver. Deut. Ing.*, **77**, 318–320 (1933).

3-18. R. B. Bird, W. E. Stewart, and E. N. Lightfoot, *Transport Phenomena* (John Wiley and Sons, New York, 1960).

3-19. M. Ishii and K. Mishima, "Two Fluid Model and Hydrodynamic Constitutive Relations," *Nucl. Eng. and Design*, **82**, 107–126 (1984).

3-20. G. B. Wallis, *One Dimensional Two Phase Flow* (McGraw-Hill Book Company, New York, 1969).

3-21. Y. Taitel and A. E. Dukler, "A Model for Predicting Flow Regime Transitions in Horizontal and Near Horizontal Gas-Liquid Flow," *AIChE J.*, **22** (1), 47–55 (1976).

3-22. A. Ohnuki, H. Adachi, and Y. Murao, "Scale Effects on Countercurrent Gas-Liquid Flow in Horizontal Tube Connected to Inclined Riser," American Nuclear Society, ANS 1987 National Heat Transfer Conference (Pittsburgh, Pennsylvania, August 9-12, 1987), pp. 40-49.

3-23. J. G. Collier, *Convective Boiling and Condensation*, (McGraw-Hill Book Company, New York, 1972).

3-24. M. W. Cappiello, "A Model for the Interfacial Shear in Vertical, Adiabatic Annular-Mist Flow," Los Alamos National Laboratory document LA-CP-89-392 (October 1989).

3-25. S. W. Churchill, "Friction-Factor Equation Spans All Fluid-Flow Regimes," *Chemical Engineering*, pp. 91–92 (Nov. 7, 1977).

3-26. Y. M. Chen and F. Mayinger, "Measurement of Heat Transfer at the Phase Interface of Condensing Bubbles," *ANS Proc. 1989 National Heat Transfer Conf.* (Philadelphia, Pennsylvania, August 6-9, 1989) HTC-Vol. 4, pp. 147-152.

3-27. S. Whittaker, "Forced Convection Heat Transfer Correlations for Flows in Pipes, Past Flat Plates, Single Cylinder, Single Sphere, and Flows in Packed Beds and Tube Bundles," *AIChE J.*, **18**, 361–372 (1972).

3-28. R. T. Lahey and F. J. Moody, *The Thermal-Hydraulics of a Boiling Water Nuclear Reactor*, ANS monograph, American Nuclear Society, LaGrange Park, Illinois, (1977).

3-29. K. Pasamehmetoglu and R. Nelson, "Transient Direct-Contact Condensation on Liquid Droplets," *Nonequilibrium Transport Phenomena* (American Society of Mechanical Engineers, New York, 1987), HTD-Vol. 77, pp. 47–56.

3-30. M. Ishii, "One Dimensional Drift-Flux Model and Constitutive Equations for Relative Motion between Phases in Various Two-Phase Flow Regimes," Argonne National Laboratory report ANL-77-47 (1977).

3-31. G. Ryskin, "Heat and Mass Transfer from a Moving Drop—Some Approximate Relations for the Nusselt Number," *Int. Comm. Heat Mass Transfer*, **14**, 741–749 (1987).

3-32. S. G. Bankoff, "Some Condensation Studies Pertinent to Light Water Safety," *Int. J. Multiphase Flow*, **6**, 51–67 (1980).

3-33. J. H. Linehan, M. Petrick, and M. M. El-Wakil, "The Condensation of Saturated Vapor on a Subcooled Film During Stratified Flow," *Chem. Eng. Symp. Series*, **66** (102), 11–20 (1972).

3-34. C. Unal, K. Tuzla, C. A. Tuzla, and J. C. Chen, "Vapor Generation Model for Dispersed Drop Flow," *ANS Proc. 1989 National Heat Transfer Conf.* (August 1989), HTC-Vol. 4.

3-35. G. G. Sklover and M. D. Rodivilin, "Condensation on Water Jets with a Cross Flow of Steam," *Teploenergetika*, **23**, 48–51 (1976).

3-36. J. P. Holman, *Heat Transfer*, 5th ed. (McGraw-Hill Book Co., New York, 1981).

3-37. F. E. Incropera and D. P. DeWitt, *Fundamentals of Heat Transfer* (John Wiley & Sons, New York, 1981).

3-38. J. M Delhaye, M. Giot, and M. L. Riethmuller, *Thermohydraulics of Two-Phase Systems for Industrial Design and Nuclear Engineering* (Hemisphere Publishing Corporation, New York, 1981).

3-39. H. K. Forster and N. Zuber, "Bubble Dynamics and Boiling Heat Transfer," *AIChE J.*, **1**, 532–535 (1955).

3-40. W. M. McAdams, *Heat Transmission*, 3rd ed. (McGraw-Hill Book Co., New York, 1954).

3-41. L. Biasi, G. C. Clerici, S. Garribba, R. Sala, and A. Tozzi, "Studies on Burnout, Part 3: A New Correlation for Round Ducts and Uniform Heating and Its Comparison with World Data," *Energia Nucleare*, **14**, 530–536 (1967).

3-42. O. C. Jones, Jr. and S. G. Bankoff, editors, *Thermal and Hydraulic Aspects of Nuclear Reactor Safety, Volume 1: Light Water Reactors* (ASME, New York, 1977).

3-43. L. A. Bromley, "Heat Transfer in Stable Film Boiling," *Chem. Eng. Prog.*, **46** (5), 221–227 (May 1950).

3-44. S. Webb and J. C. Chen, "A Two-Region Vapor Generation Rate Model for Convective Film Boiling," Int. Workshop of Fundamental Aspects of Post-Dryout Heat Transfer, Salt Lake City, Utah, April 1–4, 1984.

3-45. J. C. Chen, F. T. Ozkaynak, and R. K. Sundaram, "Vapor Heat Transfer in Post-CHF Region Including the Effect of Thermodynamic Non-Equilibrium," *Nuclear Eng. and Design*, **51**, 143–155 (1979).

3-46. R. E. Henry, "A Correlation for the Minimum Film Boiling Temperature," *AIChE Symposium Series*, **138**, 81–90 (1974).

3-47. M. K. Denham, "Inverted Annular Film Boiling and the Bromley Model," AEEW-R 1590, Winfrith, Rochester (January 1983).

3-48. F. Kreith, *Principles of Heat Transfer*, 3rd. ed., (Harper and Row, New York, 1973).

3-49. W. M. Rohsenow and H. Choi, *Heat, Mass, and Momentum Transfer* (Prentice-Hall, Englewood Cliffs, New Jersey, 1961).

3-50. W. H. McAdams, "Vaporization Inside Horizontal Tubes-II-Benzene-Oil Mixtures," *Trans. ASME*, **64**, 193 (1942).

3-51. R. A. Nelson, Jr., D. A. Pimentel, S. J. Jolly-Woodruff, and J. W. Spore, "Reflood Completion Report, Volume I: A Phenomenological Thermal-Hydraulic Model of Hot Rod Bundles Experiencing Simultaneous Bottom and Top Quenching and an Optimization Methodology for Closure Development," Los Alamos National Laboratory report LA-UR-98-3043 (April, 1998).

3-52. B. E. Boyack, J. F. Lime, D. A. Pimentel, J. W. Spore, and T. D. Knight, "Reflood Completion Report, Volume II: Developmental Assessment of a New Reflood

Model for the TRAC-M/F77 Code," Los Alamos National Laboratory report LA-UR-98-3043 (April, 1998).

3-53. B. E. Boyack, J. F. Lime, D. A. Pimental, J. W. Spore, and J. L. Steiner, "TRAC-M/F77, Version 5.5, Developmental Assessment Manual, Volume I: Assessment Sections not Including 2D/3D Tests," Los Alamos National Laboratory document LA-UR-99-6480 (December 1999).

3-54. B. E. Boyack, J. F. Lime, D. A. Pimental, J. W. Spore, and J. L. Steiner, "TRAC-M/F77, Version 5.5, Developmental Assessment Manual, Volume II: Assessment Sections for 2D/3D Tests," Los Alamos National Laboratory document LA-CP-99-345 (December 1999).

4.0. FLOW PROCESS AND SPECIAL MODELS

Special models play an important role in the overall construction of TRAC. In the following sections, eight special models are described:

- models for critical flow,
- countercurrent flow,
- offtake flow from a large pipe in horizontal stratified flow,
- form loss,
- gap conductance,
- decay heat and void-reactivity feedback,
- reactor-vessel vent valve, and
- metal-water reaction.

The nomenclature that applies to this section follows:

NOMENCLATURE

a_{HE}: homogeneous equilibrium sound speed
A_j: flow area before the abrupt expansion
A_{j+1}: flow area after the abrupt expansion
C: virtual mass coefficient
C_B: abscissa intercept in Bankoff CCFL correlation
D: diameter
$\bar{E}$: interpolation constant used in the CCFL model
E_j: effective energy fraction of decay-heat group *j*
g: gravitational acceleration
h: critical distance from the offtake entrance plane to the liquid level
h_{gas}: heat-transfer coefficient for gap-gas conductance
H_g: dimensionless gas flux
H_j: connection of decay-heat group *j* (W · s)
H_l: dimensionless liquid delivery
j: superficial velocity
J: total number of decay-heat groups

k: phase index (liquid or gas)

k_{gas}: gap-gas thermal conductivity

K: additive loss factor

L: length

m'_{Zr}: mass per unit length of zirconium

M_B: slope in the Bankoff CCFL correlation

P: pressure or total thermal power from fission

P_c: pressure at the choking plane

P_{up}: pressure upstream of the choking plane

q'''_{mw}: heat source from the metal-water reaction

R: neutronic reactivity, including both programmed and feedback reactivity

$\bar{R}$: gas constant

R^*: nondimensional height ratio for offtake model

R_f: solid-fuel radius

R_f^*: fuel radius, including cracked fuel

R_I: cladding inner radius

$R_{I,new}$: cladding inner radius after thermal expansion

$R_{f,new}$: solid-fuel radius after thermal expansion

R_o: cladding outer radius

s: entropy

t: time

T_0: stagnation temperature

V: velocity

V_{cg}: critical velocity for single-phase vapor

V_{cl}: subcooled-liquid choking velocity

V_{up}: velocity upstream of the choking plane

W: mass flow rate in offtake model

x: distance

α: gas volume fraction

α_c: cladding fraction

α_f: fuel fraction

γ: specific heat ratio

Δr_{gap}: fuel-cladding radial gas gap

$\Delta\rho$: difference between the phasic densities

ΔT: temperature difference

Δt: time step

δ: the cracked-fuel thickness

δ_0: initial undeformed radial thickness of the cracked fuel

λ_i: decay constant for the delayed-neutron precursors in group i

λ_j^H: decay constant for decay-heat group j (s^{-1})

Λ: effective prompt-neutron lifetime

ρ: density

σ: surface tension

Subscripts

a: noncondensable gas

c: cladding

f: fuel

g: combined-gas mixture

l: liquid

m: total mixture

up: conditions upstream of the choking plane

v: vapor

4.1. Critical Flow

A detailed description of the TRAC critical flow model is provided in Appendix I, Section I.2. The critical flow model comprises three separate models:

- a subcooled-liquid choked-flow model;
- a two-phase, two-component choked-flow model; and
- a single-phase vapor choked-flow model.

Also, linear interpolation is used to treat the transition from subcooled liquid to the two-phase two-component models.

4.1.1. Subcooled-Liquid Choked Flow

During the subcooled blowdown phase, the fluid undergoes a phase change at the break because the downstream pressure is much less than the saturation pressure corresponding to the system fluid temperature. Thus, the choking velocity can be calculated following the approach of Burnell (Ref. 4-1.) until a point is reached when the system pressure is so low that the subcooled-liquid choking velocity, V_{cl}, is less than the homogeneous equilibrium sound speed, a_{HE}. Therefore, the subcooled choking criterion is given by the maximum of the homogeneous equilibrium sound speed and the Burnell

expression (a Bernoulli expansion to the point of vapor inception at the choke plane). Thus,

$$V_{cl} = \max\left\{a_{HE}, \left[V_{up,l}^2 + \frac{2(P_{up} - P_c)}{\rho_l}\right]^{1/2}\right\}, \tag{4-1}$$

where the pressure at the choking plane, P_c, is determined using the nucleation delay model of Jones (Ref. 4-2.), and the subscripts "*up*" and "*l*" denote the conditions upstream of the choking plane and liquid conditions, respectively.

4.1.2. Two-Phase, Two-Component Choked Flow

The TRAC two-phase choking model is an extension of one developed by Ransom and Trapp (Ref. 4-3.) that incorporates an additional inert gas component. Thermal equilibrium is assumed to exist between the phases. The two-fluid flow field under thermal equilibrium is described by the inert gas continuity equation, the overall continuity equation, two phasic momentum equations, and the mixture energy equation. The non-differential source terms do not enter into the characteristic analysis. Thus, the equations are

$$\frac{\partial \rho_m}{\partial t} + \frac{\partial(\rho_m V_m)}{\partial x} = 0, \tag{4-2}$$

$$\alpha\rho_g\left[\frac{\partial V_g}{\partial t} + V_g\frac{\partial V_g}{\partial x}\right] + \alpha\frac{\partial P}{\partial x} + C\alpha(1-\alpha)\rho_m\left[\frac{\partial V_g}{\partial t} + V_l\frac{\partial V_g}{\partial x} - \frac{\partial V_l}{\partial t} - V_g\frac{\partial V_l}{\partial x}\right] = 0, \tag{4-3}$$

$$(1-\alpha)\rho_l\left[\frac{\partial V_l}{\partial t} + V_l\frac{\partial V_l}{\partial x}\right] + (1-\alpha)\frac{\partial P}{\partial x} + C\alpha(1-\alpha)\rho_m\left[\frac{\partial V_l}{\partial t} + V_g\frac{\partial V_l}{\partial x} - \frac{\partial V_g}{\partial t} - V_l\frac{\partial V_g}{\partial x}\right] = 0, \tag{4-4}$$

$$\frac{\partial(\rho_m s_m)}{\partial t} + \frac{\partial[\alpha\rho_g V_g s_g + (1-\alpha)\rho_l V_l s_l]}{\partial x} = 0, \text{ and} \tag{4-5}$$

$$\frac{\partial(\alpha\rho_a)}{\partial t} + \frac{\partial(\alpha\rho_a V_g)}{\partial x} = 0, \tag{4-6}$$

where C is the virtual mass coefficient; s is the entropy; and subscripts a, g, l, and m refer to the noncondensable gas, steam/gas mixture, liquid, and total mixture, respectively. Following Ransom and Trapp's formulation (Ref. 4-3.), the energy equation is written in the form of the mixture-specific entropy that is conserved for adiabatic flow (with the irreversibilities associated with interphasic mass transfer and relative phase acceleration neglected).

In the thermal-equilibrium case, ρ_a, ρ_v, ρ_l, s_g, s_l, and s_m are known functions of P_a and P_v. If we assume that Dalton's law of partial pressures applies, the above five characteristic equations for two-phase, two-component choked flow can be written in terms of the five unknowns P_a, P_v, α, V_g, and V_l with the characteristic roots, λ_v, given by the roots of a fifth-order polynomial. Choking occurs when the signal propagating with the largest velocity relative to the fluid is stationary; that is, $\lambda_{t,re,max}=0$. An analytic solution for the characteristic roots is difficult to obtain. Thus, the characteristic roots are obtained numerically.

4.1.3. Single-Phase Vapor Choked Flow

The single-phase vapor choked-flow model is based on isentropic expansion of an ideal gas (Ref. 4-4.). The continuity equation, in conjunction with the ideal gas relations, yields the following expression for the critical velocity:

$$V_{cg} = \sqrt{\frac{2\gamma}{\gamma+1}\bar{R}T_0} \ , \tag{4-7}$$

where γ is the specific heat ratio, T_0 is the stagnation temperature, and $\bar{R}$ is the gas constant. When the downstream throat temperature is greater than the saturation temperature at the throat pressure, the fluid flow at the throat is predicted to be superheated by the ideal gas relations, and the single-phase vapor choked-flow model is applied. Appendix I discusses an iterative method that is used when the downstream throat temperature is less than or equal to the saturation temperature at the throat pressure.

4.2. Countercurrent Flow

A detailed description of the TRAC countercurrent-flow model is provided in Appendix I (Section I.3.). Characteristic countercurrent-flow-limiting (CCFL) correlations can be invoked by the user at specific locations. The basic correlation model implemented in TRAC is provided by Bankoff (Ref. 4-5.). The Bankoff correlation is given as

$$H_g^{1/2} + M_B H_l^{1/2} = C_B \ , \tag{4-8}$$

where H_g is the dimensionless gas flux, H_l is the dimensionless liquid delivery, C_B is the abscissa intercept, and M_B is the slope. The Bankoff relationship is sufficiently general that either Wallis scaling for diameter dependence (Ref. 4-6.), Kutateladze scaling for surface-tension dependence (Ref. 4-7.), or a combination of the two can be implemented. This is performed by defining a variable-length scale in the determination of the dimensionless flux as follows:

$$H_k = j_k\left(\frac{\rho_k}{gw\Delta\rho}\right)^{1/2} \ , \tag{4-9}$$

$$w = D^{1-\bar{E}} L^{\bar{E}}, \tag{4-10}$$

and

$$L = \left(\frac{\sigma}{g\Delta\rho}\right)^{1/2}, \tag{4-11}$$

where

- k = phase (liquid or gas),
- j = superficial velocity,
- D = diameter of holes,
- g = gravitational acceleration,
- σ = surface tension,
- ρ = density,
- $\Delta\rho$ = difference between the phasic densities, and
- $\bar{E}$ = interpolation constant between 0 and 1.

The Bankoff correlation reverts to Wallis scaling for $\bar{E}=0$ and to Kutateladze scaling for $\bar{E}=1$. For $\bar{E}$ between 0 and 1, the Bankoff scaling applies (Ref. 4-5.).

4.3. Offtake

A detailed description of the TRAC offtake model is provided in Appendix I (Section I.4.). The TEE-component offtake model is designed specifically to handle the case when a small break is made in a large pipe containing horizontal stratified flow. The model predicts the offtake flow quality that exits the break based on conditions in the main pipe, following the approach of Ardron and Bryce (Ref. 4-8.). When the entrance plane to the break is submerged, the offtake flow consists mostly of liquid and possibly an entrained gas component. When the entrance plan is above the liquid level, the offtake flow is mostly gas and possibly an entrained liquid component.

The offtake model is specific to three geometries: upward, downward, and side offtakes. Offtake flow quality has been correlated as a function of the nondimensional height ratio, R^*, where

$$R^* = \frac{h}{h_b}, \text{ and} \tag{4-12}$$

h is the actual or measured critical distance from the offtake entrance plane to the liquid level and the critical height at which gas or liquid entrainment begins, and h_b is determined from the expression

$$h_b = \frac{C_1 W_k^{0.4}}{(g\rho_k \Delta\rho)^{0.2}}, \tag{4-13}$$

where

C_1 = constant determined from data,
W_k = major-phase mass flow rate,
ρ_k = major-phase density, and
$\Delta\rho$ = difference between the phasic densities.

4.4. Form Loss

Detailed descriptions of the TRAC form-loss model are provided in Section 2.1.7.1. and in Appendix I, Section I.1. Irrecoverable pressure losses occur across abrupt area changes. In TRAC, only reversible losses across area changes are obtained when solving the field equations. Irreversible losses must be accounted for by using an additional form-loss term. Theoretically- and experimentally-derived form-loss terms are added to the momentum equations only if the user requests this approach via an input option at the desired cell interfaces.

For an abrupt expansion, the theoretically derived additive loss factor is

$$K = \left(1 - \frac{A_j}{A_{j+1}}\right)^2, \tag{4-14}$$

where A_j and A_{j+1} are the flow areas before and after the abrupt expansion, respectively.

A theoretical derivation of the additive loss factor for an abrupt contraction is not possible. Thus, the data for the standard loss coefficient for an abrupt contraction cited in Massey (Ref. 4-9., p. 219) are incorporated into TRAC using a curve fit.

The user may have to account for turning losses at TEE-component internal junctions with appropriate input-specified friction factors (or K-factors). Also, there is no input option to select automatic internal calculation of losses from abrupt expansions or contractions at the three interfaces of the TEE joining cell.

The existence of a thin-plate orifice creates an abrupt flow-area change and also results in irrecoverable pressure losses. In practice, it has been found that many TRAC input-data models have cell-edge flow areas that are less than both of the bounding mesh-cell flow areas, even though in reality there is no thin-plate orifice. Therefore, if a thin-plate orifice exists, the user is advised to account for irreversible losses through the use of input-specified friction factors (or K-factors). There is no internal calculation for such a loss that can be selected via the input. A recommendation for user determination of an appropriate loss coefficient is given in Appendix I.

4.5. Fuel-Cladding Gap Conductance

A detailed description of the TRAC fuel-cladding gap-conductance model is provided in Appendix L. The user must specify the initial value of the gap conductance and appropriate geometric data. At the user's option, either the initial gap conductance is used throughout the calculation or the initial gap-conductance value is modified via a thermal-expansion model.

If we assume that the user seeks a transient evaluation, the fuel-cladding gap conductance is given by

$$h_{gas} = \frac{k_{gas}}{(\Delta r_{gap} + \delta_r)} , \tag{4-15}$$

where k_{gas} is the gap-gas thermal conductivity. A value of 4.4×10^{-6} m is used for δ_r, which includes the mean surface roughness of the fuel and the cladding plus the temperature jump differences (Refs. 4-11. and 4-12.). The fuel-cladding radial gas gap, Δr_{gap}, is developed following Boley and Weiner (Ref. 4-13.). The uncoupled, quasi-static approximation is applied, which eliminates the mechanical coupling term in the energy equation and the inertial term in the mechanical force balance. With these assumptions, the fuel-cladding strains minimally affect the temperature distribution; displacements are instantaneous. The fuel-cladding gap system is modeled as comprising three regions: solid fuel, cracked fuel, and cladding. Gap changes are found by calculating the radial displacement of each region caused by thermal expansion.

The gap width after a period of thermal expansion is given by

$$\text{gap width} = R_{I,new} - R_{f,new} - \delta , \tag{4-16}$$

where $R_{I,new}$ and $R_{f,new}$ are the cladding inner radius and the solid-fuel radius after thermal expansion, respectively, and δ is the cracked-fuel thickness. These are defined by the following expressions:

$$R_{I,\,new} = R_I + \frac{2\alpha_c R_I}{R_o^2 - R_I^2} \int_{R_I}^{R_o} \Delta T_c \, r \, dr , \tag{4-17}$$

$$R_{f,\,new} = R_f + \frac{2\alpha_f}{R_f} \int_{o}^{R_f} \Delta T_f \, r \, dr , \text{ and} \tag{4-18}$$

$$\delta = \delta_o \left[1 + \frac{\alpha_f}{R_f^* - R_f} \int_{R_f}^{R_f^*} \Delta T_f \, dr \right] , \tag{4-19}$$

where δ_o is the initial undeformed radial thickness of the cracked fuel, $\delta_o = R_f^* - R_f$; R_o is the initial cladding outer radius; and ΔT_c and ΔT_f are temperature differences with respect to a reference temperature (298 K) in the fuel and cladding, respectively.

4.6. Decay Heat and Reactivity Feedback

The code uses the solution of the point-reactor-kinetics model for the total fission power, P, in the decay-heat equations to obtain the decay heat. Detailed descriptions of the kinetics and associated models are provided in Appendix M. The decay-heat equations are

$$\frac{dH_j}{dt} = -\lambda_j^H H_j + E_j P \text{ , for } j = 1, 2, 3, \ldots, J \text{ ,} \tag{4-20}$$

where

H_j = energy of the decay-heat precursor concentration in group j (W-s),
λ_j^H = decay constant for decay-heat group j (s^{-1}),
E_j = effective energy fraction of decay-heat group j, and
J = number of decay-heat groups.

TRAC contains default data for the delayed-neutron constants λ_i, decay-heat group constants λ_j^H, and decay energy. The effective energy fraction, E_j, is obtained from the decay energy. The default values for the parameters for the decay-heat equation are taken from the 1979 American Nuclear Society (ANS) decay-heat standard (Ref. 4-14.). The code user can either use the default values or input other sets of constants.

The reactor-power and decay-heat models are fundamental standard models for the kinds of applications of interest to TRAC.

The total thermal power generated in the fuel is calculated from the sum of the nuclear fission, fission-product decay, and any external source.

The neutronic reactivity [see Appendix M, Eq. (M-6)] includes accounting for the effects of core-average fuel temperature, coolant temperature, coolant void fraction, and boron (i.e., solute) concentration. The user supplies reactivity coefficients for each of the reactivity independent-variable parameters: fuel temperature, coolant temperature, coolant void fraction, and boron concentration. The TRAC modeling again is based on widely used standard models.

It is the void reactivity-feedback coefficient that causes the shutdown of power generation for an LBLOCA. The rapid increase in void as the pressure in the core attains the saturation pressure effectively stops power production. The void increase due to flashing of the liquid in the core is so rapid that the power-generation shutdown is

almost independent of the numerical value of the user-supplied feedback coefficient. (within reasonable engineering values).

The code solves the point-reactor-kinetics equations by modifications to the Kaganove method (Ref. 4-15.), an approximate analytical method. The modifications consist of using a second-order polynomial for the power, P; using a first-order polynomial for the neutronic reactivity, R; and taking the effective prompt-neutron lifetime, Λ, as a constant.

The core-power model in TRAC, with all the options and features, has proved to be sufficiently general for describing the core assemblies in most of the reactor-safety-related experiments and in reactor plants, provided that the power shape changes only in the axial direction. The option to specify core power directly with a tabular prescription is generally sufficient for modeling most transients of interest. The decay-heat model is based on the 1979 ANS standard and is thus the best available model at this time.

The deficiencies of the core-power model are related principally to the fact that the reactor kinetics is based on the point-reactor assumption. Reactivity feedback also is based on the point-reactor assumption.

The point-reactor model has no limitations relative to applications involving LBLOCA analyses.

4.7. Reactor-Vessel Vent Valve

Reactor-vessel vent valves, such as those used in Babcock and Wilcox (B & W) plants, are modeled in the VESSEL component with user-specified values for flow-loss resistance as a function of pressure drop across the valve at user-specified locations in the VESSEL mesh. Leakage flow can be modeled. The vent-valve logic is only applicable at the outer radial (or x) interface of a 3D VESSEL mesh cell. Only a single vent valve may be specified at any one such interface; additional valves at the same interface would have to be lumped together. The user-supplied resistances are applied in the radial momentum equations of TRAC's 3D hydrodynamics. The inertial effects of the vent valve opening and closing are not modeled in TRAC. Additional details on TRAC's vent-valve logic are given in Appendix I, Section I.5., and complete input specifications are given in the TRAC-M/F90 User's Manual (Ref. 4-16.). Both Appendix I and the user's manual describe the form of flow-loss resistance that must be supplied by the user.

4.8. Metal-Water Reaction

When Zircaloy cladding reaches a sufficiently high temperature in a steam environment, an exothermic reaction may occur that influences the peak cladding temperature. This exothermic reaction is given by

$$Zr + 2H_2O \rightarrow ZrO_2 + 2H_2 + \text{heat} . \qquad (4\text{-}21)$$

TRAC accounts for this reaction by calculating an additional heat source q'''_{mw} that is added to the heat-conduction equation. The code assumes a single-region cladding and that there is enough steam to allow use of a standard reaction-rate equation. The term q'''_{mw} is calculated according to

$$q'''_{mw} = 6.45 \times 10^6 m'_{Zr}[\Delta t(R_o^2 - R_I^2)\pi]^{-1} , \quad (4\text{-}22)$$

where m'_{Zr} is the mass per unit length of zirconium consumed by the reaction in one time step, Δt is the time-step size, R_o and R_I are the cladding outer and inner radii, respectively, and 6.45×10^6 J/kg is the energy released per kilogram of oxidized zirconium.

The derivation of Eq. (4-22) is given in Appendix L, Section L.2.

TRAC only applies this model at nodes that are at hydrodynamic cell boundaries, and accounts for its effect at intervening fine mesh nodes by linear interpolation. This could result in a significant underprediction of clad temperature in cells with a quench front. Section L.2. of Appendix L discusses the possibility of TRAC's underprediction of peak clad temperature when the peak clad temperature is in the same hydrodynamic cell as a quench front and rod temperatures exceed 1273 K (the onset of the metal-water reaction).

REFERENCES

4-1. "RELAP5/MOD1 Code Manual, Volume 1: System Models and Numerical Methods," Idaho National Engineering Laboratory report EGG-2070 Draft, Rev. 1, also NUREG/CR1826 (March 1981).

4-2. O. C. Jones, Jr., "Flashing Inception in Flowing Liquids," Brookhaven National Laboratory report BNL-NUREG-51221 (1980).

4-3. V. H. Ransom and J. A. Trapp, "The RELAP5 Choked Flow Model and Application to a Large Scale Flow Test," in *ANS/ASME/NRC International Topical Meeting on Nuclear Reactor Thermal-Hydraulics* (Saratoga Springs, New York, 1980), pp. 799–819.

4-4. F. M. White, *Fluid Mechanics* (McGraw-Hill, Inc., New York, 1979).

4-5. S. G. Bankoff, R. S. Tankin, M. C. Yuen, and C. L. Hsieh, "Countercurrent Flow of Air/Water and Steam/Water through a Horizontal Perforated Plate," *International Journal of Heat and Mass Transfer*, **24**:8, pp. 1381–1395 (1981).

4-6. G. B. Wallis, *One Dimensional Two Phase Flow* (McGraw-Hill Book Company, New York, 1969).

4-7. S. S. Kutateladze, *Izv. Akad. Nauk SSSR, Otd. Tekhn. Nauk*, Vol. 8, p. 529 (1951).

4-8. K. H. Ardron and W. M. Bryce, "Assessment of Horizontal Stratification Entrainment Model in RELAP5/MOD2," United Kingdom Atomic Energy Authority, AEE Winfrith draft report AEEW-R 2345 (April 1988).

4-9. B. S. Massey, *Mechanics of Fluids*, D. Van Nostrand Co., New York (1968).

4-10. "Flow of Fluids through Valves, Fittings, and Pipes," Metric Edition-SI Units of the Crane Manual, Technical Paper No. 410M, Crane Co., New York (1977).

4-11. L. S. Tong and J. Weisman, *Thermal Analysis of Pressurized Water Reactors*, (American Nuclear Society, LaGrange Park, Illinois, 1979), 2nd Ed.

4-12. P. E. MacDonald and J. Weisman, "Effect of Pellet Cracking on Light Water Reactor Fuel Temperatures," *Nuclear Technology*, **31**, 357–366 (1976).

4-13. B. A. Boley and J. H. Weiner, *Theory of Thermal Stresses* (John Wiley and Sons, Inc., New York, 1960).

4-14. "American National Standard for Decay Heat in Light Water Reactors," American Nuclear Society publication ANSI/ANS-5.1 (1979).

4-15. J. J. Kaganove, "Numerical Solution of the One-Group Space-Independent Reactor Kinetics Equations for Neutron Density Given the Excess Reactivity," Argonne National Laboratory Report ANL-6132 (1960).

4-16. R. G. Steinke, V. Martinez, N. M. Schnurr, J. W. Spore, and J. V. Valdez, "TRAC-M Fortran 90 (Version 3.0) User's Manual," Los Alamos National Laboratory document LA-UR-00-835 (February 2000).

5.0. SPECIAL COMPONENT MODELS

Some 1D components in TRAC perform special functions that require modification of the solution of the 1D fluid equations. These modifications include the modeling of the behavior of pumps, valves, pressurizers, and accumulators. Also, a TRAC model of a reactor system requires appropriate boundary conditions, and it is often very useful to be able to connect several 1D components at a common point in a flow network.

The PUMP component produces a momentum source term in the form of an additional ΔP on the right-hand side of the momentum equation. The VALVE component has a variety of options to adjust the flow area at a user-specified cell face. The PRIZER component models a PWR pressurizer. PWR accumulators are modeled by special logic that is built into TRAC's PIPE component, which is triggered by one of two PIPE input options. (Note that the ACCUM component that was part of early versions of the TRAC series was removed from TRAC-PF1/MOD2, before TRAC-M development started.) The FILL and BREAK components provide boundary conditions to the normal 1D components by allowing the user to specify either flows (FILL) or pressures (BREAK) at the boundary, together with the fluid state if an inflow condition exists. The PLENUM component is a special, single-cell, 1D component that allows the user to connect as many normal 1D components as desired. To accomplish this objective, the PLENUM component interacts with the networking logic in the code and changes the form of the momentum flux terms.

Note: **ACCUM (Accumulator) and STGEN (Steam Generator) Components.** The ACCUM and STGEN components that were part of early versions of the TRAC series were removed from TRAC-PF1/MOD2, before TRAC-M development started. Steam generators can be modeled with a combination of PIPE, TEE, and HTSTR components. Accumulators can be modeled with special options that are built into the PIPE component. Guidelines for steam generator and accumulator modeling are given in the TRAC-M User's Manual (Ref. 5-8.). The modeling of steam generators does not involve special modification to TRAC's basic internal models. The PIPE component's special accumulator logic is described in this section and in more detail in Appendix J.

Note: **Separator (SEPD) and Turbine (TURB) Components.** The base code for both TRAC-M/F77 and TRAC-M/F90 had components to model steam/water separators (SEPD) and turbines (TURB). The TRAC-P SEPD component permits the user to specify the separation efficiency in such locations as the separator at the top of a normal U-tube steam generator. The TRAC-P SEPD component received minimal support over the years, and its general use was not, and is not, recommended. (It should be used with caution.) Both TRAC-M/F77, Version 5.5.2, and TRAC-M/F90 (Version 3.0), have an SEPD component that was brought over directly from TRAC-P, and the same caution applies. The separator capability will be improved in a future TRAC-M/F90 version. In the TURB component, energy is removed from the fluid as a result of work performed by the turbine. The turbine model calculates the momentum and

energy losses and the angular velocity as a function of the fluid flow rate, fluid properties, and turbine nozzle and blade geometry. These momentum and energy losses are subsequently subtracted from the TRAC momentum and energy equations, respectively. The TURB component received minimal support over its years in TRAC-P, and its general use was not, and is not, recommended. (It should be used with caution.) The TRAC-P TURB was brought over directly to TRAC-M. Currently, the TURB component is only available in TRAC-M/F77, and the same caution applies. The TRAC-P TURB has been removed entirely from TRAC-M/F90. An improved turbine modeling capability is to be included in a future TRAC-M/F90 version.

Note: **Future Versions of TRAC-M/F90.** Future versions of TRAC-M/F90 (post-Version 3.0) will include enhanced modeling capability, including BWR models and RELAP-5 style modeling. New components will include a vessel channel (CHAN) with leak paths, jet pump (JETP), heater, turbine (TURB, replacing the TRAC-P TURB), separator (SEPD, replacing the TRAC-P SEPD), and single-junction component (SJC, which will be used by the forthcoming leak path logic for the CHAN component and will facilitate RELAP-5-style modeling).

NOMENCLATURE

g:	gravitational acceleration
h:	normalized pump head
h_1:	normalized pump head from the single-phase performance curve
h_2:	normalized pump head from the fully degraded performance curve
H:	pump head
H_R:	rated pump head
H_1:	single-phase pump head
H_2:	fully degraded pump curve
I:	pump moment of inertia
$M(\alpha)$:	pump head degradation multiplier
$P_{dynamic}$:	dynamic pressure
P_{static}:	static pressure
q:	normalized pump volumetric flow
Q:	pump volumetric flow
Q_R:	rated pump volumetric flow
t:	time
T:	pump hydraulic torque acting on the impeller
T_f:	pump friction torque acting on the rotating parts of the motor
V_{inflow}:	inflow velocity (at BREAK boundary condition)

α: void fraction
ρ: density
ω: normalized pump speed
Ω: pump speed
Ω_R: rated pump speed
Ω_s: pump specific speed

5.1. Pump Component

The pump component in TRAC describes the momentum interaction between the coolant and the pump. The model calculates the pressure difference across the pump and the angular speed of the pump impeller and rotor as a function of the coolant flow rate and thermodynamic state. The modeling approach used in TRAC is the standard engineering method for TRAC applications and is used in the RELAP5 (Ref. 5-1.) and RETRAN (Ref. 5-2.) codes, as well as in TRAC. The model includes accounting for two-phase flow effects on pump performance. Relative to analysis of a LBLOCA in PWRs, the degradation of the pump under two-phase fluid-state conditions is the important aspect of the model. More detail on TRAC's PUMP model can be found in Appendix J, Section J.1.

5.1.1. Specific Speed

The similarity parameter that allows comparison of different pumps is the specific speed, Ω_s, given by

$$\Omega_s = \Omega Q^{1/2}/(gH)^{3/4} \quad , \tag{5-1}$$

where

Ω_s = pump specific speed,
Ω = pump speed,
Q = pump volumetric flow,
g = gravitational acceleration, and
H = pump head.

The specific speed is a constant for all similar pumps and ideally does not change as the pump speed changes. However, when comparing two pumps, the specific speed should be calculated at the point of highest operating efficiency.

The specific speed is presented to allow the user to determine that the built-in pump curves in TRAC are applicable to the system to which TRAC is to be applied. If the built-in performance curves are not appropriate for the user's system, the correct curves can be given as input to TRAC.

There are two sets of pump curves available in TRAC: the Semiscale Mod-1 system pump (Refs. 5-3. through 5-5.) and the LOFT system pump (Refs. 5-6. and 5-7.). We recommend that for full-scale pressurized-water-reactor (PWR) analyses, plant-specific pump curves be input. However, if those data are not available, the LOFT pump curves should be used.

5.1.2. Pump Head

The pump modeling in TRAC is based on the standard homologous-curves approach. These curves represent the performance of the pump in a normalized format, given the normalized pump head as a function of the normalized volumetric flow and normalized pump speed. That is, at higher pump speeds ($0 \le |q/\omega| \le 1$),

$$h/\omega^2 = f(q/\omega) \quad . \tag{5-2}$$

At low pump speed ($0 \le |\omega/q| < 1$), better results are obtained by using

$$h/q^2 = f(\omega/q) \quad . \tag{5-3}$$

In these equations, the normalized pump head is $h=H/H_R$, the normalized volumetric flow is $q=Q/Q_R$, and the normalized speed is $\omega=\Omega/\Omega_R$, where the subscript R refers to rated condition.

The normalized pump performance curves are input into TRAC as two sets of curves. One set describes the single-phase performance over the complete range of normal and off-normal operating conditions. The second set provides the same information for a reference two-phase state of the coolant. A head degradation multiplier also is used in the model. With the performance curves and head degradation factor, the pump head is obtained from

$$H = H_1 - M(\alpha)\,(H_1 - H_2) \quad , \tag{5-4}$$

where

H	=	pump head,
H_1	=	the single-phase pump head, $H_1 = h_1 H_R$,
H_2	=	the fully degraded pump curve, $H_2 = h_2 H_R$,
$M(\alpha)$	=	the head degradation multiplier,
α	=	void fraction,

and h_1 and h_2 are the normalized head values from the single-phase and fully degraded performance curves, respectively.

5.1.3. Pump Torque

Development of the homologous torque curves exactly parallels that just given for the pump head curves. The development is not repeated here, although this information can be found in Appendix J, Section J.1.

5.1.4. Pump Speed

The TRAC pump model holds the pump speed constant as long as the pump motor is energized. After a trip of the power to the pump motor, the pump speed will change according to the forces (torque) acting on the rotor. The balance of momentum applied to the motor rotor gives an equation for the rotor speed to be

$$I\,(\Omega/dt) = -\,(T + T_f)\ , \tag{5-5}$$

where

I = moment of inertia,
T = hydraulic torque acting on the impeller, and
T_f = friction torque acting on the rotating parts of the motor.

The hydraulic torque is obtained from the pump-performance curves, the frictional torque is represented by a third-order polynomial in the pump rotational speed, and the coefficients for the polynomial are input by the user.

The pump rotational speed may be represented by a table of input values instead of the dynamic model. For this case, the pump speed is constant at the initial input value until a trip condition is met. Following the trip, the speed is taken from the table. The user may specify a variety of signal variables in addition to time as the independent variable for the pump-speed table.

5.2. Boundary-Condition Components

The BREAK and FILL components are used to impose boundary conditions at any 1D hydraulic-component junction. Consequently, these components differ from the other hydraulic components in that they do not model any physical-system component, per se, and they do not perform any hydrodynamic or heat-transfer calculations; however, they are treated as any other component with respect to ID, input, and initialization.

The BREAK- and FILL-component-specified fluid pressure, gas volume fraction, fluid temperatures, noncondensable-gas partial pressure, and solute concentration in liquid define the properties of the fluid convected into the adjacent component if an inflow condition occurs. By convention, inflow to the adjacent component corresponds to a positive velocity at the FILL component's JUN2 junction and to a negative velocity at the BREAK component's JUN1 junction. A FILL or BREAK component may not be connected directly to a VESSEL component-source connection junction or a PLENUM component junction.

5.2.1. FILLS

A FILL component imposes a coolant-velocity or mass-flow boundary condition at the junction with its adjacent component. For example, the ECC injection or secondary-side feedwater may be modeled with a FILL component.

The velocity or mass-flow boundary condition, as well as its fluid properties, are specified by user input in one of three ways, according to the FILL-type IFTY option selected. For the first type, the homogeneous fluid velocity and fluid properties are specified; for the second type, the homogeneous fluid mass flow and fluid properties are specified; and for the third type, nonhomogeneous fluid velocities and fluid properties are specified. For each type, the relevant parameters may be constant, interpolated from input FILL-component action tables, constant until a controlling trip is set ON to require their evaluation from their action tables, or defined by signal-variable or control-block signals. The independent variable of the FILL table's tabular data is a signal-variable modeled-system parameter or a control-block output signal. When the FILL's coolant velocity or mass flow varies rapidly, using this value may lead to a hydrodynamic instability in the numerical solution. This can be avoided by using a TWTOLD-weighted average of the parameter's previous value and the current specified value or by limiting the parameter's time rate of change by RFMX. (All FILL input parameters are explained in the TRAC User's Manual, Ref. 5-8.)

Additional remarks on the TRAC FILL component are given in Appendix J, including a summary of general cautions on its use.

5.2.2. BREAKs

The BREAK component imposes a pressure boundary condition one cell away from its adjacent component. This component commonly is used to model the containment system in LOCA calculations or the coolant pressure at an outflow boundary of the modeled system. The pressure boundary condition, as well as the fluid properties associated with the BREAK cell for inflow donor-cell convection, may be specified by user input as constants, defined individually by signal variables or control blocks, or defined as tabular functions of a signal variable or control block. They can also be constant until a controlling trip is set ON and then evaluated based on the tabular-function BREAK tables while the controlling trip remains ON.

Inflow momentum flux from a BREAK cell is not modeled internally by TRAC because its contribution to the momentum-convection term of the junction-interface motion equation can be numerically unstable. The inflow momentum flux must be modeled by the user through input by defining a dynamic-pressure rather than a static-pressure boundary condition as

$$P_{dynamic} = P_{static} + \rho \cdot V_{inflow}^2/2 \ . \qquad (5\text{-}6)$$

Averaging the BREAK component's properties with those of its adjacent cell for their junction momentum cell can be eliminated by defining in the BREAK's user input a very small BREAK-cell DXIN length (weighting factor). The user also must input a very large

BREAK-cell volume or very small BREAK-cell length (for example, VOLIN = 10^{10} or DXIN = 10^{-10}) to model a very large inflow area (VOLIN/DXIN). Use of these BREAK input parameters is explained in the TRAC User's Manual (Ref. 5-8.).

Additional remarks on TRAC's BREAK component are given in Section 2.0. and in Appendix J, where general cautions on the use of the component are summarized.

5.3. PLENUM Component

The PLENUM component models the thermal hydraulics of a volume connected to an arbitrary number of 1D hydraulic components. The PLENUM is a single-cell component that the user can set up either as a momentum sink (where all inflow momentum is converted to a coolant pressure rise) and/or for convecting momentum across the cell from one side (having user-specified junctions) to the other side (also having user-specified junctions). The effect of an elevation change between the PLENUM cell and its adjacent-component junction cells is evaluated. There are single values for the coolant pressure, noncondensable-gas pressure, gas volume fraction, liquid temperature, vapor temperature, and solute concentration in the PLENUM cell. At each of its user-specified junctions, TRAC evaluates the standard 1D, two-fluid motion equations with the PLENUM-cell momentum flux either set to zero or convected across the cell in one direction, according to user specification. There is no requirement that the liquid and gas velocities be equal at a junction. The constitutive correlations will detect stratified flow at each PLENUM-cell junction if the momentum-cell mean coolant velocity falls below a threshold velocity and the elevation change falls below a threshold slope.

The user specifies a cell length at each PLENUM junction; these lengths need not be equal. TRAC uses the PLENUM-cell length for each junction in its motion equation solution for the junction. In particular, the GRAV elevation parameter at a given junction (input by the adjacent 1D hydraulic component) is defined in terms of the cell lengths from the adjacent-component cell and the PLENUM-cell junction.

Currently, TRAC does not allow HTSTR components to be coupled by convection heat transfer to a PLENUM cell. A PLENUM-component junction cannot be connected to a BREAK, FILL, PLENUM, or VESSEL component junction. Signal variables cannot define a PLENUM-cell parameter. If needed, the signal variable should be defined in the adjacent 1D hydraulic-component cell.

Additional remarks on TRAC's PLENUM component are given in Appendix J.

5.4. Pressurizer Component (PRIZER)

A PWR pressurizer is a large fluid-volume reservoir that maintains the coolant pressure within the reactor primary-coolant system and compensates for changes in the coolant volume caused by system transients. During normal operation, this reservoir contains the highest-energy fluid in the primary-coolant system. It is usually kept 50%–60% full of saturated liquid that is pressurized by saturated steam (vapor) above it.

The pressurizer controls the primary-coolant system pressure by hydraulic coupling through a long surge line connected to one of the PWR hot legs.

TRAC's PRIZER component simulates the PWR pressurizer. Normally, the PRIZER models only the pressurizer reservoir, with the connecting surge line modeled by a PIPE or TEE component. The PRIZER component may be connected at both its junctions to other 1D hydraulic components.

For TRAC steady-state calculations, the PRIZER component is replaced automatically with the equivalent of a BREAK component at each of its junctions. User-specified thermal-hydraulic conditions in the PRIZER component during steady-state calculations remain unchanged except for the component's wall temperature, which is calculated by conduction heat transfer to obtain a steady-state, wall temperature profile.

Additional details on TRAC's PRIZER component are given in Appendix J.

5.5. VALVE Component

The VALVE component is used to model various types of valves associated with light-water reactors (LWRs). The valve action is modeled by adjustment of the flow area and form loss at a user-specified cell interface of a 1D (PIPE-like) hydraulic component.

The adjustable flow area of the VALVE component can be specified in two basic ways. The flow area can be computed directly from an adjustable flow-area fraction and a user-specified fully open flow area. In the second form, the flow area is calculated from the relative position of the valve stem, where a guillotine-like blade is assumed to cut a circular cross-section flow channel with a user-specified fully open area.

Many different types of valves can be modeled because of the flexibility to choose the independent variable of VALVE component-action tables and to perform table evaluation under trip control. These include simple valves to model pipe breaks or the opening of rupture disks, check valves, power-operated relief valves, banks of power-operated relief valves, steam-flow control valves, turbine stop valves, turbine bypass valves, main-steam isolation valves, safety relief valves, and atmospheric dump valves. Guidelines for valve modeling are given in the TRAC-M User's Manual (Ref. 5-8.).

The VALVE component's adjustable flow area may not be located at a VALVE-component junction unless that junction is connected to a BREAK component.

The VALVE closure state adjustment is made with a step change at the beginning of a hydrodynamic time step; the VALVE state is held constant during the time step.

Additional details on TRAC's VALVE component are given in Appendix J.

5.6. Accumulator Option in PIPE Component

A PWR accumulator can be modeled by use of special logic that is built into the PIPE component. This logic, when triggered by user input, evaluates a gas/liquid interface sharpener and (optionally) prevents gas outflow with a liquid separator model. To allow the accumulator-like behavior to be measured, TRAC calculates water level, volumetric flow, and liquid volume discharged from the component.

Additional details on the PIPE component accumulator model are given in Appendix J.

REFERENCES

5-1. K. E. Carlson, R. A. Riemke, S. Z. Rouhani, R. W. Shumway, and W. L. Weaver, "RELAP5/MOD3 Code Manual — Volume 1: Code Structure, System Models, and Solution Methods," Idaho National Engineering Laboratory report NUREG/CR-5535, EGG-2596 (Draft) (June 1990).

5-2. J. H. McFadden, M. P. Paulsen, G. C. Gose, C. E. Peterson, P. J. Jensen, J. A. McClure, J. L. Westacott, and J. G. Shatford, "RETRAN-3D — A Program for Transient Thermal-Hydraulic Analysis of Complex Fluid-Flow Systems, Volume 1: Theory and Numerics," Computer Simulation and Analysis, Inc. report NP-7450, Volume 1, Revision 1 (January 1996).

5-3. D. J. Olson, "Experimental Data Report for Single– and Two–Phase Steady–State Tests of the 1-1/2-Loop Mod-1 Semiscale System Pump," Aerojet Nuclear Company ANCR–1150 (May 1974).

5-4. G. G. Lomis, "Intact Loop Pump Performance During the Semiscale MOD-1 Isothermal Test Series," Aerojet Nuclear Company ANCR–1240 (October 1975).

5-5. D. J. Olson, "Single– and Two–Phase Performance Characteristics of the MOD-1 Semiscale Pump under Steady–State and Transient Fluid Conditions," Aerojet Nuclear Company ANCR–1150 (October 1974).

5-6. D. L. Reeder, "LOFT System and Test Description (5.5-Ft. Nuclear Core 1 LOCES)," EG&G Idaho, Inc. TREE–1208 (NUREG/CR–0247) (July 1978).

5-7. US Nuclear Regulatory Commission memorandum, L. E. Phillips to U. S. Standard Problem Participants, Subject: Additional Information for Prediction of LOFT L2–3 (March 1979).

5-8. R. G. Steinke, V. Martinez, N. M. Schnurr, J. W. Spore, and J. V. Valdez, "TRAC-M Fortran 90 (Version 3.0) User's Manual," Los Alamos National Laboratory document LA-UR-00-835 (February 2000).

6.0. SUMMARY

This document consists of many individual, complete descriptions that, in themselves, stand alone. The presence of the field equations, numerical methods, and the flow-regime map provides a cohesive thread linking all of the parts into a whole.

We believe that the document is structured well enough to permit the reader to find readily the discussion of any closure relation or other model contained in TRAC-M. Section 2.0. describes the numerical methods used in the code to solve all of the equations. Section 3.0. provides a basic description of TRAC-M's closure relations (including a "roadmap" that relates the closure relations to the hydrodynamic field equations), which are described in further detail in the appendices to this document (Appendices D through H).

Section 3.2. describes the basic flow-regime map that forms the basis for linking correlations into models spanning a wide variety of flow conditions. Each collection of related correlations and models, whether they describe interfacial shear or interfacial heat transfer or wall heat transfer, etc., modifies the basic map to account for the amount of knowledge available about a given phenomenon. Generally, the more detailed the knowledge is concerning a particular phenomenon, the more detailed the flow regimes must be. Section 3.3. describes TRAC-M's logic for calculation of flow-regime-dependent interfacial area.

Section 3.4. describes the code's interfacial mass transfer. Sections 3.5., 3.6., 3.7., and 3.8. cover the interfacial drag, the wall drag, the interfacial heat transfer, and the wall heat transfer, respectively. Each section (and related appendix) clarifies the modifications required to the basic flow-regime map for each process. Section 4.0. and Appendix I describe those models that are not component-oriented (in the TRAC-M sense of components) and that generally have an impact on the momentum equation and/or interfacial drag. Three main examples of these models are critical flow, CCFL, and form loss. Section 5.0. and Appendix J cover the special TRAC-M components with specific functions that are not available in other TRAC-M components (e.g., the PUMP component). Appendices A and B cover the code's thermodynamic and transport fluid properties, and material properties, respectively. Appendix K provides the thermodynamic and transport properties for the noncondensable-gas field and the solubility of the liquid solute. Discussions of the noncondensable-gas and liquid-solute effects on other models are provided as appropriate with each model. Appendix L describes fuel-cladding gap conductance and the metal-water reaction model. Appendix M describes in detail the reactor-core power model. Finally, Appendix N gives details on the code's control procedure, including signal variables, control blocks, and trips. Whereas we have tried to state explicitly when the code lacks a model or ignores an effect, the reader should assume that if an aspect or effect of something is not discussed, the code does not consider it.

The level of quality in the code is fairly uniform in that there are no big surprises lurking in the correlations, models, and logic. We expected this general level of quality because

of the long-term development program that always built on the preceding code version and because of the large variety of applications and assessments of the code over the years. This process has resulted in a mature code that is generally not susceptible to the major problems that plagued earlier versions. The development and application history of the code is summarized in the introduction in Section 1.0.

The TRAC-M code invests most of its resources in solving the thermal-hydraulic problem of the fluid. For the most part, the solution of energy generation and conduction within solid structures is straightforward. The basic problem of the thermal hydraulics is to calculate the liquid inventory and its distribution. At PWR scale, the interfacial drag has a significant impact on the calculation of the inventory distribution. Also, interfacial condensation can set up pressure gradients that can move significant amounts of liquid. The correlations that govern interfacial drag and interfacial heat and mass transfer have generally performed well even though the results in Appendices F, (Section F.1.), G, and H, (Section H.1.) show some deficiencies in the models; certain isolated analysis results relate directly to the deficiencies. In some cases for integral experiments, the biggest problem is to identify the correct flow regime on which to base the interfacial interactions. As can be seen by the application of TRAC-M/F77 to UPTF tests in that code's Developmental Assessment Manual (Refs. 6-1. and 6-2.), the interfacial models are more than adequate for full-scale geometry.

Although the TRAC-M flow-regime maps are simple, comparisons to data indicate adequate accuracy. Additional accuracy has been attempted by modifying the basic TRAC-M flow regime within components where the data indicate that modifications are necessary (i.e., lower plenum, downcomer, etc.).

Although we do not believe that we have found the best available correlations and/or model for each closure relation in all cases, we do believe that we have found a set of closure correlations and/or models that work well with the TRAC-M numerics and result in a computer code that can be used as a tool in the hands of a knowledgeable engineer or scientist to investigate and simulate many transients in PWRs. This document supports the application of the code and aids in understanding the calculated results. The code structure and numerics are sound, although some changes can be made to take better advantage of new computer architecture and new advances in numerical techniques. However, we believe that as research continues in the area of two-phase flow and heat transfer, advances in modeling flow regimes and interfacial phenomena will continue. Therefore, improvements can be obtained in TRAC-M's ability to accurately model a wide range of flows and geometries.

Future versions of this TRAC-M/F90 Theory Manual will address TRAC-M/F90's capabilities, which are now under development, for analysis of BWRs.

REFERENCES

6-1. B. E. Boyack, J. F. Lime, D. A. Pimental, J. W. Spore, and J. L. Steiner, "TRAC-M/F77, Version 5.5, Developmental Assessment Manual, Volume I: Assessment Sections not Including 2D/3D Tests," Los Alamos National Laboratory document LA-UR-99-6480 (December 1999).

6-2. B. E. Boyack, J. F. Lime, D. A. Pimental, J. W. Spore, and J. L. Steiner, "TRAC-M/F77, Version 5.5, Developmental Assessment Manual, Volume II: Assessment Sections for 2D/3D Tests," Los Alamos National Laboratory document LA-CP-99-345 (December 1999).

APPENDIX A

THERMODYNAMIC AND TRANSPORT FLUID PROPERTIES

The thermodynamic- and transport-properties subroutines used in TRAC are based on polynomial fits to steam-table data for water, and on ideal gas behavior for the noncondensable-gas component. Transport property fits were obtained from Ref. A-1. All TRAC component modules use the same property routines. Table A-1. through A-11., which list the values of the constants used to obtain property values, are provided throughout this appendix.

NOMENCLATURE

c_p:	constant-pressure specific heat ($J \cdot kg^{-1} \cdot K^{-1}$)
c_v:	constant-volume specific heat ($J \cdot kg^{-1} \cdot K^{-1}$)
e:	internal energy
ELP:	change in energy required to move along the isotherm at T_ℓ between two different pressure values
h:	enthalpy
h_{fg}:	latent heat of vaporization
h_{fgs}:	enthalpy of evaporation
k:	thermal conductivity
M:	numerical constant
p:	pressure (Pa)
PSL:	saturation pressure corresponding to T_ℓ
R:	gas constant ($J \cdot kg^{-1} \cdot K^{-1}$)
T:	temperature (K)
v:	specific volume
γ:	ratio of specific heats
μ:	viscosity
ρ:	density
σ:	surface tension

Subscripts

a:	noncondensable gas
approx:	approximate
critical:	critical
g:	gas
ideal:	ideal gas behavior

ℓ: liquid

m: steam-gas mixture

sat, s: saturation

v: steam

A.1. Thermodynamic Properties

Subroutine THERMO supplies thermodynamic properties for TRAC. The input variables are the total pressure; the partial pressure of the noncondensable gas, if any is present; and the liquid- and gas-phase temperatures, where the gas phase is either steam, a noncondensable gas, or a steam-gas mixture. The output variables include the saturation temperature corresponding to the total pressure and its derivative with respect to the total pressure; the saturation temperature corresponding to the partial pressure of steam and its derivative with respect to the steam partial pressure; the internal energies and densities of the liquid and gas phases, and their partial derivatives with respect to pressure (at constant temperature) and with respect to temperature (at constant pressure); and, finally, the saturated liquid and saturated steam enthalpies and their derivatives with respect to pressure.

THERMO supplies thermodynamic properties valid for temperatures and pressures within the following ranges:

$$273.15\ \text{K} \le T_\ell \le 713.94025779311\ \text{K} \quad ,$$

$$273.15\ \text{K} \le T_g \le 3000.0\ \text{K} \quad ,$$

and

$$1.0\ \text{Pa} \le p \le 45.0 \times 10^6\ \text{Pa}.$$

If THERMO is provided with data outside this range, it adjusts the data to the corresponding limit and issues a warning message.

Equations for the various properties used in THERMO are given below. Tables A-1. through A-6. list the values of the constants.

A.1.1. Saturation Properties

A.1.1.1. Relationship Between Saturation Temperature and Pressure. Subroutine SATPRS calculates the saturation pressure for a given temperature, while subroutine SATTMP calculates the saturation temperature for a given pressure. Subroutine SATDER evaluates the derivative of saturation temperature with respect to saturation pressure when given the values of the saturation temperature and pressure. Four temperature and pressure regions are used to evaluate the saturation pressure, saturation

temperature, and derivative of saturation temperature with respect to saturation pressure.

A.1.1.1.1. 610.8 Pa $\leq p_s <$ 90.56466 $\times 10^3$ Pa and 273.15 K $\leq T_s <$ 370.4251 K.
In subroutine HEV, a linear function of temperature accurately represents the enthalpy of evaporation $h_{\ell vs}$, such that

$$h_{\ell vs} = 3180619.59 - 2470.2120\, T_s$$

for all $T_s \leq 425.01$ K (corresponding to all $p_s \leq 0.5 \times 10^6$ Pa). The Clausius-Clapeyron equation, which assumes that steam is an ideal gas and neglects liquid volume compared to steam volume, can be written as

$$\frac{dp_s}{dT_s} = \frac{h_{\ell vs} p_s}{R_v T_s^2} \quad ,$$

where R_v is the gas constant for steam (Table A-1.). Substituting for $h_{\ell vs}$ and integrating using the boundary condition $p_s = 24821$ Pa at $T_s = 338$ K, gives

$$p_s = 24821.0(T_s / 338.0)^{-5.3512} \exp\,[20.387(T_s - 338.0)/T_s] \quad .$$

TRAC calculations also require determination of T_s from a given p_s, which can only be calculated by trial and error from the above equation. A simplified logic for calculating T_s is used that guarantees solution in two iterations with an error of only a fraction of a percent. First, an approximate value of T_s is calculated from

$$T_{s,\,\text{approx}} = \frac{-2263.0}{0.434 \ell n(p_s/100000.0) - 6.064} \quad ,$$

which gives $T_{s,\text{approx}}$ within a few degrees of the actual value. Integration of the Clausius-Clapeyron equation, assuming constant $h_{\ell vs}$ between $T_{s,\text{approx}}$ and T_s, calculates the first iteration value of T_s to be

$$T_s = \frac{T_{s,\text{approx}}}{1 - \frac{R_v T_{s,\text{approx}}}{h_{\ell vs,\text{approx}}} \ell n\left(\frac{p_s}{p_{s,\text{approx}}}\right)} \quad .$$

The resulting T_s value is then input into this equation again as the new $T_{s,\text{approx}}$ value. Both $h_{\ell vs,\text{approx}}$ and $p_{s,\text{approx}}$ are calculated corresponding to $T_{s,\text{approx}}$ using the equations given above.

TABLE A-1.
Ideal Gas Constants

R_v	=	461.4975 [J/(kg·K)]	R_a	=	287.0516 [J/(kg·K)] for air 4124.2988 [J/(kg·K)] for hydrogen
g_{ideal}	=	1.3			2077.2345 [J/(kg·K)] for helium
$c_{pv,ideal}$	=	$\frac{\gamma_{ideal} R_v}{\gamma_{ideal} - 1}$	c_{pa}	=	1004.832 [J/(kg·K)] for air 14533.2 [J/(kg·K)] for hydrogen 5193.086 [J/(kg·K)] for helium
$c_{vv,ideal}$	=	$\frac{R_v}{\gamma_{ideal} - 1}$	c_{va}	=	$c_{pa} - R_a$

Inverting the Clausius-Clapeyron equation allows the derivative of the saturation temperature with respect to the saturation pressure to be evaluated, such that

$$\frac{dT_s}{dp_s} = \frac{R_v T_s^2}{h_{\ell vs} p_s} \quad .$$

Note: For values of p_s such that

$$1.0 \text{ Pa} \leq p_s < 610.8 \text{ Pa} \quad ,$$

subroutines SATTMP and SATDER reset the value of p_s to 610.8 Pa, and proceed with the calculation of T_s and dT_s/dp_s.

A.1.1.1.2. 90.56466×10^3 Pa $\leq p_s <$ $13.969971285053 \times 10^6$ Pa and $370.4251 \leq T_s <$ 609.62462615967 K. Ref. A-2. recommends using the following relationships between saturation temperature and pressure within this range:

$$p_s = 1.0 \times 10^5 \left(\frac{T_s - 255.2}{117.8} \right)^{\frac{1}{0.223}} \quad ,$$

$$T_s = 117.8 \left(1.0 \times 10^{-5} p_s \right)^{0.223} + 255.2 \quad ,$$

and

$$\frac{dT_s}{dp_s} = \frac{0.223(T_s - 255.2)}{p_s} \quad .$$

A.1.1.1.3. $13.969971285053 \times 10^6$ Pa $\leq p_s <$ 22.12×10^6 Pa and 609.62462615967 K $\leq T_s <$647.3 K. The relationships given below are based on an equation-of-state of the form

$$\ell n(p_r) = a + \frac{b}{T_r} + \frac{c}{T_r^2} \quad .$$

In the above relation,

$$p_r = \frac{p_s}{p_{\text{critical}}}$$

and

$$T_r = \frac{T_s}{T_{\text{critical}}} \quad ,$$

where p_s and T_s are the saturation pressure and temperature and p_{critical} and T_{critical} are the critical pressure and temperature (Ref. A-3.). These relationships were formulated to provide a good fit to the data and to provide a smooth transition between the preceding and the following temperature and pressure ranges:

$$p_s = 7.2166948490268 \times 10^{11} \exp\left(\frac{-8529.6481905883 + \frac{1166669.3278328}{T_s}}{T_s}\right) \quad ,$$

$$T_s = \frac{4264.8240952941 + \sqrt{-13666986.708428 + 1166669.3278328\ \ell n\ p_s}}{27.304833093884 - \ell n\ p_s} \quad ,$$

and

$$\frac{dT_s}{dp_s} = \frac{-T_s^2}{p_s\left(-8529.6481905883 + \frac{2333338.6556656}{T_s}\right)} \quad .$$

A.1.1.1.4. 22.12×10^6 Pa $\leq p_s \leq 45.0 \times 10^6$ Pa and 647.3 K $\leq T_s \leq$ 713.94025779311 K. The relationships given below are based on an equation-of-state of the form

$$\frac{d[\ell n(p_r)]}{d\left[\ell n\left(\frac{1}{T_r}\right)\right]} = M \quad ,$$

where p_r and T_r are defined as in the previous pressure and temperature range and M is a constant (Ref. A-3.):

$$p_s = 22.12 \times 10^6 \exp\left(7.6084087 - \frac{4924.9229}{T_s}\right) ,$$

$$T_s = \frac{4924.9229}{24.520401 - \ell n(p_s)}$$

and

$$\frac{dT_s}{dp_s} = \frac{2.0304886238506 \times 10^{-4}\ T_s^2}{p_s} \quad .$$

A.1.1.2. Saturated Steam Internal Energy. Two main pressure regions exist when calculating the internal energy of steam at saturation, e_{vs}, and the derivative of e_{vs}, with respect to the partial pressure of steam, p_v. In this section, T_{sv} denotes the saturation temperature corresponding to p_v.

A.1.1.2.1. 1.0 Pa $< p_v <$ 0.5 $\times 10^6$ Pa.

$$e_{vs} = h_{vs} - \frac{p_v}{\rho_{vs}} = h_{vs} - R_v T_{sv}$$

and

$$\frac{de_{vs}}{dp_v} = \frac{dh_{vs}}{dp_v} - R_v \frac{dT_{sv}}{dp_v} \quad ,$$

where h_{vs} and $\frac{dh_{vs}}{dp_v}$ are calculated as described in Section A.1.1.4. for the same pressure range, 1.0 Pa $\leq p_v \leq 0.5 \times 10^6$ Pa.

A.1.1.2.2. 0.5×10^6 **Pa**$< p_v \leq 45.0 \times 10^6$ **Pa.** A sequence of polynomials in the partial pressure of steam, p_v, is used to calculate e_{vs} and de_{vs}/dp_v as

$$e_{vs} = AVE(i) + BVE(i)\, p_v + CVE(i)\, p_v^2 + DVE(i)\, p_v^3$$

and

$$\frac{de_{vs}}{dp_v} = BVE(i) + 2\, CVE(i)\, p_v + 3\, DVE(i)\, p_v^2 \quad ,$$

where

$i = 1$ for $0.5 \times 10^6 < p_v \leq 2.0 \times 10^6$ Pa ,
$i = 2$ for $2.0 \times 10^6 < p_v < 5.0 \times 10^6$ Pa ,
$i = 3$ for $5.0 \times 10^6 \leq p_v < 10.0 \times 10^6$ Pa ,
$i = 4$ for $10.0 \times 10^6 \leq p_v < 15.0 \times 10^6$ Pa ,
$i = 5$ for $15.0 \times 10^6 \leq p_v < 20.0 \times 10^6$ Pa ,
$i = 6$ for $20.0 \times 10^6 \leq p_v \leq 22.0 \times 10^6$ Pa ,
$i = 7$ for $22.0 \times 10^6 < p_v < 25.0 \times 10^6$ Pa ,
$i = 8$ for $25.0 \times 10^6 \leq p_v < 30.0 \times 10^6$ Pa ,
$i = 9$ for $30.0 \times 10^6 \leq p_v < 35.0 \times 10^6$ Pa ,
$i = 10$ for $35.0 \times 10^6 \leq p_v < 40.0 \times 10^6$ Pa , and
$i = 11$ for $40.0 \times 10^6 \leq p_v \leq 45.0 \times 10^6$ Pa .

Table A-2. lists the constants *AVE(i)*, *BVE(i)*, *CVE(i)*, and *DVE(i)* for the given pressure ranges.

Function de_{vs}/dp_v is discontinuous near the critical point at junction point $p_v = 22.0 \times 10^6$ Pa. At this point the left-side value of the function is 4.37931×10^{-3} while the right-side value is 0.0, giving a fractional change across the junction point of 1.00.

A.1.1.3. Saturated Liquid Internal Energy. A sequence of polynomials in the saturated liquid temperature, T_{sat}, is used to calculate the internal energy of saturated liquid, $e_{\ell s}$, and its derivatives with respect to T_{sat}. We use

$$e_{\ell s} = ALE(i) + BLE(i)\, T_{sat} + CLE(i)\, T_{sat}^2 + DLE(i)\, T_{sat}^3$$

TABLE A-2.
Saturated Steam Internal Energy Constants

i	*AVE(i)*	*BVE(i)*	*CVE(i)*	*DVE(i)*
1	2.4949771766385E+06	2.0855856331827E–01	– 1.3553894579716E–07	2.8522684989198E–14
2	2.5600870370371E+06	3.1086111111026E–02	–6.8988888888580E–09	4.3203703703379E–16
3	2.5915500000006E+06	8.7749999997567E–03	–1.7499999999663E–09	4.2999999998503E–17
4	2.6606000000024E+06	–1.3545000000581E–02	6.4250000004682E–10	–4.2100000001248E–17
5	3.8201600000097E+06	–2.3019900000170E–01	1.4068900000098E–08	–3.1786000000187E–16
6	–1.2103411633350E+08	1.8018803375785E+01	–8.7442426507726E–07	1.4091076856088E–14
7	2.2000000000000E+06	0.	0.	0.
8	2.2000000000000E+06	0.	0.	0.
9	2.2000000000000E+06	0.	0.	0.
10	2.2000000000000E+06	0.	0.	0.
11	2.2000000000000E+06	0.	0.	0.

and

$$\frac{de_{\ell s}}{dT_{sat}} = BLE(i) + 2\,CLE(i)\,T_{sat} + 3\,DLE(i)\,T_{sat}^2 \quad ,$$

where

$i = 1$ for $273.15 \leq T_{sat} <$ 423.15 K ,
$i = 2$ for $423.15 \leq T_{sat} <$ 473.15 K ,
$i = 3$ for $473.15 \leq T_{sat} <$ 523.15 K ,
$i = 4$ for $523.15 \leq T_{sat} <$ 573.15 K ,
$i = 5$ for $573.15 \leq T_{sat} <$ 623.15 K ,
$i = 6$ for $623.15 \leq T_{sat} \leq$ 645.15 K ,
$i = 7$ for $645.15 < T_{sat} <$ 673.15 K , and
$i = 8$ for $673.15 \leq T_{sat} \leq$ 713.94025779311 K .

Table A-3. lists the constants *ALE(i)*, *BLE(i)*, *CLE(i)*, and *DLE(i)* for the given temperature ranges.

TABLE A-3.
Saturated Liquid Internal Energy Constants

i	*ALE(i)*	*BLE(i)*	*CLE(i)*	*DLE(i)*
1	–1.1436668993222E+06	4.1868000000000E+03	0.	0.
2	8.0957542810383E+06	–5.7008855264640E+04	1.3443632119671E+02	–9.7879669155946E–02
3	–1.9373932457007E+06	9.7492797103351E+03	–1.3299615999876E+01	1.0879999999922E–02
4	–5.3245827703670E+06	2.9179372045334E+04	–5.0452192000967E+01	3.4560000000583E–02
5	–6.3583523639930E+07	3.2873715263424E+05	–5.6371182000208E+02	3.2760000000116E–01
6	–6.6239163195929E+09	3.1605562257270E+07	–5.0263730855532E+04	2.6650075114186E+01
7	–5.4759091078157E+09	2.4635618770681E+07	–3.6931079506707E+04	1.8454719393083E+01
8	–7.1536399439453E+07	3.0560801674842E+05	–4.2424553999630E+02	1.9719999999823E–01

A.1.1.4. Saturated Steam Enthalpy. Two main pressure regions exist when the enthalpy of steam at saturation is calculated. T_{sv} in this section denotes the saturation temperature corresponding to the partial pressure of steam, p_v.

A.1.1.4.1. $1.0\ \text{Pa} \le p_v \le 0.5 \times 10^6\ \text{Pa}$. Within this pressure region, the enthalpy of saturated steam at temperature T_{sv} is approximated as the sum of the enthalpy of saturated liquid water at the reference temperature of 273.15 K, plus the enthalpy necessary to raise the saturated liquid water temperature from 273.15 K to T_{sv}, plus the latent heat of vaporization needed to convert saturated liquid water at T_{sv} to saturated steam at T_{sv}. If we define the enthalpy of saturated water at 273.16 K to be exactly zero, this gives

$$h_{vs} = 4186.8(273.15 - 273.16) + 4186.8\,(T_{sv} - 273.15) + h_{\ell vs} \quad ,$$

where $h_{\ell vs}$ is evaluated at T_{sv} in subroutine HEV as described earlier in Section A.1.1.1. The derivative with respect to the partial pressure of the vapor, p_v, becomes

$$\frac{dh_{vs}}{dp_v} = 4186.8\,\frac{dT_{sv}}{dp_v} + \frac{dh_{\ell vs}}{dp_v} = (4186.8 - 2470.2120)\,\frac{dT_{sv}}{dp_v} \quad .$$

A.1.1.4.2. $0.5 \times 10^6\ \text{Pa} < p_v \le 45.0 \times 10^6\ \text{Pa}$.

$$h_{vs} = e_{vs}\gamma_s$$

and

$$\frac{dh_{vs}}{dp_v} = \gamma_s \frac{de_{vs}}{dp_v} + e_{vs} \frac{d\gamma_s}{dp_v} \quad ,$$

where

$$\gamma_s = AVG(i) + BVG(i)\, p_v + CVG(i)\, p_v^2 + DVG(i)\, p_v^3 \, ,$$

$$\frac{d\gamma_s}{dp_v} = BVG(i) + 2\, CVG(i)\, p_v + 3\, DVG(i)\, p_v^2 \quad ,$$

and

$i = 1$ for $0.5 \times 10^6 < p_v \leq 2.0 \times 10^6$ Pa ,
$i = 2$ for $2.0 \times 10^6 < p_v < 5.0 \times 10^6$ Pa ,
$i = 3$ for $5.0 \times 10^6 \leq p_v < 10.0 \times 10^6$ Pa ,
$i = 4$ for $10.0 \times 10^6 \leq p_v < 15.0 \times 10^6$ Pa ,
$i = 5$ for $15.0 \times 10^6 \leq p_v < 20.0 \times 10^6$ Pa ,
$i = 6$ for $20.0 \times 10^6 \leq p_v \leq 22.0 \times 10^6$ Pa ,
$i = 7$ for $22.0 \times 10^6 < p_v < 25.0 \times 10^6$ Pa ,
$i = 8$ for $25.0 \times 10^6 \leq p_v < 30.0 \times 10^6$ Pa ,
$i = 9$ for $30.0 \times 10^6 \leq p_v < 35.0 \times 10^6$ Pa ,
$i = 10$ for $35.0 \times 10^6 \leq p_v < 40.0 \times 10^6$ Pa , and
$i = 11$ for $40.0 \times 10^6 \leq p_v \leq 45.0 \times 10^6$ Pa .

Table A-4. lists the constants *AVG(i)*, *BVG(i)*, *CVG(i)*, and *DVG(i)* for the given pressure ranges.

Functions h_{vs}/dp_v and $d\gamma_s/dp_v$ are both discontinuous near the critical point at junction point $p_v = 22.0 \times 10^6$ Pa. At this point, the left-side value of h_{vs}/dp_v is 4.6073×10^{-3} and the right-side value is -5.1790×10^{-6} for a fractional change here of 1.0011. The left-side value of $d\gamma_s/dp_v$ is 6.6694×10^{-12} and the right-side value is -2.3541×10^{-2} giving a fractional change at this junction point of 1.3530.

TABLE A-4.
Saturated Steam Enthalpy Constants

i	*AVG(i)*	*BVG(i)*	*CVG(i)*	*DVG(i)*
1	1.0666845123419E+00	2.8310838172462E–08	–2.1151097428905E–14	4.7404001285964E–21
2	1.0735412407407E+00	2.6518055555551E–09	–6.3461111111128E–16	3.9824074074117E–23
3	1.0777730000000E+00	–2.4300000008021E–11	–7.1979999998378E–17	4.8799999990422E–25
4	1.0851130000007E+00	–1.9307000001824E–09	8.9100000014826E–17	–3.8960000003946E–24
5	1.1639800000015E+00	–1.6338350000254E–08	9.5856000001448E–16	–2.1194000000274E–23
6	3.8898867259868E+00	–3.8595945559811E–07	1.7476370114910E–14	–2.6377008249858E–22
7	2.7168710524682E+00	–2.2832718294604E–07	1.0417331983836E–14	–1.5842822199773E–22
8	3.9749829999964E+00	–3.0657099999960E–07	1.0637899999985E–14	–1.2257999999981E–22
9	1.2946929999997E+00	–2.4834999999979E–08	7.8979999999944E–16	–8.0799999999948E–24
10	1.0590519999963E+00	–2.4615999996941E–09	8.8399999991573E–17	–8.0799999992269E–25
11	1.1430199999838E+00	–7.7095999988588E–09	1.9335999997331E–16	–1.4639999997924E–24

A.1.1.5. Saturated Liquid Enthalpy. From the definition of enthalpy,

$$h_{\ell s} = e_{\ell s} + \frac{p}{\rho_{\ell s}}$$

and

$$\frac{dh_{\ell s}}{dp} = \frac{de_{\ell s}}{dT_{sat}} \frac{dT_{sat}}{dp} + \frac{1}{\rho_{\ell s}} - \frac{p}{\rho_{\ell s}^2} \left[\left(\frac{\partial \rho_{\ell s}}{\partial p} \right)_{T_{sat}} + \left(\frac{\partial \rho_{\ell s}}{\partial T_{sat}} \right)_p \frac{dT_{sat}}{dp} \right] ,$$

where $e_{\ell s}$ and its derivative are evaluated as shown in Section A.1.1.3., and where $\rho_{\ell s}$ and its derivatives are evaluated using the equations in Section A.1.2.2. with T_ℓ equal to T_{sat}.

A.1.1.6. Heat Capacity of Saturated Steam at Constant Pressure. Although the heat capacity of saturated steam is not an output variable of THERMO, subsequent steam property calculations require its definition. In this section, T_{sv} denotes the saturation temperature corresponding to the partial pressure of steam, p_v. The heat capacity of saturated steam is

$$c_{pvs} = ACP(i) + BCP(i)\, T_{sv} + CCP(i)\, T_{sv}^2 + DCP(i)\, T_{sv}^3$$

and

$$\frac{dc_{pvs}}{dp_v} = \left[BCP(i) + 2\,CCP(i)\,T_{sv} + 3\,DCP(i)\,T_{sv}^2\right]\frac{dT_{sv}}{dp_v} \quad ,$$

where

$i = 1$ for $273.15 \leq T_{sv} < 323.15$ K ,
$i = 2$ for $323.15 \leq T_{sv} < 373.15$ K ,
$i = 3$ for $373.15 \leq T_{sv} < 423.15$ K ,
$i = 4$ for $423.15 \leq T_{sv} < 473.15$ K ,
$i = 5$ for $473.15 \leq T_{sv} < 523.15$ K ,
$i = 6$ for $523.15 \leq T_{sv} < 573.15$ K ,
$i = 7$ for $573.15 \leq T_{sv} < 623.15$ K ,
$i = 8$ for $623.15 \leq T_{sv} < 647.3$ K ,
$i = 9$ for $647.3 < T_{sv} < 673.15$ K , and
$i = 10$ for $673.15 \leq T_{sv} < 713.94025779311$ K .

Table A-5. lists the constants *ACP(i), BCP(i), CCP(i), and DCP(i)* for the given temperature ranges.

TABLE A-5.
Saturated Steam Heat Capacity Constants

i	*ACP(i)*	*BCP(i)*	*CCP(i)*	*DCP(i)*
1	–7.9678485852270E+02	2.8187658437259E+01	–1.0180624999920E–01	1.2499999999912E–04
2	–9.7082632232795E+02	2.8324981030402E+01	–9.7656200001157E–02	1.1600000000110E–04
3	–1.6649701690752E+03	3.3159363169596E+01	–1.0861179999898E–01	1.2399999999915E–04
4	–6.1420486441088E+03	6.3630987079837E+01	–1.7762319999965E–01	1.7599999999975E–04
5	–8.2289951961933E+04	5.3773958896061E+02	–1.1612491999609E+00	8.5599999997375E–04
6	–6.5842104212475E+05	3.7934294783212E+03	–7.2924928000022E+00	4.7040000000014E–03
7	3.4561620732510E+05	–2.2129380791446E+02	–2.4524285999925E+00	3.1479999999958E–03
8	1.9798369474597E+06	–1.4782551342826E+04	3.1656481897637E+01	–2.0843356864237E–02
9	–9.6249385211359E+07	4.3633668884423E+05	–6.5887615106930E+02	3.3146147264269E–01
10	–1.1074934463333E+07	4.8073794630970E+04	–6.9212173247881E+01	3.3091693999800E–02

A.1.2. Liquid Properties

A.1.2.1. Internal Energy. Given a liquid at some temperature, T_ℓ, and some pressure, p, the liquid internal energy associated with that state is calculated by beginning with the internal energy of the saturated liquid state described by T_ℓ and PSL, where PSL is the saturation pressure corresponding to T_ℓ, and adding an additional term that represents the change in internal energy from the state (T_ℓ, PSL) to the state T_ℓ, p. That is,

$$e_\ell(T_\ell, p) = e_{\ell s}(T_\ell, \text{PSL}) + \text{ELP} \quad .$$

The additional term, ELP, which represents the change in energy required to move along the isotherm at T_ℓ between two different pressure values, namely PSL and p, is represented as

$$\text{ELP} = (p - \text{PSL}) \left(\frac{\partial e_\ell}{\partial p} \right)_{T_\ell} \quad ,$$

where

$$\left(\frac{\partial e_\ell}{\partial p} \right)_{T_\ell} = -8.329595 \times 10^{-4} \left[1 - \exp\left(1.450382 \times 10^{-6} \cdot \text{PSL}\right) \right] - 2.245825 \times 10^{-17} \cdot \text{PSL}^2 \quad .$$

Therefore, the partial derivative with respect to T_ℓ of the internal energy is calculated as

$$\left(\frac{\partial e_\ell}{\partial T_\ell} \right)_p = \frac{de_{\ell s}}{dT_{sat}} + \text{ERT} \quad ,$$

where

$$\text{ERT} = \left[\frac{\partial}{\partial T_\ell} (\text{ELP}) \right]_p = \left\{ -8.329595 \times 10^{-4} \left[-1 + \exp\left(-1.450382 \times 10^{-6} \cdot \text{PSL} \right) \times \left[1 + 1.450382 \times 10^{-6} \, (p - \text{PSL}) \right] \right] - 2.245825 \times 10^{-17} \left(2p \cdot \text{PSL} - 3 \, \text{PSL}^2 \right) \right\} \frac{d}{dT_\ell} (\text{PSL}) \quad ,$$

and $de_{\ell s}/dT_{sat}$ is calculated as in Section A.1.1.3.

A.1.2.2. Density.

A.1.2.2.1. Initial Calculation. Given the pressure p and temperature T_ℓ of liquid water, Tait's equation-of-state in the form

$$\frac{v(0,T_\ell)-v(p,T_\ell)}{v(0,T_\ell)} = \frac{1}{n}\,\ell n\left[1+\frac{p}{B(T_\ell)}\right]$$

is used to determine the liquid density and its partial derivatives, where v is the specific volume of the liquid. The constant n is quoted in work by Richardson, Arens, and Haverson (Ref. A-4.) to be 7.146. The terms $v(0,T_\ell)$ and $B(T_\ell)$ are third-order polynomials of liquid temperature fitted to steam-table data, such that

$$v(0,T_\ell) = AVO(i) + BVO(i)\,T_\ell + CVO(i)\,T_\ell^2 + DVO(i)\,T_\ell^3$$

and

$$B(T_\ell) = AFN(i) + BFN(i)\,T_\ell + CFN(i)\,T_\ell^2 + DFN(i)\,T_\ell^3 ,$$

where

$i = 1$ for $273.15 \le T_\ell < 373.15$ K ,
$i = 2$ for $373.15 \le T_\ell < 473.15$ K ,
$i = 3$ for $473.15 \le T_\ell < 573.15$ K ,
$i = 4$ for $573.15 \le T_\ell < 603.15$ K ,
$i = 5$ for $603.15 \le T_\ell < 613.15$ K ,
$i = 6$ for $613.15 \le T_\ell < 623.15$ K ,
$i = 7$ for $623.15 \le T_\ell < 633.15$ K ,
$i = 8$ for $633.15 \le T_\ell < 643.15$ K ,
$i = 9$ for $643.15 \le T_\ell < 653.15$ K ,
$i = 10$ for $653.15 \le T_\ell < 663.15$ K ,
$i = 11$ for $663.15 \le T_\ell < 673.15$ K , and
$i = 12$ for $673.15 \le T_\ell \le 713.94025779311$ K .

Table A-6. lists the constants $AVO(i)$, $BVO(i)$, $CVO(i)$, $DVO(i)$, $AFN(i)$, $BFN(i)$, $CFN(i)$, and $DFN(i)$ for the given temperature ranges.

TABLE A-6.
Liquid Density Constants

i	*AVO(i)*	*BVO(i)*	*CVO(i)*	*DVO(i)*
1	1.7057666777468E–03	–6.0320895569365E–06	1.5944423965594E–08	–1.2149418561177E–11
2	5.2145931517155E–04	3.5189228252915E–06	–9.7304881862624E–09	1.0856688130631E–11
3	–1.4931865836934E–02	9.7931556400429E–05	–2.0172817692512E–07	1.4080475270259E–10
4	–4.9334201381918E–01	2.5928571576499E–03	–4.5387107397840E–06	2.6537936475365E–09
5	–3.4558955902321E+00	1.7351793841884E–02	–2.9047483637289E–05	1.6220227777320E–08
6	–1. 1952528427292E+01	5.8904962031842E–02	–9.6786687447220E–05	5.3029284583415E–08
7	–3.7446629978341E+01	1.8173474403006E–01	–2.9404991620713E–04	1.5863005350824E–07
8	–3.9713284923576E+02	1.8801824705202E+00	–2.9673900150051E–03	1.5612171739106E–06
9	–2.3142714272157E+03	1.0710216457395E+01	–1.6521763202064E–02	8.4955209566212E–06
10	2.0481569977849E+03	–9.3452783115489E+00	1.4212077056589E–02	–7.2037202704367E–06
11	–7.3864713248117E+01	3.3144939132191E–01	–4.9608715522591E–04	2.4771793009809E–07
12	–2.1891320674084E+01	9.6758467414310E–02	–1.4289074953436E–04	7.0567217785700E–08

i	*AFN(i)*	*BFN(i)*	*CFN(i)*	*DFN(i)*
1	–4.2486354144244E+09	3.7516769853867E+07	–1.0064945851796E+05	8.7507285129715E+01
2	–2.7936308563236E+08	5.5663179995300E+06	–1.4921749894688E+04	1.0834095198280E+01
3	–1.1761210016041E+08	4.3832221802974E+06	–1.2088373365747E+04	8.6034520917150E+00
4	–4.5415129389018E+09	2.7368608704680E+07	–5.1 894794477625E+04	3.1581281016141E+01
5	–4.0104325667716E+10	2.0292575433752E+08	–3.4075971373732E+05	1.9000660267975E+02
6	–6.0173879922257E+10	2.9984925450490E+08	–4.9675963282729E+05	2.7368658401451E+02
7	2.0678826351719E+10	–8.9503807129603E+07	1.2822787819385E+05	–6.0722291833340E+01
8	8.3793557728900E+10	–3.8997180562867E+08	6.0502628698976E+05	–3.1291965911464E+02
9	9.2402374347985E+10	–4.2674923965292E+08	6.5695613829284E+05	–3.3711122197289E+02
10	–2.7547713637194E+10	1.2580004134443E+08	–1.9147491048695E+05	9.7136148925404E+01
11	6.8608195287374E+08	–3.0636028439513E+06	4.5613625244005E+03	–2.2642074876391E+00
12	4.3458430609231E+07	–1.8379937116289E+05	2.5971646178490E+02	–1.2244044950391E–01

This allows the density, ρ_ℓ, to be calculated as

$$\rho_\ell = \frac{1}{v(0,T_\ell)\left\{1.0 - \frac{1}{7.146}\,\ell n\left[1.0+\frac{p}{B(T_\ell)}\right]\right\}} \quad .$$

Therefore,

$$\left(\frac{\partial \rho_\ell}{\partial p}\right)_{T_\ell} = \frac{\rho_\ell^2\, v(0,T_\ell)}{7.146\,[p + B(T_\ell)]}$$

and

$$\left(\frac{\partial \rho_\ell}{\partial T_\ell}\right)_p = -\rho_\ell \frac{v'(0,T_\ell)}{v(0,T_\ell)} - B'(T_\ell)\,\frac{p}{B(T_\ell)}\left(\frac{\partial \rho_\ell}{\partial p}\right)_{T_\ell} \quad ,$$

where

$$v'(0,T_\ell) = BVO(i) + 2\,CVO(i)\,T_\ell + 3\,DVO(i)\,T_\ell^2$$

and

$$B'(T_\ell) = BFN(i) + 2\,CFN(i)\,T_\ell + 3\,DFN(i)\,T_\ell^2 \quad .$$

The polynomial constants for $v'(0,T_\ell)$ and $B'(T_\ell)$ are the same as for $v(0,T_\ell)$ and $B(T_\ell)$ and are given in Table A-6.

A.1.2.2.2. Residual Void Correction.[1] After evaluation in the above section, ρ_ℓ and its derivatives are corrected to reflect a residual void fraction. In the following, the values calculated above are denoted by a tilde (~).

A.1.2.2.2.1. $p \geq 4.0 \times 10^5$ Pa.

$$\left(\frac{\partial \rho_\ell}{\partial T_\ell}\right)_p = \left(1-\frac{1000}{p}\right)\left(\frac{\partial \tilde{\rho}_\ell}{\partial T_\ell}\right)_p \quad ,$$

$$\left(\frac{\partial \rho_\ell}{\partial p}\right)_{T_\ell} = \left(1-\frac{1000}{p}\right)\left(\frac{\partial \tilde{\rho}_\ell}{\partial p}\right)_{T_\ell} + \frac{1000\tilde{\rho}_\ell}{p^2} \quad ,$$

1. This artificial compressibility of liquid is presently turned off in the code. It can be turned on by setting the flag NOAC to 0 in subroutine RHOLIQ if it is needed.

and

$$\rho_\ell = \left(1 - \frac{1000}{p}\right)\tilde{\rho}_\ell \ .$$

A.1.2.2.2.2. $p < 4.0 \times 10^5$ Pa.

$$\left(\frac{\partial \rho_\ell}{\partial T_\ell}\right)_p = (0.995 + 6.25 \times 10^{-9} p)\left(\frac{\partial \tilde{\rho}_\ell}{\partial T_\ell}\right)_p \quad ,$$

$$\left(\frac{\partial \rho_\ell}{\partial p}\right)_{T_\ell} = (0.995 + 6.25 \times 10^{-9} p)\left(\frac{\partial \tilde{\rho}_\ell}{\partial p}\right)_{T_\ell} + 6.25 \times 10^{-9}\ \tilde{\rho}_\ell \quad ,$$

and

$$\rho_\ell = (0.995 + 6.25 \times 10^{-9} p)\ \tilde{\rho}_\ell \quad .$$

A.1.3. Steam Properties

A.1.3.1. Superheated Vapor. $(T_g - T_{sv}) > 0$, where T_{sv} is the saturation temperature corresponding to the partial pressure of the vapor, p_v, throughout this section. The constant-pressure specific heat of steam at temperature T_g is approximated as

$$c_{pv} = \left(\frac{\partial h_v}{\partial T_v}\right)_{p_v} = \frac{c_{pv,\text{ideal}}}{2}\left[1 + \frac{T_g}{\left(T_g^2 - \beta\right)^{\frac{1}{2}}}\right] \quad ,$$

where

$$\beta = T_{sv}^2\left[1 - \frac{1}{\left(\frac{2\, c_{pvs}}{c_{pv,\text{ideal}}} - 1\right)^2}\right] \quad .$$

The term c_{pvs} is calculated as defined in Section A.1.1.6., and $c_{pv,\text{ideal}}$ is defined by ideal gas behavior, such that

$$c_{pv,\text{ideal}} = \frac{R_v \gamma_{\text{ideal}}}{\gamma_{\text{ideal}} - 1} \quad ,$$

where R_v is the gas constant for steam (Table A-1.) and γ_{ideal} is the ratio of ideal specific heats for steam (Table A-1.).

Integrating the equation for c_{pv} along a constant p_v line gives

$$h_v = h_{vs} + \frac{c_{pv,\text{ideal}}}{2}\left[\left(T_g - T_{sv}\right) + \left(T_g^2 - \beta\right)^{\frac{1}{2}} - \frac{T_{sv}}{\left(\frac{2c_{pvs}}{c_{pv,\text{ideal}}} - 1\right)}\right] .$$

The internal energy of vapor is therefore calculated as

$$e_v = e_{vs} + \frac{c_{pv,\text{ideal}}}{2}\left[\left(T_g - T_{sv}\right) + \left(T_g^2 - \beta\right)^{\frac{1}{2}} - \frac{T_{sv}}{\left(\frac{2c_{pvs}}{c_{pv,\text{ideal}}} - 1\right)}\right] - p_v\left(\frac{1}{\rho_v} - \frac{1}{\rho_{vs}}\right) .$$

The definitions of enthalpy and internal energy allow the density of the water vapor to be written, such that

$$\rho_v = \frac{p_v}{h_v - e_v} = \frac{p_v}{\left[h_{vs} + c_{pv,\text{ideal}}\left(T_g - T_{sv}\right)\right] - \left[e_{vs} + c_{vv,\text{ideal}}\left(T_g - T_{sv}\right)\right]}$$

$$= \frac{p_v}{(h_{vs} - e_{vs}) + (\gamma_{\text{ideal}} - 1)(e_v - e_{vs})} ,$$

where $c_{vv,\text{ideal}}$ is defined in Table A-1.

A.1.3.1.1. Internal Energy. Substitution of ρ_v and ρ_{vs}, as defined by the preceding equation, into the equation for the internal energy of the vapor gives the following equations.

For $p_v \leq 1.9 \times 10^7$ Pa,

$$e_v = e_{vs} + \frac{c_{vv,\text{ideal}}}{2}\left[\left(T_g - T_{sv}\right) + \left(T_g^2 - \beta\right)^{\frac{1}{2}} - \frac{T_{sv}}{\left(\frac{2c_{pvs}}{c_{pv,\text{ideal}}} - 1\right)}\right] ,$$

where again $c_{vv,\text{ideal}}$ is the constant-volume specific heat for steam, as defined by ideal gas behavior (Table A-1.). Therefore,

$$\left(\frac{\partial e_v}{\partial T_g}\right)_{p_v} = \frac{c_{vv,\text{ideal}}}{\left(1 - \frac{\beta}{\kappa^2}\right)}$$

and

$$\left(\frac{\partial e_v}{\partial p_v}\right)_{T_g} = -\frac{1}{2}\left(\frac{\partial e_v}{\partial T_g}\right)_{p_v}\left[\left(1-\frac{\beta}{\kappa^2}\right)\kappa'_p + \frac{1}{\kappa}\frac{d\beta}{dp_v}\right] \quad ,$$

where

$$\kappa = \frac{2}{c_{vv,\text{ideal}}}(e_v - e_{vs}) + T_{sv}\left[1 + \frac{1}{\frac{2c_{pvs}}{c_{pv,\text{ideal}}} - 1}\right] \quad ,$$

and

$$\kappa'_p = \left(\frac{\partial \kappa}{\partial p_v}\right)_{T_g} = -\frac{2}{c_{vv,\text{ideal}}}\frac{de_{vs}}{dp_v} + \left[1 + \frac{1}{\left(\frac{2c_{pvs}}{c_{pv,\text{ideal}}} - 1\right)}\right]\frac{dT_{sv}}{dp_v}$$

$$- \frac{2}{c_{pv,\text{ideal}}}\left[\frac{T_{sv}}{\left(\frac{2c_{pvs}}{c_{pv,\text{ideal}}} - 1\right)^2}\right]\frac{dc_{pvs}}{dp_v} \quad ,$$

and

$$\frac{d\beta}{dp_v} = \frac{2}{T_{sv}}\left\{\beta\frac{dT_{sv}}{dp_v} + \frac{2}{c_{pv,\text{ideal}}}\left[\frac{T_{sv}}{\left(\frac{2c_{pvs}}{c_{pv,\text{ideal}}} - 1\right)}\right]^3\frac{dc_{pvs}}{dp_v}\right\} \quad .$$

For $p_v \geq 2.0 \times 10^7$ Pa,

$$e_v = e_{vs} + \frac{c_{pv,\text{ideal}}}{2\gamma_s}\left[\frac{(T_g - T_{sv}) + (T_g^2 - \beta)^{1/2} - T_{sv}}{\left(\frac{2c_{pvs}}{c_{pv,\text{ideal}}} - 1\right)}\right] ,$$

$$\left(\frac{\partial e_v}{\partial T_g}\right)_{p_v} = \frac{c_{pv,\text{ideal}}}{2\gamma_s}\left(1 + \frac{T_g}{\left(T_g^2 - \beta\right)^{\frac{1}{2}}}\right) ,$$

and

$$\left(\frac{\partial e_v}{\partial p_v}\right)_{T_g} = \frac{de_{vs}}{dp_v} - \frac{e_v - e_{vs}}{\gamma_s}\frac{d\gamma_s}{dp_v} + \frac{c_{pv,\text{ideal}}}{2\gamma_s} \cdot \left[\left(-\frac{dT_{sv}}{dp_v}\right) - \frac{1}{2}\frac{d\beta}{dp_v}\frac{1}{\left(T_g^2 - \beta\right)^{\frac{1}{2}}}\right.$$

$$\left. - \frac{dT_{sv}}{dp_v} \cdot \left(\frac{1}{\frac{2c_{pvs}}{c_{pv,\text{ideal}}} - 1}\right) + \frac{2}{c_{pv,\text{ideal}}}\left[\frac{T_{sv}}{\left(\frac{2c_{pvs}}{c_{pv,\text{ideal}}} - 1\right)^2}\right]\frac{dc_{pvs}}{dp_v}\right] ,$$

where

$$\frac{\partial \beta}{\partial p_v} = \frac{2}{T_{sv}}\left\{\beta\frac{dT_{sv}}{dp_v} + \frac{2}{c_{pv,\text{ideal}}}\left[\frac{T_{sv}}{\left(\frac{2c_{pvs}}{c_{pv,\text{ideal}}} - 1\right)}\right]^3\frac{dc_{pvs}}{dp_v}\right\} .$$

For 1.9×10^7 Pa $< p_v <$ 2.0×10^7 Pa, the values of e_v and its derivatives are calculated by interpolating between the values of the two curve fits.

A.1.3.1.2. Density. If $p_v \leq 1.9 \times 10^7$ Pa, the vapor density is calculated as

$$\rho_v = \frac{p_v}{(\gamma_s - 1)e_{vs} + (\gamma_{\text{ideal}} - 1)(e_v - e_{vs})} .$$

Therefore,

$$\left(\frac{\partial \rho_v}{\partial T_g}\right)_{p_v} = -\left(\frac{\partial e_v}{\partial T_g}\right)_{p_v}\left[\frac{(\gamma_{\text{ideal}} - 1)\rho_v}{(\gamma_s - 1)e_{vs} + (\gamma_{\text{ideal}} - 1)(e_v - e_{vs})}\right] ,$$

and

$$\left(\frac{\partial \rho_v}{\partial p_v}\right)_{T_g} = \left\{(1 - \rho_v)\left[e_{vs}\frac{d\gamma_s}{dp_v} + (\gamma_s - \gamma_{\text{ideal}})\frac{de_{vs}}{dp_v}\right]\right.$$

$$\left. \times \left[\frac{1}{(\gamma_s - 1)e_{vs} + (\gamma_{\text{ideal}} - 1)(e_v - e_{vs})}\right]\right\} + \left(\frac{\partial \rho_v}{\partial e_v}\right)_{p_v}\left(\frac{\partial e_v}{\partial p_v}\right)_{T_g} ,$$

where

$$\left(\frac{\partial \rho_v}{\partial e_v}\right)_{p_v} = -\frac{(\gamma_{\text{ideal}} - 1)\rho_v}{\left[(\gamma_s - 1)e_{vs} + (\gamma_{\text{ideal}} - 1)(e_v - e_{vs})\right]} \quad .$$

If $p_v \geq 2.0 \times 10^7$ Pa, the vapor density is calculated as

$$\rho_v = \frac{p_v}{(\gamma_s - 1)e_v} \quad .$$

Therefore,

$$\left(\frac{\partial \rho_v}{\partial T_g}\right)_{p_v} = \left(\frac{\partial \rho_v}{\partial e_v}\right)_{p_v}\left(\frac{\partial e_v}{\partial T_g}\right)_{p_v} \quad ,$$

and

$$\left(\frac{\partial \rho_v}{\partial p_v}\right)_{T_g} = \left(1 - \rho_v e_v \frac{d\gamma_s}{dp_v}\right)\frac{1}{(\gamma_s - 1)e_v} + \left(\frac{\partial \rho_v}{\partial e_v}\right)_{p_v}\left(\frac{\partial e_v}{\partial p_v}\right)_{T_g} \quad ,$$

where

$$\left(\frac{\partial \rho_v}{\partial e_v}\right)_{p_v} = -\frac{\rho_v}{e_v} \quad .$$

If $1.9 \times 10^7 < p_v < 2.0 \times 10^7$ Pa, the vapor density and its derivatives are calculated by linearly interpolating between the values of the two curve fits.

Minimum and maximum limits are placed on the calculated values of the density, and its partial derivatives. In low-pressure regions where the above equations may predict a negative density, the density and its derivatives are recalculated based on ideal gas behavior. If ρ_v is less than zero, the vapor density and its derivatives are superseded by

$$\rho_v = \frac{p_v}{R_v T_g} \quad ,$$

$$\left(\frac{\partial \rho_v}{\partial T_v}\right)_{p_v} = -\frac{\rho_v}{T_g} \quad ,$$

and

$$\left(\frac{\partial \rho_v}{\partial p_v}\right)_{T_g} = \frac{\rho_v}{p_g} \quad .$$

Near the critical point, it is necessary to impose the following limit on the density ratio

$$\frac{\rho_v}{\rho_\ell} \leq 0.999 \quad ,$$

to avoid singularities when calculating certain parameters. If the calculated value of ρ_v exceeds 0.999 ρ_ℓ, the vapor density and its derivatives are superseded by

$$\rho_v = 0.999 \rho_\ell \ ,$$

$$\left(\frac{\partial \rho_v}{\partial T_g}\right)_{p_v} = 0.999 \left(\frac{\partial \rho_\ell}{\partial T_\ell}\right)_p \ ,$$

and

$$\left(\frac{\partial \rho_v}{\partial p_v}\right)_{T_g} = 0.999 \left(\frac{\partial \rho_\ell}{\partial p}\right)_{T_\ell} \quad .$$

A.1.3.1.3. Enthalpy. Subroutine FPROP calculates the enthalpy of the superheated vapor using the definition of enthalpy, such that

$$h_v = e_v + \frac{p_v}{\rho_v} \quad ,$$

where e_v and ρ_v are calculated according to Sections A.1.3.1.1. and A.1.3.1.2., respectively.

A.1.3.2. Subcooled Vapor. $(T_g - T_{sv}) \leq 0$, where T_{sv} refers to the saturation temperature corresponding to the partial pressure of the vapor, p_v, throughout this section.

A.1.3.2.1. Internal Energy.

$$e_v = e_{vs} + (T_g - T_{sv}) \frac{c_{pvs}}{\gamma_{\text{ideal}}} \quad ,$$

$$\left(\frac{\partial e_v}{\partial T_g}\right)_{p_v} = \frac{c_{pvs}}{\gamma_{\text{ideal}}} \quad ,$$

and

$$\left(\frac{\partial e_v}{\partial p_v}\right)_{T_g} = \frac{de_{vs}}{dp_v} + \left(\frac{e_v - e_{vs}}{c_{pvs}}\right)\frac{dc_{pvs}}{dp_v} - \frac{\partial e_v}{\partial T_g}\frac{dT_{sv}}{dp_v} \quad .$$

A.1.3.2.2. Density. The method used to determine the subcooled vapor density, and its derivatives for all pressure ranges is identical to the one outlined in the case of superheated vapor for $p_v \leq 1.9 \times 10^7$ Pa in Section A.1.3.1.2.

A.1.3.2.3. Enthalpy. Subroutine FPROP calculates the enthalpy of the subcooled vapor using the definition of enthalpy, such that

$$h_v = e_v + \frac{p_v}{\rho_v} \quad ,$$

where e_v and ρ_v are calculated according to Sections A.1.3.2.1. and A.1.3.2.2., respectively.

A.1.4. Noncondensable Gas (Air, Hydrogen, or Helium) Properties
Additional information on the noncondensable-gas thermodynamic properties is provided in Appendix K.

A.1.4.1. Internal Energy.

$$e_a = c_{va}T_g \quad ,$$

$$\left(\frac{\partial e_a}{\partial T_g}\right)_{p_a} = c_{va} \quad ,$$

and

$$\left(\frac{\partial e_a}{\partial p_a}\right)_{T_g} = 0.0 \quad .$$

The constant-volume specific heat, c_{va}, is calculated from

$$c_{va} = c_{pa} - R_a \quad ,$$

where c_{pa} is determined as described in Section A.2.2.3. for noncondensable gases and where R_a is the gas constant for the noncondensable gas (Table A-1.).

A.1.4.2. Density.

$$\rho_a = \frac{p_a}{R_a T_g} \quad ,$$

$$\left(\frac{\partial \rho_a}{\partial p_a}\right)_{T_g} = \frac{1}{R_a T_g} \quad ,$$

and

$$\left(\frac{\partial \rho_a}{\partial T_g}\right)_{p_a} = -R_a \rho_a \left(\frac{\partial \rho_a}{\partial p_a}\right)_{T_g} \quad .$$

A.1.4.3. Enthalpy. Subroutine FPROP calculates the enthalpy of the noncondensable gas, such that

$$h_a = e_a + \frac{p_a}{\rho_a} \quad ,$$

where e_a and ρ_a are calculated as described in the two previous Sections, A.1.4.1. and A.1.4.2., respectively.

A.1.5. Steam-Gas Mixture Properties

A.1.5.1. Internal Energy. Subroutine THERMO calculates the steam-air, steam-hydrogen, or steam-helium mixture internal energy, such that

$$e_m = \frac{e_v \rho_v + e_a \rho_a}{\rho_v + \rho_a} \quad ,$$

where e_v is calculated according to Sections A.1.3.1.1. or A.1.3.2.1., depending on whether the vapor is superheated or subcooled, e_a is calculated as described in Section A.1.4.1., ρ_v is the water vapor density as calculated in Section A.1.3.1.2., and ρ_a is the noncondensable-gas density as calculated in Section A.1.4.2.

A.1.5.2. Density. Subroutine THERMO calculates the steam-air, steam-hydrogen, or steam-helium mixture density, such that

$$\rho_m = \rho_v + \rho_a \quad ,$$

where ρ_v is the water vapor density as calculated in Section A.1.3.1.2. and ρ_a is the noncondensable-gas density as calculated in Section A.1.4.2.

A.1.5.3. Enthalpy. Subroutine FPROP calculates the steam-air, steam-hydrogen, or steam-helium mixture enthalpy, such that

$$h_m = \frac{h_v\rho_v + h_a\rho_a}{\rho_v + \rho_a}$$
$$= e_m + \frac{p}{\rho_m} \quad ,$$

where e_m is calculated according to Section A.1.5.1., ρ_m is calculated as described in Section A.1.5.2., and p is the total pressure.

A.2. Transport Properties

Subroutine FPROP is used to obtain transport properties for liquid- and vapor-phase water, noncondensable gases, and steam-gas mixtures. The input variables for this subroutine are the saturation temperature corresponding to the total pressure; the internal energies, densities, and temperatures of the liquid and gas phases where the gas is either steam, a noncondensable gas, or a steam-gas mixture; the total pressure; and the partial pressure of the noncondensable gas, if any is present. The output transport variables include the latent heat of vaporization, the constant-pressure specific heats, viscosities, and thermal conductivities of the liquid and gas phases, and the surface tension of the liquid.

The transport property calls are function calls within the FPROP subroutine. Function CPLL calculates the constant-pressure specific heat of the liquid, while function CPVV1 determines the value of the constant-pressure specific heat of the steam, noncondensable gas, or steam-gas mixture. Function THCL evaluates the liquid thermal conductivity, and function THCV calculates the steam, noncondensable-gas, or steam-gas mixture thermal conductivity. Similarly, functions VISCL and VISCV determine viscosity values. Finally, function SIGMA calculates the surface tension of the liquid water.

The polynomial equation fits for the transport properties used in FPROP are described in the remainder of this section. Values of the constants are given in Tables A-7. through A-11. Additional information on the noncondensable-gas transport properties is provided in Appendix K.

A.2.1. Latent Heat of Vaporization

Subroutine FPROP calculates the latent heat of vaporization as

$$h_{\ell v} = h_{vs} - h_{\ell s} \quad ,$$

where $h_{\ell v}$ and $h_{\ell s}$ are calculated according to Sections A.1.1.4. and A.1.1.5., respectively.

A.2.2. Constant-Pressure Specific Heat

Functions CPLL and CPVV1 calculate the constant-pressure specific heats for the liquid and the steam, gas, or steam-gas mixture, respectively. Constants used in this section are given in Table A-7.

A.2.2.1. Liquid. Function CPLL calculates the liquid constant-pressure specific heat, such that

$$c_{p\ell} = \left\{h_\ell[h_\ell(D_{0\ell} + D_{1\ell}p) + (C_{0\ell} + C_{1\ell}p)] + B_{0\ell} + B_{1\ell}p\right\}^{-1} \quad .$$

The maximum permitted value for $c_{p\ell}$ is 4.0×10^4, and if the above calculation of $c_{p\ell}$ yields a value greater than this, it is reset to be 4.0×10^4.

A.2.2.2. Steam. Function CPVV1 calculates the steam constant-pressure specific heat, such that

$$c_{pv} = C_{1v} + C_{2v}T_g + \frac{C_{3v}p}{\left(C_{5v}T_g - C_{6v}\right)^{2.4}} + \frac{C_{4v}p^3}{\left(C_{5v}T_g - C_{6v}\right)^{9}} \quad .$$

TABLE A-7.
Constant-Pressure Specific Heat Constants

$B_{0\ell}$	=	2.394907×10^{-4}	$B_{1\ell}$	=	$-5.196250 \times 10^{-13}$
$C_{0\ell}$	=	1.193203×10^{-11}	$C_{1\ell}$	=	2.412704×10^{-18}
$D_{0\ell}$	=	$-3.944067 \times 10^{-17}$	$D_{1\ell}$	=	$-1.680771 \times 10^{-24}$

C_{1v}=1.68835968×10^3
C_{2v}=0.6029856
C_{3v}=4.820979623×10^2
C_{4v}=2.95317905×10^7
C_{5v}=1.8
C_{6v}=4.60×10^2

A.2.2.3. Noncondensable Gas. Function CPVV1 assumes the constant-pressure specific heat of the noncondensable gas to be constant, such that

c_{pa} = 1004.832 [J/(kg·K)] for air,

c_{pa} = 14533.2 [J/(kg·K)] for hydrogen,

and

c_{pa} = 5193.086 [J/(kg·K)] for helium.

A.2.2.4. Steam-Gas Mixtures. Function CPVV1 uses an averaging technique to calculate the specific heat of a steam-air, steam-hydrogen, or steam-helium mixture, such that

$$c_{pg} = \frac{(p - p_a)\, c_{pv} + p_a\, c_{pa}}{p} \quad ,$$

where c_{pv} and c_{pa} are calculated as in Sections A.2.2.2. and A.2.2.3.

Note: Because these values of specific heats are used only for calculating heat-transfer coefficients, these fits were chosen for simplicity and smoothness and are not necessarily consistent with those derivable from the thermodynamic routines.

A.2.3. Fluid Viscosity

Functions VISCL and VISCV calculate the fluid viscosities for the liquid and the steam, for the gas, or for the steam-gas mixture, respectively. Constants used in this section are given in Tables A-8., A-9., and A-10.

A.2.3.1. Liquid. Function VISCL divides the evaluation of liquid viscosity into three different enthalpy ranges. Table A-8. gives the constants used in this section.

A.2.3.1.1. $h_l \le 0.276 \times 10^6$ J/kg.

$$\mu_\ell = \left[A_{0\ell} + A_{1\ell}x + A_{2\ell}x^2 + A_{3\ell}x^3 + A_{4\ell}x^4\right] - \left[B_{0\ell} + B_{1\ell}\eta + B_{2\ell}\eta^2 + B_{3\ell}\eta^3\right](p - p_i) \quad ,$$

where

$$x = (h_\ell - c_{on})h_0$$

and

$$\eta = (h_\ell - e_{con})e_{h0} \quad .$$

TABLE A-8.
Liquid Viscosity Constants

$A_{0\ell} = 1.298\ 102\ 340 \times 10^{-3}$

$A_{1\ell} = -9.264\ 032\ 108 \times 10^{-4}$

$A_{2\ell} = 3.810\ 470\ 61 \times 10^{-4}$

$A_{3\ell} = -8.219\ 444\ 458 \times 10^{-5}$

$A_{4\ell} = 7.022\ 437\ 984 \times 10^{-6}$

$B_{0\ell} = -6.595\ 9 \times 10^{-12}$

$B_{1\ell} = 6.763 \times 10^{-12}$

$B_{2\ell} = -2.888\ 25 \times 10^{-12}$

$B_{3\ell} = 4.452\ 5 \times 10^{-13}$

$D_{0\ell} = 3.026\ 032\ 306 \times 10^{-4}$

$D_{1\ell} = -1.836\ 606\ 896 \times 10^{-4}$

$D_{2\ell} = 7.567\ 075\ 775 \times 10^{-5}$

$D_{3\ell} = -1.647\ 878\ 879 \times 10^{-5}$

$D_{4\ell} = 1.416\ 457\ 633 \times 10^{-6}$

$E_{0\ell} = 1.452\ 605\ 261\ 2 \times 10^{-3}$

$E_{1\ell} = -6.988\ 008\ 498\ 5 \times 10^{-9}$

$E_{2\ell} = 1.521\ 023\ 033\ 4 \times 10^{-14}$

$E_{3\ell} = -1.230\ 319\ 494\ 6 \times 10^{-20}$

$F_{0\ell} = -3.806\ 350\ 753\ 3 \times 10^{-11}$

$F_{1\ell} = 3.928\ 520\ 767\ 7 \times 10^{-16}$

$F_{2\ell} = -1.258\ 579\ 929\ 2 \times 10^{-21}$

$F_{3\ell} = 1.286\ 018\ 078\ 8 \times 10^{-27}$

$h_0 = 8.581\ 289\ 699 \times 10^{-6}$

$c_{0n} = 4.265\ 884 \times 10^{4}$

$p_i = 6.894\ 575\ 293 \times 10^{5}$

$h_{00} = 3.892\ 077\ 365 \times 10^{-6}$

$e_{con} = 5.535\ 88 \times 10^{4}$

$e_{h0} = 6.484\ 503\ 981 \times 10^{-6}$

$c_n = 4.014\ 676 \times 10^{5}$

A.2.3.1.2. 0.276×10^6 **J/kg** $< h_l \leq 0.394 \times 10^6$ **J/kg.**

$$\mu_\ell = \left[E_{0\ell} + E_{1\ell}h_\ell + E_{2\ell}h_\ell^2 + E_{3\ell}h_\ell^3\right] + \left[F_{0\ell} + F_{1\ell}h_\ell + F_{2\ell}h_\ell^2 + F_{3\ell}h_\ell^3\right](p - p_i) \quad .$$

A.2.3.1.3. $h_l > 0.394 \times 10^6$ **J/kg.**

$$\mu_\ell = \left[D_{0\ell} + D_{1\ell}z + D_{2\ell}z^2 + D_{3\ell}z^3 + D_{4\ell}z^4\right] \quad ,$$

where

$$z = (h_\ell - c_n)h_{00} \quad .$$

A.2.3.2. Steam. Function VISCV uses three gas temperature ranges to evaluate the steam viscosity. Constants used in this section are given in Table A-9.

A.2.3.2.1. $T_g \leq 573.15$ K.

$$\mu_v = \left[B_{1v}\left(T_g - 273.15\right) + C_{1v}\right] - \rho_v\left[D_{1v} - E_{1v}\left(T_g - 273.15\right)\right] \quad .$$

If $\mu_v < 10^{-7}$, it is set to that value.

A.2.3.2.2. 573.15 K < T_g < 648.15 K.

$$\begin{aligned}\mu_v &= B_{1v}(T_g - 273.15) + C_{1v} + \rho_v\left[F_{0v} + F_{1v}(T_g - 273.15)\right. \\ &+ \left. F_{2v}(T_g - 273.15)^2 + F_{3v}(T_g - 273.15)^3\right] \\ &+ \rho_v\left[G_{0v} + G_{1v}(T_g - 273.15) + G_{2v}(T_g - 273.15)^2\right. \\ &+ \left. G_{3v}(T_g - 273.15)^3\right]\left(A_{0v} + A_{1v}\rho_v + A_{2v}\rho_v^2\right) \quad .\end{aligned}$$

A.2.3.2.3. $T_g \geq 648.15$ K.

$$\mu_v = B_{1v}(T_g - 273.15) + C_{1v} + \rho_v\left(A_{0v} + A_{1v}\rho_v + A_{2v}\rho_v^2\right) \quad .$$

TABLE A-9.
Noncondensable-Gas Viscosity Constants

H_{a0}	=	1.707623×10^{-5}	H_{b0}	=	1.735×10^{-5}
H_{a1}	=	5.927×10^{-8}	H_{b1}	=	4.193×10^{-8}
H_{a2}	=	-8.14×10^{-11}	H_{b2}	=	-1.09×10^{-11}
H_{c0}	=	4.175×10^{-6}	H_{d1}	=	5.9642×10^{-6}
H_{c1}	=	1.588×10^{-8}	H_{d2}	=	5.2047×10^{-8}
H_{c2}	=	7.6705×10^{-13}	H_{d3}	=	-1.5345×10^{-11}

A.2.3.3. Noncondensable Gas. Constants used in this section are given in Table A-10.

A.2.3.3.1. Air. If the noncondensable gas is air, function VISCV uses two ranges of T_g to determine the gas viscosity.

A.2.3.3.1.1. $T_g \leq 502.15$ **K.** $\mu_a = H_{a0} + H_{a1}(T_g - 273.15) + H_{a2}(T_g - 273.15)^2$.

A.2.3.3.1.2. $T_g > 502.15$ **K.** $\mu_a = H_{b0} + H_{b1}(T_g - 273.15) + H_{b2}(T_g - 273.15)^2$.

A.2.3.3.2. Hydrogen. If the noncondensable gas is hydrogen, function VISCV calculates the gas viscosity as

$$\mu_a = H_{c0} + H_{c1}T_g + H_{c2}T_g^2 \quad .$$

A.2.3.3.3. Helium. If the noncondensable gas is helium, function VISCV calculates the gas viscosity as

$$\mu_a = H_{d0} + H_{d1}T_g + H_{d2}T_g^2 \quad .$$

TABLE A-10.
Thermal Conductivity Constants

h_0	=	5.815×10^5
A_{l0}	=	0.573738622
A_{l1}	=	0.2536103551
A_{l2}	=	–0.145468269
A_{l3}	=	–0.01387472485
C	=	2.1482×10^5
A_{v0}	=	1.76×10^{-2}
A_{v1}	=	3.87×10^{-5}
A_{v2}	=	1.04×10^{-7}
A_{v3}	=	-4.51×10^{-11}
B_{v0}	=	1.0351×10^{-4}
B_{v2}	=	0.4198×10^{-6}
B_{v3}	=	-2.771×10^{-11}

A.2.3.4. Steam-Gas Mixture. Function VISCV uses an averaging technique to calculate the viscosity of a steam-air, steam-hydrogen, or steam-helium mixture, such that

$$\mu_g = \frac{(p - p_a)\,\mu_v + p_a \mu_a}{p} ,$$

where μ_v and μ_a are calculated as in Sections A.2.3.2. and A.2.3.3.

A.2.4. Fluid Thermal Conductivity

Functions THCL and THCV calculate the fluid thermal conductivities for the liquid and the steam, gas, or steam-gas mixture, respectively. Constants used in this section are given in Table A-11.

A.2.4.1. Liquid. Function THCL calculates the liquid-water thermal conductivity, such that

$$k_\ell = A_{\ell 0} + A_{\ell 1} x_k + A_{\ell 2} x_k^2 + A_{\ell 3} x_k^3 ,$$

TABLE A-11.
Thermal Conductivity Constants

h_0	=	5.815×10^5
A_{l0}	=	0.573738622
A_{l1}	=	0.2536103551
A_{l2}	=	–0.145468269
A_{l3}	=	–0.01387472485
C	=	2.1482×10^5
A_{v0}	=	1.76×10^{-2}
A_{v1}	=	3.87×10^{-5}
A_{v2}	=	1.04×10^{-7}
A_{v3}	=	-4.51×10^{-11}
B_{v0}	=	1.0351×10^{-4}
B_{v2}	=	0.4198×10^{-6}
B_{v3}	=	-2.771×10^{-11}

where

$$x_k = \frac{h_\ell}{h_0} \quad .$$

If $k_\ell < 0.09$, it is set to that value.

A.2.4.2. Steam. Function THCV uses two gas temperature ranges to calculate the steam thermal conductivity.

A.2.4.2.1. 273.15 K ≤ T_g ≤ 273.25 K.

$$k_v = x_1 + \rho_v \left[x_2 + \frac{C\ \rho_v}{(0.1)^{4.2}} \right] \quad ,$$

where

$$x_1 = A_{v0} + A_{v1}(0.1) + A_{v2}(0.1)^2 + A_{v3}(0.1)^3$$

and

$$x_2 = B_{v0} + B_{v1}(0.1) + B_{v2}(0.1)^2 \quad .$$

A.2.4.2.2. 273.25 K < T_g ≤ 713.94025779311 K.

$$k_v = x_1 + \rho_v \left[x_2 + \frac{C\ \rho_v}{\left(T_g - 273.15\right)^{4.2}} \right] \quad ,$$

where

$$x_1 = A_{v0} + A_{v1}\left(T_g - 273.15\right) + A_{v2}\left(T_g - 273.15\right)^2 + A_{v3}\left(T_g - 273.15\right)^3$$

and

$$x_2 = B_{v0} + B_{v1}\left(T_g - 273.15\right) + B_{v2}\left(T_g - 273.15\right)^2 \quad .$$

If $k_v < 1.0 \times 10^{-4}$, it is set equal to that value.

A.2.4.3. Noncondensable Gas. Function THCV assumes the thermal conductivity of the noncondensable gas to be an exponential function of temperature, such that

$$k_a = 2.091\ x\ 10^{-4} T_g^{0.846}\ [\mathrm{W/m \cdot K}] \text{ for air} \quad ,$$

$$k_a = 1.6355\ x\ 10^{-3} T_g^{0.8213}\ [\mathrm{W/m \cdot K}] \text{ for hydrogen} \quad ,$$

and

$$k_a = 3.366\ x\ 10^{-3} T_g^{0.668}\ [\mathrm{W/m \cdot K}] \text{ for helium} \quad .$$

A.2.4.4. Steam-Gas Mixtures. Function THCV uses an averaging technique to calculate the thermal conductivity of a steam-air, steam-hydrogen, or steam-helium mixture, such that

$$k_g = \frac{(p - p_a)\, k_v + p_a\, k_a}{p} \quad ,$$

where k_v and k_a are calculated as in Sections A.2.4.2. and A.2.4.3.

A.2.5. Surface Tension

Function SIGMA uses two ranges of the saturation temperature corresponding to the total pressure to determine the surface tension of liquid water.

A.2.5.1. 273.15 K ≤ T_{sat} ≤ 582.435 K. Within this range, the surface tension of liquid water is calculated using the following ASME Steam Tables Recommended Interpolation Equation (Ref. A-5.):

$$\sigma = 0.2358 \left(1 - 0.625 \frac{647.15 - T_{sat}}{647.15}\right) \left(\frac{647.15 - T_{sat}}{647.15}\right)^{1.256} \quad .$$

The ASME Steam Tables state that this equation is valid for temperatures between the triple point (273.16 K) and the critical point, which the reference assumes to be 647.15 K. It is necessary in TRAC, however, to place a lower limit on the calculated value of the surface tension to avoid singularities when evaluating such things as the Chen nucleate-boiling relation. For this reason, the surface tension is set equal to a constant value for the remaining TRAC temperature range, 582.435 K to 713.94025779311 K.

A.2.5.2. 582.435 K < T_{sat} ≤ 713.94025779311 K. A constant value of surface tension is calculated in this range to keep the surface tension from becoming too low. Constraining the temperature difference ratio to be no less than 0.1 gives

$$\sigma = 0.2358\ [1 - 0.625\ (0.1)]\ (0.1)^{1.256} \quad .$$

A.3. Verification

The thermodynamic and transport property fits used in TRAC have been compared with steam-table data over a wide range of parameters. The agreement is satisfactory in the saturation region and in the superheated steam region for $p < p_{\text{critical}}$ and $T_g < 823.0$ K. For example, the saturation temperature corresponding to a given pressure is always calculated within a maximum error of ± 1 K. However, in most situations, the error is significantly smaller. The agreement also is good in the subcooled-water region for $T_\ell < T_{\text{critical}}$.

Further verification was performed by comparing the TRAC polynomial fits with the WATER package (Ref. A-1.) over a wider range of nonequilibrium [99 K of both superheat and subcooling (liquid superheat or vapor subcooling exceeding 99 K are highly unlikely in reactor applications)] for pressures up to 20 MPa. The comparisons showed good agreement for both the thermodynamic and transport properties throughout the saturation and nonequilibrium regions, except for very extreme cases. However, at high degrees of subcooling or superheat, some minor inconsistencies were noticed. Because there are no data in these extreme cases, it is impossible to compare TRAC and the WATER package adequately.

In addition, the output of subroutine THERMO variables p_v, e_v, ρ_v, and e_ℓ was checked against values generated from the Sesame database. Sesame is a database, developed by members of the Theoretical Division at LANL, that includes various equation-of-state data (Ref. A-6.). For all of the results below, we used the EOSPAC program (Ref. A-7.) to read the Sesame data. Sesame material 7152 (water) was used in these data comparisons. This particular data fit for water was originally developed by the National Bureau of Standards [NBS, now known as the National Institute for Standards and Technology (NIST)]. A 64-term fit was used by the NBS to closely model equation-of-state data (Ref. A-8.). Sesame data for material 7152 can be assumed to be accurate to within 1% for materials on the saturation line and within 5% for metastable regions off the saturation line. Because the NBS data were based on a fit to experimental data for equilibrium states, no attempt has been made to compare the data with our values for the metastable states corresponding to subcooled steam or superheated liquid.

The ρ_v values from THERMO agreed very well with Sesame data. On the saturation line at pressures below the critical pressure ($p_{\text{crit}} = 2.232 \times 10^7$ Pa), the agreement is excellent. Here the fractional error is less than 1%. Above p_{crit} (Fig. A-1.), the THERMO ρ_v values also agree with the Sesame data (dashed lines in graphs), often to better than 1% accuracy. However, there is a slight departure between the two curves in the pressure range $p_{\text{crit}} < p_v < 2.8 \times 10^7$ Pa. Here the fractional error is about 5%. For superheating, the plots near the saturation line also appear good. For superheats of 8 K and less, the THERMO ρ_v plot follows the Sesame data fairly well. Larger than 10 K superheat yields fractional errors larger than 10% (Fig. A-2.).

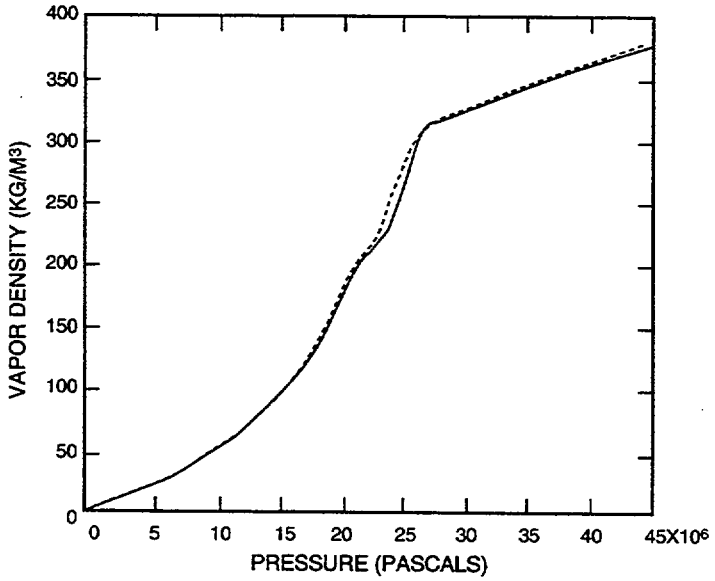

Fig. A-1. Vapor density vs. pressure along the saturation line.
Solid: TRAC; Dashed: Sesame.

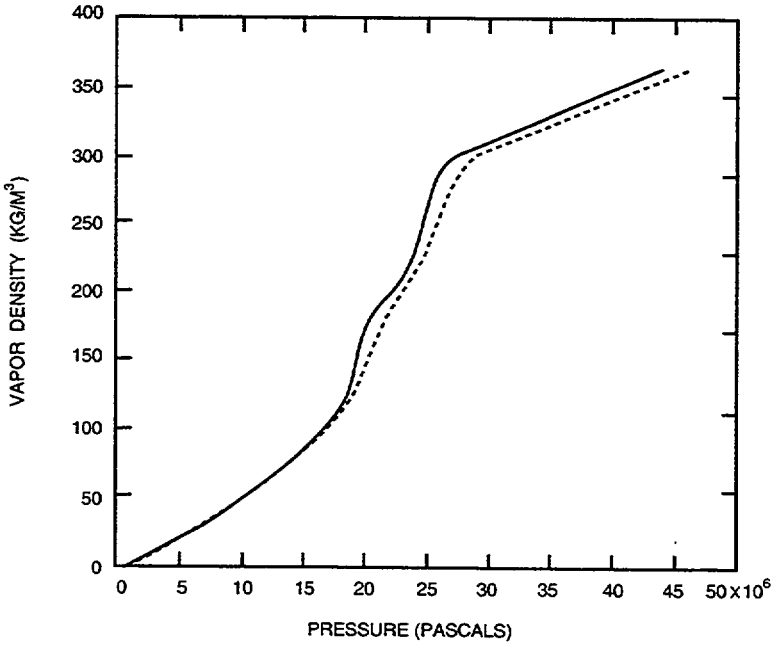

Fig. A-2. Vapor density vs. pressure at a superheat of 8 K.
Solid: TRAC; Dashed: Sesame.

For the e_v plot on the saturation line, Sesame and THERMO seem to agree well up to p_{crit} (Fig. A-3.). However, one significant departure is noted in the pressure range $1.0 \times 10^5 < p_v < 2.0 \times 10^6$ Pa. Here, although the fractional error is only 0.5%, the slope of the THERMO plot goes slightly negative in the pressure range $1.3 \times 10^6 < p_v < 2.0 \times 10^6$ Pa, while the Sesame slope remains positive. It should be noted that the THERMO e_v slope is only slightly negative, and then only for a short pressure range. At pressures above p_{crit} along the saturation line (Fig. A-3.), the difference between the THERMO curve and the Sesame data becomes more significant. At approximately $p_v = 2.75 \times 10^7$ Pa, the fractional error between the two curves is almost 4%. The fractional error decreases as pressure increases until, at $p_v = 4.5 \times 10^7$ Pa, the fractional error between the two curves is about 1.5%. For superheating, the Sesame data follow the THERMO e_v plot well up to p_{crit}, and departures between the Sesame and THERMO curves are more significant above p_{crit} (Fig. A-4.). Superheated conditions yield small departures of the THERMO e_v curve from the Sesame data above p_{crit}. Superheats as great at 100 K have fractional errors less than 6% across the pressure range $2.5 \times 10^7 < p_v < 3.0 \times 10^7$ Pa. Here also, the fractional error is only about 3% at $p_v = 4.5 \times 10^7$ Pa.

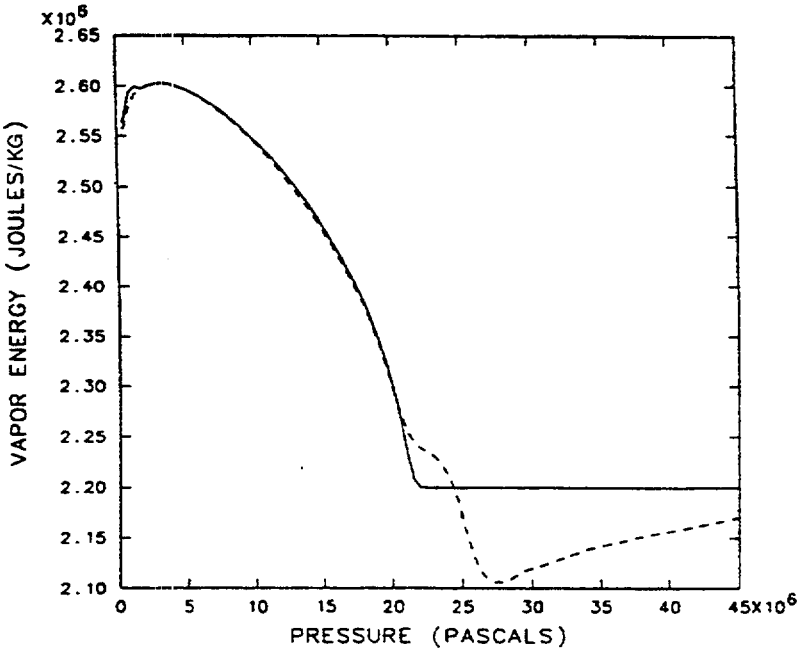

Fig. A-3. Vapor energy vs. pressure along the saturation line.
Solid: TRAC; Dashed: Sesame.

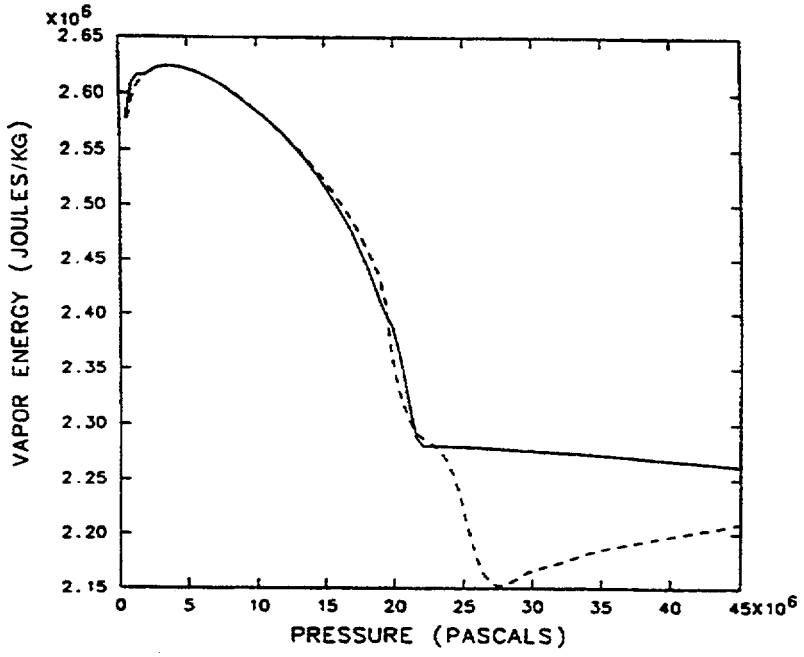

Fig. A-4. Vapor energy vs. pressure at a superheat of 8 K.
Solid: TRAC; Dashed: Sesame.

The ρ_ℓ plot of THERMO seems to agree well with the Sesame liquid density data on the saturation line over the full range of pressures $(1.0 < p_v < 4.5 \times 10^7$ Pa) (Fig. A-5.). However, significant "scalloping" in the Sesame plot is evident. This is due to errors in the EOSPAC interpolation between different data sets to generate a pressure-vs.-liquid density plot. For greater than 100 K subcooling values, the THERMO plots show general agreement with the Sesame subroutine. Here also, however, there is scalloping present. Because of the presence of this scalloping, it is difficult to establish whether there are any departures between the THERMO ρ_ℓ curve and true data points.

The THERMO plot of e_ℓ on the saturation line agrees very well with the Sesame data for liquid internal energy, at pressures below p_{crit}. In this range, accuracy appears to be far better than 1%. At pressures above p_{crit}, a departure between the two curves is noted (Fig. A-6.). In the pressure range $2.1 \times 10^7 < p_v < 3.0 \times 10^7$ Pa, fractional errors as great as 8% between the curves for the e_ℓ data are observed. These departures, however, occur when the curves of the Sesame and THERMO e_ℓ plots are rising steeply. For this reason, the size of the fractional errors is not as significant. Also, because the THERMO output variable ρ_ℓ must be input into the Sesame routine to generate the Sesame data for liquid energy and because of the aforementioned difficulty in determining the accuracy of the

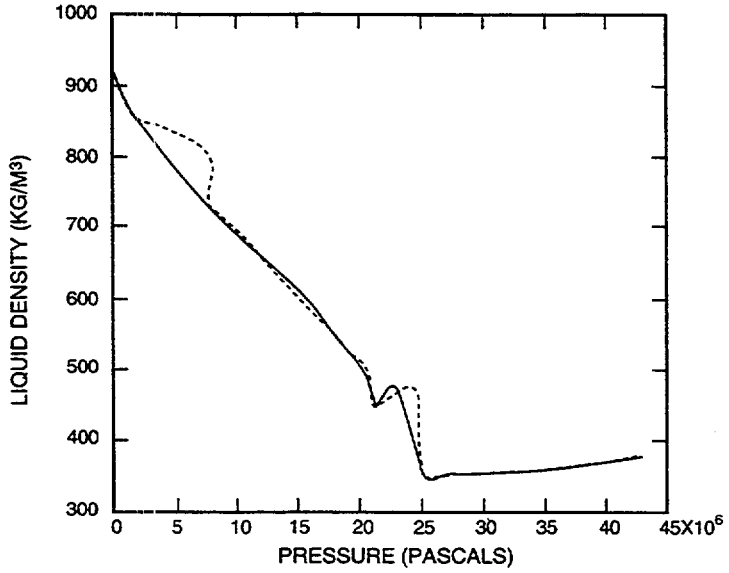

Fig. A-5. Liquid density vs. pressure along the saturation line.
Solid: TRAC; Dashed: Sesame.

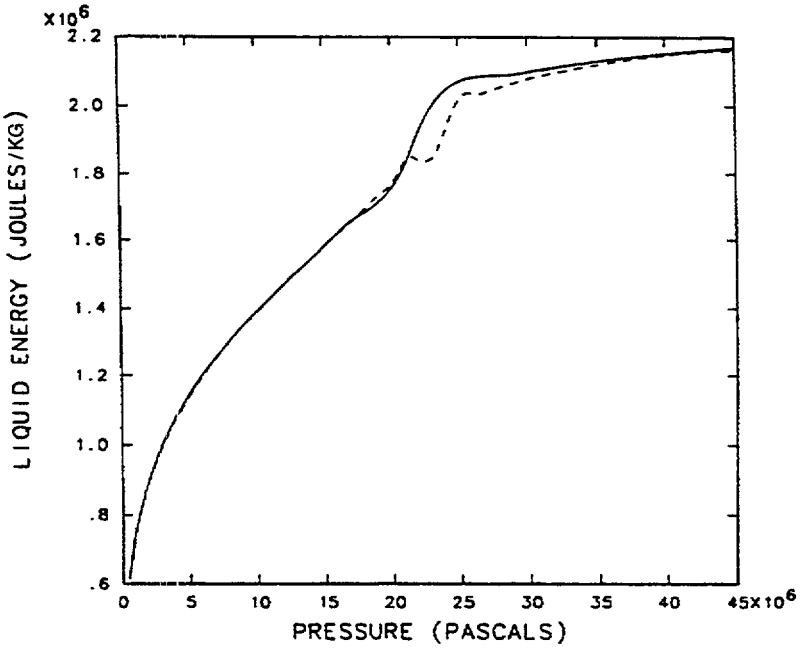

Fig. A-6. Liquid energy vs. pressure along the saturation line.
Solid: TRAC; Dashed: Sesame.

THERMO ρ_ℓ data, it follows that the validity of departures in the e_ℓ plots is also questionable. THERMO plots of subcooled liquid also follow Sesame e_ℓ data closely (Fig. A-7.). For subcooling as great as 100 K for pressures below p_{crit}, the THERMO and the Sesame plots are quite close, with fractional errors in e_ℓ between the two curves of less than 1%. The Sesame and THERMO curves, however, begin to depart in the region $p_{crit} < p_v < 3.3 \times 10^7$ Pa. Here the fractional errors in e_ℓ between the two curves reach as high as 8%, although the errors are not as significant, as they again occur where both the Sesame and the THERMO curves are rising steeply. At pressures above 3.3×10^7 Pa, the curves begin to depart again, although here reaching only a 3% fractional error.

In conclusion, for most TRAC applications, the thermodynamic and transport property routines provide realistic values up to the critical point. The simplified polynomial fits provide an efficient and low-cost method compared to such other approaches as steam-table interpolation.

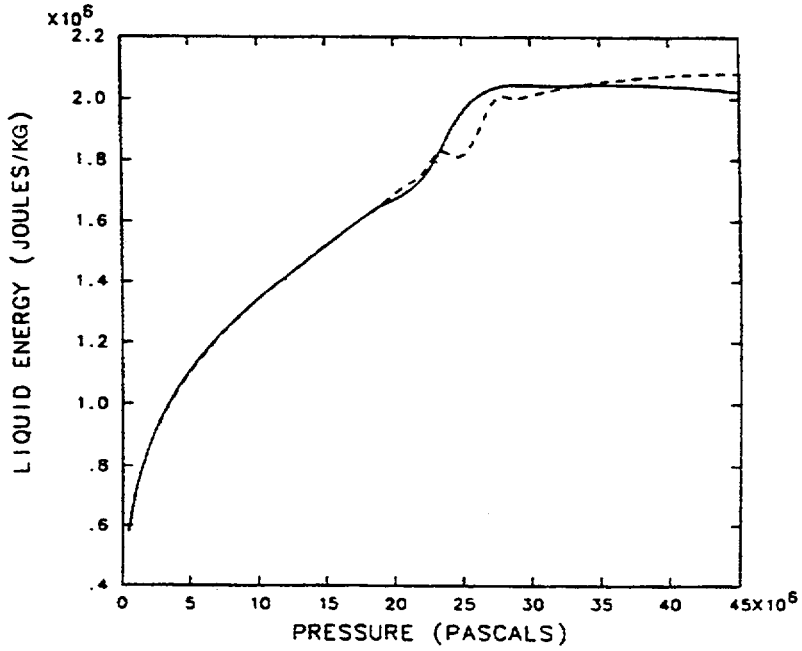

Fig. A-7. Liquid energy vs. pressure for 8 K subcooling.
Solid: TRAC; Dashed: Sesame.

REFERENCES

A-1. W. A. Coffman and L. L. Lynn, "WATER: A Large Range Thermodynamic and Transport Water Property FORTRAN-IV Computer Program," Bettis Atomic Power Laboratory report WAPD-TM-568 (December 1966).

A-2. W. C. Rivard and M. D. Torrey, "Numerical Calculation of Flashing from Long Pipes Using a Two-Field Model," Los Alamos Scientific Laboratory report LA-6104-MS (November 1975).

A-3. J. J. Martin and Y. Hou, "Development of an Equation of State for Gases," *AIChE Jour.* **1**(2), 142–151 (1955).

A-4. J. M. Richardson, A. B. Arons, and R. R. Halverson, "Hydrodynamic Properties of Sea Water at the Front of a Shock Wave," *The Journal of Chemical Physics* **15**(11), 785–794 (1947).

A-5. *ASME Steam Tables: Thermodynamic and Transport Properties of Steam,* 5th ed. (The American Society of Mechanical Engineers, New York, 1983).

A-6. K. S. Holian, "T-4 Handbook of Material Data Bases Volume 1C: Equations of State," Los Alamos National Laboratory, report LA-10160-MS (November 1984).

A-7. C. Cranfill, "EOSPAC: A Subroutine Package for Accessing the Los Alamos Sesame EOS Data Library," Los Alamos National Laboratory report LA-9728-M (August 1983).

A-8. L. Haar, J. Gallagher, and G. Kell, "A Thermodynamic Surface for Water: The Formulation and Computer Program," National Bureau of Standards report NBSIR 81-2253 (May 1981).

APPENDIX B

MATERIAL PROPERTIES

The following nomenclature is used in this appendix:

NOMENCLATURE

c_p:	specific heat capacity at constant pressure ($J \cdot kg^{-1} \cdot K^{-1}$)
f:	weight fraction
k:	Boltzmann's constant ($J \cdot K^{-1}$) in Section B.2.1. or thermal conductivity ($W \cdot m^{-1} \cdot K^{-1}$) in Sections B.2.3. and B.4.
k_{gap}:	gap-mixture thermal conductivity
$\frac{\Delta L}{L_0}$:	linear strain caused by thermal expansion
M:	molecular weight
p:	pressure (Pa)
T:	temperature (K)
x:	mole fraction
ε:	emissivity
λ:	characteristic fuel RMS roughness (m)
ρ:	density ($kg \cdot m^{-3}$)

Subscripts

c:	Celsius (°C)
f:	Fahrenheit (°F)
g:	gas gap
i:	constituent gas
PuO_2:	plutonium oxide
r:	radial direction
steam:	steam
TD:	theoretical fuel density
UO_2:	uranium oxide
z:	axial direction

Superscripts

n:	time step
$n+1$:	time-step increment

B.1. Introduction

An extensive library of temperature-dependent material properties is incorporated in the TRAC code. The entire library is accessible by the ROD and SLAB (heat-structure) components; however, the remaining components have access to structural material-property sets only. There are 12 sets of material properties that make up the library. Each set supplies values for thermal conductivity, specific heat, density, and spectral emissivity for use in the heat-transfer calculations. The first 5 sets and set 11 contain properties for nuclear-heated or electrically heated fuel-rod simulation. Included are nuclear fuels, Zircaloy cladding, fuel-cladding gap gases, electrical heater-rod filaments, electrical heater-rod insulating material, and Zircaloy dioxide. Sets 6 through 10 and set 12 are for structural materials, including stainless steels, carbon steel, and Inconels. In addition, fuel and cladding coefficients of thermal expansion obtained from MATPRO (Refs. B-1. through B-3.) subroutines FTHEX and CDTHEX are available when the gap-conductance thermal-expansion model is used.

Figure B-1. illustrates the calling tree for obtaining the property values. The subroutines MFROD and MPROP are simple processors for calculating the average temperature and calling the appropriate subroutine based on the user-specified material index. Subroutine FROD controls the fuel-cladding gap conductance and fuel-rod thermal conduction calculations.

The figure further indicates that the material properties are evaluated at the beginning of the time step, the prepass at time level n, while the gap conductance and fuel-rod thermal expansion and conduction are evaluated at the end of the time-step advancement, the postpass at time level $n+1$.

The subroutines called out in Fig. B-1. perform the following functions (we have listed the subroutines alphabetically for convenience):

CDTHEX – calculates the thermal expansion of Zircaloy cladding;

CORE1 – controls the thermal analysis for the heat-structure component including fuel and electrically heated rods, in the prepass;

CORE3 – controls the heat-structure component in the postpass;

DELTAR – calculates the fuel-cladding gap dimension in the fuel rod based on thermal expansion;

FROD – calculates the rod temperature distribution, including fuel-cladding conductance and metal-water reaction models;

FTHEX – calculates the thermal expansion of the fuel;

GAPHT – calculates the fuel-cladding gap conductance;

MBN – calculates the properties of boron nitride;

MFROD – controls the calculation of heat-structure and rod properties;

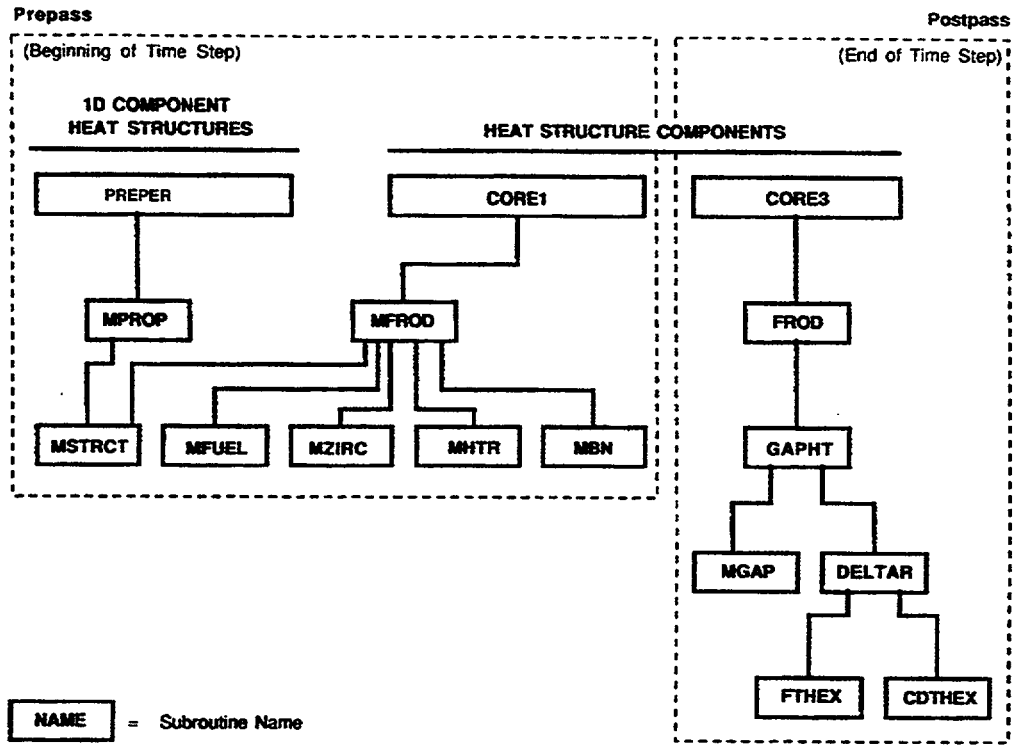

Fig. B-1. Material-properties code organization.

MFUEL – calculates the properties of UO_2 and mixed-oxide fuel;
MGAP – calculates the thermal conductivity of the gap-gas mixture;
MHTR – calculates the properties for the electrical heater element;
MPROP – controls the calculation of heat-structure properties;
MSTRC – calculates the properties of the various steels and Inconels;
MZIRC – calculates the Zircaloy and oxidized-Zircaloy properties; and
PREPER – controls the prepass calculations for all 1D components.

The material indexes in the library are

1 – mixed-oxide fuel;
2 – Zircaloy;
3 – fuel-clad gap gases;
4 – boron-nitride insulation;
5 – Constantan/Nichrome heater coil;
6 – stainless steel, type 304;
7 – stainless steel, type 316;

8 – stainless steel, type 347;
9 – carbon steel, type A508;
10 – Inconel, type 718;
11 – Zircaloy dioxide; and
12 – Inconel, type 600.

Gap-gas properties are calculated only when the dynamic fuel-cladding-gap HTC option is used (NFC = 1). Also, while all properties include an emissivity for doing a radiative-heat-transfer calculation, the calculation is only done in connection with the gap-conductivity calculation. The film-boiling heat-transfer model also includes a radiative-heat-transfer calculation, but the emissivity is specified in connection with that model (see Appendix F).

B.2. Nuclear Fuel Mixed-Oxide Properties

Subroutine MFUEL calculates the properties for mixed-oxide (UO_2 and PuO_2) nuclear fuels. Values obtained are influenced by three user-specified input variables: the fraction of theoretical density, the fraction of plutonium dioxide in the fuel, and the fuel burnup. Property changes upon melting are not included in this code version.

B.2.1. Density

The mixed-oxide fuel density is calculated with a correction factor to account for thermal expansion, which is assumed to be axisymmetric, as

$$\rho = \frac{d}{\left(1+3\frac{\Delta L}{L_0}\right)} \quad ,$$

where

ρ = density $(\mathrm{kg \cdot m^{-3}})$,

d = $f_{TD}\left[\left(1-f_{PuO_2}\right)\rho_{UO_2}+f_{PuO_2}\rho_{PuO_2}\right]$,

f_{TD} = fraction of theoretical fuel density,

f_{PuO_2} = weight fraction of PuO_2 in the fuel,

ρ_{UO_2} = 1.097×10^4 $(\mathrm{kg \cdot m^{-3}})$,

ρ_{PuO_2} = 1.146×10^4 $(\mathrm{kg \cdot m^{-3}})$, and

$\frac{\Delta L}{L_0}$ = linear thermal expansion.

The value calculated for the linear thermal expansion is based on the following MATPRO formulation [Ref. B-1., Eq. (A-4.1)]

$$\frac{\Delta L}{L_0} = K_1 T - K_2 + K_3 \exp\left(-E_D / kT\right) \quad ,$$

where

$\frac{\Delta L}{L_0}$ = inner strain caused by thermal expansion (equal to 0 at 300 K, unitless),
T = temperature (K), and
k = Boltzmann's constant (1.38×10^{-23} J·K^{-1}) .

The constants K_1, K_2, K_3, and E_D are listed below.

Constants	Uranium Dioxide	Mixed Oxides	Units
K_1	1.0×10^{-5}	9.0×10^{-6}	K^{-1}
K_2	3.0×10^{-3}	2.7×10^{-3}	Unitless
K_3	4.0×10^{-4}	7.0×10^{-2}	Unitless
E_D	6.9×10^{-20}	7.0×10^{-20}	J

B.2.2. Specific Heat

The following mixed-oxide fuel-specific heat correlations are taken from the MATPRO reports [Ref. B-1.; Ref. B-2., Eq. (A-1.1)]:

$$c_p = 15.496 \left\{ \frac{b_1 b_4^2 \exp(b_4 / T)}{T^2 \left[\exp(b_4 / T) - 1\right]^2} + 2 b_2 T + \frac{b_3 b_5}{b_6 T^2} \exp(-b_5 / b_6 T) \right\} \quad ,$$

where c_p = specific heat capacity (J·kg^{-1}·K^{-1}) and T = fuel temperature (K). The constants b_1 through b_6 are listed below.

Constants	Uranium Dioxide (Ref. B-1.)	Mixed Oxides (Ref. B-2.)
b_1	19.145	19.53
b_2	7.8473×10^{-4}	9.25×10^{-4}
b_3	5.6437×10^{6}	6.02×10^{6}
b_4	535.285	539.0
b_5	37694.6	40100.0
b_6	1.987	1.987

The resulting correlation for c_p for uranium dioxide is essentially that given in the latest revision of the MATPRO document [Ref. B-3., Eq. (A-1.8)].

B.2.3. Thermal Conductivity

The mixed-oxide fuel thermal conductivity correlations are taken from the MATPRO report [Ref. B-2., Eqs. (A-2.1a) and (A-2.1b)] and include porosity and density correction factors. For $T_c \le T_1$,

$$k = c\left[\frac{c_1}{c_2 + T_c} + c_3 \exp(c_4 T_c)\right] ,$$

and for $T_c > T_1$,

$$k = c\left[c_5 + c_3 \exp\left(c_4 T_c\right)\right] ,$$

where

T_c = temperature (°C) ,

$$c = 100.0\left[\frac{f_{TD}}{1-\beta(1-f_{TD})}\left(\frac{1+0.04\beta}{0.96}\right)\right]$$ if using mixed-oxide fuel,

$$c = 100.0\left[\frac{1-\beta(1-f_{TD})}{1-0.05\beta}\right]$$ if using uranium dioxide fuel,

$\beta = c_6 + c_7 T_c$, and

f_{TD} = fraction of theoretical fuel density.

The constants c_1 through c_7 and T_1 are listed below.

Constants	Uranium Dioxide (Ref. B-1.)	Mixed Oxides (Ref. B-2.)
c_1	40.4	33.0
c_2	464.0	375.0
c_3	1.216×10^{-4}	1.54×10^{-4}
c_4	1.867×10^{-3}	1.71×10^{-3}
c_5	0.0191	0.0171
c_6	2.58	1.43
c_7	-5.8×10^{-4}	0.0
T_1 (°C)	1650.0	1550.0

The mixed-oxide values for the constants c_6 and c_7 above are from the coding shown in Ref. B-2. (Table A-2. III).

B.2.4. Spectral Emissivity

The uranium-dioxide spectral emissivity is calculated as a function of temperature based on the MATPRO correlations (Ref. B-2., Appendix A, Section 3.1, p. 29).

The following values for uranium dioxide and mixed oxide fuels are assumed equivalent:

$$\varepsilon = 0.8707 \qquad \text{for } T \le 1000\ \text{K},$$

$$\varepsilon = 1.311 - 4.404 \times 10^{-4} T \qquad \text{for } 1000 < T \le 2050\ \text{K},$$

and

$$\varepsilon = 0.4083 \qquad \text{for } T > 2050\ \text{K}.$$

B.3. Zircaloy Cladding Properties

Subroutine MZIRC calculates the properties for Zircaloy and oxidized Zircaloy cladding. The values obtained are for Zircaloy-4. Zircaloy-2 properties are assumed to be identical. The equations used are based on the correlations in the MATPRO report (Ref. B-2.). The only difference in properties between Zircaloy and oxidized Zircaloy is in the thermal conductivity.

B.3.1. Density

Zircaloy cladding exhibits an asymmetric thermal-expansion behavior. Thermal expansion is calculated in the radial and axial directions, and these effects are included in the density calculation as follows:

$$\rho = \frac{6551.4}{1+\left[2\left(\frac{\Delta L}{L}\right)_r + \left(\frac{\Delta L}{L}\right)_z\right]} \ ,$$

where

$$\left(\frac{\Delta L}{L}\right)_r = -2.373\times10^{-4} + 6.721\times10^{-6} T_c$$

and

$$\left(\frac{\Delta L}{L}\right)_z = -2.506\times10^{-5} + 4.441\times10^{-6} T_c \ ,$$

for $T \le 1073.15$ K;

$$\left(\frac{\Delta L}{L}\right)_r = 5.1395\times10^{-3} - 1.12\times10^{-5}(T - 1073.15)$$

and

$$\left(\frac{\Delta L}{L}\right)_z = 3.5277 \times 10^{-3} - 1.06385 \times 10^{-5}(T - 1073.15)$$

for $1073.15 < T \leq 1273.15$ K; and

$$\left(\frac{\Delta L}{L}\right)_r = -6.8 \times 10^{-3} + 9.7 \times 10^{-6} T_c$$

and

$$\left(\frac{\Delta L}{L}\right)_z = -8.3 \times 10^{-3} + 9.7 \times 10^{-6} T_c \quad ,$$

for $T > 1273.15$ K; where T = temperature (K) and T_c = temperature (°C).

B.3.2. Specific Heat

Because Zircaloy undergoes a phase change (alpha to beta) from 1090 to 1248 K, with a resultant sharp spike in the specific-heat value during the transition, the specific heat is calculated by linear interpolation. Table B-1. is used for $T \leq 1248$ K. For $T > 248$ K, $c_p = 356$ J · kg^{-1} · K^{-1}.

TABLE B-1.
Zircaloy Specific Heat vs. Temperature for the α Phase and the Transition to the β Phase

T (K)	c_p (J · kg^{-1} · K^{-1})
300	281
400	302
640	381
1090	375
1093	502
1113	590
1133	615
1153	719
1173	816
1193	770
1213	619
1233	469
1248	356

B.3.3. Thermal Conductivity

Four-term polynomials are used to calculate the Zircaloy and oxidized Zircaloy thermal conductivities. The Kelvin temperature is the independent variable; the polynomial constants are listed below.

Constants	Zirconium	Zirconium Dioxide
a_0	7.51	1.96
a_1	2.09×10^{-2}	-2.41×10^{-4}
a_2	-1.45×10^{-5}	6.43×10^{-7}
a_3	7.67×10^{-9}	-1.95×10^{-10}

The form of the polynomial used in this section and in the subsequent material-properties sections is

$$y = a_0 + a_1 x + a_2 x^2 + \ldots + a_m x^m \quad .$$

B.3.4. Spectral Emissivity

The emissivity of Zircaloy and the emissivity of Zircaloy oxide are temperature-dependent. For simplicity, a constant value of $\varepsilon = 0.75$ is used.

B.4. Fuel-Cladding Gap-Gas Properties

Subroutine MGAP calculates values for the gap-gas-mixture thermal conductivity that are used in predicting gap HTCs. The method is taken from the MATPRO report (Ref. B-1.) and is based on calculating mixture values for seven possible constituent gases as follows:

$$k_{gap} = \sum_{i=1}^{n} \left(\frac{k_i x_i}{x_i + \sum_{\substack{j=1 \\ j \neq 1}}^{n} \Psi_{ij} x_j} \right) ,$$

where

k_{gap} = gap mixture thermal conductivity $(W \cdot m^{-1} \cdot K^{-1})$,

$$\psi_{ij} = \phi_{ij}\left[1+2.41\frac{\left(M_i - M_j\right)\left(M_i - 0.142M_j\right)}{M_j\left(M_i + M_j\right)^2}\right] ,$$

$$\phi_{ij} = \frac{\left[1+\left(\frac{k_i}{k_j}\right)^{1/2}\left(\frac{M_i}{M_j}\right)^{1/4}\right]^2}{2^{3/2}\left(1+\frac{M_i}{M_j}\right)^{1/2}} ,$$

k_i = constituent gas thermal conductivity $(\mathrm{W \cdot m^{-1} \cdot K^{-1}})$, M_i = constituent gas molecular weight, and x_i = constituent gas mole fraction. In the code $2^{3/2}$ is approximated as 2.8284.

The seven constituent gases considered are helium, argon, xenon, krypton, hydrogen, air/nitrogen, and water vapor. Except for water vapor, their thermal conductivities are defined as

$$k = aT^b ,$$

where T is the gap-gas temperature (K). The constants in the above thermal conductivity equation for the various gases are listed below.

Gas	a	b
helium	3.366×10^{-3}	0.668
argon	3.421×10^{-4}	0.701
xenon	4.0288×10^{-5}	0.872
krypton	4.726×10^{-5}	0.923
hydrogen	1.6355×10^{-3}	0.823
air/nitrogen	2.091×10^{-4}	0.846

For water vapor the following correlation is used:

$$k_{\text{steam}} = (-2.8516 \times 10^{-8} + 9.424 \times 10^{-10}T - 6.004 \times 10^{-14}T^2)\frac{p}{T}$$
$$+ \frac{1.009p^2}{T^2(T-273)^{4.2}} + 8.4083 \times 10^{-3} + 1.19998 \times 10^{-5}T$$
$$+ 6.706 \times 10^{-8}T^2 + 4.51 \times 10^{-11}T^3 ,$$

where p is the gap-gas pressure (Pa).

When the gap dimension shrinks to the order of the gas mean-free path, a correction factor is applied to the light-gas thermal conductivities to account for the change in energy exchange between the gas and the surface. Again, using the MATPRO recommendations (Ref. B-1.), the correction factor for hydrogen and helium is

$$k = \frac{k_i}{1 + f k_i} \quad ,$$

where

$$f = \frac{0.210\ 3\ \sqrt{T_g}}{p_g \lambda} \quad ,$$

T_g is the average gap-gas temperature (K), p_g is the gap-gas pressure, and λ is the characteristic fuel RMS roughness equal to 4.389×10^{-6} m. The correction is only made for hydrogen and helium; no correction is applied to the other component gases.

B.5. Electrical Fuel-Rod Insulator (BN) Properties

Subroutine MBN calculates values for boron nitride insulators that are used in electrically heated nuclear fuel-rod simulators. Magnesium oxide insulators are assumed to have roughly equivalent values.

B.5.1. Density

A constant value of 2002 $kg \cdot m^{-3}$ from Ref. B-4. is used.

B.5.2. Specific Heat

A four-term polynomial is used to calculate the specific heat. The independent variable is temperature in degrees Fahrenheit, and the constants, which are modifications of those reported in an EPRI report (Ref. B-5.), are listed below.

a_0	a_1	a_2	a_3
760.59	1.7955	-8.6704×10^{-4}	1.5896×10^{-7}

B.5.3. Thermal Conductivity

The boron-nitride thermal-conductivity calculation, based on a conversion to SI units of a curve fit reported in Ref. B-6., is

$$k = 25.27 - 1.365 \times 10^{-3}\ T_f \quad ,$$

where k is the thermal conductivity ($W \cdot m^{-1} \cdot K^{-1}$) and T_f is the temperature (°F).

B.5.4. Spectral Emissivity

A constant value of unity is used for the boron nitride spectral emissivity.

B.6. Electrical Fuel-Rod Heater-Coil (Constantan) Properties

Subroutine MHTR calculates property values for Constantan heater coils as used in electrically heated nuclear fuel-rod simulators. We assume that Nichrome coils, used in some installations in place of Constantan, have similar properties. The correlations used are from Ref. B-6.

B.6.1. Density

A constant value of 8393.4 $kg \cdot m^{-3}$ is used.

B.6.2. Specific Heat

The specific heat is

$$c_p = 110\ T_f^{0.207\ 5} \quad ,$$

where c_p is the specific heat $(J \cdot kg^{-1} \cdot K^{-1})$ and T_f is the temperature (°F).

B.6.3. Thermal Conductivity

The thermal conductivity is

$$k = 29.18 + 2.683 \times 10^{-3}\ (T_f - 100) \quad ,$$

where k is the thermal conductivity $(W \cdot m^{-1} \cdot K^{-1})$ and T_f is the temperature (°F).

B.6.4. Spectral Emissivity

A constant value of unity is used.

B.7. Structural Material Properties

Subroutine MSTRCT supplies property values for six types of structural materials normally used in LWRs: stainless steel, type 304; stainless steel, type 316; stainless steel, type 347; carbon steel, type A508; and Inconel, types 718 and 600. These properties were obtained from Refs. B-6. through B-8. A tabulation of the correlations used is given in Tables B-2. through B-7.

TABLE B-2.
Structural Material Properties
Stainless Steel, Type 304

Property	Independent Variable	Polynomial Constants	Reference Number
ρ	T	$a_0 = 7984.0$ $a_1 = -2.651 \times 10^{-1}$ $a_2 = -1.158 \times 10^{-4}$	B-7.
c_p	T_f	$a_0 = 426.17$ $a_1 = 0.43816$ $a_2 = -6.3759 \times 10^{-4}$ $a_3 = 4.4803 \times 10^{-7}$ $a_4 = -1.0729 \times 10^{-10}$	B-7.
k	T	$a_0 = 8.116$ $a_1 = 1.618 \times 10^{-2}$	B-7.
ε	—	$a_0 = 0.84$	B-7.

ρ = density ($kg \cdot m^{-3}$)

c_p = specific heat ($J \cdot kg^{-1} \cdot K^{-1}$)

k = thermal conductivity ($W \cdot m^{-1} \cdot K^{-1}$)

T = temperature (K)

T_f = temperature (°F)

$y = a_0 + a_1 x = a_2 x^2 + \ldots + a_m x^m$

TABLE B-3.
Structural Material Properties
Stainless Steel, Type 316

Property	Independent Variable	Polynomial Constants	Reference Number
ρ	T	$a_0 = 8084.0$ $a_1 = -4.209 \times 10^{-1}$ $a_2 = -3.894 \times 10^{-5}$	B-8.
c_p	T_f	$a_0 = 426.17$ $a_1 = 0.43816$ $a_2 = -6.3759 \times 10^{-4}$ $a_3 = 4.4803 \times 10^{-7}$ $a_4 = -1.7029 \times 10^{-10}$	B-8.
k	T	$a_0 = 9.248$ $a_1 = 1.571 \times 10^{-2}$	B-8.
ε	—	$a_0 = 0.84$	B-8.

ρ = density ($kg \cdot m^{-3}$)

c_p = specific heat ($J \cdot kg^{-1} \cdot K^{-1}$)

k = thermal conductivity ($W \cdot m^{-1} \cdot K^{-1}$)

T = temperature (K)

T_f = temperature (°F)

$y = a_0 + a_1 x = a_2 x^2 + \ldots + a_m x^m$

TABLE B-4.
Structural Material Properties
Stainless Steel, Type 347

Property	Independent Variable	Polynomial Constants	Reference Number
ρ	T	$a_0 = 7913.0$	B-6.
c_p	$(T_f - 240)$	$a_0 = 502.416$ $a_1 = 0.0984$	B-6.
k	T_f	$a_0 = 14.1926$ $a_1 = 7.269 \times 10^{-3}$	B-6.
ε	—	$a_0 = 0.84$	B-6.

ρ = density ($kg \cdot m^{-3}$)

c_p = specific heat ($J \cdot kg^{-1} \cdot K^{-1}$)

k = thermal conductivity ($W \cdot m^{-1} \cdot K^{-1}$)

T = temperature (K)

T_f = temperature (°F)

$y = a_0 + a_1 x = a_2 x^2 + \ldots + a_m x^m$

TABLE B-5.
Structural Material properties
Carbon Steel, Type A508

Property	Independent Variable	Polynomial Constants	Reference Number
ρ	T_f	$a_0 = 7859.82$ $a_1 = -2.6428 \times 10^{-2}$ $a_2 = -4.5471 \times 10^{-4}$ $a_3 = 3.3111 \times 10^{-7}$	B-7.
c_p	T_f	$a_0 = 66.155$ $a_1 = 0.4582$ $a_2 = -6.5532 \times 10^{-4}$ $a_3 = 5.3706 \times 10^{-7}$	B-7.
k	T_f	$a_0 = 66.1558$ $a_1 = 1.4386 \times 10^{-2}$ $a_2 = -2.6987 \times 10^{-4}$ $a_3 = 1.8306 \times 10^{-6}$ $a_4 = -6.0673 \times 10^{-9}$ $a_5 = 1.0524 \times 10^{-11}$ $a_6 = -9.1603 \times 10^{-15}$ $a_7 = 3.1597 \times 10^{-18}$	B-7.
ε	—	$a_0 = 0.84$	B-7.

ρ = density ($kg \cdot m^{-3}$)
c_p = specific heat ($J \cdot kg^{-1} \cdot K^{-1}$)
k = thermal conductivity ($W \cdot m^{-1} \cdot K^{-1}$)
T = temperature (K)
T_f = temperature (°F)
$y = a_0 + a_1x = a_2x^2 + \ldots + a_mx^m$

TABLE B-6.
Structural Material properties
Inconel, Type 718

Property	Independent Variable	Polynomial Constants	Reference Number
ρ	T_f	$a_0 = 8233.4$ $a_1 = -1.8351 \times 10^{-1}$ $a_2 = -9.8415 \times 10^{-6}$ $a_3 = -6.5343 \times 10^{-9}$	B-7.
c_p	T_f	$a_0 = 418.18$ $a_1 = 0.1204$	B-7.
k	T_f	$a_0 = 10.8046$ $a_1 = 8.8293 \times 10^{-3}$	B-7.
ε	—	$a_0 = 0.84$	B-7.

ρ = density ($kg \cdot m^{-3}$)

c_p = specific heat ($J \cdot kg^{-1} \cdot K^{-1}$)

k = thermal conductivity ($W \cdot m^{-1} \cdot K^{-1}$)

T = temperature (K)

T_f = temperature (°F)

$y = a_0 + a_1x = a_2x^2 + \ldots + a_mx^m$

TABLE B-7.
Structural Material properties
Inconel, Type 600[a]

Property	Independent Variable	Polynomial Constants	Reference Number
ρ	T_f	$a_0 = 5.261008 \times 10^{2}$	B-7.
		$a_1 = -1.345453 \times 10^{-2}$	
		$a_2 = -1.194357 \times 10^{-7}$	
c_p	T_f	$a_0 = 0.1014$	B-7.
		$a_1 = 4.378952 \times 10^{-5}$	
		$a_2 = -2.046138 \times 10^{-8}$	
		$a_3 = 3.418111 \times 10^{-11}$	
		$a_4 = -2.060318 \times 10^{-13}$	
		$a_5 = 3.682836 \times 10^{-16}$	
		$a_6 = -2.458648 \times 10^{-19}$	
		$a_7 = 5.597571 \times 10^{-23}$	
k	T_f	$a_0 = 8.011\,332$	B-7.
		$a_1 = 4.643\,719 \times 10^{-3}$	
		$a_2 = 1.872\,857 \times 10^{-6}$	
		$a_3 = -3.914\,512 \times 10^{-9}$	
		$a_4 = 3.475\,513 \times 10^{-12}$	
		$a_5 = -9.936\,696 \times 10^{-16}$	
ε	—	$a_0 = 0.84$	B-7.

ρ = density ($kg \cdot m^{-3}$)
c_p = specific heat ($J \cdot kg^{-1} \cdot K^{-1}$)
k = thermal conductivity ($W \cdot m^{-1} \cdot K^{-1}$)
T = temperature (K)
T_f = temperature (°F)
$y = a_0 + a_1x = a_2x^2 + \ldots + a_mx^m$

a. Inconel type 600 coefficients are in British units; ρ is multiplied by 16.01846 $(kg \cdot m^{-3})/(lb_m \cdot ft^{-3})$, c_p by 4.1868×10^3 $(J \cdot kg^{-1} \cdot K)/(Btu \cdot lb_m^{-1} \cdot °F^{-1})$, and k by 1.729577 $(W \cdot m^{-1} \cdot K^{-1})/(Btu \cdot h^{-1} \cdot ft^{-1} \cdot °F^{-1})$. The conversion factor for the thermal conductivity k assumes the thermochemical Btu instead of the international Btu.

REFERENCES

B-1. D. L. Hagerman, G. A. Reymann, and R. E. Mason, "MATPRO–Version 11 (Revision 1): A Handbook of Material Properties for Use in the Analysis of Light Water Reactor Fuel Rod Behavior," EG&G Idaho, Inc. report TREE-280, Rev. 1 (NUREG/CR-0479) (February 1980).

B-2. Philip E. MacDonald and Loren B. Thompson, compilers and editors, "MATPRO–Version 09: A Handbook of Materials Properties for Use in the Analysis of Light Water Reactor Fuel Rod Behavior," EG&G Idaho, Inc. report (TREE-NUREG-1005) (December 1976).

B-3. Donald L. Hagerman, Gregory A. Reymann, and Richard E. Mason, "MATPRO-Version 11 (Revision 2): A Handbook of Material Properties for Use in the Analysis of Light Water Reactor Fuel Rod Behavior," EG&G Idaho, Inc. report TREE-1280, Rev. 2 (NUREG/CR-0479) (August 1981).

B-4. Y. S. Touloukian, editor, Thermophysical Properties of High Temperature Solid Materials (MacMillan Co., New York, 1967).

B-5. "A Prediction of the SEMISCALE Blowdown Heat Transfer Test S-02-8 (NRC Standard Problem Five)," Electric Power Research Institute report EPRI/NP-212 (October 1976).

B-6. W. L. Kirchner, "Reflood Heat Transfer in a Light Water Reactor," US Nuclear Regulatory Commission report (NUREG-0106) Vols. I and II (August 1976).

B-7. J. C. Spanner, editor, "Nuclear Systems Materials Handbook—Vol. 1 Design Data," Hanford Engineering Development Laboratory report TID-26666 (1976).

B-8. "Properties for LMFBR Safety Analysis," Argonne National Laboratory report ANL-CEN-RSD-76-1 (1976).

APPENDIX C

This appendix is intentionally left blank.

APPENDIX D

IMPLICATIONS OF THE QUASI-STEADY ASSUMPTION AND THE AVERAGING OPERATORS

The coupled-equation set that combines the single-phase, multidimensional, fluid field equations for mass, momentum, and energy with the equation for heat diffusion within a bounding wall is called the conjugate problem. The transient two-phase flow problem becomes even more difficult because an additional set of field equations for the second fluid phase must be solved simultaneously together with the necessary closure relations to couple the two fluid phases. The TRAC code, as well as most other similar codes, invokes a quasi-steady approach to the heat-transfer coupling between the wall and the fluid as well as the closure relations for interfacial heat transfer and drag and wall-to-fluid drag. This quasi-steady approach assumes detailed knowledge of the local fluid parameters and ignores time dependencies such that the time rate of change in the closure relationships becomes infinite and the time constants are zero. The quasi-steady approach has the advantages of being reasonably simple and generally applicable to a wide range of problems and of not requiring previous knowledge of the given transient.

In this appendix, the quasi-steady approach and the averaging operators used in TRAC are discussed. The following nomenclature is valid for Appendix D.

NOMENCLATURE

A:	area
A_{wg}:	fraction of wall contacted by gas
A_{wl}:	fraction of wall contacted by liquid
f_ℓ:	area fraction contacted by liquid
q:	local phasic heat flux
q_{total}:	total heat flux
q':	area-averaged effective phasic heat flux
q'':	area-averaged phasic heat flux
S:	dimensionless number defined by Eq. (D-15)
t:	time
X:	generic for independent variable
Y:	generic for dependent variable
Δt *or* δt:	time-step size
θ:	ratio of transient and phenomenological time constants
τ:	transient time constraint
τ_c:	phenomenological time constant
ψ:	weighting factor between old- and new-time values

Subscripts

g:	gas
i:	independent-variable indices
ℓ:	liquid
max:	maximum
min:	minimum
qs:	quasi-steady
ss:	steady state
tr:	transient
used:	old-time weighted new-time value
w:	wall
wg:	wall-to-gas
$w\ell$:	wall to-liquid

Superscripts

n:	new-time value
$n-1$:	old-time value

An alternative to the quasi-steady approach does exist on a case-by-case basis. If the necessary initial and boundary conditions are known, the solution of the conjugate problem requires no a priori knowledge of the wall-to-fluid convective heat transfer. Studies such as those of Sucec (Refs. D-1. and D-2.) have used this latter approach to obtain both analytical and numerical solutions for many single-phase transients. The results, when compared to those using the quasi-steady approach, have led to an understanding of the conditions under which the quasi-steady approach produces valid results.

For the heat-transfer coupling between the wall and the fluid, the quasi-steady approach works well provided that the fluid responds more rapidly than the wall. For example, the fluid boundary layer responds so quickly that the surface temperature of a thick, high-conductivity wall does not have time to change. When the wall changes faster than the fluid, however, one must use transient closure relations to solve the problem accurately.

Despite the difficulties and limitations of the quasi-steady solution approach to the conjugate problem for two-phase flow, this approach is the only method available to simulate transient conditions in large, complex, two-phase systems such as a nuclear power plant. Often, in order to obtain an answer to a difficult problem, engineers apply codes like TRAC even when the quasi-steady assumption is not valid. The literature does contain many papers in which the closure relationships have been modified to

obtain agreement with what is, in fact, transient data. Although this process can provide valuable insight, the resulting relationships may be misleading and may produce inaccurate results when applied either to other transient experiments or to truly quasi-steady transients. Unfortunately, within the English literature, there are very few systematic studies of the problems inherent to the quasi-steady assumptions. The initial study by Nelson (Ref. D-3.) and the more recent work of Pasamehmetoglu and Nelson (Ref. D-4.) do address the problem. As Kuznetsov (Ref. D-5.) presented in his overview, the Soviets at least may have defined more clearly the existence of these limitations.

Section 2.1.1. indicated the importance of the quasi-steady assumption and the averaging operators (volume and temporal) on the closure relationships. While these considerations are of equal importance to all the closure relationships, it is not possible to discuss each set individually. This section will investigate those considerations relative to the wall-to-fluid heat-transfer process. Extension to the other relationships follows similar logic.

The wall-to-fluid heat transfer appears in the two-phase-fluid equation set within the total-energy equation [Eq. (2-1)] as $q_{w\ell} + q_{wg}$ and the combined-gas-energy equation [Eq. (2-2)] as q_{wg}. These terms, $q_{w\ell}$ and q_{wg}, represent the rate of sensible energy per unit volume being transferred into the phasic components of the fluid [see Eqs. (2-11) and (2-12)]. Mass transfer resulting from the superheating of a liquid and its subsequent evaporation, for example, must take place through the phasic-change equation represented by Eqs. (2-8) through (2-10). The total wall-to-fluid heat flux, $q'_{w\ell} + q'_{wg}$ is also required in order to provide the boundary condition necessary for the solution of all structures exposed to the fluid.

Perhaps the easiest way to envision these phasic terms arising is to realize that, within the volume-averaged equations, the total surface area over which one integrates can be decomposed into two parts [see term number 5 of Ref. D-6., Eq. (2-125), p. 70]. One part has liquid contacting it while the other has gas contacting it, so that

$$A_w = A_{w\ell} + A_{wg} \ . \tag{D-1}$$

Thus,

$$\int_{A_w} q dA = \int_{A_{w\ell}} q dA + \int_{A_{wg}} q dA \ . \tag{D-2}$$

By defining the following terms,

$$\int_{A_{w\ell}} q dA \equiv q''_{w\ell} A_{w\ell} \ , \tag{D-3}$$

$$\int_{A_{wg}} q dA \equiv q''_{wg} A_{wg} \ , \tag{D-4}$$

and

$$\int_{A_w} q dA \equiv q_{\text{total}} A_w \ , \tag{D-5}$$

Eq. (D-2) becomes

$$q_{\text{total}} = q'_{wg} + q'_{w\ell} = q''_{w\ell} f_\ell + q''_{wg}(1 - f_\ell) \ , \tag{D-6}$$

where

$$f_\ell = A_{w\ell} / A_w \ .$$

Integration of Eqs. (D-2) through (D-6) with respect to time is an obvious step not shown here and produces "volume-time" averaged quantities required by the two-phase conservation equations [Eqs. (2-1) through (2-6)]. The time interval δt over which the integration is performed must meet those requirements described by Bergles et al. (Ref. D-6., pp. 70–71). The right-hand sides of Eqs. (D-3) through (D-5) and Eq. (D-6) are assumed to reflect the temporal averaging without any further notation change.

The influence of the spatial-averaging operator is realized principally through its influence in data reduction and is therefore inherent within the closure relationships. The code makes no checks to investigate the influence of the spatial averaging, and we delay further discussion of this effect until Appendix F, Section F.2.

A temporal effect is present in both the quasi-steady assumption and the temporal-averaging operator. To further differentiate between the problems that may arise from these two sources, we will first assume that the transient under consideration is slow enough that the quasi-steady assumption is valid. The question becomes what is the relationship among the time-step size desired by the code, Δt, the time constant of the physical phenomena, τ_c (the minimum time of integration for the temporal averager), and the time constant of the transient, τ (some fraction of this time will be the maximum time of integration for the temporal averager). This relationship is the point raised by Bergles et al. (Ref. D-6., pp. 70-71), which was noted earlier. Nelson (Ref. D-3., p. 1133) further refined the question concerning the minimum time of integration, denoted as δt_{min}, by pointing out that δt_{min} must include a sufficient number of events of the governing phenomena, reflected by τ_c, to make the integral "independent" of time. Therefore, the question becomes what should happen when $\Delta t < \delta t_{\text{min}}$ or $\Delta t > \tau$.

Generally, the second part of the above question, $\Delta t > \tau$ is not important in TRAC because calculations are controlled frequently by the rate of change of the quantities. In the future, however, as time-step sizes continue to increase as a result of improved numerics, this portion of the question may become more important. For TRAC, the first part of the question is important and is a condition that frequently arises in the code. Again, Nelson (Ref. D-3., pp. 1127–1129) has pointed out that in addressing this question, we must decide which of two questions we wish to answer. If we wish to model the instantaneous response inside the time interval represented by $\delta t_{\min}$, a transient closure model is required even for "steady-state" conditions. In general, this representation is beyond the state of the art. Thus, only the average response during these "small" time steps, $\Delta t < \delta t_{\min}$, can be defined and the quasi-steady closure relationship should be constant over the time interval corresponding to $\delta t_{\min}$. Early in the TRAC development, we observed the effect of $\delta t_{\min}$ and developed crude averagers to minimize the observed problems. (It is not clear that early code developers had interpreted these problems as arising from this cause.) Only recently have calculations again identified these temporal-averaging problems as significant; the new observations center on noding and time-step sensitivities in the calculated results. Sections D.1. and D.2. will discuss the models currently in TRAC to address this problem of $\Delta t < \delta t_{\min}$.

In the preceding discussion, we assumed the quasi-steady assumption was valid. The question remains as to when the assumption breaks down. As pointed out by Nelson (Ref. D-3., pp. 1132-1133), one way of perceiving this breakdown arises from temporal-averaging considerations. The observed characteristic is that when Δt is decreased to the $\delta t_{\min}$, the resulting quantity will still show a sensitivity to Δt. Once this happens, the transient is a true transient. Section D.3. will discuss more recent techniques for determining when the quasi-steady assumption is valid. Because the code at this time only implements the quasi-steady assumption, we offer no alternative procedures for dealing with a true transient.

D.1. Averagers and Limiters Arising from Temporal-Averager Considerations

A potential problem that one sees in transient analysis using the quasi-steady approach is that the closure relations are free to respond instantaneously (within a single time step) to any changes occurring within the flow field. Thus, unless some type of averager and/or limiter is used, flow regimes may change instantly. While the averagers/limiters used in TRAC-PF1/MOD1 vary among closure packages, they are typically represented by the following relations. Averagers from one time step to the next generally appear as

$$Y^n_{\text{used}} = \psi Y^{n-1} + (1-\psi) Y^n \ , \tag{D-7}$$

where Y represents some closure quantity, ψ is a fraction between zero and one, and the superscripts $n-1$ and n indicate old- and new-time values of Y, respectively. The Y^n_{used} is the closure-relationship value used in the current time step and becomes Y^{n-1} for the next

time step. Thus, as ψ approaches one, Y_{used} would change very slowly, and for ψ equal to zero, Y_{used} would change instantly. Typical limiters are given as

$$Y_{min} < Y^n < Y_{max} ,$$

where Y_{min} and Y_{max} are reasonable bounds for Y and depend on the phenomenon addressed by the closure relationship.

An alternative method to these averagers and/or limiters is the use of additional transport equations within the code to convect such quantities as interfacial area or drop/bubble diameter. While these transport equations do "stabilize" the potential "instantaneous-response" problem, however, they do not directly address the problem that still exists—that the closure relationships are quasi-steady at best.

D.2. Variations in the Application of Temporal Averagers and Limiters

The problem with the above averager [given by Eq. (D-7)] is that it produces a time-averaging scheme which is time-step-size dependent. For example, if we were to run a transient calculation with a fixed time-step size of 100 ms and then repeat the calculation with a time-step size of 10 ms, we would obtain a change in the answer because of this type averager. Fortunately, this sensitivity has been found to be limited to those flow regimes where either large interfacial heat-transfer or interfacial area changes may take place. Appendix F, Section F.1.8. discusses an averager/limiter that minimizes the time-step size sensitivity and is based upon the concept that below δt_{min}, the closure property should remain constant.

Another potential problem with Eq. (D-7) can occur when Δt is very small. For example, assume that due to a rapid transient, the time-step size, Δt, is reduced by the time-step controller to 10^{-6} s. This might occur as the code limits Δt as a result of the allowable changes in the void fraction, pressure, temperature, etc. This Δt is typically much smaller than any δt that an experimentalist might use in time averaging his data. This example is another case where the code should hold this closure quantity constant. But, due to the time averaging currently used, Eq. (D-7) this quantity would be allowed to change over short time spans (remember 10 time steps would still be only 10^{-5} s) and could further aggravate the problem. In effect, the numerics of the code are being forced to track unreal physical phenomena within the time interval δt_{min} and the time-step controls may continue to prevent the time-step size from increasing.

Consequently, during transient calculations, we chose to use relaxation-type relations as limiters during transient calculations. These relaxation relationships can be cast into the following general format:

$$Y^{n-1} C_1^{-C_2 \Delta t} \le Y^n_{used} \le Y^{n-1} C_1^{C_2 \Delta t} . \qquad \text{(D-8)}$$

While this kind of approach reduces the time-step dependency of a transient solution, it does not eliminate it completely. Furthermore, C_1 and C_2 and are currently based upon engineering judgment. As our understanding of transient problems and phenomenological time constants continues to evolve, the relaxation relationships will possibly receive further improvements.

D.3. Validity of the Quasi-Steady Assumption

This section contains information on how the quasi-steady assumption should enter into the consideration of whether the use of quasi-steady closure relations is valid. The information is principally of recent origin and was unavailable to earlier code developers. It is included within this document, however, to provide a basis for understanding some problems that exist within the current code and the need for future work.

A generic and systematic discussion of the quasi-steady versus transient heat-transfer problems was provided by Nelson (Refs. D-3. and D-7.). This discussion is based upon the total rate of change of the dependent variable when the independent variable(s) is (are) under transient. For example, let us assume a simple steady-state constitutive relationship in the form

$$Y_{ss} = F(X_i) \ , \tag{D-9}$$

where i is the index denoting the different independent variables. If the independent variable, X_i, changes with time, then the time, t, must enter into the closure relationship as another independent variable as follows:

$$Y_{tr} = F(t, X_i) \ . \tag{D-10}$$

As a result, the total rate of change of the dependent variable, Y_{tr}, becomes

$$\frac{dY_{tr}}{dt} = \frac{\partial Y_{tr}}{\partial t} + \sum_{i=1}^{N} \frac{\partial Y_{tr}}{\partial X_i} \frac{dX_i}{dt} \ , \tag{D-11}$$

where N is the total number of time-dependent independent variables. In Eq. (D-11), if

$$\left| \frac{\partial Y_{tr}}{\partial t} \right| \ << \ \left| \frac{\partial Y_{tr}}{\partial X_i} \frac{dX_i}{dt} \right| \ ,$$

and

$$\left| \frac{\partial Y_{tr}}{\partial t} \right| \ << \ \left| \sum_{i=1}^{N} \left| \frac{\partial Y_{tr}}{\partial X_i} \frac{dX_i}{dt} \right| \ ,$$

then the problem becomes quasi-steady for both separate-effects and combined-effects transients. Consequently, a steady-state closure relationship may be used to quantify the transient-dependent parameter, Y_{tr}, such that

$$Y_{tr} \equiv Y_{qs} = F\{X_i(t)\} \quad . \tag{D-12}$$

Further discussion of Eqs. (D-10), (D-11), and (D-12) may be found in the studies of Nelson and Pasamehmetoglu (Refs. D-3. and D-4.). This discussion includes consideration of the time constant of the physical phenomena and the influence of the averaging operator (Ref. D-3., pp. 1132-1133). Equation (D-11) has its merits in the original discussion of the quasi-steady versus transient problems, and provides a sound mathematical basis for differentiating them. The practical use, however, of Eq. (D-11) is difficult. The different terms on the right-hand side of Eq. (D-11) cannot be readily quantified. Because the decision on whether a problem is quasi-steady is based upon the relative magnitude of these terms, Eq. (D-11) does not directly lead to a firm criterion.

A more practical equivalent to Eq. (D-11) may be developed (see Ref. D-4.) by considering Eq. (D-11) relative to a simple generic transient model. The physical model with a single independent variable (N =1) consists of a signal source that emits signals with a time-dependent property, a filter or amplifier that processes this signal in a prescribed form, and a receiver that receives the altered signals delayed by τ_c. In this simple example, τ_c may be regarded as the time required for a signal to travel from the source to the receiver. In a more general case, τ_c represents the time constant of the phenomena and may vary in time. The τ_c may be a function of the characteristic properties of the signal or the signal processor or both. This model may symbolize a more concrete example, such as the transient heat-transfer problem, in which the signal emitted may represent a time-dependent wall temperature, the processor may represent the convective heat-transfer phenomena, and the received signal may represent the fluid temperature.

From this simple model, the signal received at time t is equal to the delayed signal emitted at time t - τ_c and processed through the filter. Thus if we assume Y_{ss} to be the filter (we will determine the requirement for this assumption to be valid),

$$Y_{tr}(t,X) = Y_{ss}[X(t-\tau_c)] \; . \tag{D-13}$$

Using the Taylor series expansion for small τ_c, the right-hand side of Eq. (D-13) can be rewritten to yield

$$Y_{tr}(t,X) = Y_{ss}(X) - \tau_c \frac{dY_{ss}}{dX}\frac{dX}{dt} \; , \tag{D-14}$$

where higher-order terms are neglected. Defining a parameter S to be

$$S = \frac{X}{Y_{ss}} \frac{dY_{ss}}{dX} \quad , \tag{D-15}$$

Eq. (D-14) may be written as

$$Y_{tr}(t,X) = Y_{ss}[X(t)] \left[1 - S \frac{\tau_c}{X} \frac{dX}{dt} \right] . \tag{D-16}$$

Equation (D-16) suggests that, for the quasi-steady approach to be valid as assumed by Eq. (D-13) the following condition must be satisfied:

$$\left| \frac{dX}{dt} \frac{\tau_c}{X} \right| \quad << \quad \left| \frac{1}{S} \right| \quad , \tag{D-17}$$

where S can be calculated by using the definition given by Eq. (D-15) once the steady-state closure relationship Y_{ss} is known. When the inequality in Eq. (D-17) is satisfied, the problem is quasi-steady and

$$Y_{qs}(t,X) \cong Y_{ss}[X(t)] \quad . \tag{D-18}$$

Otherwise, the problem is a true transient. In this case, Eq. (D-18) is no longer valid, and a transient closure relationship is required.

It is important to note that Eq. (D-16) is merely an approximation for a transient closure relationship obtained by simply translating the steady-state closure relationship along the time axis by an amount τ_c. It is derived for the purpose of obtaining a criterion for limiting the quasi-steady approach. In reality, τ_c is not constant but is a function of time and of the magnitudes and time rates of changes of the dependent and independent variables. This functionality is why each transient yields a unique closure relationship. If τ_c can be appropriately correlated as a function of these variables, however, Eq. (D-16) may be used as a generic form for transient closure relationships. Equation (D-16) is a practical alternative to Eq. (D-11) because it can be used more easily to identify and quantify the time constants of the different phenomena.

Another commonly used qualitative criterion for the quasi-steady approach is in terms of the time-constants ratio. If the time constant of the transient is much greater than the time constant of the representative phenomenon, then the problem is quasi-steady. Notice that, when applied to an exponential transient in the form,

$$X = X_o \exp(\pm t / \tau) \ , \tag{D-19}$$

Eq. (D-17) reduces to

$$\left|\frac{1}{\theta}\right| \;<<\; \left|\frac{1}{S}\right| , \qquad \text{(D-20)}$$

where $\theta = \tau / \tau_c$. This example readily illustrates the concepts of time-constants ratio mentioned above, although Eq. (D-17) is not restricted to exponential transients. For an exponential decay, then, we can classify the transient problem as follows:

θ	>>	$\lvert S \rvert$	(quasi-steady)
θ	<<	$\lvert S \rvert$	(truly transient)
θ	~	$\lvert S \rvert$	(transition) .

Figure D-1. shows a tentative map for the quasi-steady criterion from Ref. D-4. In Fig. D-1., the boundaries between the different transients are tentatively assigned, assuming that << or >> means at least an order of magnitude difference. Especially, the difference between the transition and truly transient problems is not very clear but the problem is, at some point, within the transition region when the quasi-steady approach becomes invalid.

The dimensionless group on the left-hand side of Eq. (D-17) was previously discussed by Pasamehmetoglu and Gunnerson (Refs. D-8. and D-9.) in the context of transient critical heat flux (CHF). The final transient CHF correlation explicitly includes the time-constants ratio in Ref. D-10., Eq. (12). From the overview of Kuznetsov (Ref. D-5.), the Soviets appear to use a similar dimensionless group in conjunction with *unsteady problems*.[1] However, to the best of our knowledge, the English literature does not contain anything regarding the origin or the quantitative application of this dimensionless group.

D.4. Summary and Conclusions

This appendix has discussed the influence of the quasi-steady assumption and the temporal-averaging operator upon the closure relations. It has been pointed out in Sections D.1. and D.2. that most of the code's current time averagers are time-step-size insensitive. Work needs to continue in this area on either development of improved averagers or use of additional transport equations within the code to minimize the use of averagers and limiters. No estimate of how much inaccuracy is introduced into the code due to current averagers is available, but it is a function that will increase as the speed of the transient increases. The discussion of the influence of spatial averaging has been delayed until Appendix F, Section F.2., because its effects are typically included within data-reduction techniques used in correlation development.

---

1. In Soviet literature, the term *unsteady problem* is equivalent to what we refer to as a truly transient problem.

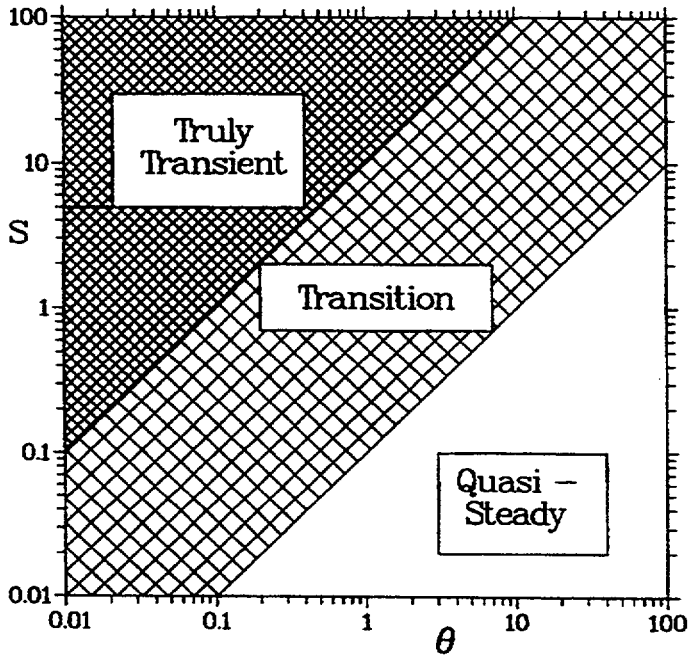

Fig. D-1. Tentative map for transient problems.

REFERENCES

D-1. J. Sucec, "Unsteady Heat Transfer Between a Fluid, With a Time Varying Temperature, and a Plate: An Exact Solution," *International Journal of Heat Mass Transfer* 18, 25–36 (1975).

D-2. J. Sucec, "Analytical Solution for Unsteady Heat Transfer in a Pipe," presented at the ASME Winter Annual Meeting (Anaheim, California, December 7-12, 1986) ASME paper 86-WA/HT-75.

D-3. R. A. Nelson, "Mechanisms of Quenching Surfaces," in *Handbook of Heat and Mass Transfer*, N. P. Cheremisinoff, Ed., Vol. 1: Heat Transfer Operations (Gulf Publishing Company, Houston, Texas, 1986), pp. 1103–1153.

D-4. K. O. Pasamehmetoglu and R. A. Nelson, "Investigation of The Quasi-Steady Approach Used In Transient Two-Phase Flow Analysis," ANS Proceedings of 1988 National Heat Transfer Conf. (Houston, Texas), HTC-Vol. 3, pp. 279-290.

D-5. Y. Kuznetsov, "Overview of Mathematical Models for Nuclear Reactor Safety Heat Transfer Codes and Experiments," in *Heat Transfer in Nuclear Reactor Safety*, S. G. Bankoff and N. H. Afgan, Eds. (Hemisphere Publishing Corporation, New York, 1982), pp. 111–132.

D-6. A. E. Bergles, J. S. Collier, J. M. Delhaye, G. F. Hewitt, and F. Mayinger, *Two-Phase Flow and Heat Transfer in the Power and Process Industries* (Hemisphere Publishing Corp., New York; McGraw-Hill Book Co., New York, 1981).

D-7. R. A. Nelson, "Forced Convective Post-CHF Heat Transfer and Quenching," *Trans. ASME, Journal of Heat Transfer* 104, 48-54 (1982).

D-8. K. O. Pasamehmetoglu, "Transient Critical Heat Flux," Ph. D. Dissertation, University of Central Florida (August 1986) (also EIES report number 86-87-1).

D-9. K. O. Pasamehmetoglu and F. S. Gunnerson, "Theoretical Considerations of Transient Critical Heat Flux," *Proceedings of the 3rd International Topical Meeting on Reactor-Thermal Hydraulics* (Newport, Rhode Island, October 15–18, 1985), Vol. 2, paper 18-F.

D-10. K. O. Pasamehmetoglu, R. A. Nelson, and F. S. Gunnerson, "A Theoretical Prediction of Critical Heat Flux in Saturated Pool Boiling During Power Transients," in *Nonequilibrium Transport Phenomena* (ASME, New York, 1987), HTD-Vol. 77, pp. 57–64.

APPENDIX E

BASIC FLOW-REGIME MAPS

To get estimates for the interfacial heat and momentum transfer needed by the fluid field equations, first we have chosen to define a flow regime. We felt that this would be more accurate than trying to arrive at these interfacial quantities directly by "full range" models, as has been done with the normal wall-shear package. The flow-regime specification described here does not, in general, affect the wall shear or wall heat transfer. Exceptions are noted in the appropriate sections of this manual.

Because the flow map is an intermediate calculation needed by the interfacial heat and momentum transfer, some comments on the correlations used in those packages will be made in this appendix to improve the reader's understanding.

In this appendix, we provide a brief description of the basic flow-regime map defined on a mass-flux void-fraction plane and employed at various parts of the code. Special flow regimes implemented for specific closure relationships are not included here. For such special flow regimes, the readers are referred to Appendix F, Section F.2., and Appendix H, Section H.1., where interfacial-shear and heat-transfer closure relationships are described.We first discuss the basis for the vertical flow map followed by that for the horizontal map. Comparisons with some other maps will be made and conclusions drawn for full-size systems.

The entire matter of flow regimes is somewhat subjective. For example, larger capped bubbles can coexist with smaller spherical or oblate bubbles. Churn flow, which is a chaotic oscillating mixture of gas and liquid with relatively indistinct entities, is considered by some to be a precursor to bubbly slug flow or more generally a transition region between bubbly/bubbly slug and annular-mist flow. Entrance effects as well as both the imagination and measurement techniques of the experimentalists can affect the flow-regime descriptions.

This is primarily an audit document for TRAC. The emphasis is on describing what is in the code rather than on reviewing the literature extensively. Excellent reviews of two-phase flow-regime maps and flow-pattern transitions are provided by Rouhani and Sohal (Ref. E-1.) and Dukler and Taitel (Ref. E-2.). We give a brief description of the flow regimes considered. Correlation comparisons are limited to relatively recent analyses of steady-state "fully developed" data. In this appendix, the following nomenclature is used.

NOMENCLATURE

A: flow area

C_o: bubble distribution parameter

D_b: bubble diameter

D_e: equivalent bubble diameter in bubbly slug flow

D_H: hydraulic diameter

D_s: maximum bubble diameter for bubbly slug interfacial-drag model

g: gravitational acceleration

G: mass flux ($kg \cdot m^{-1} \cdot s^{-1}$)

H_l: liquid height

j: superficial velocity ($m \cdot s^{-1}$)

$j_{g,\,bubble}$: terminal bubble rise velocity

N_μ: viscosity number

V: velocity

W: weighting factor

X: dummy variable representing a given closure quantity

α: void fraction

α_{gs}: average void fraction in liquid slug

Δz: elevation difference

μ: dynamic viscosity ($kg \cdot m^{-2} \cdot s^{-1}$)

ρ: density ($kg \cdot m^{-3}$)

σ: surface tension (N/m)

Subscripts

annular: annular-mist flow

bubbly: bubbly and bubbly slug flow

cr: critical

g: gas

hor: horizontal

ℓ: liquid

map: flow-regime map

r: radial or relative

s: bubbly slug flow

st: stratified flow

t: transition (churn) flow

θ: azimuthal

E.1. Basis for the Flow-Regime Map

This section discusses the original foundation (references) for the flow map used in TRAC. Since the vertical map was basically invented to fulfill a need, no original reference for this map exists.

E.1.1. Vertical Flow

We decided to develop a very simple flow-regime map for the P1 version of TRAC. It was sufficiently successful and, with the primary addition of a stratified-flow regime, the map has remained basically unchanged through all subsequent versions of the code.

We assumed that it was sufficient to consider bubbly, bubbly slug, churn (or transition), and annular-mist flows. The bubbly flow regime occurs for $\alpha \leq 0.3$, the bubbly slug regime for $0.3 < \alpha \leq 0.5$, the churn regime for $0.5 < \alpha \leq 0.75$, and the annular-mist regime for $\alpha > 0.75$. These limits were initially based on physical intuition. In addition, bubbly slug flow could not occur if the total mass flux exceeded 2700 $kg \cdot m^{-2} \cdot s^{-1}$. This limit was obtained from an article by Choe et al. for horizontal pipe flow (Ref. E-3., p. 1368, Eq. 2, where the English value $G = 2 \times 10^6$ $lb_m \cdot ft^{-2} \cdot h^{-1}$ was rounded to 2700 $kg \cdot m^{-2} \cdot s^{-1}$). We assumed that at these higher mass fluxes, the angle of inclination was irrelevant. The authors showed good agreement with the transition line for air/water flows in 1/2-, 1- and 2-in. pipes, and reasonable agreement with other experimental data with other working fluids for small-diameter pipes.

Figure E-1. shows this basic map. The crosshatched region $0.5 < \alpha \leq 0.75$ is referred to in this discussion as a churn (transition) region. The values for interfacial drag and heat transfer in TRAC are interpolated between the values at $\alpha = 0.5$ and $\alpha = 0.75$ as described in Appendices H and F, respectively, rather than determined using separate correlations specifically derived from churn flows. In a similar fashion, we do not switch from bubbly slug to dispersed bubbly flow at a total mass flux of 2700, but rather interpolate the results smoothly over the arbitrary range $2000 < G < 2700$ $kg \cdot m^{-2} s^{-1}$.

Although this map was based originally more on physical intuition than on data, it has served TRAC reasonably well for a wide variety of transients. We felt that the then-existing j_g and j_l maps, which are more complex and difficult to code and use, were not in general physically based and might give more numerical problems than this simpler map.

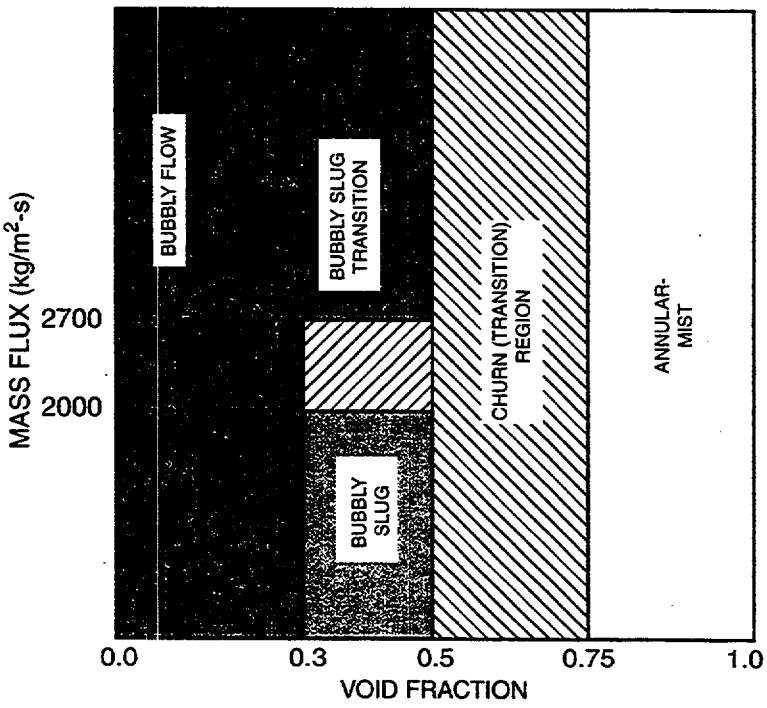

Fig. E-1. Basic flow-regime map of TRAC.

E.1.2. Horizontal Flow

The horizontal flow-regime map is identical to the vertical flow-regime map with the exception of horizontal stratification. The horizontal stratification model, used in the 3D VESSEL component of TRAC, is based upon the study of Mishima and Ishii (Ref. E-4.). Using potential flow analysis with waves of finite amplitude, Mishima and Ishii developed a relative velocity criterion above which horizontal stratification is impossible. The critical relative velocity is obtained as (Ref. E-4., Eq. 38)

$$V_{r,cr} = V_g - V_\ell = 0.487\sqrt{\frac{g(\rho_\ell - \rho_g)(D_H - H_\ell)}{\rho_g}} \quad . \tag{E-1}$$

The authors reported that this model agrees very well with a large number of experimental data and other empirical correlations (see, for instance, Fig. 4 in Ref. E-4.).

For 1D components, a simplified version of the existing flow-regime map is implemented for critical velocity. The basis is the horizontal flow-regime map that was developed by Mandhane et al. (Ref. E-5.). The authors developed their map using 5935 flow-pattern observations contained in the University of Calgary Multiphase Pipe Flow Data Bank. The parametric range of the database is reported as follows (Ref. E-5., p. 541):

Pipe i.d.:	1.27 — 16.51 cm
Liquid Density:	706 — 1010 kg/m^3
Gas Density:	0.8 — 50.6 kg/m^3
Liquid Viscosity:	3×10^{-4} — 9×10^{-2} kg/m-s
Gas Velocity:	1×10^{-5} — 2.2×10^{-5} kg/m-s
Surface Tension	0.024 — 0.103 N/m
Liquid Superficial Velocity:	0.001 — 7 m/s
Gas Superficial Velocity:	0.04 — 171 m/s

The basic flow-regime map was developed from flow-pattern observations in 1-in.-i.d. pipes with air-water flow at atmospheric pressure. The results were mapped on a phasic superficial-velocity plane, as shown in Fig. E-2. The authors also proposed fluid properties correction factors normalized with respect to the standard problem (air-water at atmospheric pressure). These factors are multiplied by either the j_ℓ or j_g superficial-velocity coordinate of a given point on the map. However, within the database examined, the authors concluded that property correction was negligible and the standard map could be used for practical purposes. Dukler and Taitel (Ref. E-2., p. 28) state that high viscosity has a strong effect on transition in or out of stratified flow. However, the viscosities quoted in the Dukler and Taitel study are a few orders of magnitude greater than water viscosities at various temperatures. As a result, we concluded that the fluid properties have little influence on transition to stratified flow.

Mandhane et al. (Ref. E-5.) also reported that the basic flow regime performed reasonably for larger-diameter pipes and no correction for pipe diameter was deemed necessary. Subsequently, Dukler and Taitel (Ref. E-2.) developed theoretical models for flow-pattern transitions in horizontal flow. The transition from stratified to elongated bubble (called intermittent flow by Dukler and Taitel) and from wave to annular-mist flow is given by (Ref. E-2., Eqs. 26 and 28)

$$V_g = \left(1-\frac{H_\ell}{D_H}\right)\sqrt{\frac{(\rho_\ell-\rho_g)gA_g}{\rho_g(dA_\ell/dH_\ell)}} \quad . \tag{E-2}$$

Note that for a rectangular channel Eq. (E-2) is almost identical to Eq. (E-1), except for the coefficient in front of the square root sign. Dukler and Taitel converted Eq. (E-2) into a liquid superficial-velocity criterion using the appropriate relationships between the liquid flow rate and liquid height. The resulting equation yielded a transition to intermittent flow criterion which is independent of gas flow rate and in perfect agreement with the constant liquid volumetric-flux criterion of Mandhane et al.

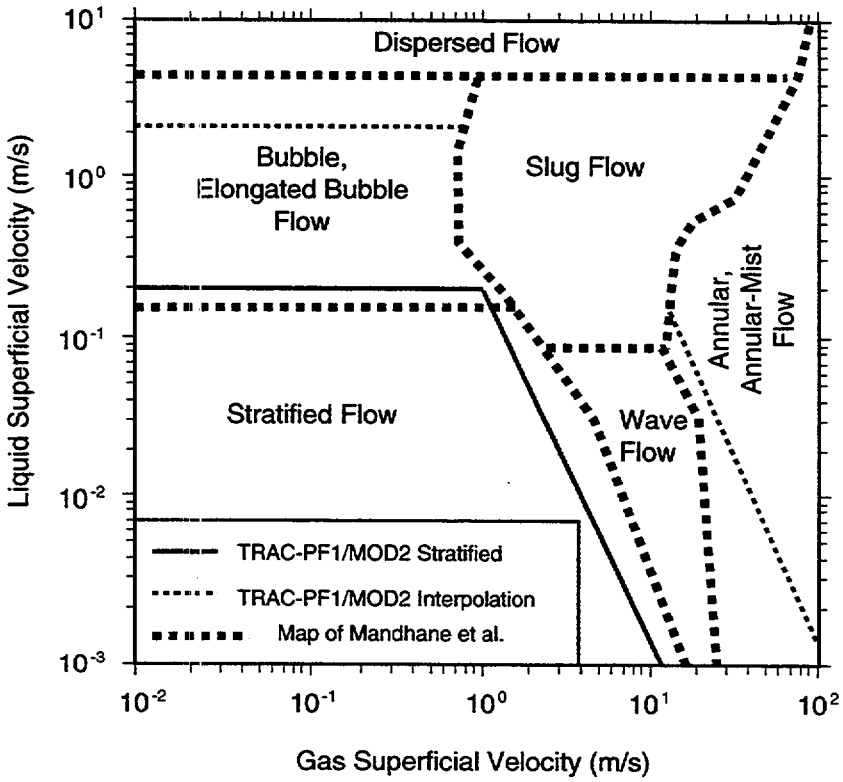

Fig. E-2. Flow-regime map of Mandhane et al., and TRAC criteria for horizontal stratified flow.

At higher void fractions, the transition between stratified flow and wave flow is formulated by Dukler and Taitel (Ref. E-2., Eq. 32) as

$$V_g = 20\sqrt{\frac{\mu_\ell(\rho_\ell - \rho_g)g}{\rho_g V_\ell}} \ . \qquad \text{(E-3)}$$

Figures 14 and 15 in Ref. E-2. show that these theoretically based equations are in good agreement with the empirical map of Mandhane et al. (Ref. E-5.) and the more recent data of Barnea et al. (Ref. E-6.).

In the code, we used simple expressions, which are in reasonable agreement with the above cited references. For transition from bubbly slug to stratified flow, we formulated the liquid critical velocity as

$$V_{\ell,cr}(1-\alpha) = 0.2 \ . \qquad \text{(E-4)}$$

The transition from annular-mist to stratified flow is formulated as

$$\alpha V_{g,cr} = \left[\frac{0.2}{V_\ell(1-\alpha)}\right]^{0.435} . \qquad \text{(E-5)}$$

The TRAC horizontal flow-regime map is illustrated in Fig. E-3. The transition between churn and stratified flows is treated as an interpolation region as described in Section E.2.7.

In TRAC, we do not have specific interfacial-shear and heat-transfer models for elongated bubbles, wave flow, or other intermittent flows. Thus, the transitions are treated as interpolation between the basic flow-map closure relationships and stratified-flow relationships. These interpolation regimes also are illustrated in Fig. E-2.

E.2. Flow-Regime Models as Coded

The basic flow map implementation is discussed in the following subsections. Note that, for the 3D VESSEL component, the flow-regime map is implemented separately in each direction, except for stratified flow, as discussed in Section E.2.7.

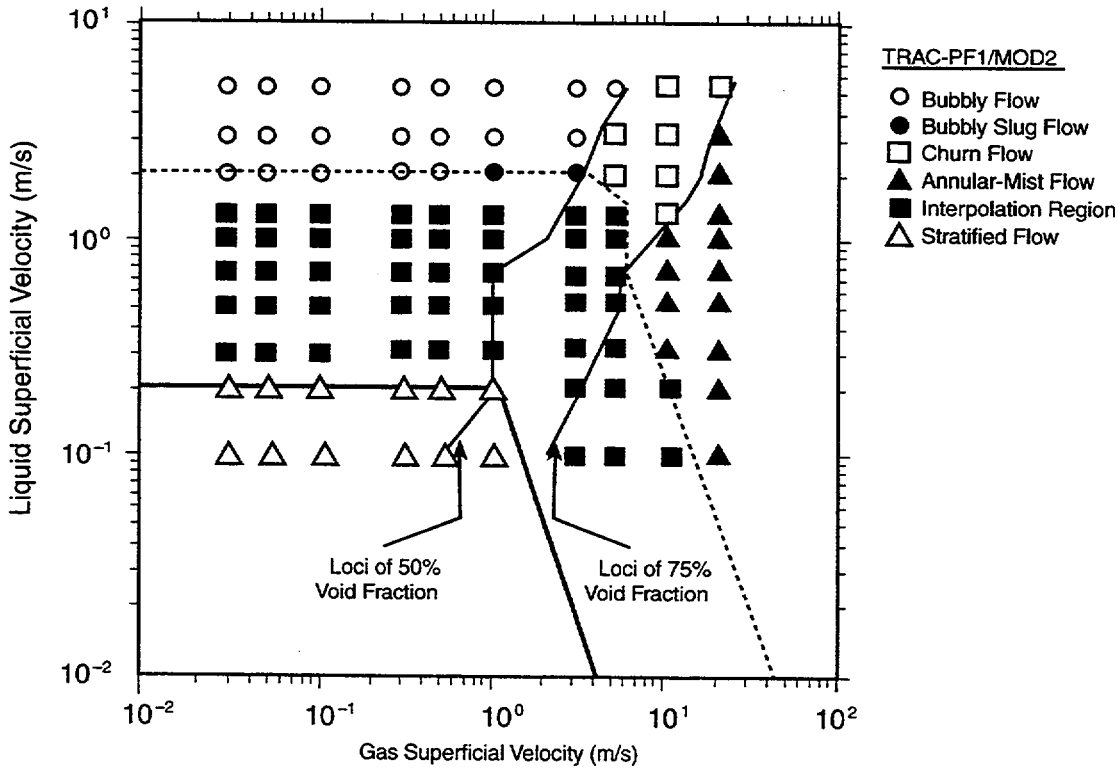

Fig. E-3. TRAC flow-pattern prediction for horizontal flow.

E.2.1. Single-Phase Flow

Single-phase gas or liquid flow occurs according to the following limits on void fraction: $\alpha < 1.0 \times 1\ 0^{-6}$ or $\alpha > 0.999999$. The limits help to provide the necessary drag calculation in the code to couple the velocity of the non-existing phase to that of the other phase and to prevent having to accelerate either the incipient bubble or droplet from zero velocity when it appears.

E.2.2. Bubbly Flow

For interfacial-shear and heat-transfer calculations, bubbly flow occurs in the following ranges of void fraction and mass flux: $1.0 \times 10^{-6} \le \alpha < 0.30$ for all values of the mass flux and $1.0 \times 10^{-6} \le \alpha \le 0.50$ for $G \ge 2700$ kg/m^2-s.

E.2.3. Bubbly Slug Flow

For interfacial-shear and heat-transfer calculations, if $G<2700$ kg/m^2-s then slugs can form in the void-fraction range of $0.30<\alpha\le0.50$. If $G>2700$ kg/m^2-s, slugs are not allowed to form. The region between void-fraction values of 0.3 and 0.5 and mass flux values of 2000 and 2700 kg/m^2-s is treated by interpolation between the bubbly flow and bubbly slug flow regimes. Note that, if the hydraulic diameter is greater than a critical diameter, slugs are replaced by cap bubbles. This transition is further discussed in Section F.1.1.1.2. In bubbly slug flow, vapor slugs and bubbles coexist.

For the interfacial drag, an equivalent bubble diameter is calculated through a linear weighting as follows:

$$D_e = (1 - W_s)D_b + W_s D_s \ , \tag{E-6}$$

where the weighting factor is defined as

$$W_s = \begin{cases} 0 & \text{if } G \ge 2700 \text{kg/m}^2\text{-s} \\ (5\alpha - 1.5)\left(\dfrac{2700 - G}{700}\right) & \text{if } 2000 < G < 2700 \text{kg/m}^2\text{-s} \\ (5\alpha - 1.5) & \text{if } G \le 2000 \text{kg/m}^2\text{-s} \end{cases} \tag{E-7}$$

and $0.0 \le W_s \le 1.0$.

For the interfacial heat-transfer calculations, the average void fraction in the liquid slug is used as the weighting factor and formulated as

$$\alpha_{gs} = \begin{cases} 0.5 & \text{if } G \ge 2700 \text{ kg/m}^2\text{-s} \\ 0.3 + 0.2\left(\dfrac{G - 2000}{700}\right) & \text{if } 2000 \le G < 2700 \text{ kg/m}^2\text{-s} \\ 0.3 & \text{if } G < 2000 \text{ kg/m}^2\text{-s} \ . \end{cases} \tag{E-8}$$

Further discussion of these models can be found in Sections F.1.1. and H.1.1.

E.2.4. Annular-Mist Flow

For interfacial-drag and heat-transfer calculations, annular-mist flow occurs if $0.75 < \alpha \leq 0.999999$. The models for partitioning the liquid phase into liquid film and droplets are discussed in Sections F.1.2. and H.1.2.

E.2.5. Mist Flow

In annular-mist flow, if one of the phasic velocities is very large, then all the liquid is entrained in terms of liquid droplets. The criterion for complete entrainment is formulated as

$$\max(V_\ell, V_g) \geq 12\left[\frac{g\sigma(\rho_\ell - \rho_g)}{\rho_g^2}\right]^{1/4} . \tag{E-9}$$

This model is further discussed in Sections F.1.2. and H.1.2.

E.2.6. Churn (Transition) Flow

Churn flow occurs if the void fraction is in the following range: $0.50 < \alpha \leq 0.75$ TRAC does not have a churn region per se but rather interpolates between the bubbly/bubbly slug values and the annular-mist values for both interfacial drag and heat transfer. The linear interpolation is done as follows:

$$X_{\text{churn}} = (1 - W_t)X_{\text{bubbly/bubbly slug}(\alpha = 0.50)} + W_t X_{\text{annular-mist}(\alpha = 0.75)} \tag{E-10}$$

where X represents the desired closure relationship for interfacial shear or heat transfer. The weighting factor is defined as

$$0 \leq W_t = \frac{\alpha - 0.5}{0.25} \leq 1 . \tag{E-11}$$

E.2.7. Horizontal Stratified Flow

For 1D components, the component inclination from horizontal must be within ±10 degrees for stratification to occur. The stratified flow is superimposed on the basic map as follows:

$$X_{\text{map/stratified}} = (1 - W_{st})X_{\text{map}} + W_{st}X_{\text{stratified}} , \tag{E-12}$$

where X represents the desired closure relationship.

For the 3D VESSEL component, the stratification in the vertical direction is allowed if there is a steep void profile in the axial direction. For this, the void fractions in two consecutive levels are checked. If α in the lower level is less than 0.1 and α in the upper level is greater than 0.9, stratification is allowed. Furthermore, the horizontal gas velocity must be less than the critical velocity defined by Eq. (E-1). The horizontal gas velocity is defined as the average vector velocity as follows:

$$V_{g,\text{hor}} = \sqrt{V_{g,r}^2 + V_{g,\theta}^2} \ , \tag{E-13}$$

where $V_{g,r}$ and $V_{g,\theta}$ are the radial and azimuthal velocity components. The stratified flow is superimposed on the basic map also through Eq. (E-12). However, the weighting factor is defined differently as

$$0 \le W_{st} = 2 - \frac{V_{g,\text{hor}}}{V_{r,cr}} \le 1 \ , \tag{E-14}$$

where $V_{r,cr}$ is obtained from Eq. (E-1) by replacing $(D_H - H_\ell)$ by the arithmetic average of Δz_s for the two levels.

For 1D components, the weighting factor is modeled as void-fraction dependent. For bubbly and bubbly slug flow ($\alpha \le 0.5$), the weighting factor is formulated as

$$0 \le W_{st,\text{bubbly}} = \frac{1}{9}\left(10 - \frac{V_\ell}{V_{\ell,cr}}\right) \le 1 \ , \tag{E-15}$$

where $V_{l,cr}$ is given by Eq. (E-4). For annular-mist flow ($\alpha > 0.75$), the weighting factor is calculated as

$$0 \le W_{st,\text{annular}} = \frac{1}{9}\left(10 - \frac{V_g}{V_{g,cr}}\right) \le 1 \ , \tag{E-16}$$

where $V_{g,cr}$ is given by Eq. (E-5). For churn flow ($0.5 < \alpha \le 0.75$), a linear weighting based upon void fraction is used to calculate the weighting factor, which yields

$$W_{st,\text{churn}} = \left(\frac{0.75 - \alpha}{0.25}\right) W_{st,\text{bubbly}} + \left(\frac{\alpha - 0.5}{0.25}\right) W_{st,\text{annular}} \ . \tag{E-17}$$

The resulting flow-regime map of TRAC for the standard problem is shown in Fig. E-3.

E.2.8. Vertical Stratified Flow

In case of liquid downflow, 1D components are allowed to stratify regardless of orientation. The critical velocities for this kind of stratification also are given by Eqs. (E-4) and (E-5). Likewise, the weighting factors are obtained from Eqs. (E-15), (E-16), and (E-17).

For 3D components, the vertical stratification criterion is obtained through comparison with a terminal bubble rise velocity, which is computed as

$$j_{g,\text{bubble}} = \frac{\alpha}{1-C_o\alpha}\sqrt{2}\left[\frac{g\sigma(\rho-\rho_g)}{\rho^2}\right]^{1/4}, \tag{E-18}$$

where

$$C_o = 1.2 - 0.2\sqrt{\frac{\rho_g}{\rho}}\ . \tag{E-19}$$

In this formulation α is set to 0.3. A stratified-flow weighting factor is calculated as

$$0 \le W_{st} = 2 - \frac{|j_g|}{j_{g,\text{bubble}}} \le 1\ . \tag{E-20}$$

This weighting factor is computed if (*i*) there is no subcooled boiling, and (*ii*) the cell void fraction is less than 0.1, or (*iii*) void fractions at two consecutive levels are less than 0.1 and greater than 0.9, respectively. Otherwise, W_{st} is set to zero. For the stratified-flow weighting factor in the axial direction, the maximum obtained from Eq. (E-20) or (E-14) is used.

E.3. Assessment and Closing Remarks

In the literature, many flow-regime maps exist that could be used for assessment. Many are not mechanistic and simply are correlations of the data, often in terms of phasic volumetric fluxes. Assumptions about the interfacial drag or relative velocity are required to convert this type of map to the *G-vs.-*α map used in TRAC. We decided not to do an extensive assessment against the *G-vs.-*α map. It is important for us to note that the flow regime per se is not used by the field equations; instead these equations use the values of the interfacial parameters. In this context, the important assessment must reside with comparisons involving interfacial drag and interfacial heat transfer. In general also, we expect the flows in a reactor system to be somewhat more homogeneous than otherwise predicted in pipes with long length-to-diameter ratios, since the primary piping of nuclear plants generally has many bends.

One of the important flow-regime transitions in two-phase flow is the slug formation. In TRAC, we restricted this formation to void fractions greater than 0.3 and mass fluxes less than 2700 kg/m^2-s The upper bound of the mass flux is obtained from the study of Choe et al. (Ref. E-3.). Their data showed reasonable agreement with this fixed mass flux value for slug formation. However, there is no reason to believe that this observation is independent of pressure and pipe diameter for the entire range of steam/water cases of interest.

For slug formation the limiting void fraction is reported to be around 0.30 by various investigators. Taitel et al. (Ref. E-7.) reported this value as 0.25. Ishii and Mishima (Ref. E-8.) employed the argument regarding the effect of agglomeration of smaller bubbles as the main mechanism in bubbly slug flow transition. They postulated that 0.3 is the maximum possible void fraction for sustaining isolated bubbles. This criterion is identical to that used in TRAC for small mass fluxes. Ishii and Mishima do not consider the inability of bubbles to coalesce at high mass fluxes even though some data that are used (Ref. E-9.) to compare with the model occasionally show this trend.

Inserting $\alpha = 0.3$ into the drift velocity equation given by Mishima and Ishii (Ref. E-9., Eq. 3) obtained the following transition criterion on the superficial-velocity plane between bubbly and slug flows (Ref. E-9., Eq. 7):

$$j_\ell = \left(\frac{3.33}{C_o} - 1\right) j_g - \frac{0.76}{C_o}\left[\frac{\rho g(\sigma_\ell - \rho_g)}{\rho_g^2}\right]^{1/4}, \tag{E-21}$$

where C_o is defined earlier by Eq. (E-19).

For slug-to-churn-flow transition, the following relationship is developed by Mishima and Ishii (Ref. E-9., Eq. 29):

$$\alpha = j_g\left[C_o(j_\ell + j_g) + 0.35\frac{gD_H(\rho_\ell - \rho_g)}{\rho_\ell}\right]^{-1}, \tag{E-22}$$

where a complicated expression for the void fraction as a function of diameter, fluid properties, and volumetric fluxes is provided in the same reference (Ref. E-9., Eq. 28). However, for all practical purposes and for a wide range of fluid properties, tube diameters, and volumetric fluxes, the critical void fraction expression can be replaced by $\alpha = 0.765$. Then, Eq. (E-22) yields the following transition criterion on the superficial-velocity plane:

$$j_\ell = \frac{1 - 0.765C_o}{0.765C_o} j_g - 0.268\frac{gD_H(\rho_\ell - \rho_g)}{\rho_\ell}. \tag{E-23}$$

For churn-to-annular-mist flow transition in small-diameter tubes, Mishima and Ishii obtained (Ref. E-9., Eq. 32)

$$j_g = (1 - \alpha)\sqrt{\frac{gD_H(\rho_\ell - \rho_g)}{\rho_g}}, \tag{E-24}$$

where α can be approximated by 0.765. However, for large-diameter tubes satisfying

$$D_H > \left(\frac{C_o}{1-0.11C_o}\right)^2 \sqrt{\frac{\sigma}{g(\rho_\ell - \rho_g)}} N_\mu^{-0.4} , \tag{E-25}$$

where the viscosity number is defined as

$$N_\mu = \mu_\ell \left[\rho_\ell \sigma \sqrt{\frac{\sigma}{g(\rho_\ell - \rho_g)}}\right]^{-1/2} , \tag{E-26}$$

the criterion becomes (Ref. E-9., Eq. 35)

$$j_g = \left[\frac{g\sigma(\rho_\ell - \rho_g)}{\rho_g^2}\right]^{1/4} N_\mu^{-0.2} . \tag{E-27}$$

Mishima and Ishii (Ref. E-9.) compared these theoretically based transition criteria with other maps and data in the literature. The criteria agreed reasonably well in most comparisons. TRAC predictions for fully developed adiabatic air-water flow in a 2.54-cm-i.d. pipe are shown in comparison with these criteria in Fig. E-4. Water and air properties are evaluated at atmospheric pressure and at 300 K. Curves A, B, C, and D in this figure correspond to the respective Eqs. (E-21), (E-23), (E-24), and (E-27). As shown, the agreement is quite good except for slug-to-churn-flow transition. However, as mentioned earlier, TRAC does not have a churn flow per se and treats this flow regime as an interpolation region. We do not have specific closure relationships for churn flow and, rather, we interpolate between bubbly/bubbly slug and annular-mist-flow closure relationships. Consequently, the transition in or out of churn flow is immaterial to the field equations.

As a closing remark on assessment, we must note that TRAC's simple flow-regime map agrees well with the observations of Jones and Zuber (Ref. E-10.).

In closing, we must note that the majority of the flow-pattern transition studies available in the open literature deal with steady-state, adiabatic, fully developed flow in pipes with large length-to-diameter ratios. The applicability of such models to real reactor flow situations, especially under transient conditions, is highly questionable. As outlined by Rouhani and Sohal (Ref. E-1.), there are very few studies dealing with the effect of the following parameters on flow-regime transition:

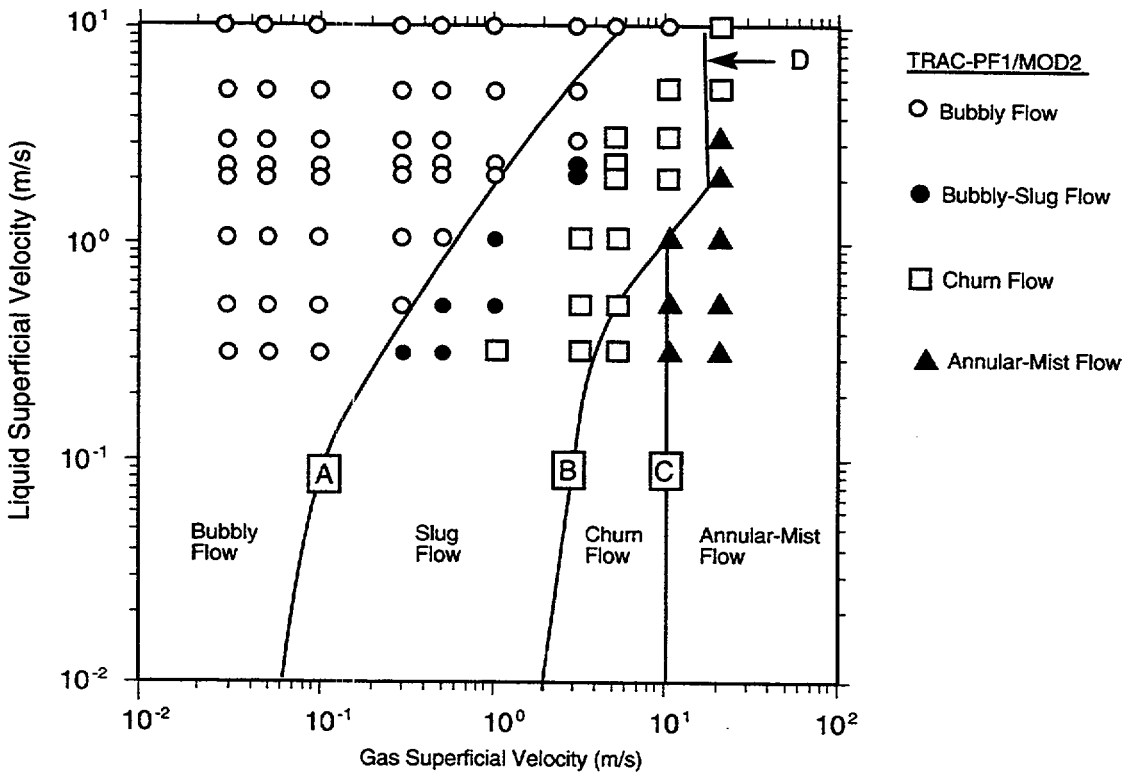

Fig. E-4. Comparison of TRAC results with the flow-pattern transition criteria of Mishima and Ishii for vertical upflow.

1. wall roughness,
2. boiling on the heater wall,
3. flow acceleration or deceleration due to local changes in volumetric fluxes or pressure resulting from condensation or boiling,
4. relaxation time constants during transient flow,
5. effect of large hydraulic diameters, and
6. entry-length effects for short pipes or channels.

All these parameters are involved in two-phase flow situations during nuclear reactor operations and cannot be neglected. Unfortunately, they are shown to have appreciable effects on the flow-regime transitions. An accurate quantification of these effects requires further studies. This is an actively evolving area of research in two-phase flow. Naturally, the models of TRAC are expected to improve along with our understanding of two-phase flow.

REFERENCES

E-1. S. Z. Rouhani and M. S. Sohal, "Two-Phase Flow Patterns: A Review of Research Results," Progress in Nuclear Energy 11, 219-259 (1983).

E-2. A. E. Dukler and Y. Taitel, "Flow Pattern Transitions in Gas-Liquid Systems: Measurements and Modeling," Chapter 1 in *Multiphase Science and Technology,* G. F. Hewitt, J. M. Delhaye, and N. Zuber, editors (Hemisphere Publishing Company, New York, 1986), Vol. 2, 1-94.

E-3. W. G. Choe, L. Weinberg, and J. Weisman, "Observation and Correlation of Flow Pattern Transitions in Horizontal Cocurrent Gas-Liquid Flow," in *Two-Phase Transport and Reactor Safety,* T. N. Veziroglu and S. Kakac, editors (Fort Lauderdale, Florida, 1976), Vol. IV, 1357-1393.

E-4. K. Mishima and M. Ishii, "Theoretical Prediction of Onset of Horizontal Slug Flow," *Trans. ASME, J. Fluids Engineering* 102, 441-445 (1980).

E-5. J. M. Mandhane, G. A. Gregory, and K. Aziz, "A Flow Pattern Map for Gas Liquid Flow in Horizontal Pipes," *Int. J. Multiphase Flow* 1, 537-553 (1974).

E-6. D. Barnea, O. Shoham, and Y. Taitel, "Flow Pattern Transition for Downward Inclined Two-Phase Flow; Horizontal to Vertical," *Chem. Eng. Sci.* 37, 741 (1982).

E-7. Y. Taitel, D. Barnea, A. E. Dukler, "Modeling Flow Pattern Transitions for Steady Upward Gas-Liquid Flow in Vertical Tubes," *AIChE J.* 26, 345-354 (1980).

E-8. M. Ishii and K. Mishima, "Study of Two-Fluid Model and Interfacial Area," Argonne National Laboratory report ANL-80-111 (NUREG/CR-1873) (1980).

E-9. K. Mishima and M. Ishii, "Flow Regime Transition Criteria for Upward Two-Phase Flow in Vertical Tubes," Int. J. Heat Mass Transfer 27, 723-737 (1984).

E-10. O. C. Jones and N. Zuber, "The Interaction between Void Fraction Fluctuations and Two-Phase Flow Patterns in Two-Phase Flow," Int. J. Multiphase Flow 2, 273-306 (1975).